Phase transition in the 1/1 approximant to the Tsai type quasicrystal : atomic structure , diffuse scattering and atomic scale simulation

Dan Liu

UNIVERSITÉ DE GRENOBLE

THÈSE

Pour obtenir le grade de

DOCTEUR DE L'UNIVERSITÉ DE GRENOBLE

Spécialité : physique des matériaux

Arrêté ministériel : 7 août 2006

Présentée par **Dan Liu**

Thèse dirigée par **Marc de Boissieu**

préparée au sein du **Laboratoire de Science et Ingénierie des Matériaux et Procédés**

dans **l'École Doctorale de Physique**

Transitions de phase dans l'approximant 1/1 des quasicristaux de type Tsai: structure atomique, diffusion diffuse et simulation à l'échelle atomique

Thèse soutenue publiquement le **14 Jan 2015**, devant le jury composé de:

Mr. Chuang Dong
Professeur à l'Université de Technologie de Dalian, Republic populaire de Chine, Examinateur, Président

Mr. Philippe Rabiller
Professeur à l'Université de Rennes 1, Institut de Physique de Rennes, Rapporteur

Mr. Vincent Fournée
Directeur de Recherche au CNRS, Institut Jean Lamour, Rapporteur

Mr. Vincent Favre Nicolin
Maître de Conférences à l'Université Joseph Fourier, Examinateur

Mr. Marc de Boissieu
Directeur de recherche au CNRS, SIMAP, Grenoble, Directeur de thèse.

Université Joseph Fourier / Université Pierre Mendès France / Université Stendhal / Université de Savoie / Grenoble INP

To my beloved families

献给亲爱的父母

Table of Contents

List of Symbols and Abbreviations

CMA	Complex metallic alloy
RTH	Rhombic triacontahedron
T_c	Phase transition temperature
XRD	X-ray diffraction
ESRF	European Synchrotron Radiation Facility
LT	Low temperature (below Tc)
HT	High temperature (above Tc)
RT	Room temperature
Soleil	French national synchrotron facility
MD	Molecular dynamic
LAMMPS	Large-scale Atomic/Molecular Massively Parallel Simulator
VASP	The Vienna *Ab initio* simulation package
s.r.o	Short range order
FT	Fourier transform
QC	Quasicrystal
AC	Approximant crystal
i-QC	Icosahedral quasicrystal
OD	Occupation domain
$\mathbf{a}_1, \mathbf{a}_2, \mathbf{a}_3$	Unit vectors of the parallel space
$\mathbf{a}_4, \mathbf{a}_5, \mathbf{a}_6$	Unit vectors of the perpendicular space
d_i^*, d_i	Unit vectors in 6D reciprocal and real space
τ	Golden mean
$\mathbf{Q}_{par}$	Physically observable component of the 6D **Q**
$\mathbf{Q}_{per}$	Virtually complementary component of the 6D **Q**
K_1, K_2	Phason elastic constant
τ	Characteristic time of phason diffusing
HRTEM	High resolution transmission electron microscopy
L and S	Long and short segments of the Fibonacci sequence

BW	Energy bandwidth
c	Light speed
ρ	The radius of the electron orbit
γ	The electron energy in units of its rest mass energy
ε_e	Energy of the electron
ω_c	Characteristic frequency for the bending magnets radiation
$\vec{S}$	Poynting vector
ϵ_0	Permittivity of free space
	Apparent acceleration
λ_u	Undulator spatial period
λ_1	Fundamental wavelength of undulator radiation
K	Inflection parameter
B_0	Maximum magnetic field
σ_n	Opening angle of the undulator radiation cone
AIMD	*ab initio* molecular dynamics
EAM	*Embedded atom model*
NVE	Micro-canonical ensemble
NVT	Canonical ensemble
CGA	Conjugate gradient algorithm
FWHM	Full width at half maximum
ξ	Correlation length

Résumé

Nous avons étudié les transitions de phases structurales dans une série d'approximant 1/1 de quasicristaux de type CdYb. Les approximants 1/1 partagent le même environnement local que les quasicristaux, mais sont périodiquement ordonnés.

L'approximant 1/1 Cd_6Tb est particulièrement intéressant puisqu'il présente un ordre magnétique à longue distance en dessous de 20K. Une transition structurale est observée à T_c=192K. Nous avons déterminé la structure atomique de la phase cubique haute température ainsi que celle de la phase monoclinique observée en dessous de T_c. La dépendance en température de la mise en ordre du tétraèdre central a été étudiée en détail entre 192 et 180K. La distorsion de l'icosaèdre Tb_{12} joue certainement un rôle important dans la formation de l'ordre magnétique à longue distance.

Nous avons confirmé que la transition de phase dans Cd_6Yb n'est pas de type [110] mais de type [111] avec un groupe d'espace de la phase basse température P2/m. De plus l'influence de l'ordre chimique sur la transition a été étudié sur Cd_6Pr and $(Cd\text{-}Mg)_6Pr$ avec 10% at. Mg. Dans ces deux cas la mise en ordre se fait le long de la direction [110].

Des simulations de dynamique moléculaire ont été conduite en utilisant des potentiels de pairs oscillant pour les phases approximantes Zn_6Sc 1/1, $Zn_{85.12}Sc_{14.88}$ 5/3, et $Zn_{85.16}Sc_{14.84}$ 8/5. Le système Zn-Sc est isostructural au système Cd-Yb et les approximant 5/3 et 8/5 ont une maille suffisamment grande pour simuler un quasicrystal de manière réaliste. Dans les trois systèmes nous avons simulés les diagrammes de diffusion diffuse pour une température comprise entre 500 et 100K.

Dans l'approximant 1/1 Zn_6Sc l'évolution du signal de diffusion diffuse est en accord avec une augmentation de l'ordre à courte distance lorsque la température diminue. La comparaison de la diffusion diffuse entre l'approximant 1/1 et l'approximant 5/3 montre clairement un excès de diffusion diffuse pour l'approximant 5/3 qui est interprété comme résultant des fluctuations de phasons.

Dans les trois approximants nous avons mis en évidence un phénomène de diffusion atomique entre le tétraèdre et le dodécaèdre. Pour l'approximant 1/1 cette diffusion se produit le long des diagonales de la maille cubique avec une énergie d'activation de l'ordre de 0.1 eV. Les simulations sur les approximants 5/3 et 8/5 ont montré que la dynamique du tétraèdre et la diffusion atomique dépendent de la complexité de la structure.

Cette étude monte que la structure des amas atomiques et leur environnement local jouent certainement un rôle important pour les mécanismes de stabilisation de ces phases.

Abstract

We have studied the structural phase transitions occurring in a series of periodic 1/1 approximant to the CdYb type quasicrystals. 1/1 approximants share the same local environment as the parent quasicrystal, yet with a periodic long range order.

The Cd_6Tb 1/1 approximant is of particular interest owing to its long range magnetic order observed below 20K. A structural phase transition is observed at T_c= 192K. The atomic structures of the high temperature cubic phase and the low temperature monoclinic phase has been determined. The temperature dependence of the central tetrahedron ordering and its connection to the phase transition has been studied in details between 192 and 180K. The distortion of the Tb_{12} icosahedron resulting from the ordering of the tetrahedron at low temperature is supposed to play a crucial role in the formation of the long range magnetic order. Diffuse scattering, characteristic of a short range order has also been observed above T_c.

For the Cd_6Yb approximant we have confirmed that the phase transition does not correspond to an ordering along $[1\bar{1}0]$. The space group of the low temperature phase is proposed as $P2/m$. Furthermore, the effects of chemical order on the ordering mechanism of the tetrahedra are investigated on Cd_6Pr and $(Cd\text{-}Mg)_6Pr$ with 10% at. Mg. The ordering scheme of both Cd_6Pr and $(Cd\text{-}Mg)_6Pr$ is of the [110] type instead of the previously claimed [111] type.

Molecular dynamic simulations are carried out on the Zn_6Sc 1/1, $Zn_{85.12}Sc_{14.88}$ 5/3, and $Zn_{85.16}Sc_{14.84}$ 8/5 approximants using an effective oscillating pair potential. The Zn-Sc system is isostructural to the Cd-Yb one and the 5/3 and 8/5 approximant have a unit cell large enough to mimic a real quasicrystal. In the three systems we have simulated the diffraction pattern as the temperature goes from 500K to 100K.

In the Zn_6Sc 1/1 approximant, the temperature dependence of the simulated diffuse scattering evidenced a short range order forming in the low temperature phase. It most likely correspond to the pretransitional short range order as observed experimentally. The comparison of the simulated diffuse scattering between the 1/1 and 5/3 approximants demonstrates an excess of diffuse scattering in the latter phase which is likely the contribution from phasons modes.

We have evidenced an atomic diffusion taking place between tetrahedra and dodecahedra in all three approximants. The long range atomic diffusion in the 1/1 approximant is only observed along space diagonal directions of the cubic cell, with an activation energy of 0.1 eV. Further investigation on the 5/3 and 8/5 approximants have shown that the orientational dynamics of the central tetrahedra as well as the atomic diffusion are dependent on the complexity of the structures.

The configuration of the clusters and their local environment are considered to play a crucial role in the stabilization mechanism of the quasicrystals and their periodic approximants.

Key words: quasicrystal approximant, quasicrystal, structure, diffuse scattering, phason, molecular dynamics

Introduction (Français)

Les composés Cd_6RE (RE= Terre rare) sont une série de composés bcc isostructuraux qui sont faits des mêmes briques élémentaires, c'est-à-dire les agrégats dits de Tsai, que les quasicristaux *i*-$Cd_{5.7}Yb$ et *i*-$Cd_{5.7}Ca$[1][2]. Bien que leur composition soit très proche des deux quasicristaux binaires sus-cités et des quasicristaux binaires magnétiques à base Cd récemment découverts [3], certaines de leurs propriétés physiques montre des différences notables. Par conséquent, une comparaison entre quasicristaux et leurs approximants peut apporter un éclaircissement important dans la compréhension des mécanismes de stabilité de ces phases complexes.

Structure atomique de la phase Cd_6RE

De manière générale, on peut décrire la structure de la phase Cd_6RE de deux manières. La première est l'empilement de 12 polyhèdres RCd_{16} où chaque atome R est entouré de 16 atomes Cd. Dans cette description, huit cubes Cd_8 peuvent être générés automatiquement, comme sur la Figures 4.1.1[4]. Ces cubes seront discutés en détails dans le chapitre sur les simulations.

La description la plus populaire et la plus largement acceptée de la phase Cd_6RE est un empilement de triacontahèdres imparfaits s'interpénétrant, connus sous le nom d'aggrégats de type Tsai, selon une structure *bcc,* comme sur les Figures 4.1.2[5]. La structure de la phase Cd_6RE se caractérise par l'absence complète d'atomes « de colle » en utilisant de tels triacontahèdres rhombiques (RTH). L'aggrégat élémentaire RTH est composé de cinq coquilles denses successives, soit 158 atomes au total. Le tetrahèdre central, désordonné car violant la symétrie globale de l'aggrégat, peut être modélisé par une dégénérescence triple des positions atomiques formant le tétrahèdre. Tous les tétrahèdres désordonnés connus de la série Cd_6RE peuvent être correctement décrits par ce modèle en augmentant successivement la taille de la dégénérescence positionnelle. De plus, le cube Cd_8 mentionné plus haut partage deux sites communs avec deux dodécahèdres adjacents le long de la grande diagonale de la maille cubique.

Des études antérieures ont montré que la transition de phase structurelle ordre – désordre est liée à la mise en ordre du tétrahèdre central. A haute température, les tétrahèdres occupent de manière dynamique toutes les orientations équivalentes, et se figent en s'ordonnant de manière antiparallèle quand la température décroit [6][7][8]. La structure de la phase monoclinique à basse température de Zn_6Sc a été déterminée par Ishimasa [8] par diffraction des rayons X sur poudre. En plus de ces résultats expérimentaux, de nombreux travaux numériques ont été faits sur Cd_6Yb et Cd_6Ca selon un calcul de premiers principes. Ces résultats confirment une petite inclinaison du tétrahèdre pour éviter une distance irréaliste avec la couche dodécahèdrique. Expérimentallement, l'inclinaison est évaluée à ~15", et un calcul *ab initio* de Hatakeyama *et al* [9] l'évalue à 6". De plus, des mesures de diffusion diffuse des rayons X [11] montrent que la longueur de corrélation à courte distance augmente rapidement lors de la mise en ordre des tétrahèdres et diverge presque à la température de transition.

La phase à basse température a été caractérisée comme étant monoclinique avec groupe d'espace *Cc* ou *C2/c* [12] et par un doublement de maille élémentaire le long de la direction [101], comme illustré sur la Figure 4.1.3. En ignorant la distortion induite par la mise en ordre des tétrahèdres, les vecteurs de base des mailles des phases à haute et basse températures sont liés par la relation suivante : $\mathbf{a_L = a_H - c_H}$, $\mathbf{b_L = b_H}$, $\mathbf{c_L = a_H + c_H}$.

Etude de la structure de l'approximant 1/1 Cd_6Tb

Cd_6Tb, un membre de la famille isostructurelle Cd_6RE, et un approximant 1/1 du quasicristal *i*-Cd-Mg-RE et des quasicristaux binaires $Cd_{5.7}Ca$ et $Cd_{5.7}Yb$ [1][2]. Une transition de phase unique à basse température a été mise en évidence dans la plupart des composés Cd_6RE par mesure de résistance électrique, diffraction électronique, mesures de chaleur spécifique et ainsi de suite [12]. Dans les travaux antérieurs, la transition de phase a été interprétée comme induite par la mise en ordre des tétrahèdres centraux de Cd4, dont l'orientation est désordonnée à haute température. Tous les approximants Cd_6RE possède le même réseau *bcc* à haute température, différant seulement légèrement par leur tétrahèdre central, qui a été étudié de manière détaillée par Gómez *et al* [4]. La mise en ordre et la phase basse température ont également été étudiées par Nishimoto *et al* [13]. La détermination de la structure à basse température a été faite sur le cristal isostructural Zn_6Sc par Ishimasa *et al* [8]. L'intérêt d'étudier Cd_6Tb ne se limite pas à la transition ordre – désordre, mais aussi à cause de l'observation inédite d'une mise en ordre magnétique à longue distance [14].

En effet, il est étonnant de trouver de telles transitions magnétiques, à 24K, 19K et 2.4K dans Cd_6Tb, qui ont été mises en évidence par des mesures de susceptibilité magnétique et de chaleur spécifique. Bien qu'on s'attende à découvrir un ordre magnétique inédit sur un cristal apériodique composé d'éléments chimiques portant un moment magnétique, jusqu'à présent tous les quasicristaux connus n'ont montré qu'au mieux un comportement de verre de spin à basse température. L'ordre magnétique à longue distance est absent non seulement dans les quasicristaux, mais également dans leurs approximants périodiques, sauf Cd_6RE. L'ordre magnétique à longue distance dans Cd_6Tb a été confirmé récemment par diffraction résonnante magnétique des rayons X par Kim *et al* [15]. La finesse des pics magnétiques correspondent à une longueur de corrélation d'au moins 500Å, et les ions Tb3+ de manière antiferromagnétique entre aggrégats voisins le long de l'axe de symétrie d'ordre 3. On peut supposer que ce cas exceptionnel est dû à la compétition entre deux interactions, c'est-à-dire les interactions Tb – Tb intra- et inter-aggrégats. Par conséquent, il est important de déterminer la structure cristalline des phases de Cd6Tb au dessus et en-dessous de *Tc*.

Nous avons mené une mesure systématique *in situ* d'un monocristal de Cd_6Tb de température ambiante jusqu'à 40K sur la ligne de lumière CRISTAL du synchrotron SOLEIL. La transition de phase structurelle est observée vers 190K par la fragmentation des pics de Bragg principaux. Les mesures de diffraction sur monocristal et sur poudre montrent toutes les deux une augmentation soudaine de la distortion monoclinique entre 190K et 184K. Une anomalie est observée vers 45K, température en-dessous de laquelle les paramètres de maille ne semblent plus évoluer. Ceci pourrait être l'explication du comportement anormal de la résistivité électronique en-dessous de ~40K.

En utilisant différents filtres d'atténuation, nous avons collecté des données dont l'intensité s'étale sur une large gamme dynamique, obtenant ainsi plus de 60000 reflexions uniques de la maille monoclinique *C2/c* de la phase basse température. Les valeurs finales *wR2* pour les affinements à température ambiante et à 40K sont de 0.0726 et 0.0905 respectivement. Conformément aux hypothèses de Tamura *et al* [14] et de Kim *et al* [15], les liaisons ioniques intra-aggrégat entre Tb3+ sont compatibles avec les distances inter-aggrégats. Dans la phase monoclinique, les interactions intra-aggrégat et inter-aggrégats deviennent plus frustrées à cause de la distortion monoclinique, ce qui joue certainement un rôle crucial dans la formation d'un ordre magnétique à longue distance.

La dépendence en température de la structure de Cd_6Tb est analysée. Une forte distortion des couches successives est observée le long de l'axe de symétrie d'ordre 3. Une investigation approfondie montre que la distortion est induite par la mise en ordre des tétrahèdres. Le comportement des paramètres de déplacement isotropique équivalent des deux sites uniques du tétrahèdre suggère que le tetrahèdre se comporte comme une seule molécule.

En regard du quasicristal, les résultats de l'approsimant 1/1 sont importants quant à l'étude de la stabilité des quasicristaux, et en particulier la phase Cd6Tb, qui réalise un ordre magnétique à longue distance en-dessous de 24K. La découverte d'une série de quasicristaux icosahèdriques binaires magnétiques ouvre la voie pour de nouvelles études sur ce comportement magnétique inédit.

Transition de phase dans Cd_6Yb

La phase Cd_6Yb a été identifiée pour la première fois en 1964 par Johnson *et al* [16]. Depuis, de nombreux efforts ont été faits pour déterminer sa structure [17][4][18]. En particulier, la découverte du premier quasicristal binaire stable $Cd_{5.7}Yb$ [2] et l'observation de la transition ordre-désordre à basse température dans Cd_6Tb [19][20] ont renouvelé l'intérêt de la communauté scientifique pour ce problème fascinant.

Nous avons fait des mesures synchrotron sur différents aspects de l'approximant 1/1 Cd_6Tb. La transition de phase est observée et la valeur de T_c est confimé vers 113K, en accord avec les mesures de résistance électrique et de chaleur spécifique [19]. La distortion de la maille est observée sur les spectres de diffraction X de poudre et les mesures de diffusion diffuse. L'apparition des réflections (6.5 7.5 0.5) et (351) indiquent que le mécanisme de la transition de phase de Cd_6Tb est différent de celui de Zn_6Sc et des autres composés Cd_6RE. La longueur de corrélation augmente rapidement en-dessous de *Tc* jusqu'à ~1200Å, ce qui correspond à l'ordre de grandeur des domaines.

Ces résultats, dans le contexte de la transition de phase ordre – désordre de l'approximant 1/1 Cd_6Yb appellent des mesures complémentaires sur ce système. Un modèle de la structure de la phase basse température et du mécanisme de transition de phase fournira certainement un éclairement approfondi sur la stabilité des approximants et quasicristaux.

Effet du Mg sur la transition de phase du Cd_6Pr

La structure du Cd_6Pr à température ambiante a été résolue en utilisant les données de diffraction de rayons X de monocristal par Gomez et Lidin [5]. Il s'agit d'un prototype de Cd_6 Y et l'occupation du tétraèdre central d'atomes a été déterminée à une valeur d'environ 0.216. La transition de phase du Cd_6Pr a été étudiée par Nishimoto *et al* [12], et une T_c d'environ 150K a été confirmée par des anomalies dans les mesures de résisitivité electrique. Il est suggéré que la superstructure est formée suivant le mécanisme décrit dans la section **4.1.** Cependant d'autres résultats ont reporté qu'un second type de mise en ordre apparait pour les Cd_6Pr et Cd_6Ce, où les tétraèdres centraux Cd4 sont orientés selon [1 1 1] et aucune déformation de la maille cristalline n'est observée à basse température [21]. De plus, il est également suggéré que l'ajout de l'élément Mg améliore la diffusion diffuse des réflections de surstructure. Par conséquent, il apparait intéressant de clarifier l'origine de la mise en ordre du tétrahèdre apparaissant pour le Cd_6Pr ainsi que le rôle du magnesium dans la diffusion diffuse des réflections de surstructure.

Des mesures de la diffusion diffuse des approximants 1/1 des systèmes Cd_6Pr et $(Cd\text{-}Mg)_6Pr$ avec 10 % at. Mg ont été effectuées dans une gamme de température comprise entre 300K et 20K sur la ligne de lumière D2AM au synchrotron ESRF. Une transition de phase est mise en évidence pour les deux systèmes et un mécanisme de mise en ordre non pas selon[1 1 1] mais selon [1 1 0] est observé. La *Tc* du Cd_6Pr est determinée entre 200K et 150K, mais des mesures plus détaillées seront nécessaires pour confirmer la valeur exacte.

Comme reporté récemment le signal associé à la surstructure du Cd_6Pr est très faible. Il est montré dans cette étude que les réflections de surstructure ne se renforcent pas à basse température, impliquant une très faible longueur de corrélation. Bien que la diffusion diffuse aux positions de surstructure du Cd_6Pr soit visible à basse température, elle n'augmente pas beaucoup avec la diminution de la température.

Des comparaisons entre le Cd_6Pr et $(Cd\text{-}Mg)_6Pr$ suggèrent que le désordre chimique joue un rôle important dans le mécanisme de mise en ordre. L'effet de substitution sur la transition de phase des approximants 1/1 à base Zn et Cd a été étudiée par Yamada et Tamura [22], où un faible pourcentage des atoms de Zn ont été remplacées par des atomes de Cu. Il a été conclu que l'ajout de l'élément Cu entraîne une occupation des sites dodécaèdraux et une suppression de la mise en ordre du tetraèdre Zn4. D' après les résultats de Lin et Corbett[23], ces alliages ternaires conservent la même symétrie et construction de cluster que l'approximant 1/1 Zn6Sc, les atomes additionnels de Cu occupant les sites Zn5, i.e, les sites dodécaèdraux. La substitution par les atomes de Cu réduit les distances de liaison entre les atomes dodécaèdriques du Zn, impliquant un volume plus faible de l'enveloppe du dodécaèdre. Néanmoins, dans notre cas, le troisième élèment Mg (~160 pm) possède un rayon atomique plus large que le Cd (~151 pm) entraînant un agrandissement de l'enveloppe du dodécaède. Par conséquent, du fait de l'effet stérique, la suppression de la mise en ordre du tétraèdre Zn4 est partiellement relachée, et d'autre part, la déformation de maille résultant de l'intéraction entre les deux enveloppes devient plus faible.

L'approximant 1/1 Zn_6Sc

La structure initiale de l'approximant 1/1 Zn_6Sc pour des simulations de dynamique moléculaire a été optimées à partir de calculs VASP. Suivant le procédé de minimisation

d'énergie, la cellule élémentaire de surstructure 4x4x4 a été dans un premier temps relaxée jusqu'à l'équilibre à 500K puis refroidie de 400K à 60K utilisant le logiciel LAMMPS. De nombreuses simulations entre 200K et 60K par pas de 10K ont été réalisées. Pour chaque température, 5 millions de pas sont calculés et 2000 configurations sont collectées pour l'analyse des données. Afin d'éviter de rester bloqué dans un minimum d'énergie local, des pas de temps plus grands ont été utilisés à basse température.

Les simulations de dynamique moléculaire du procédé de refroidissement de l'approximant 1/1 Zn6Sc ont étés réalisées en utilisant un potentiel de paire affiné par le biais d'une base de données *ab-initio*. Une comparaison détaillée avec les résultats expérimentaux pour le Zn6Sc et le Cd6M (M=Ce, Pr et Eu) est ici présentée. Le spectre de diffraction est reconstitué pour les couches *l=0 l=demi-entiers* via une transformée de Fourier. La diffusion diffuse devient ordonnée avec la réduction de la température, conséquence de la mise en ordre du tétraèdre. La mise en ordre à faible distance selon <1 1 0> est observée constituant une bonne indication de la présence d'une prétransition.

Le tétraèdre le plus interne se réoriente de manière dynamique dans la phase à haute température. Cette réorientation est ralentie avec la réduction de la température, et finit par se figer dans un état spécifique. La fréquence d'oscillation suit une règle d'Arrhenius et la barrière énergétique est determinée à une valeur de 32meV un ordre de grandeur similaire à celui obtenu expérimentalement, i.e 60 meV.

La diffusion atomique le long des diagonales d'espace de la cellule élementaire cubique est étudiée en détails. L'énergie d'activation de la diffusion atomique est confirmée autour de 106±11meV, et est pratiquement supprimée en dessous de 200K. D'autre part, la diffusion atomique décrit bien l'occupation additionnelle au centre des cubes Cd_8/Zn_8, ainsi que l'élongation des atomes partagés entre les cubes Cd_8/Zn_8 et les dodécaèdres Cd_{20}/Zn_{20} observée expérimentalement. L'apparition de la diffusion atomique est supposément reliée à la différence d'énergie potentiel entre les sites du tetraèdre et du dodécaèdre.

Modellisation de l'approximant 5/3

Les approximant de haut degré n'ont jamais été observés experimentalement. Dans ce quasicristal de la famille des Cd Yb, l'approximant de plus haut degré observé est le cubique 2/1. Nous avons donc utilisé des approximants périodiques de haut dégré pour simuler le quasicristal. En ce qui concerne les simulations de dynamique moléculaire, la modélisation de la structure est réalisée en plaçant le triacontaèdre rhombique sur les vortexs de l'approximant 5/3 est réalisée par canonical cell tilling suivie d'une procédure de décoration [24][25]. La configuration finale a été optimisée en réalisant une minimisation de l'énergie totale du système via des calculs *ab-initio* utilisant le programme de DFT VASP [26][27]. La cellule élémentaire de l'approximant 5/3 obtenu est de l'ordre de ~58.46 Å et contient plus de 10000 atomes par cellule élémentaire. Les détails de la détermination du modèle sont détaillées dans la réfèrence [24].

La simulation de dynamique moléculaire réalisée sur l'approximant 5/3 $Zn_{85.12}Sc_{14.88}$ est un refroidissement, utilisant un potentiel de paire via LAMMPS. Les résultats obtenus sont comparés avec ceux de l'approximant 1/1 ainsi qu'avec les résultats expérimentaux. Les plans

de Bragg hk0 sont reconstruits pour plusieurs températures par transformée de Fourier. De la diffusion diffuse supplémentaire est observée dans le cas de l'approximant 5/3, en accord avec les résultats expérimentaux sur le quasicristal correspondant. Cependant il est pour l'instant impossible de confirmer quantitativement si les phasons contribuent à cet excès de diffusion diffuse.

Un nouveau mouvement du tétraèdre central est observé dans l'approximant 5/3. Les échelles caractéristiques de temps et de distance de l'oscillation du tétraèdre sont toutes deux plus élevées que celles de l'approximant 1/1. Ces résultats suggèrent que les orientations du tétraèdre ont besoin d'être affinées pour caractériser le phénomène d'oscillation quantitativement. D'autre part un axe de symétrie d'ordre 3 est retrouvé dans le modèle du tétraèdre à haute température. Il est aussi important de noter que les différents environnements locaux sont supposés jouer des rôles différents dans la détermination des mouvements du tétraèdre.

Modellisation de l'approximant 8/5

La modélisation de l'approximant 8/5 est réalisée par canonical cell tiling comme décrit dans la section précédente. La structure initiale est affinée par une minimisation de l'énergie totale du système via VASP. La configuration obtenue contient 8032 atomes de Sc et 46088 atomes de Zn par cellule élementaire avec un paramètre de maille de 94.584Å. D'après les configurations des environnements d'amas d'atomes, 576 amas d'atomes peuvent se classer en 6 groupes: 5-7, 6-5, 6-6, 6-7, 7-5 et 7-6, où n dans les n-m nombres précédents représente le nombre d'axes de symétrie d'ordre 2 et m est le nombre d'axes de symétrie d'ordre 3. La déformation initiale dans la structure est éliminée par minimisation d'énergie et le modèle est ensuite équilibré pour chaque température avant la collecte des données. Les mouvements du tétraèdre le plus interne de l'approximant 8/5 sont similaires à ceux observés pour l'approximant 5/3. Sa fréquence d'oscillation estimée est beaucoup plus faible que celle de l'approximant 1/1. Il est aussi supposé que les atomes du tétraèdre doivent franchir une barrière d'énergie plus haute pour diffuser.

Chapter 1. Introduction

Complex metallic alloys (CMAs) refer to a class of intermetallic alloys possessing huge or even infinite unit cells with hundreds or thousands of atoms per cell[28]. The definition of CMA can trace back to the term 'giant unit cell crystal' which was firstly coined by Samson, one of the pioneering investigators of the intermetallic compounds[29]. Some time later on, an updated term 'structurally complex alloy phases' was proposed on the 8th International Conference on Quasicrystals (ICQ) in 2002. Nowadays, for solely practical reasons, the term CMA has been widely used and it is becoming one of the booming research fields in the material academic community.

CMAs have been intensely studied for the past decades due to their unique physical properties. Although much progress has been achieved nowadays, the understanding of their physical properties is still a challenging work both experimentally and theoretically in particular the understanding of the stability of these complex metallic alloys. It is significant not only for the fundamental theory, but also for the potential industrial applications.

The structures of CMA could generally be described with several characteristics: (i) local units with defined atomic clusters; (ii) long range periodic or aperiodic order and (iii) disorder[30]. In many cases, theses structurally complex phases can be described based on clusters such as Bergman cluster, Mackay cluster and Tsai cluster, as depicted in Figures 1.1. The correlation between the two length scales, i.e. the lattice and cluster scales, has been proved crucial to understand the physical properties of CMAs. On the other hand, frequently occurred disorders in CMAs are another aspect that closely relates to the unique properties of these complex systems. Apart from that, on the basis of building scheme, the CMAs can be simply classified into two categories: periodic and aperiodic crystals. The two kinds of structures sometimes are related by sharing the same building blocks, e.g. quasicrystals (QCs) and their approximant crystals (ACs).

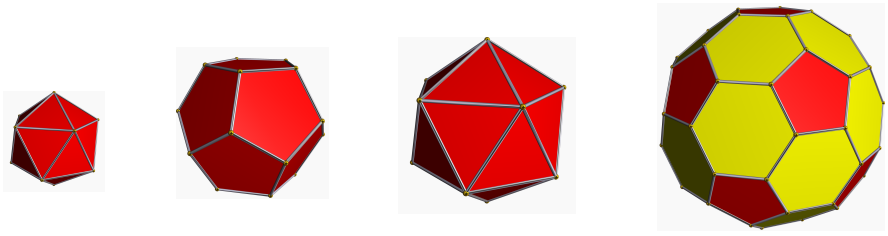

Figure 1.1 (a) Successive shells of Bergman cluster, starting with an icosahedron (12 atoms), followed by a dodecahedron (20 atoms), a bigger icosahedron (12 atoms) and ending up with a 60 sites soccer ball, making up a 104-atom cluster.

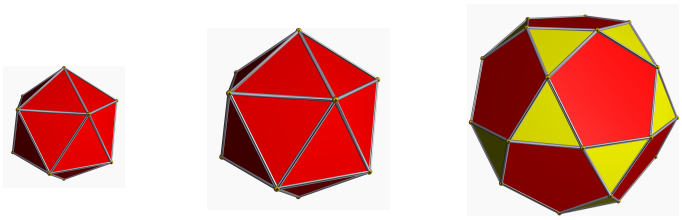

(b) Successive shells of Mackay cluster, two adjacent icosahedra (24 atoms), surrounded by an icosidodecahedron (30 atoms), forming a perfect Mackay cluster with 54 atoms.

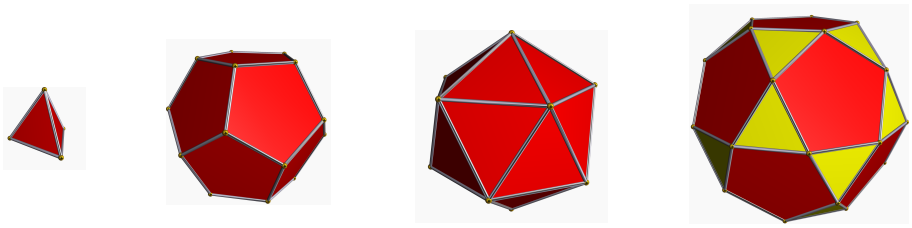

(c) Successive shells of Tsai cluster, an innermost tetrahedron (4 atoms), neighboring with a dodecahedron (20 atoms), an icosahedron (12 atoms), and finally comprising a 66-atom Tsai cluster together with an outermost icosidodecahedron (30 atoms).

1.1 Quasicrystal and their approximant crystallines

The discovery of the first synthesized Al_6Mn icosahedral QC (*i*-QC) by Dan Shechtman[31] renewed the traditional concept of crystal which was initially defined as *a material with 3 dimensional lattice periodicity in three principle axes* and eventually reformulated as *any solid having an essentially discrete diffraction diagram* in 1992[32]. Simply speaking, QCs are solids possessing long-range order which leads to discrete sets of sharp diffraction peaks, but without 3D translational symmetry which makes the quasi-crystallographic rotational symmetry (5, 10, and 12- fold *et al*) permitted (see Figures 1.2).

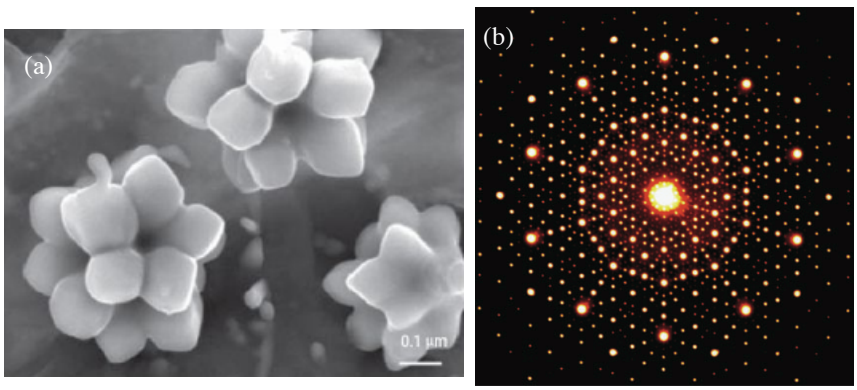

Figure 1.1.1 (a) Scanning electron microscope image of icosahedral-symmetry grains formed in a rapidly solidified Al-6at.%Mn alloy (An-Pang Tsai); (b) TEM diffraction pattern taken along 10-fold axis of the $Al_{72}Ni_{20}Co_8$ decagonal quasicrystal.

The classification of QCs is made based on their quasiperiodic dimensions and symmetry: one is dihedral (polygonal) QCs which possess a periodicity along one direction, such as octagonal (8-fold), decagonal (10-fold) and dodecagonal (12-fold) QCs; the other is icosahedral QCs having a characteristic icosahedral symmetry with six 5-fold, ten 3-fold and fifteen 2-fold axis.

Hundreds of quasicrystals have been synthesized up to now in Al-based, Cd-based, Zn-based systems and so on[33], of which most belong to intermetallic compounds. In 2004, some new members of the quasicrystal group, supramolecular dendritic liquid quasicrystals[34][35][36] and star block copolymers[37][38], were discovered. The discovery of soft quasicrystals not only extends the border of quasicrystal world but also explores a new platform for study of quasiperiodic long range order. The answer to question '*why are these soft quasicrystals stable*'[39] may give us hints on the thermodynamic stability of quasiperiodic crystalline on one hand. On the other hand, the newly discovered soft quasicrystals based on self-assembled nanoparticles cleave a new way for prospectively industrial applications.

1.1.1 Structural description of QCs

Many methods and techniques have been put to use to characterize or predict the structures of QCs[40][41][42][43]. Since no conventional 3D periodicity exist in QC, the classical crystallography can no longer be applied directly. The most widely used method nowadays investigating atomic structures of QCs is by introducing the concept of high-dimensional space[44][45][46]. The QCs could be described as periodic in a 3+*n* dimensional space where *n* is the number of dimensions with quasiperiodicity. For *i*-QCs, a class that shows quasiperiodicity in three dimensions, the atomic structures can be described periodically in a 6D space. The 6D hyperspace is composed of two orthogonal 3D spaces: the parallel (physical) and perpendicular (virtual) space. The real structures of *i*-QC in 3D physical space can be obtained by a section of the decorated 6D lattice.

The detailed atomic structures of QCs had puzzled the scientific community for more than two decades. The first detailed structural analysis on QC was performed in decagonal AlMnPd phase[47][48]. Difficulties were encountered for more accurate analysis until a breakthrough was achieved in 2000 by Tsai *et al* who synthesized the first stable binary quasicrystal with a composition $Cd_{5.7}Yb$[2]. The discovery of $Cd_{5.7}Yb$ icosahedral QC offers a unique opportunity for structural analysis of QCs by experiments owing to its advantages: (i) the $Cd_{5.7}Yb$ can be obtained as a single grain in high quality; (ii) the two constituent elements Cd (Z=48) and Yb (Z=70) display very good x-ray contrast; (iii) the atomic structures of ACs to this icosahedral i-QC has been intensely studied; (iv) the building blocks, i.e. Tsai type cluster, of both $Cd_{5.7}Yb$ i-QC and its binary ACs exhibit no chemical disorder, meaning that all polyhedra are occupied fully by one element. By means of X-ray diffraction (XRD), the detailed structure solution of $Cd_{5.7}Yb$ was successfully characterized by Takakura *et al*[49] in 2007.

The 6D lattice is decorated by 3D objects, named occupation domains (ODs), and a proper section of the 6D model to the 3D physical space is the structure of QC. Thus the key point is determining the locations, shapes and sizes of the archetype OD which is, in case of $Cd_{5.7}Yb$ as well as other i-QCs[50][51], obtained by truncating the 5-fold tips of a τ^{-2} times smaller

rhombic triacontahedron (RTH) cluster in length. The archetype ODs associating with the two additional arrangements, obtuse rhombohedron (OR) and acute rhombohedron (AR) generated from the 1/1 and 2/1 ACs of the i-QCs respectively, constitute various ODs[52][5]. The 3D ODs in 6D model act as atomic positions in 3D physical space. Finally, The 6D structure model can be achieved by decorating these ODs in a periodic 6D lattice. The structure refinement of the 6D model of i-QC is performed using a method depicted in [53]. A general procedure to determine atomic structures of QC is:

- Based on the data collection from XRD measurements, the Fourier synthesis was achieved after phasing the structure factors by applying the low-density elimination method[54] to generate the electron density in the framework of 6D unit cell.

- The primitive 6D structure model with reasonable number of parameters was designed using the information obtained from the AC structures and the 6D electron density map. In this step, generating the decorating ODs plays important role in describing the quasiperiodic structures.

- The 6D model was refined by subdividing it into fragments with individually assigned parameters such as composition, parallel shift parameter and so on.

- The resulting 3D atomic structure in physical space was achieved. Atomic arrangements in several projections as well as the clusters could be drawn for a better view.

The collection of reflections data is crucial to construct the charge density map as some weak reflections which possess large perpendicular diffraction vectors contain important information of the shape of the OD. Therefore the diffraction experiments are normally performed using synchrotron beam to obtain accurate datasets. In the meantime, another thing need to be considered is such weak reflections are easy to be affected by multiple scattering.

The 3D structure of $Cd_{5.7}Yb$ *i*-QC in physical space can be described in term of 'inflation and hierarchical packing of clusters'[49]. As illustrated in Figures 1.1.2, assuming the icosidodecahedron as a single point, a larger icosidodecahedron, so called 'cluster of clusters' is repeated in a τ^3 times length scale. The RTH clusters are the dominated arrangements in the *i*-QC as 93.8% atoms serve as RTH and the space between RTH are filled by different decorations of ORs and ARs. Furthermore, the distortions of successive shells induced by **c**-linkage, i.e. linkage along 3-fold directions, are observed in both *i*-QC and its ACs. This phenomenon as well as the ORs and ARs obtained from different ACs suggest the significant role of the ACs for better understanding the atomic structures and physical properties of QCs.

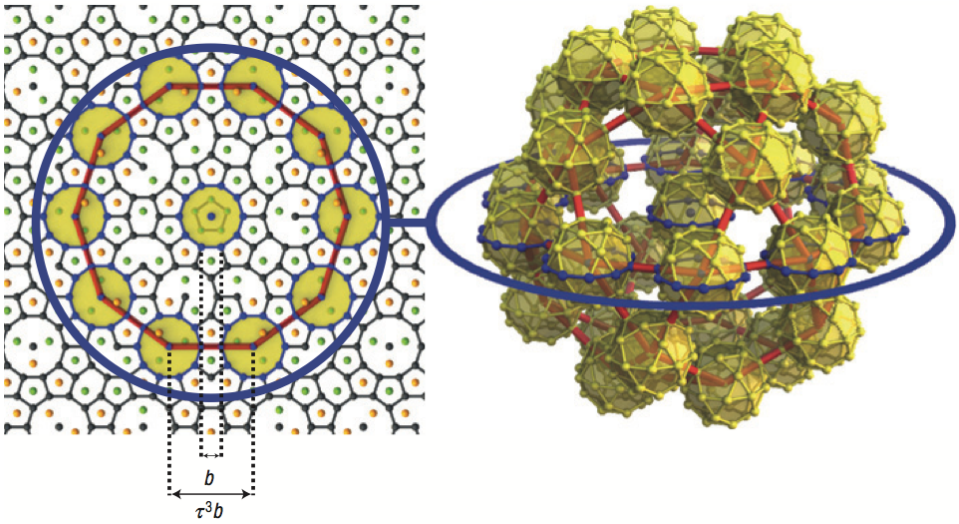

Figure 1.1.2 A plane perpendicular to 5-fold units is shown in the left figure, where a larger τ^3-inflated decagon cluster composed of RTH clusters is framed by thick red lines. The 3D perspective of the τ^3-inflated icosidodecahedron, i.e. the 'cluster of clusters', is shown in the right figure.

1.1.2 Indexing of icosahedral quasicrystal

As mentioned above, *i*-QCs are the only QCs which are quasiperiodic in all three directions of physical space. This means six vectors are necessary to index the diffraction patterns. Taking $\mathbf{a}_1$, $\mathbf{a}_2$, $\mathbf{a}_3$ as the three unit vectors of the physical space and $\mathbf{a}_4$, $\mathbf{a}_5$, $\mathbf{a}_6$ as those of the virtual space, then the unit vectors of the *i*-QCs in 6D reciprocal space are expressed as:

$$\boldsymbol{d}_1^* = (a^*/2)[\boldsymbol{a}_3 + \boldsymbol{a}_6],$$

$$\boldsymbol{d}_i^* = (a^*/2)[(c_i\boldsymbol{a}_1 + s_i\boldsymbol{a}_2)s + c\boldsymbol{a}_3 + (c_{2i}\boldsymbol{a}_4 + s_{2i}\boldsymbol{a}_5)s - c\boldsymbol{a}_6] \quad (i = 2,3,\cdots,6) \quad 1.1$$

where $c_i = cos(2\pi i/5), s_i = sin(2\pi i/5), c_0 = 1/\sqrt{5}, c_1 = 2/\sqrt{5}$.

Then the unit vectors in real space are defined as:

$$\boldsymbol{d}_1 = a[\boldsymbol{a}_3 + \boldsymbol{a}_6],$$

$$\boldsymbol{d}_i = a[(c_i\boldsymbol{a}_1 + s_i\boldsymbol{a}_2)s + c\boldsymbol{a}_3 + (c_{2i}\boldsymbol{a}_4 + s_{2i}\boldsymbol{a}_5)s - c\boldsymbol{a}_6] \; (2,3,\cdots,6) \quad 1.2$$

where $a = 1/a^*$.

In the indexing rule proposed by Cahn *et al*[55] for cubic *i*-QCs, the reflection related to a plane (HKL) can be indexed in the form of (*h*/*h*', *k*/*k*', *l*/*l*') where: $H = h + h'\tau, K = k + k'\tau, L = l + l'\tau$. The relationship between the six-index 3D vectors (*h*/*h*', *k*/*k*', *l*/*l*') and the 6D vectors ($n_1, n_2, n_3, n_4, n_5, n_6$) is:

$$h = n_1 - n_4, \qquad h' = n_2 + n_5,$$

$$k = n_3 - n_6, \qquad k' = n_1 + n_4,$$

$$l = n_2 - n_5, \qquad l' = n_3 + n_6. \tag{1.3}$$

The square of 6D diffraction vector $\boldsymbol{Q}$ can be expressed as the form:

$$Q^2 = N + M\tau \tag{1.4}$$

By mathematical derivations which will not be discussed here, another two-parameter indexing rule for a reflection of *i*-QCs which is of the form *N*/*M* can be given by:

$$N = 2\sum_{i=1}^{6} n_i^2 = h^2 + h'^2 + k^2 + k'^2 + l^2 + l'^2 \tag{1.5}$$

$$M = h'^2 + k'^2 + l'^2 + 2(hh' + kk' + ll') \tag{1.6}$$

From that we can tell that the number of *N* is always even, and *M* is constrained in a region (-N/τ, $N\tau$)[55]. When *N* is divisible by 4, *M* is divisible by 4 as well. If *N* is indivisible by 4, *M* is of the form 4*m*+1. Table 1.1 gives the 12 strong reflections of *i*-QC phase in different indexing rule.

Table 1.1 12 strong reflections of i-QC in different indexing rule.

N	*M*	(n_i)	(*h*/*h*', *k*/*k*', *l*/*l*')	multiplicity
2	1	(100000)	(1/0 0/1 0/0)	12
4	4	(100100)	(0/0 0/2 0/0)	30
6	9	(111000)	(1/1 1/1 1/1)	20
8	12	(10110$\bar{1}$)	(0/0 2/2 0/0)	30
10	13	(11101$\bar{1}$)	(1/2 2/1 0/0)	60
12	16	(210010)	(2/2 0/2 0/0)	60
		(11111$\bar{1}$)	(0/2 2/2 0/0)	12
14	21	(20110$\bar{1}$)	(1/0 2/3 0/0)	60
16	24	(21101$\bar{1}$)	(2/2 2/2 0/0)	60
18	29*	(21111$\bar{1}$)	(1/2 2/3 0/0)	12
20	32*	(20120$\bar{1}$)	(0/0 2/4 0/0)	30
22	33	(21120$\bar{1}$)	(0/1 2/4 1/0)	120
24	36	(222000)	(2/2 2/2 2/2)	20
		(21121$\bar{1}$)	(0/2 2/4 0/0)	60

* The strong 5-fold and 2-fold reflections corresponding to (530) and (600) in the 1/1 approximant, which will be discussed in Chapter 5.

1.1.3 Phason modes in QCs

The term phason was firstly put forward for investigating the lattice excitation of an incommensurate charge density wave system[56]. Soon after the discovery of QCs, the phasons are introduced for investigating many aspects from the growth mechanism to their various physical properties. The analysis of phasons in QC phases is well understood in the high-dimensional picture where phason modes can be viewed as modes with a wavevector in

parallel space and a polarization in perpendicular space, as illustrated in Figure 1.1.3. It is noteworthy that the phason modes are not propagative but diffusive.

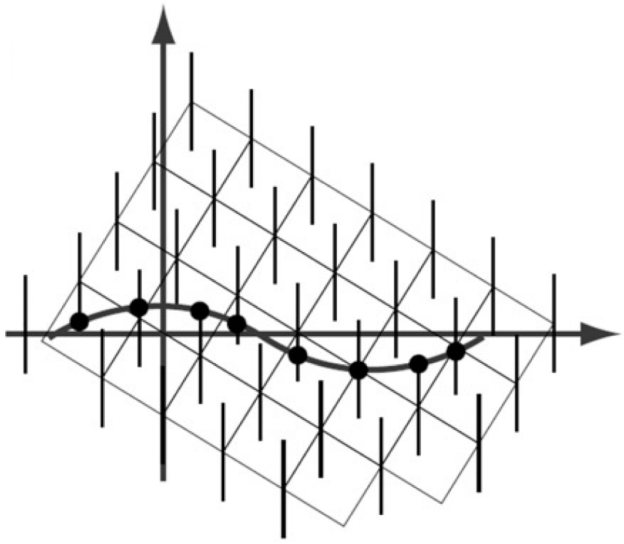

Figure 1.1.3 Illustration of a phason mode in QC phase presented in a 2D picture. The full dots present the resulting atomic positions. (from [57])

Different from the propagative long wavelength phonon modes, the phason modes have been evidenced to be collective diffusive. For QCs as well as incommensurately modulated structures, the phason modes with wavevector **q** are of the form:

$$-i\omega = D_{phason}q^2 \qquad 1.7\ (a)$$

or

$$1/\tau = D_{phason}q^2 \qquad 1.7\ (b)$$

where D_{phason} is the phason diffusion constant which possesses high spatial anisotropy. The equation indicates that the phason modes have an exponential decay with a characteristic time proportional to the square of the phason fluctuation wavelength, which has been proved in experiments[61][62][63]. The characteristic time can be extracted from the time dependent intensity correlation function of the coherent X-ray scattering:

$$F_{cor}(\boldsymbol{q}, t) = [1 + \beta g(\boldsymbol{q}, t)] \qquad 1.8$$

where $g(\boldsymbol{q}, t)$ is the function involving time dependence of a phason mode with wavevector **q**, and β is the partial coherence of the beam which depends on the experiment setup and is of a typical order of 5% and 3% for low- and high-angle reflections for a third generation synchrotron source[64]. The measurements had been performed on the well studied i-AlPdMn phase, and two characteristic times were determined for different **q**. The characteristic time τ displays a linear correlation with the square of phason wavelengths in the selected direction, giving the phason constant D_{phason} from Eq. 1.2(b). Furthermore, the measurements at lower temperature give much larger, i.e. 5 to 10 times τ of that at 650℃, which demonstrates the frozen-in of phason fluctuations.

Other than phonon contributing to the well-known thermal diffuse scattering, phason displays characteristic diffuse scattering located nearby the Bragg peaks for aperiodic crystals[30]. Quantitative phason analysis can be achieved by absolute scale measurements of the X-ray diffuse scattering in experiments. Phason diffuse scattering has been proved in some incommensurately modulated phases and all QCs experimentally.

The diffuse scattering intensity of icosahedral phases can be described with five elastic coefficients[60]: the two phonon terms (Lamé parameters λ and μ), the two phason terms K_1 and K_2, and the K_3 for the phonon-phason coupling term. The reciprocal coordinates of a Bragg peak in quasicrystals can be decomposed into two orthogonal components: one is the physically observable component, named $\mathbf{Q}_{\mathrm{par}}$, and the other is the virtually complementary component $\mathbf{Q}_{\mathrm{per}}$. When the phonon-phason coupling term could be neglected, the diffuse scattering intensity at the position $\mathbf{Q}_{\mathrm{par}}+\mathbf{q}$ can be written as:

$$S(\mathbf{Q_{par}}+\mathbf{q}) = I_{Br} q^{-2}(\alpha Q_{par}^2 + \beta Q_{per}^2) \qquad 1.9$$

where I_{Br} is the intensity of the Bragg peak, and α, β are given by the eigenvalues of the inverse of the hydrodynamic matrix. They depend on the $\mathbf{q}$ direction, as well as on the Lamé and phason elastic constants. The first term corresponds to the phonon diffuse scattering and the second term is the supplementary phason component specially for QCs. For a given QC and its approximant the Lamé parameters are almost identical, thus by subtracting the phonon contribution which can be simply evaluated from the related approximant, we can obtain a Q_{per} dependent phason diffuse scattering on the QC.

Investigation on icosahedral phases, such as i-AlPdMn and i-ZnMgSc[60][65] phases, denotes the shape of phason diffuse scattering is determined by ratio of K_1 and K_2, and the values of K_1 and K_2 are responsible for the intensity. The diffuse scattering around Bragg peaks can be well reproduced in the framework of the hydrodynamic theory using the ratio of K_2 and K_1 as demonstrated in Figures 1.1.4. Both the absolute values and the ratio of K_2 and K_1 are dependent on the composition of the investigated systems. High anisotropy of the phason diffuse scattering shape is another characteristic feature of the phason modes.

The phason fluctuations are normally frozen in at room temperature due to kinetic reasons, thus temperature dependent diffuse scattering measurements are of crucial importance to investigate the microscopic mechanism of phason fluctuations. The temperature dependent phason modes have been studied in details on the AlPdMn icosahedral phase where a phason softening is observed in a temperature interval from 550℃ to 770℃[66]. In that case, the diffuse scattering was found counter-intuitively varying with respect to the temperatures, i.e. it decreases as the temperature increases. This result can be well interpreted by the softening of the phason elastic constant K_1. This softening phason mode is most likely related to a phase transition from I_{h} through $D_{3\mathrm{d}}$ in the direction parallel to 3-fold axis. Moreover, the diffuse scattering intensity below 500℃ does not change anymore, demonstrating that the observed phason fluctuations is frozen in at room temperature.

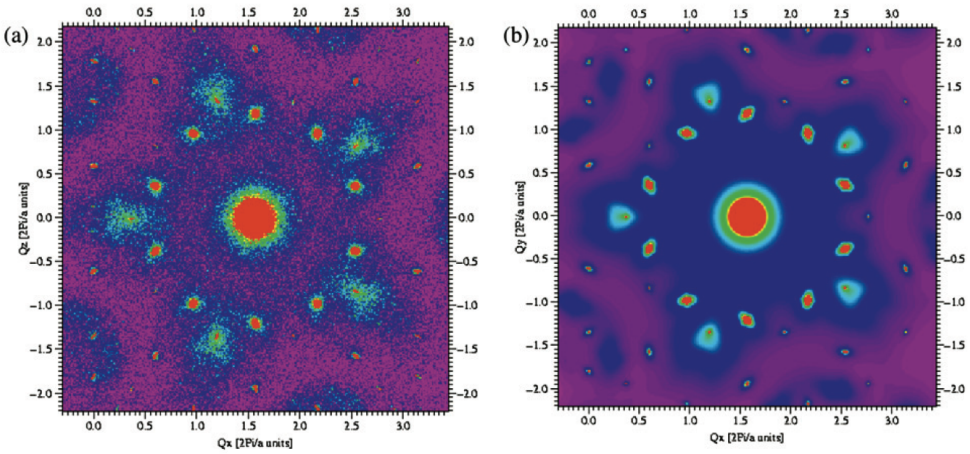

Figure 1.1.4 (a) Experimentally measured diffuse scattering in the i-AlPdMn phase on a plane perpendicular to 5-fold axis; (b) Simulated phason diffuse scattering using the two phason elastic constants.

In the picture of high-dimension, the phason modes directly result from the invariance of the free energy of the parallel space. The long-wavelength phason modes can be viewed, in some extent, as the fluctuations of the parallel space along the perpendicular direction. As a consequence, atomic flip, named 'phason flip' is expected recognizable in the structures of QCs in physical space as depicted in Figure 1.1.5, where the 1D image of Fibonacci chain on a 2D plane is taken as an example. Direct proof of 'phason flip' has been witnessed in the AlCuCo decagonal QC phase by means of high resolution transmission electron microscopy (HRTEM) by Edagawa *et al*[58][43] (see Figures 1.1.6). Two local tiles with a 2nm edge were observed shift frequently in a time scale of from tens of seconds to about ten minutes at 1123K. On the other hand, 'phason hopping' evidenced by time-of-flight neutron scattering, in which quasielastic signal is sensitive to atomic motions, has also been reported[59]. Additionally, the 'phason flip' might exist as well in tetrahedrally packed QCs and ACs in form of tetrahedron flipping[60][61].

Apart from experiments, simulations have been performed mostly on the random tiling model proposed by Elser, Henley and Mihalkovič[67][68]. These simulations were carried out by means of Monte Carlo method for studying the diffuse scattering and phason modes in QCs[69][70][71]. The details will be presented in the beginning of Chapter 5 where MD simulations have been carried out for investigation of diffuse scattering in various ACs to *i*-QCs.

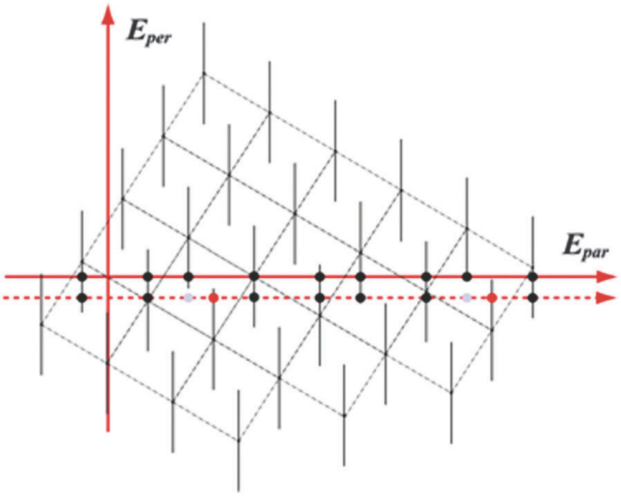

Figure 1.1.5 The invariance of free energy of the chain in parallel axis leads to a fluctuation along perpendicular axis. Some points 'jump' to nearly equivalent sites as indicated by grey and red points.

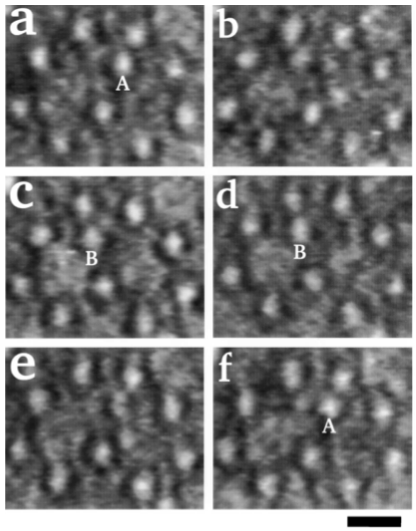

Figure 1.1.6 Direct observation of the atomic column flipping between two tile configurations A and B. Elapsed times for (a) – (f) are 0, 5, 8, 110, 113, and 115 s, respectively. The scale bar indicates 2.0 nm.

1.2 Quasicrystal Approximants

As aforementioned, ACs play crucial role in investigating the atomic structures (providing building blocks) and physical properties (quantitative analysis of phason diffuse scattering) of QCs. Considering the challenging work of studying QCs in the framework of high-dimensional space, knowledge from related ACs could greatly simplify the analysis. The definition of ACs basically lies on their structures including the same building blocks and very close chemical compositions with their QCs counterparts. The order of ACs, e.g. 1/1, 2/1 which is defined on the basis of Fibonacci sequence gives their complexity and closeness with respect to QCs. The correlation between QC and AC could simply represented by 2D image of Fibonacci chain as will be discussed in the following paragraphs.

1.2.1 Fibonacci sequence

Fibonacci chain is now frequently cited for explanation of quasiperiodic structure in 2D space[72][73]. Mathematically, it can be constructed by concatenating the two previous generations, as denoted in its formula:

$$F_n = F_{n-2} + F_{n-1} \qquad n = 3, 4, 5, 6 \ldots \tag{1.10}$$

with seed values F_1=1, F_2=1. The rule of construction depends on the two segments: long and short segments (hereafter L and S respectively) representing the old and young famous Fibonacci rabbits. The L breeds into LS and S grows as L in the next generation respectively as listed in Table 1.1.

Table 1.2 Fibonacci sequence represented by segments L and S with rule L → SL and S → L from one generation to the next.

Segments	*n*	F_n
S	1	1
L	2	1
LS	3	2
LSL	4	3
LSLLS	5	5
LSLLSLSL	6	8
…	…	…

According to mathematical deduction, as $n \to \infty$, the ratio of F_n and F_{n-1} approaches to τ.

$$\lim_{n\to\infty} \frac{F_n}{F_{n-1}} = \frac{1+\sqrt{5}}{2} = \tau \qquad 1.11$$

The number of n is the indicative of how close the sequence is to the limitation τ. In case of QCs and their ACs, the 3D building blocks correspond to the L and S segments, and the ratio of sequences tells the complexity and closeness of ACs to QCs as mentioned above. The first six ACs with respect to Fibonacci sequence are presented in Table 1.2.

Table 1.3 Fibonacci chain and periodic approximants, the complexity of unit cell increases as the ratio approaching to τ.

Sequence of unit cells	*n*	*Approximants*
S, S, S, S, S, S, …	1	0/1
L, L, L, L, L, L, …	2	1/0
LS, LS, LS, LS, …	3	1/1
LSL, LSL, LSL, …	4	2/1
LSLLS, LSLLS, …	5	3/2
LSLLSLSL, LSLLSLSL, …	6	5/3
…	…	…

1.2.2 Fibonacci sequence in 2D space

The illustration of Fibonacci sequence in 2D image is displayed in Figure 1.2.1. The plane is decomposed into two orthogonal axis: parallel and perpendicular axis. By projecting the points in gray area onto the parallel axis R^1_{par} which cuts the 2D plane with an irrational slope (τ for instance), a sequence with quasiperiodicity is obtained. The quasiperiodic sequence of L and S segments are given on the bottom of the image. The width of the gray area is $\sqrt{2}$a where a is the edge length of the repeating small squares. It shows clearly here that the

quasiperiodic 1D Fibonacci chain is periodic in 2D plane, and the small squares in 2D space act as the 2D lattice.

By cutting the 2D plane with rational slopes, e.g. 1/1, 2/1, 3/2…, one can obtain a series of periodic sequences, so called approximants, as presented in Figure 1.2.1. As the slope approaches to τ, the periodicity of approximants gets larger and larger until infinite where they will meet QCs.

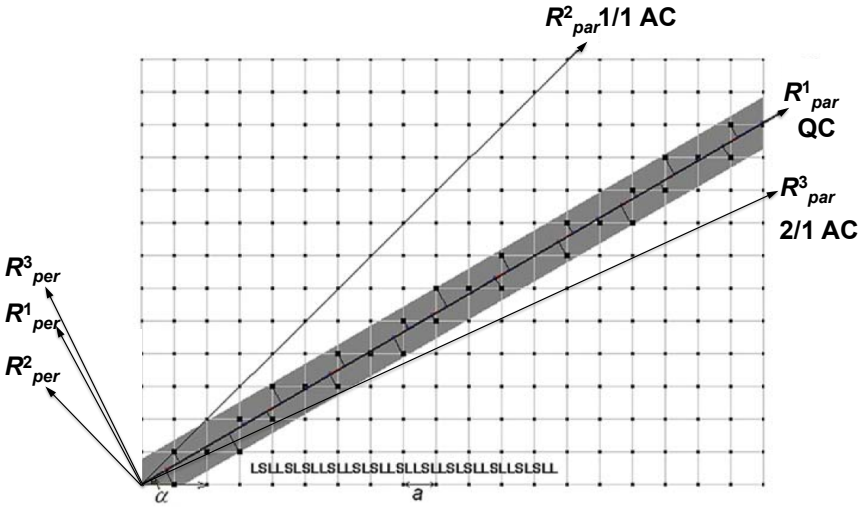

Figure 1.2.1 Periodic square lattice in 2D plane. By projecting motifs on 2D lattice to irrational and rational parallel subspace, one obtains quasiperiodic 1D chain and its approximants.

1.3 Aims of this project

Although remarkable progress has been achieved for CMAs, still there are many open questions for understanding and developing their outstanding properties. One of the most challenging questions remains the understanding of the stability of such phases. This is important from the fundamental point of view, but also for the understanding of their mechanical properties such as Al or Mg based alloys where CMAs serve as reinforcing precipitates[74].

Early studies to Cd_6Yb 1/1 AC has evidenced an order-disorder phase transition at low temperature[19][20] which has been universally observed in a series of isostructural phases, i.e. Cd_6RE (RE = Ca, Y, Sr, Pr, Nd, Sm, Gd, Tb, Dy, Ho, Er, Tm, Yb) and Zn_6Sc[75][6][13][76][12]. Similar but more abundant phase transitions are also observed in these ACs with respective to pressures[77][78]. On the contrary, the related QCs have been proved rather stable under very low temperatures and high pressures[79]. The phase transition has been proved triggered by the ordering of the innermost tetrahedron in Tsai type cluster[7][80][81][9]. Several ordering schemes have been proposed for different compositional ACs. One of the aims in this project is to clarify the ordering schemes acting in different systems.

An intriguing magnetic transition was observed recently in Cd_6Sm and Cd_6Tb 1/1 ACs[76][14][15]. Instead of spin-glass-like behavior found in relevant QCs, the ground states of Cd_6Sm and Cd_6Tb are frozen into antiferromagnetic state. Long range magnetic order with correlation length in excess of 500Å was found by means of x-ray resonant magnetic scattering. Thus the second goal of this project is to solve the atomic structure of the Cd_6Tb phase at low temperatures.

The phason modes have been well studied in QCs, but also incommensurately modulated structures[82] experimentally and theoretically. By means of molecular dynamic (MD) simulations using effectively fitted oscillating pair potential, we try in this project to reproduce the phason diffuse scattering in QCs. Moreover, trajectories of target atoms and clusters will offer hints for investigations of phason modes in atomic view.

Combination of experiments and atomistic simulations is the key point of this thesis. Results from experiments and simulations will be compared mutually. Altogether, this thesis will do helps to understand the stabilization of QCs and their ACs counterparts in depth.

Chapter 2. Synchrotron X-ray source

Synchrotron radiation, as it was named firstly by Pollock[83], is produced when charged particles with relativistic speed travel through a curved path in applied magnetic fields[84]. It may be achieved artificially in storage rings or naturally by plasmas moving through stellar nebula. Practically, all modern sources of synchrotron radiation for X-ray research are storage rings. In a storage ring, the synchrotron radiation is produced using either bending magnets or insertion devices such as undulators and wigglers. In bending magnets, the electrons are kept at constant energy travelling in a closed circular orbit during which the energy loss of electrons is radiated. In the insertion devices, electrons are forced running in an oscillating path by an alternating magnetic field.

Comparing with laboratory X-ray sources, the synchrotron radiation possesses unique properties[85]:

- Broad spectrum: it covers from microwaves to ultrahard X-rays.
- High flux: beam with high intensity photons can shorten experiments and probe very weak reflections.
- High brilliance: highly collimated photon beam generated by a small divergence and small size source.
- High stability: submicron source stability provides high accuracy.
- Polarization: linear and circular polarizations are both available.
- Pulsed time structure: pulsed length down to tens of picoseconds allows the resolution of process on the same time scale.

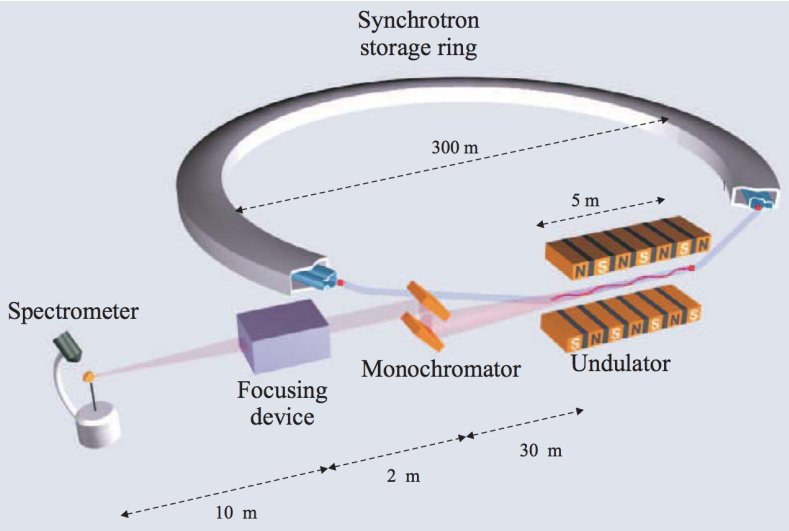

Figure 2.1 A sketch of a typical third generation synchrotron site. Electrons or positrons are accelerated in the storage ring. Radiation is emitted at each beamline and a set of optical devices such as monochromator, focusing device and so on are applied to design proper beams for users. Insertion devices like undulators, wigglers are placed in the straight sections to oscillate the charged particles and produce intense X-ray beams[84].

The quality of an X-ray beam may be described by a quantity called brilliance. The definition of brilliance combines various effects from X-ray beams including number of photons emitted per second, the collimation of the beam, source area and relative energy bandwidth (BW) of photons. Finally the brilliance is given in a form:

$$\text{Brilliance} = \frac{\text{Photons/second}}{C_b^2 A_s (0.1\%\text{BW})} \qquad 2.1$$

where C_b is collimation of the beam in unit of milli-radian, A_s is the source area given in mm2, and 0.1%BW denotes 0.1% of the relative energy BW of the monochromator crystal. The brilliance of the third generation synchrotron facilities (e.g. European Synchrotron Radiation Facility-ESRF) is about 10 orders of magnitude higher than that of laboratory source.

2.1 Bending magnet radiation

Bending magnet radiation is produced by electrons moving in a constant magnetic field which constrains the charged particles in a circular orbit. The radiation is emitted continuously throughout the whole orbit since the velocity directions of electrons keep changing. The emitted spectrum is very broad starting from far infrared until ultra-hard X-ray region. For an electron travelling with super-relativistic speed, i.e. $v \cong c$, the magnitude of its momentum is given by:

$$P = \gamma mc = \rho eB \qquad 2.2$$

where $\gamma = \varepsilon_e / mc^2$ is the electron energy in units of its rest mass energy, ρ is the radius of the circular orbit, and B is the amplitude of the magnetic field. Thus, the radius of the electron orbit is expressed as:

$$\rho[\text{m}] = \frac{\gamma mc}{eB} = 3.3 \frac{\varepsilon_e[\text{GeV}]}{B[\text{T}]} \qquad 2.3$$

The radiation emitted by an electron orbiting along a circular arc at relativistic speed is compressed into a tightly collimated cone with an opening angle 1/γ as illustrated in Figure 2.1.1 (a). The typical energy of electrons in synchrotron is 5GeV, and the rest mass of an electron is 0.511MeV, which gives the opening angle in order of 0.1mrad. As the electron moves in the circular orbit, for observers viewing along direction of tangent to point B, the emitted radiation is observable only when the charged particle appears between the circular arc $\widehat{AC}$ as indicated in Figure 2.1.1 (b). Due to the Doppler effect, the observer may see a signal as half period of an oscillation.

The Doppler effect is given by the relation between the observer time *dt*, i.e. the time interval between two sequential radiations measured by observers, and the emitter time *dt'*, i.e. the time interval between two sequential radiations being emitted, in form of differential equation:

$$\frac{dt}{dt'} = (1 - \beta_e cos\alpha) \qquad 2.4$$

α is the angle between velocity and viewing direction of the observer, and $\beta_e \equiv v/c$ is the speed of orbiting electrons in unit of light speed. As can be seen, α being 0 at point B gives the minimal differential, i.e. the most enormously compressed time and most strongest Doppler effect. This then explains the pulse signal that the observer receive in the duration when the electron moves from A to C. The finite time duration implies a characteristic frequency for the pulsed radiation, which is given by the Fourier transform of the wave:

$$\omega_c = 1.5\gamma^3\omega_0 \qquad 2.5$$

with ω_0 being the frequency of the orbiting electron. Thus $\omega_0 = \frac{2\pi}{T} = \frac{2\pi}{\left(\frac{2\pi\rho}{v}\right)} = \frac{v}{\rho}$, for super-relativistic charged particle, it is proportional to B/ε_e according to Eq. 2.2. Then by taking in the known quantities, the characteristic energy of photons is given by:

$$E_{photon}[\text{keV}] = 0.665\varepsilon_e^2[\text{GeV}]B[\text{T}] \qquad 2.6$$

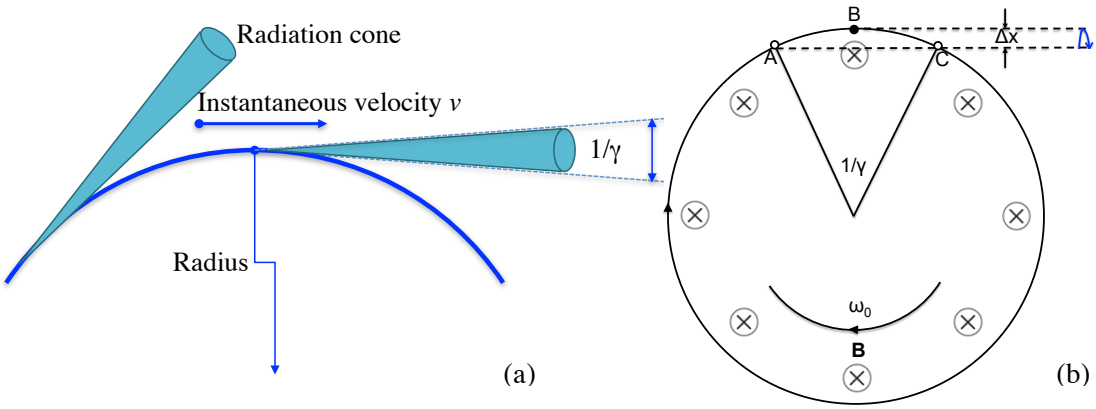

Figure 2.1.1 Bending magnet radiation in a circular orbit. (a) The radiation is emitted in form of a cone with opening angle 1/γ; (b) The radiation is only observable when charged particles appear between A and C in the circular arc. It gives a radiation with pulsed spectrum.

The phonon flux of emitted radiation by electrons orbiting in bending magnet field may be calculated by the powder density of the radiated field which is provided by the amplitude of Poynting vector:

$$\vec{S} = \frac{1}{\mu}\overrightarrow{E_{rad}} \times \overrightarrow{B_{rad}}$$

$$S[\text{Wm}^{-2}] = E_{rad}B_{rad}/\mu = c\epsilon_0 E_{rad}^2 \qquad 2.7$$

with

$$E_{rad} = \left|\vec{A}\right| e/(4\pi\epsilon_0 c^2 R) \qquad 2.8$$

where $\vec{A}$ is the apparent acceleration, and R is the observing distance. Here, the amplitude of $\vec{A}$ can be estimated by:

$$|\vec{A}| = \frac{d^2x}{dt^2} \approx \frac{\Delta x}{\Delta t^2} \approx \frac{\rho\left(1 - cos\frac{\gamma^{-1}}{2}\right)}{\left(1/\gamma^3\omega_0\right)^2} \sim \frac{\rho/\gamma^2}{(\rho/c\gamma^3)^2} \sim \frac{\gamma^4 c^2}{\rho} \qquad 2.9$$

where Δx is the distance from point B to segment AC as denoted in Figure 2.1.1 (b).

The power density then can be obtained by combing Eq. 2.7 - 2.9. Furthermore, the radiation energy emitted by the electron travelling from A to C along the arc in a time interval Δt at distance R can be calculated by:

$$\varepsilon_{rad} = c\epsilon_0 |\vec{A}|^2 \left(\frac{e}{4\pi\epsilon_0 c^2 R}\right)^2 (R^2\gamma^{-2})\Delta t$$

$$\approx \frac{1}{4\pi}\frac{e^2}{4\pi\epsilon_0}\frac{\gamma^3}{\rho} \qquad 2.10$$

The number of photons emitted from one electron then characterized by the ratio of ε_{rad} and E_{photon} which is given by Eq. 2.6:

$$N_{pho} \sim \frac{1}{4\pi}\frac{e^2/(4\pi\epsilon_0)}{\hbar c} \qquad 2.11$$

From Figure 2.1.1 (b), we see that the radiation power covers a length AC=ρ/γ, thus the energy per length unit is $\propto \gamma^4/\rho^2$. By substituting Eq. 2.3, we finally obtain the total radiation power emitted by a current *I* of electrons moving in the bending magnet field by length of *L* in form of:

$$P[\mathrm{kW}] = 1.266\varepsilon_e^2[\mathrm{GeV}]B^2[\mathrm{T}]L[\mathrm{m}]I[\mathrm{A}] \qquad 2.12$$

Altogether, skipping complex mathematical derivation, the radiation spectrum from bending magnet field is expressed as:

$$\frac{\mathrm{Photons/second}}{(\mathrm{mrad}^2)(0.1\%\mathrm{BW})} = 1.33\times10^{13}\varepsilon^2[\mathrm{GeV}]I[\mathrm{A}]\frac{\omega}{\omega_c}^2 K_{2/3}^2\left(\frac{1}{2}\frac{\omega}{\omega_c}\right) \qquad 2.13$$

where $K_{2/3}^2\left(\frac{1}{2}\frac{\omega}{\omega_c}\right)$ is the modified Bessel function. The spectrum of bending magnet radiation with respect to normalized photon energies is presented in Figure 2.1.2[84].

2.2 Insertion devices

As we depicted in Figure 2.1, apart from bending magnet, there are a set of straight sections followed by the circular arcs. These sections are equipped by so called insertion devices which are made of arrays of magnets. Alternating magnetic fields can be produced by these magnets to force the charged particles move in an oscillating path. In this way, the radiations with better brilliance can be obtained more efficiently. The two types of insertion devices: undulator and wiggler will be discussed in the following context.

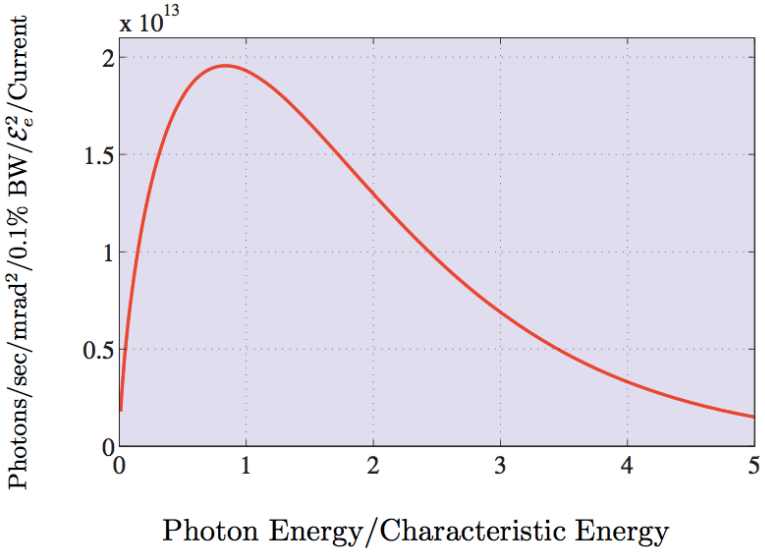

Figure 2.1.2 Spectral distribution of bending magnet radiation respective to continuous photon energies.

2.2.1 Undulator radiation

The undulator works in a way as presented in Figure 2.2.1 (a). Radiations are emitted and interfere with each other, implying a monochromatic spectrum as displayed in Figure 2.2.1 (b). The spectrum is more like 'quasi-monochromatic' since the number of periods in an undulator is finite.

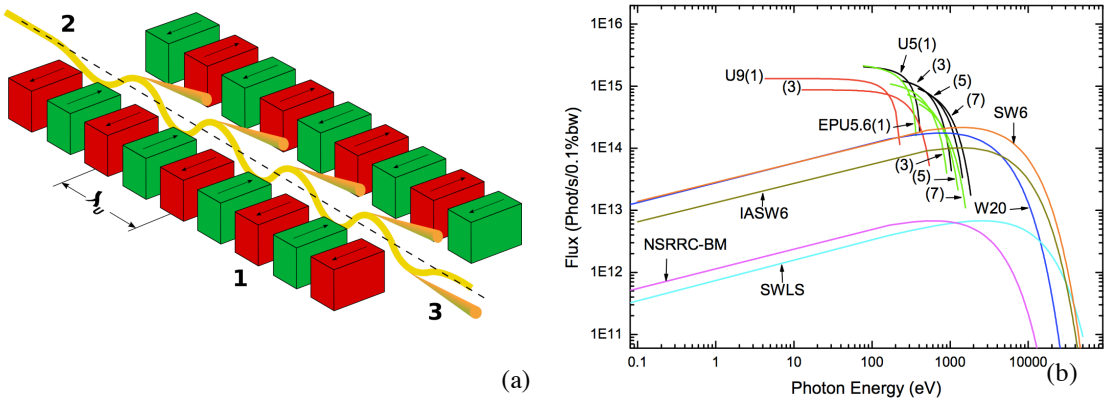

Figure 2.2.1 (a) Schematic of an undulator[86]: 1. Magnets, 2. Electrons, 3. Synchrotron radiation; (b) Comparison of flux in terms of various insertion devices and bending magnet (BM) at NSRRC[87] respective to phonon energy. W20 wiggler, U5, U9 undulators and EPU5.6 elliptically polarizing undulator are conventional permanent magnetic insertion devices. SWLS is acronym of superconducting wavelength shifter. IASW6 and SW6 denote (in achromatic) superconducting wigglers.

For characterizing the undulator radiation, apart from the natural opening angle γ, we need the undulator spatial period λ_u as indicated in Figure 2.2.1 (a), as well as the inflection parameter K which is used to describe the amplitude of the oscillations. The parameter K is given as:

$$K = \frac{eB_0\lambda_u}{2\pi mc} = 0.934\lambda_u[\mathrm{cm}]B_0[\mathrm{T}] \qquad 2.14$$

The fundamental wavelength of undulator radiation is expressed as:

$$\lambda_1(\theta) = \lambda_u\left(\frac{s}{\beta_e} - cos\theta\right) \qquad 2.15$$

where θ is the angle between observing direction and the radiation, and $s = 1 + \gamma^{-2}K^2/4$ is the ratio of electron path within one period and the wavelength λ_u. Thus we have:

$$\lambda_1(\theta) = \frac{\lambda_u}{2\gamma^2}\left(1 + \frac{K^2}{2} + (\gamma\theta)^2\right) \qquad 2.16$$

It shows that the fundamental wavelength is adjustable by changing the spatial period and the maximum magnetic field B_0.

The undulators emit radiations only at characteristic phonon energies:

$$\varepsilon_n = 0.949[\mathrm{KeV}](E[\mathrm{GeV}])^2\frac{n}{\lambda_u[\mathrm{cm}](1 + K^2/2)} \qquad 2.17$$

with the bandwidth $\frac{\Delta\varepsilon_n}{\varepsilon_n} = \frac{1}{nN}$, where N is the number of periods and n=1, 3, 5, 7… is the number of harmonics.

The opening angle of the undulator radiation cone is expressed as:

$$\sigma_n = \frac{1}{\gamma}\sqrt{\frac{(1 + K^2/2)}{2Nn}} \qquad 2.18$$

The flux of the undulator radiation within the central cone is given in practical units by:

$$Flux\left[\frac{\mathrm{Photons/seconds}}{0.1\%\mathrm{BW}}\right] \approx 1.432\times10^{14}NI[\mathrm{A}]\frac{K^2}{1 + K^2/2} \qquad 2.19$$

2.2.2 Wiggler radiation

The wiggler works in principle as illustrated in Figure 2.2.2 where the magnets are typically designed in a Halbach array[88]. Since the amplitude of the electrons' oscillations are larger in wiggler, meaning that there is no interference between radiations, the spectrum of a wiggler is broad as shown in Figure 2.2.1 (b). The wiggler can be treated as a series of bending magnets where the radiations are added incoherently. Thus the radiations are

enhanced by a factor of $2N$, where N is the number of periods. The typical number of N is about 50, suggesting a 100-times enhancement.

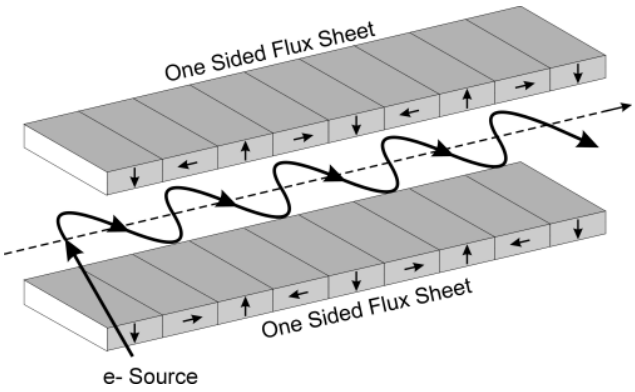

Figure 2.2.2 Schematic drawing of a wiggler arranged in Halbach array which augments the magnetic field inside the access and cancels the magnetic field outside the shells to near zero. The arrows on those permanent magnets denote the orientations.

The emitted power is expressed similarly to Eq. 2.12, only the magnitude of the magnetic field in wiggler is $B_0^2/2$, where B_0 is the maximum field:

$$P_w[\mathrm{kW}] = 0.633\varepsilon_e^2[\mathrm{GeV}]B_0^2[\mathrm{T}]L[\mathrm{m}]I[\mathrm{A}] \qquad 2.20$$

The observed length L of the electrons' path is about the same as the length of the wiggler which is typically in order of 1m.

As aforementioned, synchrotron beam plays crucial role in determining the atomic structures and physical properties of QCs, of which much important information is hidden in weak reflections. This chapter is a brief introduction on the various kinds of synchrotron radiations, therefore no abstruse mathematics are added. To whom being interested in the detailed derivations, further information can be found in [89][90].

2.3 Experiment instruments

Throughout the thesis, synchrotron radiation is applied for various X-ray measurements. The X-ray diffuse scattering is involved for characterizing the disorder features. Single crystal and powder X-ray diffraction is executed for determining the atomic structures. Experimental conditions including beam information, tested samples and adopted instruments are tabulated in Table 2.1. The description of the experimental set-up is given in the following paragraphs.

Table 2.1 Summary of synchrotron experiments in this work.

Synchrotron Radiation Facility	*Beamline*	*Sample*	*Testing Quality*	*Device*	*Detector*
ESRF	D2AM	Cd_6Pr, (Cd Mg at10%) $_6Pr$, Cd_6Yb	Diffuse scattering	Kappa diffractometer	Scintillator
Soleil	Crystal	Cd_6Tb	Structure determination	4-circle diffractometer	2D CCD

Soleil	Crystal	Cd_6Tb, Cd_6Yb	Phase transition	2-circle diffractometer	Multi-analyzer detectors
Diamond	I16	Zn_6Sc, Cd_6M (M=Tb, Yb, Ho,	Phase transition	6-circle diffractometer	Pilatus, Medipix

2.3.1 The beamline optics

Before getting to the experimental hutch, the white beam produced in the storage ring and insertion devices is selected in an optical hutch to achieve monochromatic beam. The beamline optics will be introduced by considering the example of D2am which is located at the bending magnet D2 of the ESRF.

The optical hutch in D2am and a schematic are illustrated in Figures 2.3.1 (a) and (b) respectively[91]. The white beam is first collimated by a limitor located in the first vacuum vessel. Then the attenuation is applied in the next vacuum vessel where two filter holders are designed. The first slits system is also located in this vessel to set the vertical and horizontal divergence of the incoming beam. The monochromatic beam is produced by the mirrors and monochromator following the second vessel. The mirrors are used for vertical focusing of the beam selected by a two-crystal monochromator. A secondary slits system is located in front of the second mirror to clean the monochromatic beam. The beam is kept under vacuum until getting out of the second slits system. Before used in experiments, the beam is finally adjusted by the secondary shutter and third slits system which are located between optical hutch and experimental hutch.

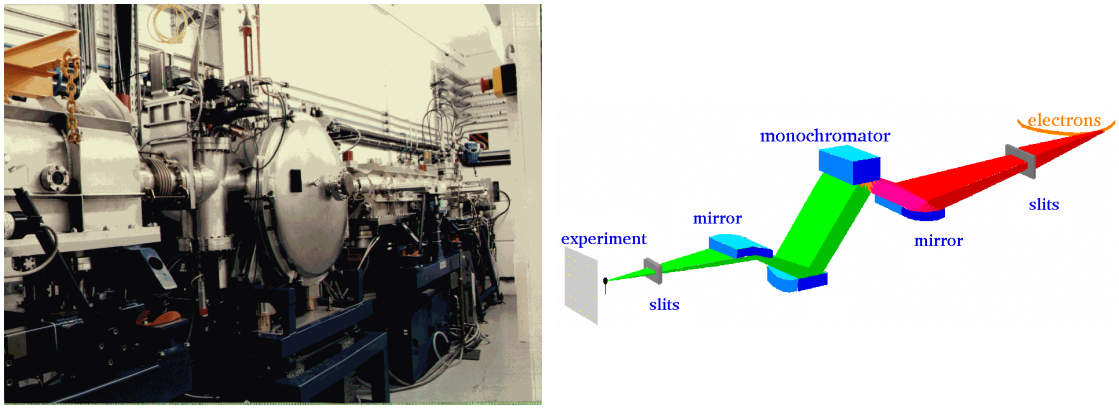

Figure 2.3.1 A view of the optical hutch in D2am (a), and a schematic of the optical hutch.

2.3.2 Diffractometer

The diffractometer can be operated in both transmission and reflection configurations. In the case of commonly used 4-circle diffractometer, the reflection one could be realized via 4 circles: Mu, Phi, Kappa and Theta (see Figures 2.3.2). The whole diffractometer is mounted on a table which could be adjusted for alignment. The incoming beam defined by the optics is

diffracted by sample, and then collected and analyzed by detectors. Depending on different experiment requirements, relevant detectors are chosen including photodiodes, 2D-CCD, photomultiplier with NaI scintillator, XPAD *etc*.

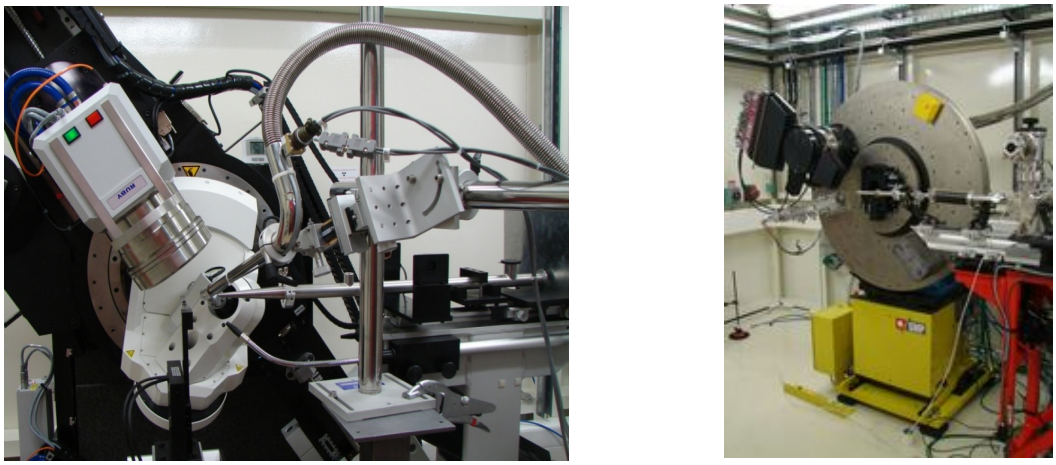

Figure 2.3.2 (a) View of the 4-circle diffractometer equipped with a gas streamer (CryoIndustries of America) to cool the sample. (b) 2-Circle diffractometer and its multi-crystal analyzer in the BC hutch. (Crystal beam, Soleil, Paris)

The 2-circle diffractometer is efficient instrument for powder diffraction as shown in Figure 2.3.2 (b). A rotating motor could be mounted on the sample holder to avoid preferred orientation. The detection is carried out via multi-analyzer detector, comprising multi-Si (111) crystal analyzers followed by scintillation detectors (LaCl3 or Ce). Two parameters are responsible to adjust the detector system, one for the multi-analyzer, and the other for related detectors. To obtain final diffraction diagram, the multiple independent diagrams are shifted and summed up simultaneously. The setup enables a data collecting with high speed and high resolution.

Comparing with 4-circle diffractometer, 6-circle diffractometer adds options for ω and 2θ, making them adjustable in both horizontal and vertical planes. For Huber 6-circle diffractometer, a specific design called 'Huber tower' could be mounted on the ω circle, allowing system work with grazing beam.

2.3.3 Detectors

Photomultiplier with NaI scintillators was used in the diffuse scattering measurements of Cd_6Pr, (Cd Mg at10%)$_6$Pr and Cd_6Yb. Filters can be inserted after the monitor to avoid saturation on the detector. A calibrated aperture can be inserted on the slit located between diffusing Kapton foil and the monitor. By adjusting the aperture, one can control the counting rate in the monitor.

XPAD pixel detector is a commonly used 2D detector developed using the pixel hybrid technology. It can provide a large dynamical range and high counting rate. The being processed XPAD3 allows a counting rate above 2×10^5 photons/pixel/s. The up-to-date

technique can reduce the pixel size to 130μm with similar or enhanced performances. Detectors using Si diode can work in the energy range 5-25keV and those with CdTe diodes are available in an energy range up to 60keV.

The multi-analyzer has been designed for powder XRD. Two adjustable rotations are available at given energy: one for the crystals and the other for detectors. The crystals (normally Si(111)) are followed by scintillation detectors mounted on the analyzer. The crystals are glued with paraffin on precisely machined supports to obtain a stable and reproducible mount with constant relative configurations between adjacent crystals. The 21-Si(111) crystal analyzer used at Crystal beam in Soleil is illustrated in Figure 2.3.3. The signal of each detector, which is detected simultaneously, is shaped and amplified using homemade amplifiers-discriminators. The collected 21 independent diagrams are then shifted and summed up to give the final diffraction diagram.

Figure 2.3.3 A view of the multi-analyzer detector used at Crystal beamline, Soleil, France.

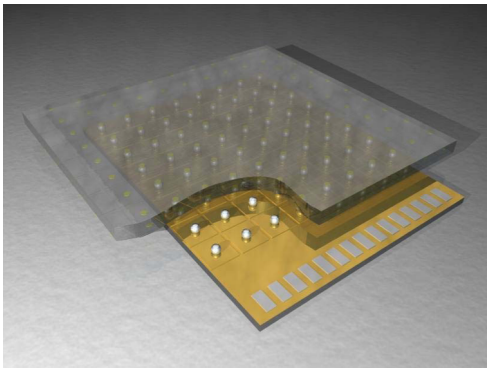

Figure 2.3.4 Schematic of a hybrid detector. The PN-diode array and the readout ASIC are connected by small metal balls.

The Medipix is a family of photon counting pixel detector where a semiconductor sensor layer made of silicon, GaAs or CdTe is bonded to an electronics layer[92]. Electron/hole clouds are made by the incident radiation in the semiconductor. Then the charges are collected and processed by the electronics layers. The stimulated electronics provide the number of events in each pixel. Medipix-2, Timepix, and Medipix-3 are all 256×256 pixels with a pixel size of 55μm. Discriminators are applied to select an energy arrange only in which the electronics count events.

PILATUS, short for Pixel Apparatus for the Swiss Light Source, is another CMOS-based photon counting detector developed at the Paul Scherrer Institute during the last decade. PILATUS detectors are 2D hybrid pixel array detectors which works in single photon counting mode[93]. They have a high dynamical range, i.e. 10^6:1, which makes it possible to collect both strong and weak reflections accurately. The single photon counting technique reduces the noise signals with a very short readout time (less than 3ms) and high counting rate (at least 2×10^6 photons/pixel/s). Moreover, the energy threshold is adjustable to suppress fluorescence background from the sample. The detector includes two parts: a 2D array of PN diodes, and the readout ASIC (Application specific integrated circuit). These two parts are

connected by bump-bonding, i.e. small metal balls. The schematic is displayed in Figure 2.3.4.

2.3.4 Temperature control

The low cryogenic temperatures applied in this thesis are obtained and maintained using cryostat. It works in different ways, most commonly with liquid gas such as nitrogen or helium. Figure 2.3.5 is a schematic of cryostat used in D2am beam in ESRF and I16 beam in Diamond.

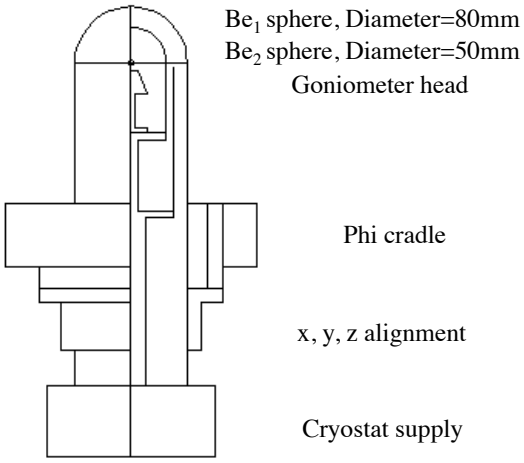

Figure 2.3.5 A view of the cryostat set inside the phi circle. The temperature auto-tuning is controlled by model 330 from Lakeshore. There are two thermometers channels, one is a silicon diode responsible to the temperature control, the other is a silicon or platinum resistor near the sample.[94]

It can be mounted on the phi circle of the goniometer. The top is domed by two Be hemispheres which allow the beam go through with negligible loss. The inner chamber can be filled with exchange gas to improve the temperature conduction between the cold exchanger and the sample.

Chapter 3. Molecular Dynamics Simulation

Molecular dynamics (MD) simulation is a powerful tool to explain or predict experiments. The booming of computing techniques (super computer, cloud computing *et al*) and dramatic progress in simulation theory (Density Functional Theory(DFT) *et al*) have enabled us to simulate very complex systems in various extreme conditions. It allows us to have a view of the motion of the atoms based on which the physical properties can be investigated in atomistic scale.

First principle calculation is a powerful method for studying properties of condensed matter. It is usually the first choice whenever being feasible because of its high accuracy and reliability. The *ab initio* calculation is a quantum mechanics method giving configuration or property of system by solving Schrödinger function. The calculation is carried out with restricted parameters such as mass of electron, proton and neutron, velocity of light. No empirical or semi-empirical parameters but proper approximation (Born–Oppenheimer Approximation[95], Hartree–Fock Approximation[96] *et al*) are applied. The introduction of approximations improved greatly the modeling of the exchange and correlation interactions in the DFT which determines properties of a many-electron system by using the spatially dependent electron density. Despite the improvements of DFT and various approximations reduce greatly the calculation amount, the computing capability of *ab initio* molecular dynamics (AIMD) simulation is still limited. Especially for complex compounds with elements as transition metal whose *s*, *p*, *d* orbital electrons are potentially easy to be stimulated as valence electrons. In general, the processing capacity of AIMD for metallic systems is ~100-200 atoms in 10-100ps.

Regarding to our systems, considering the complexity of QCs and ACs, and the limitation of computer power, *ab initio* molecular dynamics simulation is impossible to achieve in most cases. The first principle analysis to ACs up to now is mainly to achieve the energetic or electronic ground state of 1/1 approximants[10][97].

To study the long-range correlation effect, we need a supercell containing at least 2×2×2 unit cells which has been much beyond the scope of AIMD. Therefore we carried out classical MD simulation using code LAMMPS (see section 3.4), which is able to process hundreds of thousands of atoms with proper accuracy. The details of employed potential and simulation settings will be introduced in following sections.

The principle of classical MD simulation is integrating Newton's equation of motion for atoms, molecules, or other particles that interact with each other by force field. The Newton's equation can be expressed in form of vectors as:

$$\frac{d^2}{dt^2}\vec{r_i} = \frac{d}{dt}\vec{v_i} = \vec{a_i} \qquad 3.1$$

$$\vec{v_i} = \overrightarrow{v_i^0} + \vec{a_i}t \qquad 3.2$$

$$\vec{r_i} = \overrightarrow{r_i^0} + \overrightarrow{v_i^0}t + \frac{1}{2}\vec{a_i}t^2 \qquad 3.3$$

where $\vec{r_i}$ is displacement of the i^{th} atom at the moment t, and $\vec{v_i}$, $\vec{a_i}$ are velocity and acceleration respectively. Once $\vec{r_i}$ is known, the positions of atoms will be knowable.

Leak-frog integration is a popularly used algorithm for solving Newton's equation developed by Verlet[98]. The mathematical description of Leak-from method can be written as:

$$\vec{v_i}_{\left(t+\frac{1}{2}\delta t\right)} = \vec{v_i}_{\left(t-\frac{1}{2}\delta t\right)} + \vec{a_i}_t \delta t \qquad 3.4$$

$$\vec{r_i}_{(t+\delta t)} = \vec{r_i}_t + \vec{v_i}_t \delta t \qquad 3.5$$

The starting velocities and positions of atoms, i.e. $\vec{v_i}|_{t=0}$ and $\vec{r_i}|_{t=0}$, are defined beforehand. When $\vec{v_i}|_{t=t-1/2\delta t}$ is known, then by acceleration $\vec{a_i}_t$, which could be given by force field (Newton's second law), the velocity and displacement at the moment $t + 1/2\ \delta t$, i.e. $\vec{v_i}|_{t=t+1/2\delta t}$ and $\vec{r_i}|_{t=t+1/2\delta t}$, is obtained. As a consequence, the expression of velocity is given by:

$$\vec{v_i}_t = \frac{1}{2}\left[\vec{v_i}_{\left(t+\frac{1}{2}\delta t\right)} + \vec{v_i}_{\left(t-\frac{1}{2}\delta t\right)}\right] \qquad 3.6$$

Apart from velocities, the other necessary aspect to describe particles' trajectories is acceleration, which is given by force field, i.e. effective potentials.

3.1 Effective potential

As discussed above, other than Schrödinger function, the classical MD simulation determines particles' motions by effective potentials which are normally either empirical or semi-empirical. The principle of an effective potential is combing multiple interactions into a single one. Various models have been put forward for different systems in the past years. As a summary, some classical types of potentials will be introduced briefly in the following subsections.

3.1.1 Pair potential

Pair potential is the most widely used model describing the interactions between two objects. In general, some pair potentials were developed by theoretically deducing accompanying some experimental parameters, e.g. elastic constant, equilibrating lattice constant, cohesive energy and so on. Others were proposed based on empirical approximation, which is easier to realize however in many cases with lower accuracy. Pairwise potentials can be constructed in many ways, and the most widely adopted types are Lennard-Jones (LJ)[99][100], Morse[101], Born-Mayer-Huggins[95][102][103].

LJ potential

The expression of LJ potential is of the form:

$$V_r = \frac{V_0}{n-m}\left[m\left(\frac{r_0}{r}\right)^n - n\left(\frac{r_0}{r}\right)^m\right] \qquad 3.7$$

where V_0 is the amplitude of interactions, r is the distance between two interacting particles, and r_0 refers to the atom size. Values of n and m could be determined by dipole-dipole interaction in secondary perturbation theory of quantum mechanism. Then the expression could be transformed as:

$$V_{LJ} = 4\varepsilon\left[\left(\frac{\sigma}{r}\right)^{12} - \left(\frac{\sigma}{r}\right)^{6}\right] = \varepsilon\left[\left(\frac{r_m}{r}\right)^{12} - 2\left(\frac{r_m}{r}\right)^{6}\right] \qquad 3.8$$

where ε is the depth of potential well, σ is the cutoff of the potential, i.e. the interaction beyond this distance is zero, and r_m is the distance where potential gets the minimum. The 12-power term denotes the Van der Waals' force (VDW), and the 6-power term expresses the repulsive forces which result from Coulomb force between nuclei and the inter-electronic overlapping energy. So the LJ potential is also named as 12-6 potential or 6-12 potential.

Morse potential

Morse potential was proposed by Morse in 1929 to model potential energy of diatomic molecules[101]. The mathematical expression of Morse potential is given by:

$$V_r = D_e\left[1 - e^{-\beta(r-r_e)}\right] \qquad 3.9$$

where D_e is the depth of the potential well, r is the distance between interacting atoms, and r_e is the bond length where the inter-particles reach equilibrium, and

$$\beta = \pi\nu_e\sqrt{\frac{2\mu}{D_e}} \qquad 3.10$$

$$\mu = \frac{1}{\frac{1}{m_1} + \frac{1}{m_2}} = \frac{m_1 m_2}{m_1 + m_2} \qquad 3.11$$

ν_e is the vibrational constant, and m_1 and m_2 are masses of the two particles. Morse potential is usually used for constructing multi-body potential.

Born-Mayer-Huggins potential

The Born-Mayer-Huggins potential is in form of:

$$V_r = Ae^{B(\sigma-r)} - \frac{C}{r^6} - \frac{D}{r^8} \qquad 3.12$$

As in the cases above, r is the distance between inter-particles, and σ is the equilibrium distance where force is supposed to be zero. The first term is the repulsion as LJ potential, and the second and third terms indicate dipole-dipole interaction and dipole-quadrupole interaction respectively. Such potential is well used to study alkali halides.

3.1.2 Many-body potential

The pairwise potentials work efficiently for molecular crystals and ionic compounds. However, difficulties are encountered for intermetallic alloys containing transition metals because of their complicated electronic structure forming not only metallic bonds but also covalent bonds. For the sake of a better description, an additional term is in need of being introduced.

Embedded atom model (EAM) potential

In the view of Daw and Baskes[104], one nucleus is not only repulsed by its neighboring nuclei, but also interacts with electron cloud forming by extranuclear and background electron. The energy of a *N*-body system in EAM is of the form:

$$U_{tot} = \frac{1}{2}\sum_{j=1,j\neq i}^{N}\sum_{i=1}^{N}\phi_{ij}(r_{ij}) + \sum_{i=1}^{N}F_i(\rho_i) \qquad 3.13$$

Where ϕ_{ij} is the pairwise potential of the inter-nuclei, and F_i is the energy required to embed the i^{th} nucleus into the electron cloud possessing an electron density of ρ_i.

The expression of EAM for a single elementary system is determined by fitting its lattice constant, cohesive energy, elastic constant, forming energy of vacancy *et al*. The fitting could be carried out by Rose approximation:

$$U_r = -U_c\left[1 + b\left(\frac{r}{r_e} - 1\right)\right]e^{-b\left(\frac{r}{r_e}-1\right)} \qquad 3.14$$

$$b = \sqrt{\frac{V_e B}{U_c}} \qquad 3.15$$

where U_c is the combining energy, V_e is the volume of atoms in equilibrium and B is elastic module. For a binary system, the EAM potential is generally obtained by interpolating with cubic splines. EAM potential is now successfully used for in most intermetallic alloys.

Finnis-Sinclair (F-S) potential

F-S model[105] is developed based on tight binding theory and commonly used for interaction of binary systems. The total energy of system is of the form:

$$U_{tot} = \sum_{i=1}^{N}\left[\sum_{j=1\neq i}A_{ij}e^{-p_{ij}\left(\frac{r}{r_e}-1\right)} - \sqrt{\sum_{j=1\neq i}\varepsilon_{ij}^2 e^{-2q_{ij}\left(\frac{r}{r_e}-1\right)}}\right] \qquad 3.16$$

r and r_e are interacting distance and equilibrium distance respectively, and A_{ij}, ε_{ij}, p_{ij} and q_{ij} are parameters obtained from fitting in units of *e*V, *e*V, dimensionless and dimensionless. The first term indicates the interactions between two nuclei, and the second term denotes the

correlation energy of *N*-body interaction. Comparing to EAM potential, F-S model is simple in form hence easier to fit.

Modified embedded atomic model (MEAM) potential

EAM and F-S potentials are both constructed simply assuming the system as central symmetry. For materials with highly directional bonds, they work poorly until a modified version of EAM was proposed by Baskes[106][107]. And later a simplified version was developed by Lenosky[108] who employs cubic spline instead of predetermined analytic function.

The total energy of system is of the same form as EAM potential:

$$U_{tot} = \frac{1}{2}\sum_{i=1}^{N}\sum_{j=1\neq i}^{N}\Phi_{ij}(r_{ij}) + \sum_{i=1}^{N}F_i(\rho_i) \tag{3.17}$$

The angular factor is introduced in the term of embedded energy function:

$$\rho_i = \rho^{(0)} exp\left[\frac{1}{2}\sum_{h=1}^{3} t^{(h)}\left(\frac{\rho^{(h)}}{\rho^{(0)}}\right)^2\right] \tag{3.18}$$

where $\rho^{(h)}$ $(h = 0, 1, 2, 3)$ are related to electron density on orbits of s, p, d, f respectively, and $t^{(h)}$ are weighting factors of each component. The $\rho^{(h)}$ is given by:

$$\rho^{(0)} = \sum_{\alpha} f^{(0)}(r_\alpha) \tag{3.19}$$

$$\rho^{(1)} = \sqrt{\sum_{i}\sum_{\alpha,\beta} f^{(1)}(r_\alpha) f^{(1)}(r_\beta)\frac{x_\alpha^i x_\beta^i}{r_\alpha r_\beta}} \tag{3.20}$$

$$\rho^{(2)} = \sqrt{\sum_{i,j}\sum_{\alpha,\beta} f^{(2)}(r_\alpha) f^{(2)}(r_\beta)\frac{x_\alpha^i x_\alpha^j x_\beta^i x_\beta^j}{(r_\alpha r_\beta)^2} - \frac{1}{3}\sum_{\alpha,\beta} f^{(2)}(r_\alpha) f^{(2)}(r_\beta)} \tag{3.21}$$

$$\rho^{(3)} = \sqrt{\sum_{i,j,k} f^{(3)}(r_\alpha) f^{(3)}(r_\beta)\frac{x_\alpha^i x_\alpha^j x_\alpha^k x_\beta^i x_\beta^j x_\beta^k}{(r_\alpha r_\beta)^3}} \tag{3.22}$$

where α, β indicate the two interacting particles, $x_\alpha^i, x_{\alpha,}^j x_\alpha^k$ are coordinate components of atom α relatively to the i^{th} atom. And $f^{(h)}(r)$ describes the radial electron density, which is given by:

$$f^{(h)}(r) = e^{-\eta^{(h)}\left(\frac{r}{r_e}-1\right)} \tag{3.23}$$

MEAM potentials attempt to describe interactions taking account angular affect, which results from directional bonds, so the calculation is much huger. Comparing with EAM and F-S potentials, MEAM takes 3-5 times longer, however, obtaining much accurate results.

3.2 Force matching

With a bunch of potentials mentioned above, we can handle most of simple compounds and even some organics. However, obtaining practical and accurate force fields is invariably fussy especially for complicatedly interacting systems. Since quantities are needed for determination of those energy functions, nevertheless, experimental measurements on some of these complex systems are unfeasible for the time being. As a solution, force matching method crosslinking first principle calculation and classical empirical potentials was proposed[109]. Instead of obtaining potentials from a set of experimental qualities, force matching method creates potentials by fitting results against first principle calculation.

Generally, the force matching potential is obtained by performing a large number of first principle calculations with different geometries and a wide range of temperatures, and then the obtained amount of information is used to fit as closely as possible the force from first principle calculation. The matching process is carried out by minimizing the energy of the system with a set of parameters up to the order 100. Since the first principle calculations are implemented with different geometries and temperatures, the finally constructed potential is of satisfying transferability.

The potential we employed throughout the work for MD simulations is obtained from a collection of *ab-initio* data, fitted to an analytical oscillating pair potential. The database including force and energy of a set of ZnSc compounds was created by using the program VASP. The details will be presented detailedly in Chapter 6.

3.3 Simulation conditions

A classical MD simulation consists of three parts: initial configuration, potentials and input script. Proper settings act significant role in a simulation to make an emulational environment. Parameters differ between systems according to different properties. Some key variables are outlined as follows.

3.3.1 Ensemble

An ensemble is defined as a set of systems with consistent conditions. Micro-canonical ensemble is system with fixed particle number (N), fixed volume (V) and fixed energy (E), short as NVE ensemble. In case the energy minimization technique (e.g. conjugate gradient method) or a heat bath (e.g. Berendsen thermostat and Nosé–Hoover thermostat[110]) is adopted, a canonical ensemble or NVT with particle number (N), volume (V) and temperature (T) being fixed is obtained. For a system with fixed temperature and chemical potential, the correlated ensemble is grand canonical ensemble, in which systems can exchange both energy and particles, however, the total energy, particles and volume are kept constant as well as volume of each system. Similarly to canonical ensemble, if system is coupled to a barostat, which applies a fixed pressure by rescaling simulation box, i.e. exchanging energy

and volume, then the ensemble is abbreviated as NpT. For equilibrated systems, the microstates are fluctuated in time scale, and in the view of ergodic principle, the average of each physical quality in time scale in one system equals to the average of related quality to all systems. The bigger the system is, the smaller the fluctuation rate becomes. Hence for a macro-system, the physical quantities calculated from different ensembles approaches to identical.

Canonical ensemble is the most widely used ensemble. As shown in Figure 3.3.1, the ensemble is surrounded by an adiabatic hard layer, and the hard layers between systems are energy pervious but particles resistant. As a consequence, after sufficient energitic exchange, all systems reach a fixed temperature which is decided by the average of E_i. As discussed before, for macro-system the number of particles N is large enough to neglect the fluctuation of each physical quantity, and the number of systems in ensemble N', which stands for all the possible states, is ideally supposed to be ∞.

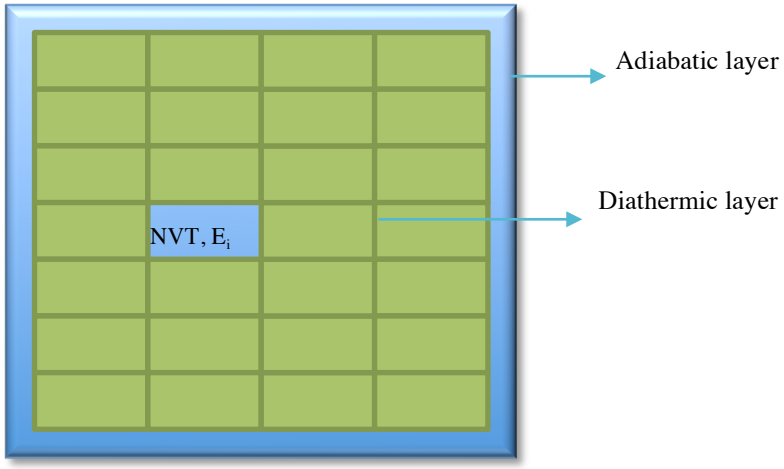

Figure 3.3.1 Schematic representation of canonical ensemble.

As systems in canonical ensemble correspond relevant microstates, and it is found that the number of systems in each microstate is proportional to $exp(-\beta E)$, where $\beta = 1/\kappa_B T$ with κ_B the Boltzmann constant equal to $1.3806488(13)\times10^{-23} JK^{-1}$.

Then the partition function of canonical ensemble is given by:

$$Z(\beta) = \sum exp(-\beta E) \qquad 3.1$$

If we do natural logarithm to the partition function, then the result gives the Helmholtz free energy:

$$F = -\kappa_B T ln Z \qquad 3.2$$

With the partition function Z, the average energy could be obtained by the first derivative of $ln\ Z$ to β:

$$\bar{E} = -\frac{\partial \ln Z}{\partial \beta} \qquad 3.3$$

3.3.2 Boundary condition

By applying effective potential and proper approximation, the processing capability of classical MD is improved greatly. Take LAMMPS as an example, the maximum number of atoms it can handle is up to 10^5, equivalently 10-20nm in length scale. However, this is still far from sufficient to do a simulation comparative to relevant experiment. Furthermore, on one hand, the smaller the simulation box is, the bigger the surface effect becomes, on the other hand, when atoms are pushed off the box by interaction, the number of particle will change. One effective and widely used solution is the periodic boundary condition.

The principle of periodic boundary condition is whenever atom moving out of the box, equivalent atom will move in on the opposite side. It means the atoms close to or on surfaces interact not only with atoms on center-close side, but also with atoms located on the opposite faces. In this case, the cutoff distance of interaction must be considered prior since if the box size were smaller than cutoff distance, atoms would impact themselves.

One thing to emphasize is that the periodic boundary condition is similar with replicating process. However, replicate is to create simulation box, and the replica are involved for relaxation and simulations as shown in Figure 3.3.2. While periodic boundary just exchange the information (position and interaction) of atoms along surfaces to create an infinite system without boundary. A scheme illustrates the mechanism how periodic boundary condition works in Figure 3.3.3.

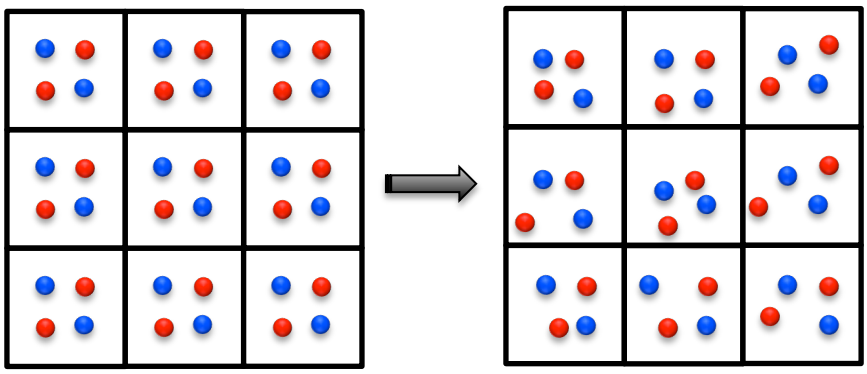

Figure 3.3.2 Scheme of duplication and relaxation in 2D image. Left: Structure is replicated at the beginning by three times; Right: By interacting with each other, system is relaxed.

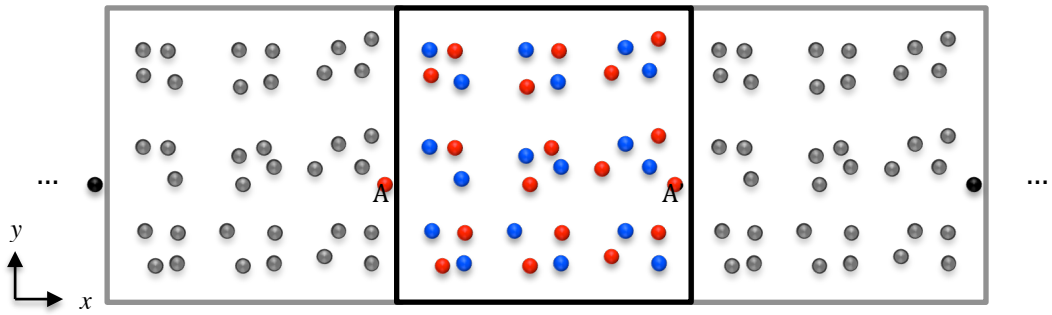

Figure 3.3.3 Presentation of periodic boundary condition along *x* direction. When atom A moves out of the simulation box, an alternative atom A' which is equivalent with A moves in on the opposite side. Therefore the number of particles keeps constant all the time.

3.3.3 Energy minimization

According to the description of inter-atomic forces in studied system, internal stress could exist in the initial configuration owing to improper atomic positions. Energy minimization is the process iteratively adjusting atom coordinates until reaching a possible local potential energy minimum. The energy minimization is terminated when one of criteria is satisfied. Mathematically, the local minimum energy should be as close as to a critical point of the objective function:

$$E(r_1, r_2, \cdots, r_N) = \sum_{i,j} E_{pair}(r_i, r_j) + \sum_{i,j} E_{bond}(r_i, r_j) + \sum_{i,j,k} E_{angle}(r_i, r_j, r_k) + \sum_{i,j,k,l} E_{dihedral}(r_i, r_j, r_k, r_l) + \sum_{i,j,k,l} E_{improper}(r_i, r_j, r_k, r_l) + \sum_{i} E_{fixes}(r_i) \quad 3.4$$

where E_{pair} is the energy of non-bonded pairwise interactions such as long range Coulomb interactions which differ from bond interactions expressed as the 2nd term. Bonds are pairs interacting between specific atoms and keep in force for the whole duration of simulation. $E_{angle}, E_{dihedral}$ and $E_{improper}$ are angle, dihedral and improper interactions between triplets, dihedral and improper quadruplets which are defined in the initial structure respectively. The last term E_{fixes} denotes energy resulting from constrains or forces applied to atoms by introducing external conditions such as a wall. Details on minimization and objective function can be found on page 747, *minimize command*, of the LAMMPS manual[111].

The methods of realizing energy minimization include conjugate gradient, deepest descent relaxation, Newton method, damped dynamics method and so on. To terminate the minimization process, one of the following criteria must be satisfied. Energy tolerance is defined as the energy change between consecutive iterations divided by the energy magnitude. The iteration process is stopped whenever energy tolerance is equal to or smaller than the

criterion. The second criterion is by evaluating the length of force vector of each atom, i.e. the three components of force to each atom should be less than a pre-setting tolerance. If the energy or force tolerance can not reach to criteria for a long time, then the iteration would be terminated by settings of maximum number of iteration or the total force evaluation. The settings of criteria differ in different systems, so one should attempt to tune the minimization process. Moreover, the efficiency of minimization is also affected by various algorithms.

Conjugate gradient is the most commonly used algorithm for searching optimization of unstrained system. It is developed by combining conjugacy with deepest descent method. The principle of conjugate gradient algorithm (CGA) is computing a new searching direction conjugate to the previous one to find a local minimum iteratively. Therefore CGA has two iteration, one named as 'outer iteration' is the time step defined for the whole duration of simulation, and the other so called 'inner iteration' is step along line search in a specific direction (conjugate operation). The following is an example setting for a LAMMPS MD simulation:

```
# minimization

min_style cg

minimize 1.0e-4 1.0e-6 100 1000
```

The minimization style is defined as CGA which is the default setting in LAMMPS. The four parameters indicate the relevant terminating criteria. The first is the stopping tolerance for energy, which means if energy magnitude is 10^4, minimization would not stop until energy change between two successive iterations come to 1. The other three are stopping force tolerance, maximum iterations of minimizer, and maximum number of force or energy evaluations, respectively. Furthermore, for CGA, when step distance of inner iteration reaches to zero, implying the iterations touch to one of the minimum, the minimization will stop automatically as well.

3.3.4 Simulation in parallel

As aforediscussed, the techniques of computer are developing greatly to meet the requirement in different fields. Parallel computing is one of the most efficient ways of improving computing power, with which many sub-tasks are executed simultaneously. The principle of parallel computation is that large calculation can be divided into many sub-calculations, and then be carried out on different processors. Each processor can communicate with others to solve the calculations in parallel. The ways of employing parallel computing include bit-level, instruction level, data and task parallelism[112].

Concerning its high efficiency and low power consumption, parallel computing has become the most popular way of constructing supercomputers. Generally it can be realized either by connecting multiple computers or running in a single computer with multicores or multiprocessors. For a parallel calculation, all subtasks must communicate with each other to synchronize together since the work of each subsystem relies on its neighboring ones. The problem is divided into many smaller ones, each subtask could be processed faster or slower.

Therefore according to the 'Buckets effect', the speed of parallel computing is determined by the slowest one. Hence it is of importance to optimize the histogram of processors to reach highest efficiency. Message Passing Interface (MPI) library is one of the most popularly used methods to pass messages between subtasks.

Regarding our simulation with LAMMPS, the parallelism is implemented by spatial-decomposition techniques partitioning simulation system into several 3D subsystems. Each subsystem is calculated by a single processor, and processors which store information of border atoms of subsystems, so called 'ghost' atoms, communicate with each other. A sketch drawing of the parallel computing is illustrated in Figure 3.3.4.

3.4 Large-scale Atomic/Molecular Massively Parallel Simulator – LAMMPS

LAMMPS is an open source code package for classical MD simulation being designed for parallel computing. It was developed by Sandia National Laboratories and funded by US Department of Energy facility. Generally speaking, LAMMPS works by integrating Newton's equations of particles' motion. Particles interact mutually via short or long-range forces that are described by potentials.

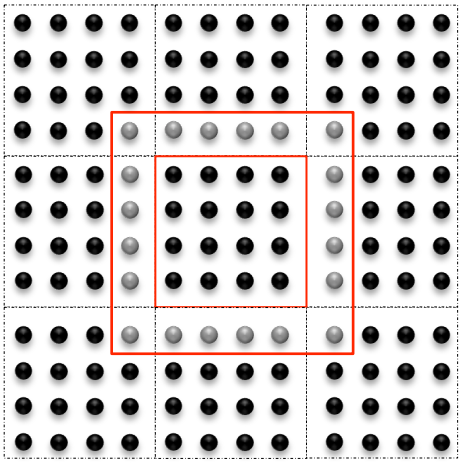

Figure 3.3.4 Sketch of parallel computing in 2D. Task is partitioned into 9 smaller subtasks, for the central one, information of 'ghost' atoms (grey ones) is stored and communicated with border atoms.

The input script of LAMMPS includes typically four parts: Initialization, Atom definition, Settings and Running simulation. Initialization is responsible for the setting of parameters for all simulation, such as units, boundary conditions, atom type and potential *et al*. Atom definition gives the initial structure of simulation, in which the box size, lattice parameters and duplication are defined. Once configuration is defined, settings for reading and writing are made. Potential coefficients, output options, and time step and so on are computed in this part. Finally the simulation is triggered by the command *run* which tells how many steps the simulation is supposed to run. The energy minimization discussed above is usually carried out before formal running.

One example of input scripts for our simulation is attached in Appendix I.

Chapter 4. Structural study on the Cd_6Tb 1/1 approximant

Cd_6RE (RE=rare elements) are a series of isostructural bcc compounds consisting of the same building blocks, i.e. Tsai clusters as their parent quasicrystals *i*-$Cd_{5.7}Yb$ and *i*-$Cd_{5.7}Ca$[1][2]. Although they possess very close composition as both the well-studied aforementioned binary quasicrystals and the recently discovered magnetic binary Cd-based quasicrystal families[3], remarkable different physical properties have been observed in many sides. Therefore a comparison between quasicrystals and their crystalline approximants may yield significant insight in understanding the stability of these complex phases.

The scientific interest in these 1/1 crystalline approximants can date back to last 60s' when a large number of Cd_6RE compounds were reported by Johnson, Schablaske, Tani and Anderson[16]. Later in 70s', Larson *et al*, Bruzzone *et al*, and Wang made more progress on structural determination of these cubic compounds[113][114][115]. The structural characterization of these compounds had been ambiguous for a long time and all arguments were focusing on the description of the local disorder residing inside the dodecahedral shell. Gómez and Lidin made a comparative study in 2003 on various of Cd_6RE compounds and proposed a model which is able to well describe the innermost Cd_4 tetrahedron[4].

The central tetrahedron residing inside the dodecahedron cavity acts crucial role for understanding the stabilizing mechanism of icosahedral quasicrystals and their crystalline counterparts. The motion of the tetrahedron is responsible to the dynamical flexibility of the lattice[81], but also to the intensively studied order-disorder phase transition occurring on most of the Cd_6RE approximants and structurally related Zn_6Sc phase at low temperature. The ordering mechanism of the central tetrahedron has been probed by various experimental means: x-ray diffuse scattering, single grain and powder diffraction using X-ray and neutron, electron diffraction and so on. Computational simulations have also been combined using methods of first principle analysis and classical MD simulation.

4.1 Atomic arrangement of the Cd_6RE phase

Generally, the structure of Cd_6RE phase can be described in two ways. One is the packing of 12 RCd_{16} polyhedra where each R atom surrounded by 16 Cd atoms. In this description, eight Cd_8 cubes can be generated automatically as shown in Figures 4.1.1[4]. These cubes will be discussed in details in the simulation chapter.

The more popular and widely accepted representation of the Cd_6RE phase is the packing of 'partially interpenetrating defect triacontahedron', named Tsai type cluster, in a frame of *bcc* structure as shown in Figures 4.1.2[5]. The structure of the Cd_6RE phase can be fully characterize without any glue atoms using such RTH. The RTH cluster unit consists of five successively close-packed shells altogether 158 atoms. The disordered and inherently symmetry-breaking tetrahedron locating in the center of the RTH cluster unit can be modeled by a triple split of the tetrahedron sites. All known disorder tetrahedron in the Cd_6RE families can be well described using this model by successively increasing the amount of the split. Furthermore, the Cd_8 cube mentioned above shares two common sites with two adjacent dodecahedron shells along the space diagonal of the cubic lattice.

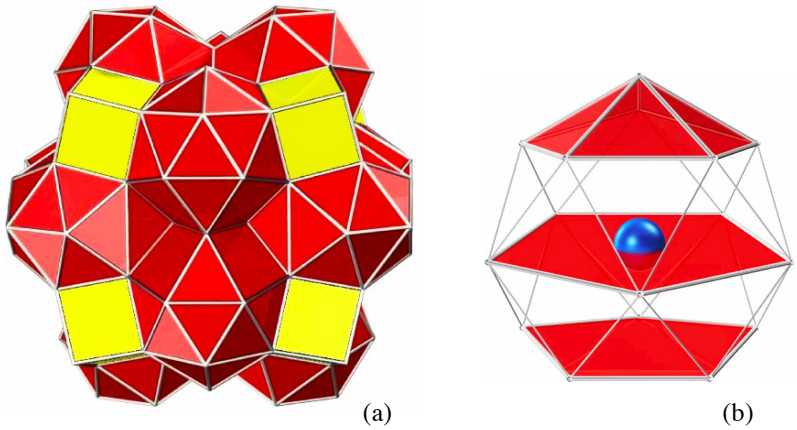

Figure 4.1.1 (a) Building block of the Cd_6M phase with 12 Cd_{16} polyhedra and 8 Cd_8 cubes; (b) Cd_{16} polyhedron with an *M* atom locating at the center. Ref. [4]

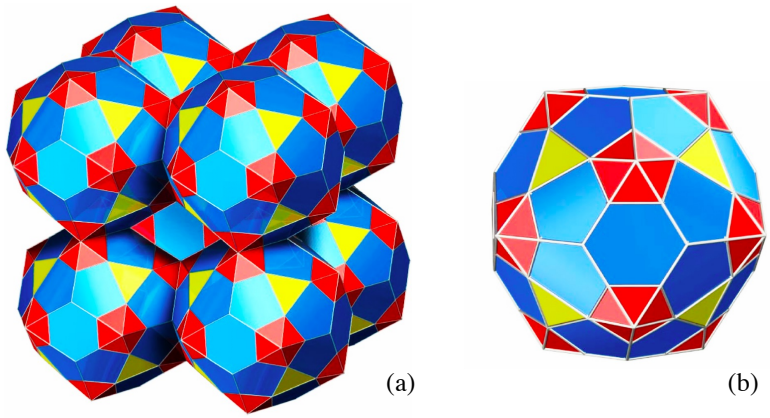

Figure 4.1.2 (a) Cubic arrangement of the Cd_6M phase with partially interpenetrating triacontahedron; (b) Triacontahedron shell comprising 92 Cd atoms. Ref. [4]

Previous studies have elucidated that the order-disorder structural phase transition is related to the ordering of the central tetrahedron. The tetrahedra dynamically reorient between equivalent orientations at high temperature, as temperature decreases, tetrahedra turn into ordering in an antiparallel type[6][7][8]. The structure determination of the Zn_6Sc monoclinic phase at low temperature has been performed by Ishimasa[8] using powder x-ray diffraction data. Apart from the experimental results, numerous simulation work has been also performed on Cd_6Yb and Cd_6Ca *via* first principle calculation[9][10]. The altogether results confirm a small tilting angle happening on tetrahedron to avoid an unrealistic short distance to the dodecahedral shell. Experimentally, the tilting angle is confirmed as ~15°, and in *ab inito* simulation executed by Hatakeyama *et al*[9], this value is around 6°. Moreover, x-ray diffuse scattering measurements[11] denote that associating with the ordering of the tetrahedron, the correlation length of short-range order increases rapidly and almost diverges as temperature gets through the transition temperature.

The low temperature phase has been determined as monoclinic with space group *Cc* or *C*2/*c*[12] and a doubled unit cell propagates along [$\bar{1}$01] as illustrated in Figure 4.1.3. Not

taking the small distortion induced by the ordering tetrahedron into account, the lattice basis vectors of high and low temperature phases are correlated with the following rule: $\mathbf{a}_L = \mathbf{a}_H - \mathbf{c}_H$, $\mathbf{b}_L = \mathbf{b}_H$, $\mathbf{c}_L = \mathbf{a}_H + \mathbf{c}_H$.

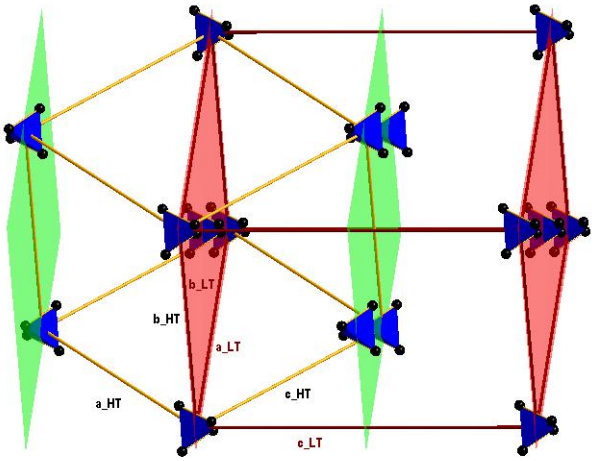

Figure 4.1.3 Representation of the ordering of the tetrahedron, both high and low temperature phases are displayed. The tetrahedra orient antiparallel in different planes.

When phase transition occurs, the symmetric order of the cubic lattice decreases from 24 ($Im\bar{3}$) to 4 ($C2/c$). According to symmetric operation, 6 domains with different orientations are obtained in the structure of the LT phase. The related six representatives are listed as follows[11]:

$$E = \begin{bmatrix} 1 & 0 & 0 \\ 0 & 1 & 0 \\ 0 & 0 & 1 \end{bmatrix} \qquad C_3([111]) = \begin{bmatrix} 0 & 0 & 1 \\ 1 & 0 & 0 \\ 0 & 1 & 0 \end{bmatrix} \qquad C_3^2([111]) = \begin{bmatrix} 0 & 1 & 0 \\ 0 & 0 & 1 \\ 1 & 0 & 0 \end{bmatrix}$$

$$m(a) = \begin{bmatrix} -1 & 0 & 0 \\ 0 & 1 & 0 \\ 0 & 0 & 1 \end{bmatrix} \qquad S_6([1\bar{1}1]) = \begin{bmatrix} 0 & 0 & -1 \\ 1 & 0 & 0 \\ 0 & 1 & 0 \end{bmatrix} \qquad S_6^5([11\bar{1}]) = \begin{bmatrix} 0 & 1 & 0 \\ 0 & 0 & 1 \\ -1 & 0 & 0 \end{bmatrix} \qquad 4.1$$

Because of the distortion of the lattice at low temperature, Bragg peaks derived from domains with different orientations will not coincide but split which is a significant sign of the phase transition. Considering two possibilities of orientating domains[1], i.e. either $\mathbf{a}^*$ or $\mathbf{c}^*$ are common axis for neighboring domains as shown in Figure 4.1.4, the distortion matrices could be expressed respectively as:

$$T1 = \begin{bmatrix} 1+\varepsilon_a & 0 & (1+\varepsilon_c)*\cos\beta \\ 0 & 1 & 0 \\ 0 & 0 & (1+\varepsilon_c)*\sin\beta \end{bmatrix} \qquad T2 = \begin{bmatrix} (1+\varepsilon_a)*\sin\beta & 0 & 0 \\ 0 & 1 & 0 \\ (1+\varepsilon_a)*\cos\beta & 1 & 1+\varepsilon_c \end{bmatrix} \qquad 4.2$$

Where

[1] This part is borrowed from the work of G. Beutier in SIMaP, University of Grenoble, Grenoble, France.

$$\varepsilon_a = \frac{a}{b\sqrt{2}} - 1 \qquad 4.3\ a$$

$$\varepsilon_c = \frac{c}{b\sqrt{2}} - 1 \qquad 4.3\ b$$

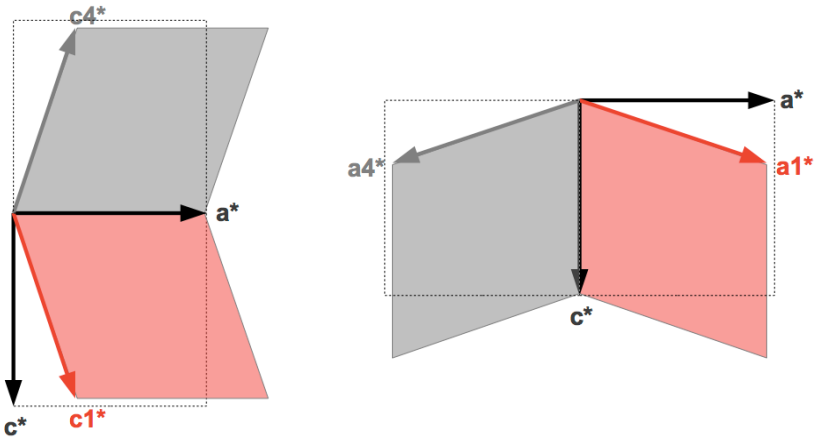

Figure 4.1.4 Two possibilities for neighboring domains: either **a*** (left) or **c*** (right) are set as common axis.

Finally, the indexing of the i^{th} domain, with respect to the cubic setting, is calculated by following equation:

$$\begin{bmatrix} h_i \\ k_i \\ l_i \end{bmatrix} = M_i T_j M_i^{-1} \begin{bmatrix} h \\ k \\ l \end{bmatrix} (j = 1,2)(i = 1,2,\dots,6) \qquad 4.4$$

In addition to temperature dependence, phase diagram with respect to pressure and temperature to Cd_6Yb and Zn_6Sc have been investigated as well systematically[77][79][78]. Different sensitivities to pressure and temperature have been observed between the Cd_6Yb and Zn_6Sc phases. The Cd_6Yb approximant has been proved stable under ultrahigh pressure up to 40GPa at room temperature. It illustrates abundant of i.e. five superstructure phases in a pressure range from room pressure to 5.2GPa and a temperature range from room temperature to 10K. Whereas, the Zn_6Sc presents only three superstructures in a wider pressure interval up to 34.8GPa. Furthermore, different from the Cd_6Yb, no ordering mechanism along <111> was observed in Zn_6Sc.

4.2 Phase transition of the Cd_6Tb

Cd_6Tb, a member of the Cd_6RE isostructural compounds family, is a 1/1 approximant of the *i*-CdMg*RE* quasicrystal as well as the stable binary quasicrystal $Cd_{5.7}Ca$[1] and $Cd_{5.7}Yb$[2] the atomic structure of which had been determined by Takakura *et al* in 2007[49]. Both the *i*-QCs and their approximants are composed of the same building blocks, i.e. Tsai type clusters. Most Cd_6RE compounds have been evidenced undergoing an unique phase transition at LT by measurements of electrical resistivity, selected area electron diffraction (SAED), specific heat capacity and so on[6][12]. Previous works have interpreted that the phase transition is

induced by the ordering of the innermost Cd_4 tetrahedron which is orientationally disordered at HT. All the Cd_6RE approximants possess the same *bcc* lattice at RT with only slight difference in the model of the tetrahedron which has been detailedly studied by Gómez *et al*[4]. The ordering scheme as well as the LT phase have also been investigated previously by Nishimoto *et al*[12]. The structural determination of the LT phase has been accomplished on the Zn_6Sc isostructural crystalline by Ishimasa *et al*[8]. The interests of studying Cd_6Tb are not only invoked by the order-disorder phase transition occurred at ~180K, but also the observation of an unique long-range magnetic order[15][14].

Indeed, it is surprising to find such magnetic transitions in Cd_6Tb at 24K, 19K and 2.4K which are evidenced by the magnetic susceptibility results as well as the specific heat measurements. In spite the aperiodic crystals containing moment bearing elements have been expected an unique magnetic ordering owing to their aperiodic lattice, all of the known QCs up to now exhibit frustration and spin-glass-like behavior at LT. The long-range magnetic order is absent not only in QCs, but also in their ACs except Cd_6Tb. The long-range magnetic order has been confirmed recently by means of x-ray resonant magnetic scattering by Kim *et al*[15]. The sharp magnetic peaks provide a correlation length at least 500Å, and the Tb^{3+} ions are correlated antiferromagnetically between clusters along the 3-fold linkage. It is supposed that the exception occurring to the Cd_6Tb results from the interplay between two competing interactions, i.e. intracluster and intercluster Tb-Tb interactions. As a consequence, it is of significance to determine the structures of the Cd_6Tb crystalline phase above and below T_c.

4.2.1 Sample preparation[2]

The single crystal samples of Cd_6Tb were synthesized by means of flux growth from the Cd rich region. The high purity metals Cd (99.9999 wt%) and Tb (99.9 wt%) were melt in an atomic ratio of 9:1 at 993K for 24h and mixed in a Al_2O_3 crucible sealed inside a quartz cube under reduced Ar. After mixing adequately, the ampule is slowly cooled down to 753K with a cooling rate 2K/h. The excess Cd melt was then removed by high-speed centrifuge. A subsequent annealing was carried out at 923K for 100h to improve the sample homogeneity. After cooling the sample down to 473K with a cooling rate 5K/h, further annealing was taken for 3 weeks to reduce the point defects. The high qualified sample with millimeter size was firstly measured in the X-ray resonant magnetic scattering experiment. A small single grain with approximately size $0.1\times0.1\times0.06$ mm^3 was cut off from the grand sample for the single crystal X-ray diffraction measurements. Some other pieces are grinded for the powder X-ray diffraction measurements.

4.2.2 Experiment measurement

The temperature dependent measurements of the Cd_6Tb was performed by means of powder and single crystal X-ray diffraction respectively. The experiments were carried out using synchrotron beamline D2AM at ESRF operated at 25.5k*e*V (λ=0.4853Å). For the single crystal X-ray diffraction, the crystal-detector distance was set to 80mm, and a full phi-scan (360°) with a step size 1° was executed at 300K (RT), 200K, 100K and 40K for data collection. For other temperatures, measurements were taken with phi scanning from 1° to

[2] The sample is prepared by Tamura's group in Science University of Tokyo, Tokyo, Japan.

180°. Because of the large difference between intensities of main reflections and superstructure reflections, each data set was collected with three different attenuation factors 1, 50, and 1000. A cryostat system was applied for controlling the temperature of the sample, which was placed in an evacuated Be hemisphere. For the powder X-ray diffraction, the measurements were accomplished over a temperature range from RT to 7K, and the data were collected twice for each temperature to reduce the effect of the preferred orientations.

The integrated intensities of reflections were computed via the program *CrysAlisPro*. The numerical absorption correction, operating via *CrysAlisPro*, was carried out based on a model of the sample which is obtained from the recorded images and optimized by the 1000 strongest equivalent reflections, as illustrated in Figures 4.2.1. The primary structure solution based on the charge density map was achieved by the program *superflip*[116] and the refinement was conducted using the program *Jana*2006[117]. For the powder X-ray diffraction, the data was treated by the LeBail fitting method using the software package, *Fullprof_suite*[118][119].

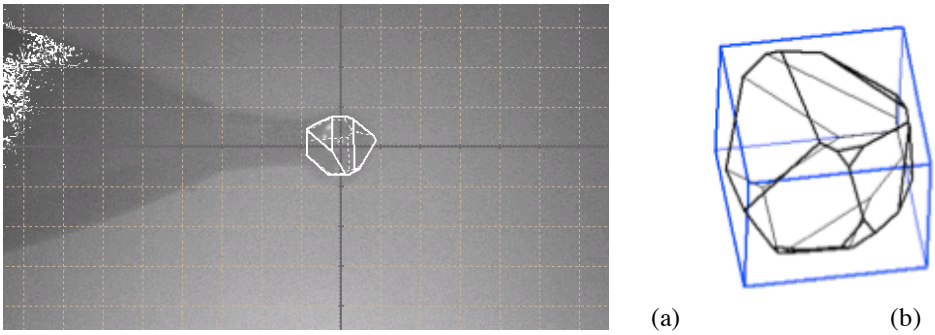

Figure 4.2.1 The image of the sample (a) and the model (b) optimized by the 1000 strongest reflections at RT. The size of the sample is ~100×100×60μm^3.

4.2.3 The superstructure of the Cd_6Tb

As previously elucidated, there exist 6 monoclinic domains in the LT phase, which results in the splitting of the main peaks. This can be observed from both the single crystal diffraction images and the powder diffraction profiles. However, the distortion of the lattice is so small that it is invisible with a crystal-detector distance of 80mm. So we designed two other detailed measurements increasing the crystal-detector distance to 340mm in a cooling and heating process respectively.

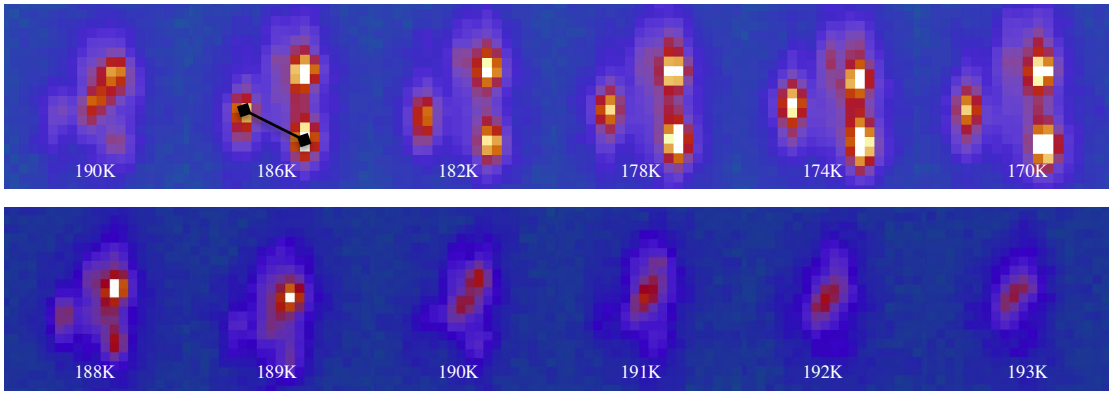

Figure 4.2.2 The temperature dependence of the splitting of the main peak (1 -19 -18) in cooling process (top) and the main peak (0 -18 -18)in heating process (bottom). The distance of the two splitting subpeaks is measured with respect to temperatures as indicated by the black segment.

Figures 4.2.2 shows the evolution of the main peaks (1 -19 -18) and (0 -18 -18) in the cooling and heating processes respectively. The peaks split distinctly in both processes indicating that the phase transition is reversible. Moreover, the T_c is determined as around 190K. On the other hand, we measured the distance of the two splitting subpeaks as indicated in Figure 4.2.2 at 186K. The result shows that the lattice distortion increases linearly as temperature decreases, as displayed in Figure 4.2.3.

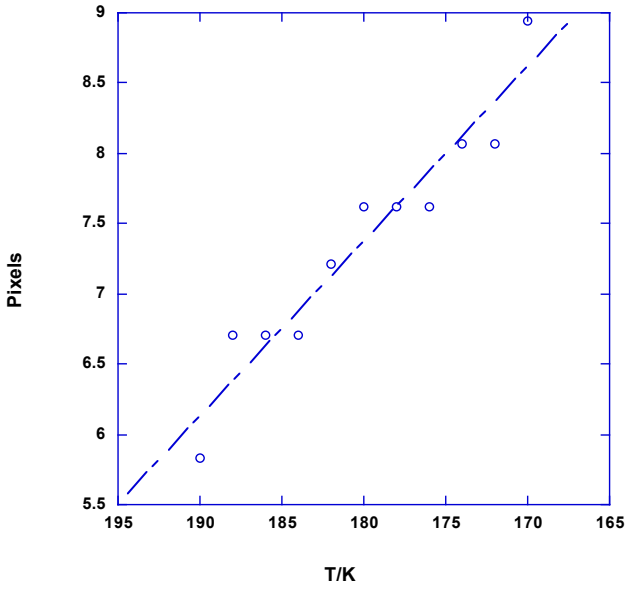

Figure 4.2.3 The distance between the two splitting subpeaks of the (1 -19 -18) on a 2-D Bragg plane as a function of temperatures, demonstrating a roughly linear increase as temperatures cool down.

The phase transition, from *bcc* to monoclinic system, leads to a doubled unit cell which in the reciprocal space corresponds to the appearance of the superstructure reflections on the half-integer Bragg planes. As can be seen in Figures 4.2.4, on hk0 layer, the main reflections at 40K are compatible with that of RT. On the hk1 layer, a large number of superstructure

reflections are clearly visible at 40K inbetween main reflections which indicates the doubling of unit cell.

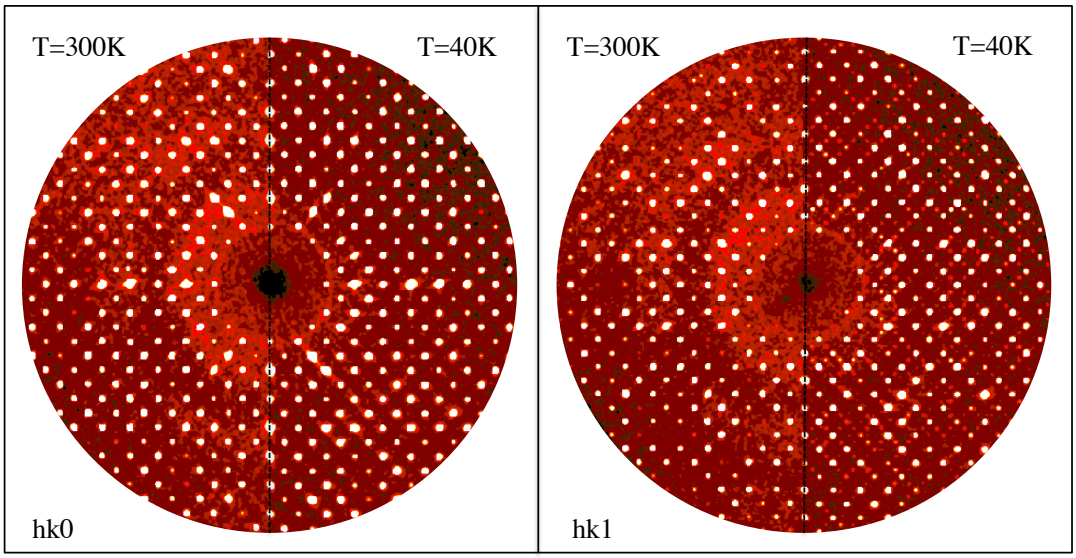

Figure 4.2.4 The reconstruction of the Bragg planes on *hk*0 and *hk*1 layers comparing between 40K and RT. The superstructure reflections are clearly visible at 40K on the *l*=1 Bragg plane.

In Section 4.1, we showed a model of the splitting peaks, based on which we calculated the positions of the subpeaks arising from the 6 different domains of the main peak (0 0 20) at 40K, and compare it with the experimental result as shown in Figures 4.2.5. Similarly, both calculated and experimental results display a distribution along $\boldsymbol{Q}_h$ and $\boldsymbol{Q}_k$ respectively. The centering peak is preserved in the model, however, disappears in experiments, which suggests that the related domain is unstable in the real phase. Furthermore, there are more subpeaks being observed experimentally than the theoretical number, which might owe to that the distortion of the monoclinic lattice happens continuously in the LT phase.

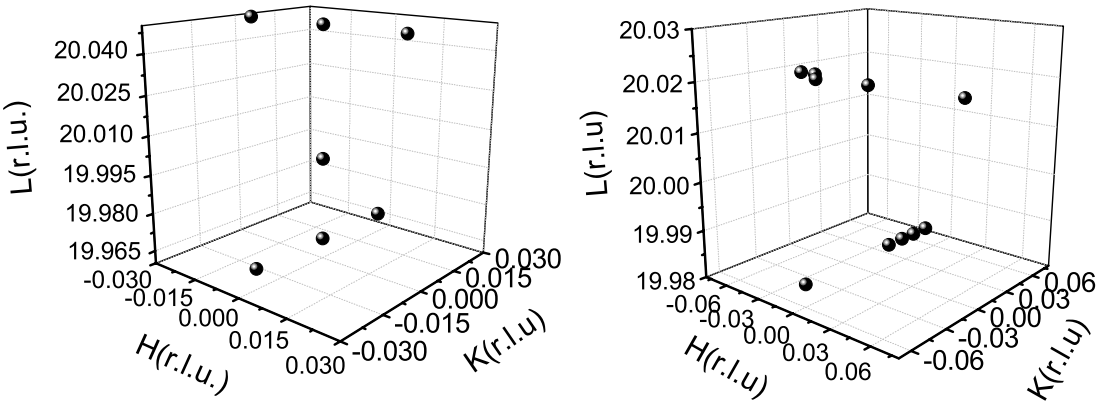

Figure 4.2.5 Positions of the splitting peaks of the (0 0 20) at 40K from calculation (top) and experiments (bottom).

The powder diffraction was carried out for a temperature interval from RT to 7K. The peaks split at LT and some superstructure reflections are identified by comparing the profiles at RT and 7K as shown in Figures 4.2.6, where an offset is applied for better comparison. As can be seen, the superstructure reflections arising from multiple domains are very weak.

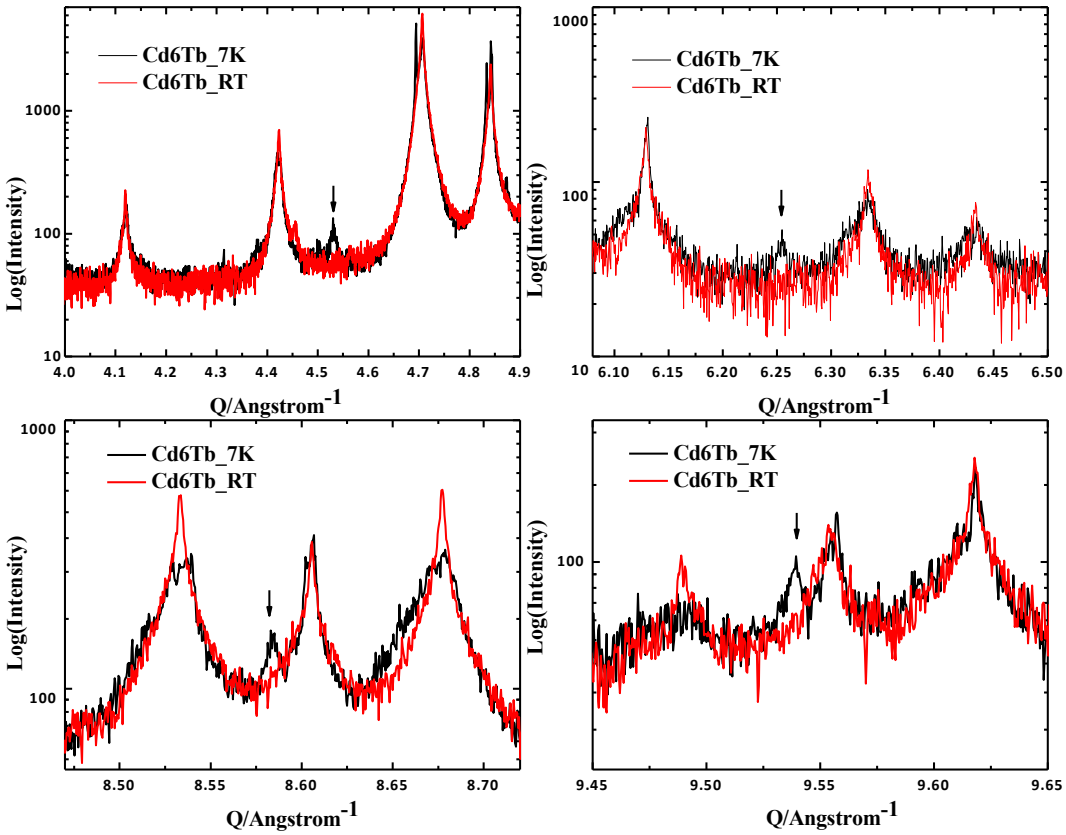

Figure 4.2.6 Peak profiles comparison between RT and 7K of Cd_6Tb, the peak splitting and superstructure peaks are distinct and indicated by arrows.

To figure out the variation of the Bragg peaks with respect to temperatures, we measured the Bragg angles of three peaks (4 4 2), (4 9 1) and (6 8 0) as a function of temperature as shown in Figures 4.2.7. An anomaly was observed to the Bragg angles at ~190K, which corresponds to the splitting of the peaks. This shows a good agreement with the results from single crystal experiments. Furthermore, both the main and splitting Bragg angles increase as temperatures decrease, and reach maximum at ~45K. Similarly as the single crystal results, the difference between the main and sub-peaks increases gradually as it is cooled down.

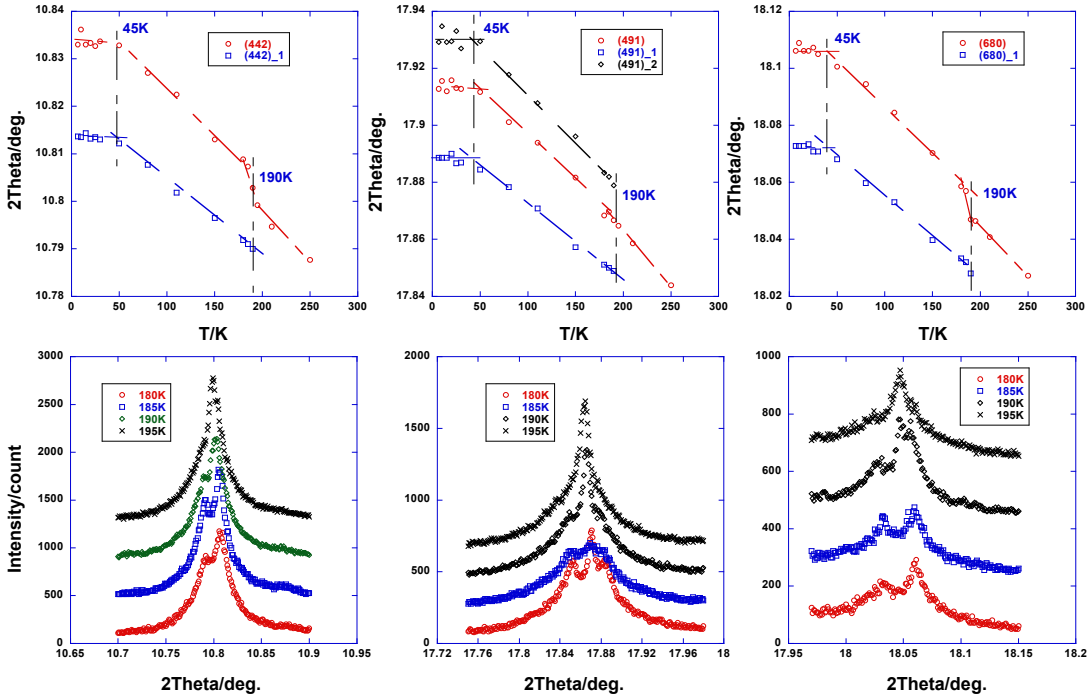

Figure 4.2.7 Rocking curves of the main peaks (4 4 2), (4 9 1) and (6 8 0) with respect to temperatures (bottom, from left to right). Variation of the main and splitting Bragg angles as a function of temperatures. The T_c is determined as ~190K, the lattice distortion increases linearly in the cooling process and the equilibrium is reached at ~45K.

4.2.4 Structural description of the Cd_6Tb 1/1 approximant above and below T_c

The structures of Cd_6Tb above and below T_c have been determined and refined successfully using single crystal high-resolution X-ray diffraction data from synchrotron measurements. Three datasets with different attenuation factors were collected for each temperature which extends the measuring range to very high Q value and dumps an extremely large number of reflections.

As we depicted above, six domains formed in the LT phase leading to the main peaks split in the reciprocal space. The best is integrating the intensities of each domain individually. However, owing to the short crystal-detector distance and the small step size, i.e. 1° for phi scan, the peak splitting is invisible on the diffraction images. On the other hand, six twining domains have been over the handling capability of the *CrysAlisPro*. An alternative method is first generating all possible indices using *Jana2006* in the form of cubic setting, and then performing intensity integration on the basis of this reflections list. It is worth noting that to collect all superstructure reflections of all domains, a 2×2×2 supercell is applied for indexing.

Considering the crystal absorption, varying experimental conditions, sensitivity difference among various detector regions, the resulting data need to be processed to minimize these negative effects. For primary data reduction, with one frame being fixed to 1, all other 359

frames have been rescaled. The scale factors of RT and 40K after absorption correction are displayed in Figures 4.2.8. The fluctuations are reasonable, i.e. less than ±7% for RT and less than ±3% for 40K.

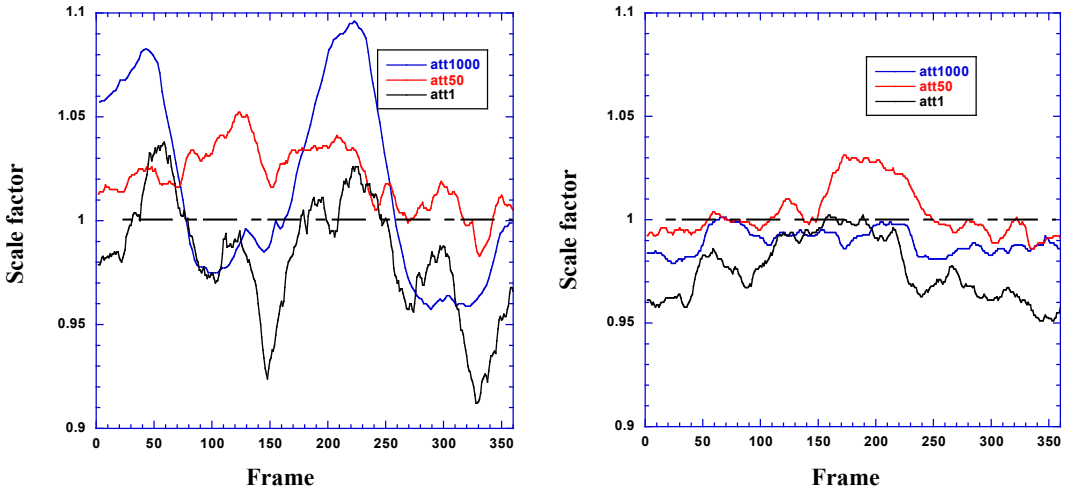

Figure 4.2.8 Scale factor versus frame number of each dataset at RT (left) and 40K (right).

The measured intensities are corrected for absorption correction using the defined shape illustrated in Figure 4.2.1 via *CrysAlisPro*. The sample model is optimized using the strongest 1000 reflections of each dataset at RT and 40K. The relevant absorption coefficients of each temperature are given in Table 4.1.

Table 4.1 Scale factors applied in *CrysAlisPro* and *Jana*2006 for each dataset at the two temperatures.

Temperature	**293K**			**40K**		
Attenuator	1	50	1000	1	50	1000
Absorption correction T min	0.356	0.397	0.354	0.342	0.354	0.354
Absorption correction T max	0.413	0.530	0.413	0.424	0.413	0.413

Two factors are adopted to rescale the three datasets collected at different attenuators. This procedure is realized on the basis of common reflections and carried out using *CrysAlisPro* and *Jana*2006 respectively. In *CrysAlisPro*, in case of the strongest reflections being saturated, the factor f_c is introduced to rescale all reflections. Keep in mind that the scale factors are independent between different datasets but closely related to the second factor derived from *Jana*2006. The *Jana* factor f_j is used to normalize intensities of different datasets. All f_c values are listed in Table 4.2. The f_j values of RT and 40K are fitted using common reflections between different datasets. We generate the common reflections between attenuator 1 and 50, 1000 and 50 respectively and the ratios are derived from the scatter plots in Figures 4.2.9. The combination of the two factors corresponds the ratio of the experimental attenuators as displayed in Table 4.2. The calculated attenuation factors of 40K are smaller than those of 293K which might be the effect of the weak superstructure reflections. Since f_c is related to the scale between strongest and weakest reflections in each dataset, the weak superstructure reflections likely biased the f_c as smaller than the cubic case at high

temperature. Finally, the grouping data collections were averaged based on the equivalent reflections by using the program *Jana*2006.

Table 4.2 Scale factors applied in *CrysAlisPro* and *Jana*2006 for each dataset at the two temperatures.

Temperature		**293K**			**40K**	
Attenuator	1	50	1000	1	50	1000
f_c	0.028	0.086	0.428	0.021	0.108	0.755
f_j	0.0568	1	4.2611	0.10951	1	3.202
Product	0.00159	0.086	1.824	0.0023	0.108	2.4175
Normalized Scale	1	54.09	1147.17	1	46.96	1051.24

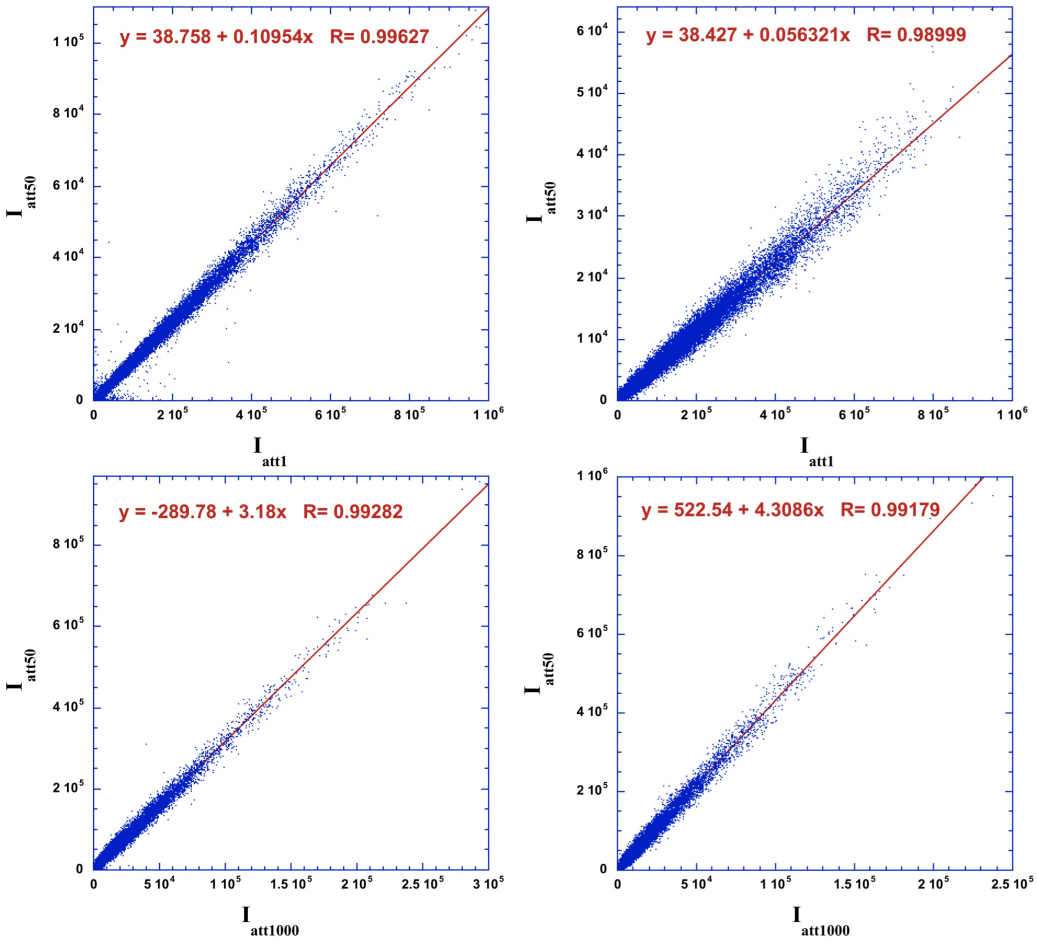

Figure 4.2.9 The three datasets of RT (right column) and 40K (left column) are grouped into one block by rescaling two of them (attenuation=1 and attenuation=1000). The scale factors are presented as the slopes of fitting lines.

The general crystallographic data is given in Table 4.3. Some R_{int} values are a bit of large which results from the high resolution of measurements, i.e. *d*-value equal to 0.8(2θ equal to 35.3°). The stated R_{int} values are given by *Jana*2006 which considers all three datasets and all twinned domains. Although more than 60000 independent reflections are taken into

refinement, the resulting *R* factor for LT phase is rather good, and it is also the first time solving the LT phase of the Cd_6R isostructural compounds using synchrotron data with such a good fitting. The refinement work is accomplished using the IUCr recommended, more strictly defined $wR_2(F^2)$ indicator.

The ratio between calculated and observed structure factors are plotted in Figures 4.2.10. The fitting is rather satisfying especially for strong reflections. It is less good for reflections with smaller structure factors because of the relatively larger errors.

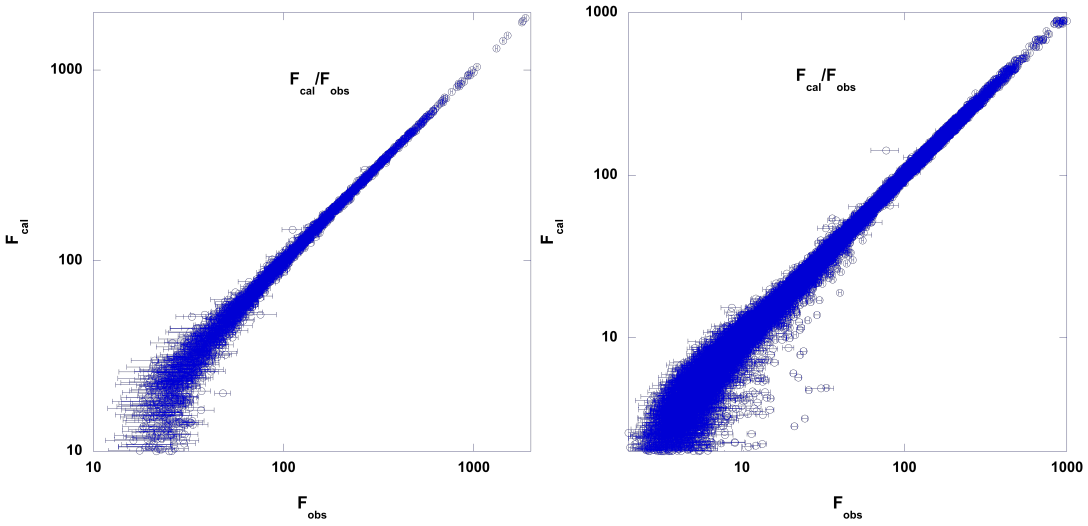

Figure 4.2.10 F_{obs}/F_{cal} in log scale at HT (left) and LT (right), good fitting is obtained for reflections with high structure factor.

Figures 4.2.11 (a) and (b) present the powder diffraction profiles of Cd_6Tb at RT and 40K over a 2θ range from 9° to 14°, respectively. They are derived from the resulting structures refined using the single crystal diffraction datasets. The strong peaks are very similar between the two phases, however, a large mount of weak superstructure reflections are clearly observable in the LT phase.

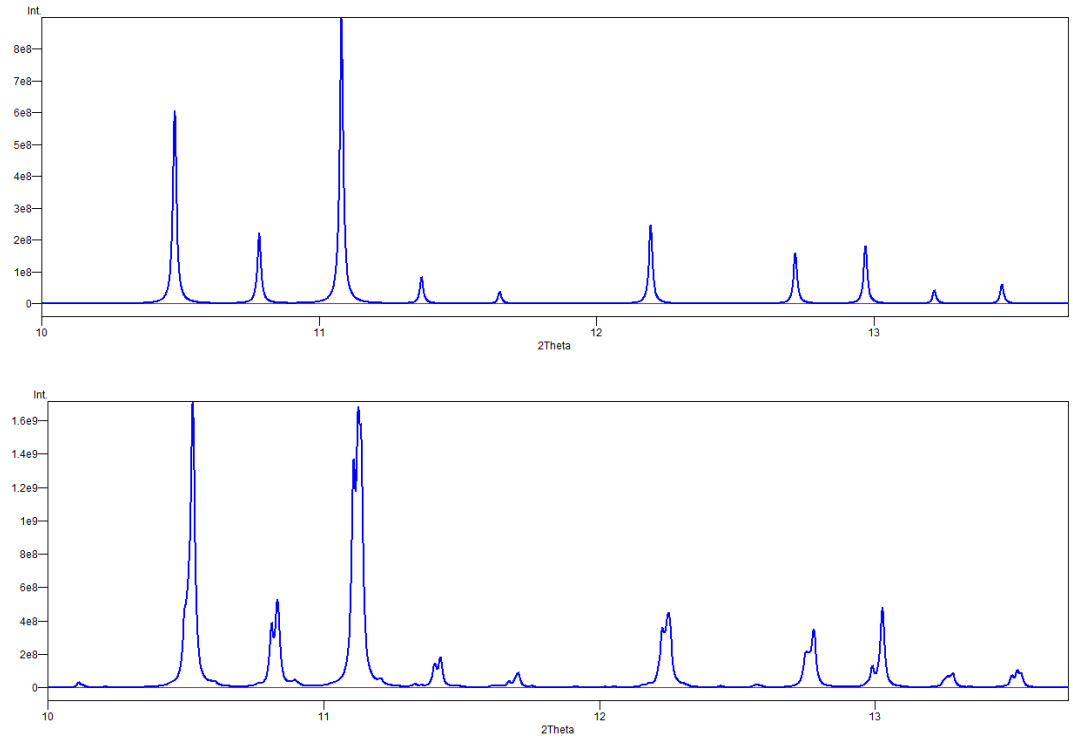

Figure 4.2.11 Simulated powder pattern based on the structures at RT (left) and 40K (right). The calculation is performed via the software Diamond. The weak superstructure reflections are clearly observable at LT.

It is proved that the phase transition for Cd_6Tb follows the same scheme as we demonstrated above, i.e. the ordering of the central tetrahedron triggers the distortion of the successive shells which leads to a doubling monoclinic lattice. The structures of Cd_6Tb above and below T_c are very close to those of Zn_6Sc determined by Ishimasa[8]. As presented in Figures 4.2.12 (a)-(d), the tetrahedron atoms residing in the dodecahedral cavities at RT shows large anisotropic displacement factors forming a well-defined cube octahedron which is consistent with the model proposed from the Cd_6Gd case[4]. It has been evidenced by previous quasielastic neutron scattering measurements and MD simulation that the innermost tetrahedra at HT are dynamically reorienting among 6 different orientations, giving an occupancy of 0.333. The structural information for the Cd_6Tb approximant containing atomic positions and equivalent displacement factors are given in Table 4.4, and the anisotropic thermal displacement parameters are given in Table 4.5. For the RT, similarly to the Zn_6Sc and Cd_6Yb cases, the dodecahedron atoms located at the 24g site shows extremely anisotropic displacement along one direction, i.e. U_{11}=0.0646(3), U_{22}=0.01297(12) and U_{33}=0.01249(12), which denotes the interaction between the dynamically oriented tetrahedra and the outer dodecahedra.

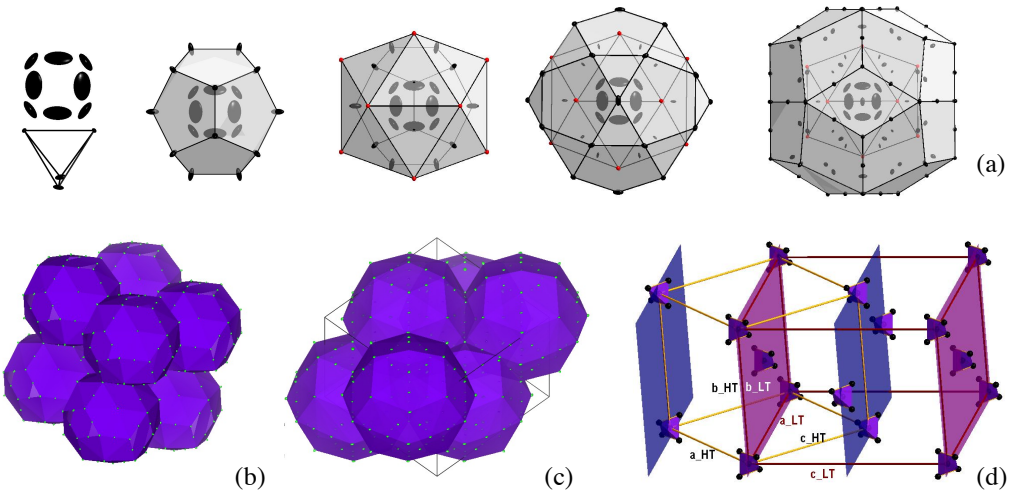

Figure 4.2.12 Schematic drawing of the ordering of the central tetrahedron. (a) The successive shells forming a Tsai-type cluster, the building blocks of both quasicrystals and their approximants, from left to right: the Cd_4 tetrahedron, then the dodecahedron containing 20 Cd atoms, followed by a Tb_{12} icosahedron and a Cd icosidodecahedron, finally an outermost rhombic triacontahedron (RTH). (b) and (c) The *bcc* and monoclinic packing of the RTH units in the 1/1 Cd_6Tb approximant above and below T_c. (d) Representation of the ordering scheme of the central tetrahedra along [$\bar{1}$01] direction with respect to the HT cubic setting. The two planes with different colors shows an antiparallel correlation between the clusters. The basis vectors for the LT phase can be obtained as follows: $a_{LT}=1/2(a_{HT}-c_{HT})$, $b_{LT}=b_{HT}$, and $c_{LT}=1/2(a_{HT}+c_{HT})$. We emphasize that for the real structures of the LT phase, due to the steric effect, the lattice angle β is deviated from 90°.

Table 4.3 Crystallographic data of Cd_6Tb 1/1 approximant at RT and 40K.

Formula	***Cd_6Tb***	***$Cd_{12}Tb_2$***
Temperature/K	293	40
Space Group	*Im*$\bar{3}$ (204)	*C*2/*c* (15)
Pearson code	*cI*184	*mC*336
a axis/Å	15.4926(3)	21.8077(4)
b axis/Å	15.4926(3)	15.4170(4)
c axis/Å	15.4926(3)	21.8193(4)
β/deg.	90	90.026(2)
Z	24	24
Cell volume/ $Å^3$	3718.54(15)	7335.9(3)
F(000)	8471	16944
Calculated density (g/cm^3)	8.9288	9.052
Absorption coefficient-mu/mm^{-1}	11.097	11.25
Range of theta/°	1.8-32.49	1.69-32.55
Index range	-31≤ *h* ≤31	-47≤ *h* ≤47
	-34≤ *k* ≤33	-33≤ *k* ≤33
	-34≤ *l* ≤34	-47≤ *l* ≤47
Independent reflections	3678	60245

Reflections>3σ	3025	52858
R_{int} (obs/all)	9.35/9.71	7.41/10.75
Number of parameters	52	386
R (all)	0.0394	0.0386
ωR_2 (all)	0.0726	0.0934
Goodness of fit (GOF)	1.44	1.84
Absorption correction	Numerical	Numerical
$\Delta\varrho$max, $\Delta\varrho$min/eÅ^{-3}	5.16, -7.19	11.53, -8.03
Mean change/s. u.	0.0008	0.0064

Table 4.4 (I) Structural information of Cd_6Tb 1/1 approximant at RT.

Atom	*Wyckoff site*	*Occ*	*x/a*	*y/b*	*z/c*	B_{iso-eq}*/Å^2
Tb1	24g	1	0.18973(1)	0.29961(1)	0	0.009(1)
Cd1	12e	1	0.50000	0.19063(3)	0	0.0148(1)
Cd2	24g	1	0.24129(7)	0.09235(4)	0	0.0300(1)
Cd3	48h	1	0.34060(1)	0.20040(1)	0.11814(2)	0.0158(0)
Cd4	16f	1	0.16098(2)	0.16098(2)	0.16098(2)	0.021()
Cd5	24g	1	0.50000	0.09570(2)	0.15384(2)	0.0125(1)
Cd6	12d	1	0.40580(3)	0	0	0.0288(2)
Cd7	24g	0.333	0.0746(2)	0.08420(18)	0	0.1054(14)

* B_{iso-eq} is defined as one third of the trace of orthorhombic B_{ij} tensors

Table 4.4 (II) Structural information of Cd_6Tb 1/1 approximant at 40K.

Atom	*Wyckoff site*	*Occ*	*x/a*	*b/y*	*c/z*	B_{iso-eq}*/Å^2
Tb1	8f	1	0.14764(1)	0.43867(1)	0.10142(1)	0.0017(0)
Tb2	8f	1	0.15133(1)	0.06147(1)	0.09996(1)	0.0018(0)
Tb3	8f	1	0.75346(1)	0.25193(1)	0.19436(1)	0.0018(0)
Tb4	8f	1	0.94416(1)	0.24937(1)	0.00520(1)	0.0017(0)
Tb5	8f	1	0.40519(1)	0.05226(1)	0.15483(1)	0.0017(0)
Tb6	8f	1	0.40437(1)	0.45467(1)	0.15442(1)	0.0017(0)
Cd1	8f	1	0.65921(2)	0.41434(3)	0.20904(2)	0.0028(1)
Cd2	8f	1	0.74697(1)	0.44072(2)	-0.00359(1)	0.0030(1)
Cd3	8f	1	0.54646(2)	0.51958(2)	0.20384(2)	0.0029(0)
Cd4	8f	1	0.95947(2)	0.59065(3)	0.41193(2)	0.0028(1)
Cd5	8f	1	0.87622(2)	0.75443(2)	0.22120(2)	0.0026(1)
Cd6	8f	1	0.97060(3)	0.75078(1)	0.12511(3)	0.0024(1)
Cd7	8f	1	0.54062(2)	0.40959(3)	0.09386(2)	0.0030(1)
Cd8	8f	1	0.90570(3)	0.75090(1)	0.34539(3)	0.0029(1)
Cd9	8f	1	0.84445(2)	0.74816(1)	0.09593(2)	0.0026(1)
Cd10	8f	1	0.88788(2)	0.55183(3)	0.52347(2)	0.0030(1)
Cd11	8f	1	0.61179(1)	0.83651(2)	0.35994(1)	0.0036(0)
Cd12	8f	1	0.79825(2)	0.59432(2)	0.04773(2)	0.0026(1)
Cd13	8f	1	0.73391(2)	0.54572(3)	0.35765(2)	0.0030(1)

Cd14	8f	1	0.65878(2)	0.59572(2)	0.25198(2)	0.0034(1)
Cd15	8f	1	0.77308(2)	0.44814(3)	0.13658(2)	0.0029(1)
Cd16	8f	1	0.77089(2)	0.62990(3)	0.18120(2)	0.0029(1)
Cd17	8f	1	0.82766(2)	0.34550(2)	-0.07705(2)	0.0025(1)
Cd18	8f	1	0.57030(2)	0.86713(3)	-0.01894(2)	0.0028(1)
Cd19	8f	1	1.00035(2)	0.40960(3)	0.40839(2)	0.0030(1)
Cd20	8f	1	0.83725(2)	0.41457(3)	0.25039(2)	0.0037(1)
Cd21	8f	1	0.49935(2)	0.58779(3)	0.08633(2)	0.0036(1)
Cd22	4e	1	0.5	0.35229(3)	0.25	0.0039(1)
Cd23	8f	1	0.67213(2)	0.34725(2)	0.07722(2)	0.0026(1)
Cd24	8f	1	0.84288(2)	0.59470(3)	0.29099(2)	0.0028(1)
Cd25	8f	1	0.79695(2)	0.90152(2)	0.04791(2)	0.0026(1)
Cd26	8f	1	0.39120(2)	0.54527(3)	0.01661(2)	0.0028(1)
Cd27	8f	1	0.57099(2)	0.74702(2)	0.08650(3)	0.0031(1)
Cd28	8f	1	0.42946(2)	0.36523(3)	0.02127(2)	0.0027(1)
Cd29	4e	1	0.5	0.16263(3)	0.25	0.0037(1)
Cd30	8f	1	0.66946(3)	0.74884(1)	0.17557(2)	0.0029(1)
Cd31	8f	1	0.72874(2)	0.36726(3)	0.32024(2)	0.0028(1)
Cd32	8f	1	0.69989(3)	0.75146(1)	0.04483(3)	0.0032(1)
Cd33	8f	1	0.70363(1)	0.77148(2)	0.45318(1)	0.0038(0)
Cd34	8f	1	0.63398(1)	0.65465(2)	0.38282(1)	0.003()
Cd35	8f	1	0.95466(2)	0.49952(2)	0.29640(2)	0.0031(0)
Cd701	8f	1	0.53972(2)	0.67810(2	0.30097(2)	0.0102(1)
Cd702	8f	1	0.55164(1)	0.81709(2	0.20960(2)	0.0090(1)

Table 4.5 (I) Anisotropic displacement parameters of Cd_6Tb 1/1 approximant at RT.

Atom	U_{11}	U_{22}	U_{33}	U_{12}	U_{13}	U_{23}
Tb1	0.00906(5)	0.01036(5)	0.00749(5)	0.00078(4)	0	0
Cd1	0.02226(18)	0.01128(13)	0.01101(13)	0	0	0
Cd2	0.0646(3)	0.01297(12)	0.01249(12)	0.01121(15)	0	0
Cd3	0.01288(8)	0.01375(7)	0.02077(9)	-0.00157(6)	-0.00353(6)	0.00483(6)
Cd4	0.02099(8)	0.02099(8)	0.02099(8)	0.01083(10)	0.01083(10)	0.01083(10)
Cd5	0.01412(10)	0.01111(9)	0.01231(10)	0	0	0.00241(7)
Cd6	0.01272(17)	0.0583(4)	0.01519(18)	0	0	0
Cd7	0.0698(17)	0.0451(13)	0.201(4)	-0.0401(12)	0	0

Table 4.5—II Anisotropic displacement parameters ($Å^2$) of the Cd_6Tb 1/1 approximant at 40K.

Atom	U_{11}	U_{22}	U_{33}	U_{12}	U_{13}	U_{23}
Tb1	0.00271(7)	0.00043(5)	0.00205(7)	0.00009(5)	0.00025(4)	-0.00027(5)
Tb2	0.00289(7)	0.00037(5)	0.00201(7)	-0.00018(5)	0.00023(4)	0.00013(5)
Tb3	0.00315(9)	0.00019(8)	0.00194(9)	-0.00001(3)	0.00028(7)	0.00005(3)
Tb4	0.00292(9)	0.00012(9)	0.00213(9)	0.00002(3)	0.00059(8)	0.00008(3)

Tb5	0.00257(7)	0.00049(5)	0.00195(7)	-0.00005(5)	0.00053(4)	0.00001(4)
Tb6	0.00262(7)	0.00055(5)	0.00192(7)	0.00003(5)	0.00065(4)	0.00016(4)
Cd1	0.00431(11)	0.00118(10)	0.00280(11)	0.00078(8)	0.00108(8)	0.00028(7)
Cd2	0.00467(11)	0.0007(1)	0.00377(11)	0.00041(5)	0.00120(8)	0.00028(6)
Cd3	0.00328(9)	0.00258(8)	0.00271(9)	0.00009(8)	0.00049(6)	0.00030(8)
Cd4	0.00353(11)	0.00078(10)	0.00414(11)	-0.00011(8)	0.00058(9)	-0.00078(8)
Cd5	0.00412(13)	0.00148(11)	0.00204(13)	0.00000(6)	0.0005(1)	-0.00008(6)
Cd6	0.00357(15)	0.00070(14)	0.00291(14)	-0.00003(5)	0.00069(11)	0.00011(5)
Cd7	0.00371(11)	0.00086(10)	0.00457(11)	-0.00024(8)	0.00104(9)	-0.00067(8)
Cd8	0.00344(16)	0.00261(11)	0.00258(16)	-0.00010(5)	0.00033(8)	-0.00011(5)
Cd9	0.00399(15)	0.00067(10)	0.00325(15)	0.00001(5)	-0.00016(8)	0.00000(5)
Cd10	0.00421(10)	0.00122(10)	0.00349(11)	-0.00051(7)	-0.00060(8)	0.00029(7)
Cd11	0.00459(9)	0.00135(7)	0.00471(9)	0.00046(6)	0.00092(7)	0.00047(6)
Cd12	0.00363(12)	0.00107(8)	0.00306(13)	0.00005(8)	0.00014(7)	-0.00033(8)
Cd13	0.00317(10)	0.00080(9)	0.00492(11)	0.00000(7)	-0.00002(8)	0.00051(7)
Cd14	0.00542(11)	0.00217(10)	0.00269(10)	-0.00201(8)	0.00019(8)	0.00024(8)
Cd15	0.00356(10)	0.00093(9)	0.00426(11)	-0.00043(7)	0.00002(8)	0.00074(7)
Cd16	0.00334(12)	0.00234(11)	0.00307(12)	0.00026(8)	0.00053(9)	-0.00100(8)
Cd17	0.00407(13)	0.00107(8)	0.00249(12)	0.00049(9)	0.00073(7)	-0.00036(9)
Cd18	0.00372(12)	0.00189(11)	0.00276(11)	-0.00043(8)	0.00033(9)	0.00004(8)
Cd19	0.00305(11)	0.00116(10)	0.00488(11)	-0.00017(8)	0.00053(9)	0.00126(8)
Cd20	0.00595(11)	0.00261(10)	0.00247(10)	-0.00215(8)	0.00031(9)	0.00028(8)
Cd21	0.00343(11)	0.00227(11)	0.00515(12)	-0.00065(8)	-0.00003(9)	0.00217(8)
Cd22	0.00525(14)	0.00109(11)	0.00536(15)	0	-0.00071(1)	0
Cd23	0.00363(13)	0.00105(8)	0.00301(13)	-0.00006(9)	0.00077(7)	0.00068(9)
Cd24	0.00402(11)	0.00143(10)	0.00285(11)	0.00041(8)	0.00105(8)	0.00009(7)
Cd25	0.00367(13)	0.00103(8)	0.00308(13)	0.00004(8)	0.00022(7)	0.00057(8)
Cd26	0.00428(10)	0.00131(9)	0.00291(10)	-0.00050(7)	-0.00050(8)	0.00004(7)
Cd27	0.00410(13)	0.00088(12)	0.00423(13)	0.00005(6)	-0.00141(1)	-0.00019(6)
Cd28	0.00411(12)	0.00160(11)	0.00249(11)	0.00074(8)	0.00043(9)	0.00007(8)
Cd29	0.00500(14)	0.00134(11)	0.00464(15)	0	-0.00037(1)	0
Cd30	0.00435(14)	0.00116(13)	0.00303(13)	0.00051(5)	-0.00054(1)	-0.00020(5)
Cd31	0.00364(12)	0.00182(11)	0.00287(11)	-0.00001(8)	0.00060(9)	-0.00077(8)
Cd32	0.00485(15)	0.00158(10)	0.00325(14)	-0.00008(5)	0.00159(10)	-0.00004(5)
Cd33	0.00398(9)	0.00363(9)	0.00372(9)	-0.00062(7)	-0.00002(6)	-0.00068(7)
Cd34	0.00366(9)	0.00122(7)	0.00396(9)	-0.00023(6)	0.00030(6)	-0.00033(6)
Cd35	0.00324(9)	0.00303(8)	0.00294(9)	-0.00046(8)	0.00043(6)	0.00030(8)
Cd701	0.01331(13)	0.0049(1)	0.01225(13)	-0.00093(9)	-0.00833(1)	0.00323(8)
Cd702	0.01067(12)	0.00356(9)	0.01275(13)	-0.00070(8)	0.00785(10)	0.00071(8)

As the temperature approaches to T_c, the reorientation of the central tetrahedron is slowed down gradually and frozen in the end. To avoid an unrealistic Cd-Cd distance, the tetrahedron is tilted from the 2-fold axis by around 7.32° at 40K which is just half of that in the Zn_6Sc approximant. As a result, two atoms are located under the pentagonal faces of the dodecahedron, and the other two shift from the 5-fold axis. As explained by Yamada *et al*[11],

this distortion of dodecahedron induced by the tetrahedron ordering has propagated through clusters leading to the formation of long-range order, and the Cd_4 tetrahedra are correlated antiparallel as displayed in Figure 4.2.12 (d).

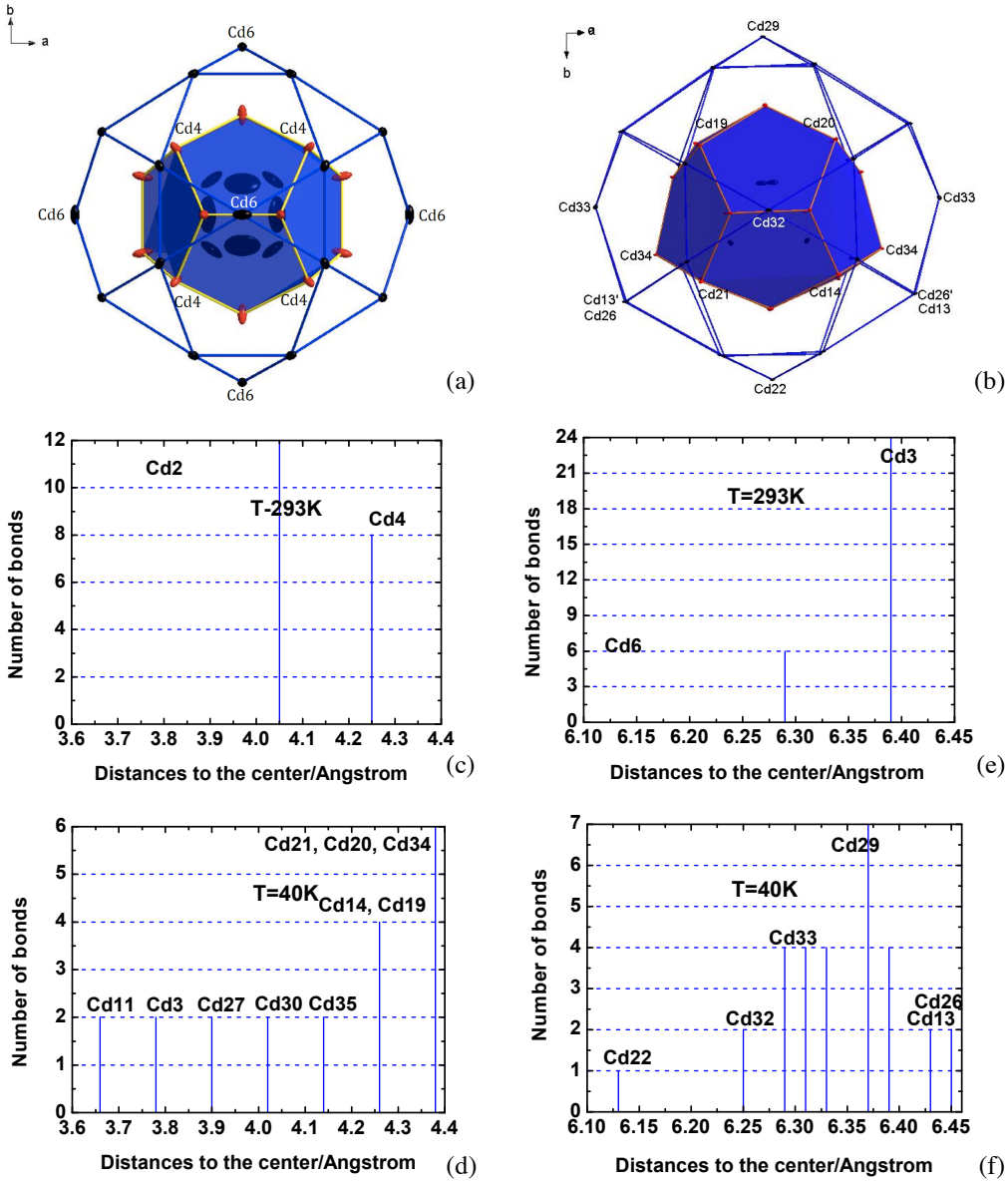

Figure 4.2.13 (a) and (b) Tsai-type clusters viewing along [001] direction of the HT phase at RT and 40K respectively, labeling atoms indicate different sites; (c)-(d) Distribution of the distances to the cluster center of the dodecahedron at RT and 40K respectively; (e)-(f) Distribution of the distances to the cluster center of the icosidodecahedron at RT and 40K respectively.

Figures 4.2.13 (a)-(f) displays the distortion occurring to the dodecahedron and icosidodecahedron shells. Figures 4.2.13 (c) and (d) illustrate the distances from the cluster center to the dodecahedron vertices at RT and 40K respectively. It shows that the dodecahedron is imperfect at RT due to the eight Cd4 atoms possessing longer distances.

Figure 4.2.13 (a) illustrates that these eight Cd4 atoms distribute along the cubic 3-fold axis. This phenomenon is likely induced by a stronger interactions with the central tetrahedron atoms. As the temperature is lowered down to 40K, the difference between the shortest and longest 'distances to the cluster center', i.e. the distances between center and vertex atoms, goes up to ~0.7Å, and the distances become more distributed as illustrated in Figure 4.2.13 (d) suggesting that the dodecahedron is strongly distorted at 40K. Furthermore, being forced by the tetrahedron atoms, two of the dodecahedron atoms, i.e. Cd34 as labeled in Figure 4.2.13 (b), are strongly pushed outward, which leads to the largest distance to the cluster center 4.37Å as shown in Figure 4.2.13 (d). The second and third longest distances, i.e. Cd21, Cd20 and Cd14, Cd19 correspond to the eight atoms located at the 3-fold axis of the cubic cell as labeled in Figure 4.2.13 (b).

The six icosidodecahedron atoms possessing shorter distances to the cluster center at RT, i.e. Cd6, occupy the sites along the three 2-fold axis parallel to the cell edges as displayed in Figure 4.2.13 (a). The triangles in the icosidodecahedron shell are inequivalent, meaning that the areas of the two triangles intersecting over the Cd6 atom are smaller than the one just above the Cd4 atoms. This difference originates from the pushing-off of the Cd4 dodecahedron atoms which possess longer distances to the cluster center. The distances to the cluster center of the icosidodecahedron turn out distributed at 40K as well which demonstrates the distortion resulting from interaction with the dodecahedron shell. Moreover, because of being pushed by the dodecahedron atom Cd34, the distances to the cluster center of Cd13 and Cd26 increase greatly as displayed in Figures 4.2.13 (b) and (f) comparing with those at RT. Similarly, the Cd29 is pushed outward by the atom Cd35, and the Cd22 moves inward because the atom Cd3 is drawn inward.

The moment bearing element Tb, existing in form of Tb^{3+}, in the Cd_6Tb approximant constitutes the icosahedron shell of the Tsai cluster. As previously described, the Tb ions occupy the 24*g* Wykoff sites and form icosahedra in the center and corner of the cubic cell. Above T_c, the icosahedron distorts slightly, i.e. the 6 out of 30 Tb-Tb edges (~5.8789Å) parallel to the cell edges are larger than others (~5.7519Å). It is found that the first nearest Tb-Tb distances (~5.7246Å) exist between neighboring icosahedra and the second nearest Tb-Tb bonds exist inside the icosahedron shells. As the temperature is cooled down to T_c, the distortion of the icosahedron arises gradually. The two distorted neighboring icosahedra found at 40K are presented in Figure 4.2.14 (a) which are connected by a yellow octahedron. The adjacent Tb-Tb distances at RT and 40K are displayed in Figures 4.2.14 (b) and (c).

For each Tb atom, there are 9 neighboring bonds containing 5 inside the icosahedra and 4 between neighboring clusters. It is distinguished in Figure 4.2.14 (a) that the two neighboring icosahedra are connected by a distorted regular octahedron which share a triangle face with the two icosahedra. Figure 4.2.14 (c) demonstrates all Tb-Tb bonds in the LT phase at 40K where the red solid bars indicate the intercluster distances and the black dashed bars refer to the intracluster distances. From top to bottom, it displays the bonds surrounding Tb1 to Tb6 respectively. Again, the 6 longest distances around 5.8Å represent the 6 bonds parallel to the cube edges. Interestingly, owning to the increasing distortion, some of the intercluster distances, which are always smallest above T_c, increase and some intracluster distances become smaller, suggesting a competition between the two types of interactions. It is

speculated that this exchange of interacting distances plays crucial role in the formation of long-rang magnetic order.

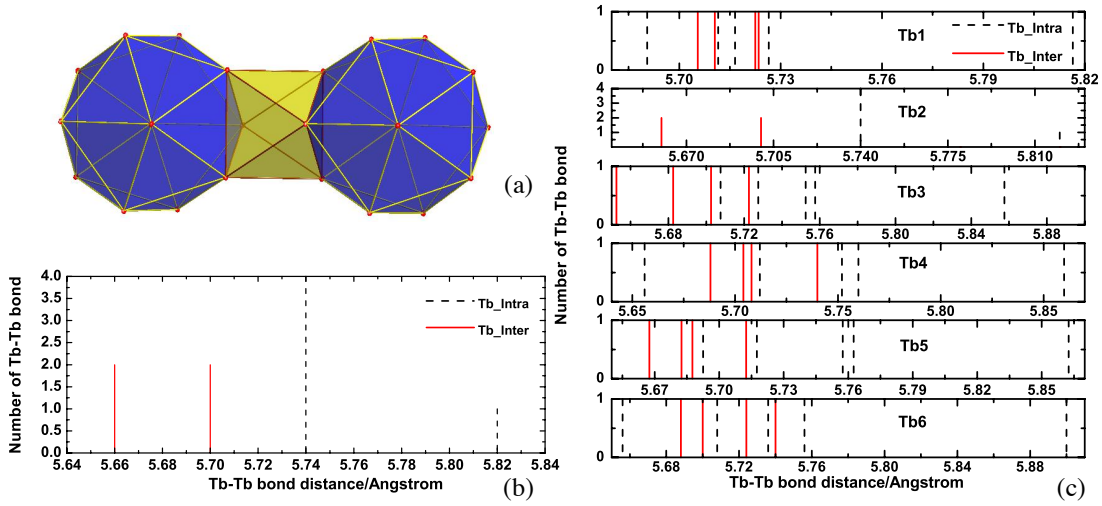

Figure 4.2.14 (a) Atomic arrangement of the Tb^{3+} in the LT phase of Cd_6Tb. The icosahedral clusters are displayed in blue and the two adjacent icosahedral clusters are connected by an yellow octahedron. The intracluster and intercluster bonds are compatible. (b) The distances of Tb-Tb bonds at RT. The red solid lines refers to the intercluster interacting distances, and the black dashed lines denote the distances of intracluster bonds. The largest distances, i.e. ~5.82Å, correspond to the bonds parallel to the cubic edges. (c) The distances of Tb-Tb bonds at 40K surrounding each Tb atom. Owning to the distortion, some intercluster bonds increase and some intracluster bonds reduce.

4.2.5 Structural temperature dependence study of the 1/1 Cd6Tb phase

To have a further insight of the transitioning scheme, we collected the single crystal X-ray diffraction data in a temperature interval from RT to 40K. The structure solutions and refinements of all temperatures were performed via *Jana2006* as described above. To collect all reflections in the 6 domains, the data reduction of 40K was carried out under the outlier rejection condition of $P\bar{1}$ with only centric symmetry. From 192K to 150K the measurements were carried out with phi scanning from 0° to 180° meaning that there were no equivalent reflections available for optimizing the sample model. Thus the absorption correction was applied using the refined model at RT as displayed in Figure 4.2.1. Moreover, for temperatures just below T_c, the superstructure reflections are too weak to achieve a satisfying wR_2 value. The R factors with the related crystallographic data at each temperature are given in Table 4.6.

The temperature dependent evolution of the anisotropic displacement factors and structural information above T_c are given in Tables 4.7 and 4.8 respectively. It shows that as temperature decreases to 196K, the Wyckoff sites of the central tetrahedron have changed from 24*g* to 48*h* which corresponds to the occurrence of pretransition.

The related structural information for the seven LT phases is attached in the Appendix. Considering the large dynamical measuring range and the number of reflections, the resulting wR_2 values are reasonably acceptable.

Table 4.6 (I) Temperature dependent crystallographic data of Cd_6Tb 1/1 approximant above T_c

Temperature/K	200	196
Space Group	$Im\bar{3}$ (204)	$Im\bar{3}$ (204)
Pearson code	*cI*184	*cI*184
Z	24	24
a axis/Å	15.4647(3)	15.4559(5)
Cell volume/ Å3	3698.68(15)	3692.18(19)
F(000)	8472	8472
Calculated density (g/cm3)	8.9767	8.9925
Absorption coefficient-mu/mm-1	11.156	11.176
Range of theta/°	1.8-32.55	1.8-32.57
Index range	-31≤ *h* ≤31	-16≤ *h* ≤31
	-34≤ *k* ≤33	-34≤ *k* ≤31
	-34≤ *l* ≤34	-23≤ *l* ≤34
Independent reflections	3476	3624
Reflections>3σ	3444	3061
R_{int} (obs/all)	9.44/9.45	14.48/14.77
Number of parameters	46	61
R (all)	0.0405	0.051
ωR_2 (all)	0.1075	0.0992
Absorption correction	Numerical	Numerical
Δρmax, Δρmin	6.26, -10.83	9.98, -11.11
Mean change/s. u.	0.0006	0.0006

Table 4.6 (II) Temperature dependent crystallographic data of Cd_6Tb 1/1 approximant below T_c

T/K	*192*	*188*	*186*	*184*	*180*	*150*	*100*
Space Group	*C*2/*c* (15)	*C*2/*c* (15)	*C*2/*c* (15)	*C*2/*c* (15)	*C*2/*c* (15)	*C*2/*c* (15)	*C*2/*c* (15)
Pearson code	*mC*336	*mC*336	*mC*336	*mC*336	*mC*336	*mC*336	*mC*336
a axis/Å	21.858(4)	21.847(4)	21.824(3)	21.856(3)	21.856(3)	21.853(3)	21.825(2)
b axis/Å	15.460(4)	15.450(3)	15.452(3)	15.456(3)	15.457(3)	15.44(3)	15.431(2)
c axis/Å	21.859(4)	21.848(4)	21.835(3)	21.857(3)	21.855(3)	21.864(3)	21.838(2)
β/deg.	90.012(2)	90.017(2)	89.932(2)	90.007(2)	90.004(2)	89.997(2)	90.020(1)
Z	24	24	24	24	24	24	24
Cell volume/ $Å^3$	7386.7(3)	7374.3(2)	7363(2)	7383.4(2)	7383.0(2)	7378(2)	7354.63(1)
F(000)	16944	16944	16944	16944	16944	16944	16944
Calculated density (g/cm^3)	8.9897	9.0048	9.0184	8.9937	8.9942	8.9998	9.0289

Absorption coefficient-mu/mm^{-1}	11.172	11.191	11.208	11.177	11.178	11.185	10.4
Range of theta/°	3.37-32.54	3.31-32.56	3.31-32.6	3.31-32.46	3.31-32.53	10.99-19.5	1.68-32.56
Index range	-44≤*h*≤47 -33≤*k*≤32 -40≤*l*≤43	-46≤*h*≤47 -33≤*k*≤33 -45≤*l*≤47	-44≤*h*≤47 -33≤*k*≤33 -46≤*l*≤46	-46≤*h*≤46 -32≤*k*≤34 -46≤*l*≤47	-46≤*h*≤47 -33≤*k*≤34 -45≤*l*≤46	-29≤*h*≤29 -20≤*k*≤20 -29≤*l*≤29	-47≤*h*≤47 -34≤*k*≤33 -47≤*l*≤47
Independent reflections	41006	63026	75712	77123	77659	15591	129033
Reflections> 3σ	40983	63026	75690	77123	77636	11738	100797
R_{int}	0.0979	0.08	0.0545	0.0535	0.0533	0.0385	0.1627
Number of parameters	487	437	407	407	406	386	386
R (all)	0.0617	0.0564	0.0544	0.0472	0.0453	0.0964	0.0541
ωR_2 (all)	0.1587	0.1403	0.1370	0.1148	0.1045	0.1358	0.1191
Goodness of fit	3.75	3.07	3.05	2.57	2.35	2.87	1.80
Absorption correction				Numerical			
Δρmax, Δρmin/e/Å^{-3}	11.44/-6.51	20.62/-10.66	20.01/-14.7	11.69/-9.41	11.03/-8.89	2.55/-2.70	10.46/-8.18
Mean change/s. u.	0.0102	0.0091	0.0031	0.0065	0.0067	0.0120	0.0016

Table 4.7 Structural information of Cd_6Tb 1/1 approximant above T_c

Symbol	*T/K*	*Wyckoff site*	*x/a*	*y/b*	*z/c*	*Occ*	B_{iso-eq}*/Å^2
Tb1	196	24g	0.18975(3)	0.29965(3)	0	1	0.0058(0)
	200		0.18974(3)	0.29964(3)	0	1	0.0059(0)
Cd1	196	16f	0.16087(2)	0.16087(2)	0.16087(2)	1	0.014()
	200		0.5	0.19056(3)	0	1	0.0099(1)
Cd2	196	12e	0.5	0.19051(3)	0	1	0.0096(1)
	200		0.75859(8)	0.09237(5)	0	1	0.0266(2)
Cd3	196	24g	0.24133(10)	0.09234(6)	0	1	0.0264(1)
	200		0.65941(1)	0.20038(1)	-0.11815(2)	1	0.0108(0)
Cd4	196	48h	0.34063(1)	0.20040(1)	0.11813(2)	1	0.0107(0)
	200		0.83912(2)	0.16088(2)	-0.16088(2)	1	0.0142(0)
Cd5	196	24g	0.5	0.09568(2)	0.15386(2)	1	0.0081(0)
	200		0.5	0.09569(2)	-0.15381(2)	1	0.0081(1)
Cd6	196	12d	0.40571(4)	0	0	1	0.0236(2)
	200		0.59428(4)	0	0	1	0.0236(2)
Cd7	196	48h	0.0757(3)	0.0837(2)	0.0152(4)	0.1667	0.058(2)
	200	24g	0.9241(2)	0.08395(19)	0	0.3333	0.0809(13)

Table 4.8 Anisotropic displacement parameters (Å^2) of Cd_6Tb 1/1 approximant above T_c

Symbol	T/K	U_{11}	U_{22}	U_{33}	U_{12}	U_{13}	U_{23}
Tb1	196	0.00578(6)	0.00699(6)	0.00472(6)	0.00058(3)	0	0
	200	0.00575(6)	0.00696(6)	0.00486(6)	0.00054(4)	0	0
Cd1	196	0.01404(8)	0.01404(8)	0.01404(8)	0.00750(8)	0.00750(8)	0.00750(8)
	200	0.01521(17)	0.00721(13)	0.00713(13)	0	0	0
Cd2	196	0.01489(16)	0.00700(12)	0.00705(12)	0	0	0
	200	0.0622(4)	0.00929(14)	0.00833(13)	-0.01090(17)	0	0
Cd3	196	0.0623(4)	0.00904(12)	0.00794(11)	0.01081(16)	0	0
	200	0.00848(8)	0.00942(8)	0.01462(9)	0.00090(6)	-0.00214(6)	-0.00393(6)
Cd4	196	0.00837(8)	0.00938(8)	0.01436(9)	-0.00085(5)	-0.00203(5)	0.00387(6)
	200	0.01424(8)	0.01424(8)	0.01424(8)	-0.00758(9)	0.00758(9)	-0.00758(9)
Cd5	196	0.00914(9)	0.00709(9)	0.00797(9)	0	0	0.00164(6)
	200	0.00922(10)	0.00723(9)	0.0079(1)	0	0	-0.00169(7)
Cd6	196	0.00939(16)	0.0520(5)	0.00958(16)	0	0	0
	200	0.00939(17)	0.0519(4)	0.00968(18)	0	0	0
Cd7	196	0.066(2)	0.0397(13)	0.067(5)	-0.0422(15)	-0.007(2)	-0.0035(17)
	200	0.0621(17)	0.0383(12)	0.142(3)	0.0394(12)	0	0

Table 4.9 lists the volume fractions of the six domains at each temperature. For temperatures from 180K to 192K, the weight of each twining domain differs from the results of 40K and 100K because only half region of the sample was probed. In overall, the most dominated domains are domains 2 and 5, and the least are domains 3 and 6. Moreover, from 100K to 40K, the volume fraction of each domain almost keeps constant. In the selected half region, the volume fraction varies strongly depending on the temperatures. For instance, from 192K to 188K, the weight of domain 4 is high up to 28.22%, however, as temperature decreases to 186K, domain 2 increases quickly becoming the dominant one. This implies that domain 4 is the easiest to form in the preliminary stage of the transition, and domain 2 is more sensitive to lower temperatures. In addition, the evolution of the volume fractions stops changing at ~184K indicating the accomplishment of the transition around this temperature which is consistent with the powder diffraction results.

Table 4.9 Temperature dependent volume fractions of different twinning domains.

Temperature	**40K**	**100K**	**180K**	**184K**	**186K**	**188K**	**192K**
Domain1	0.1702	0.1711	0.1846	0.1859	0.1944	0.1944	0.1956
Domain2	0.0913	0.0876	0.2066	0.2058	0.1938	0.1406	0.1487
Domain3	0.2648	0.2600	0.1119	0.1349	0.1173	0.1113	0.1407
Domain4	0.2098	0.2190	0.1614	0.1619	0.1650	0.2822	0.2373
Domain5	0.0864	0.0875	0.1979	0.1976	0.1866	0.1494	0.1498
Domain6	0.1775	0.1749	0.1375	0.1140	0.1430	0.1221	0.1279

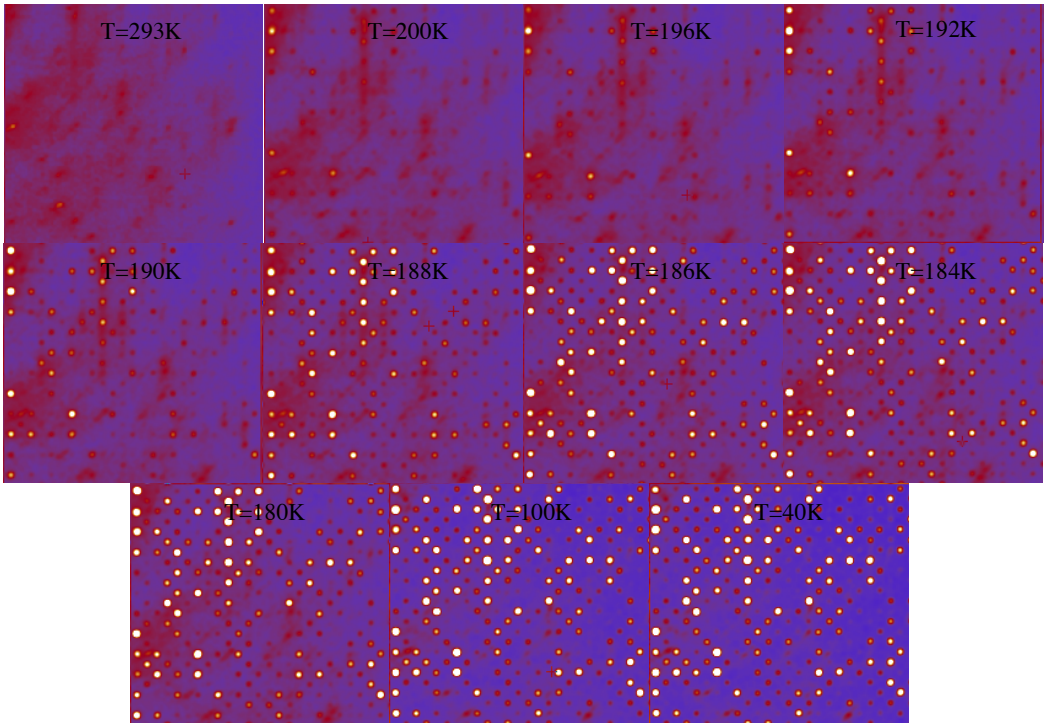

Figure 4.2.15 Reconstruction of the *hk*0.5 Bragg planes with respect to temperatures, both the number and intensity of the superstructure reflections increase as temperatures get lower.

The *hk*0.5 Bragg planes have been reconstructed for each temperature as illustrated in Figures 4.2.15. A small number of superstructure reflections have been observable at 200K which is consistent with the case of Zn_6Sc[11]. By fitting the correlation length and T-T'_c in log scale, one can derive the transition temperature for a second-order transition. Furthermore, as the temperature decreases, the superstructure reflections become stronger, in the meanwhile the thermal diffuse scattering gets weakening. A quantitative analysis is performed and shown in Figure 4.2.16 where the summing intensities of all superstructure reflections on the *hk*0.5 planes are plotted as a function of temperatures. It is manifested that a drastic increase occurs at ~193K which agrees well with the measured T_c previously. Additionally, the abrupt increase accomplished at ~184K showing a good agreement with the powder diffraction results. According to Figures 4.2.3 and Figures 4.2.7 from single crystal and powder diffraction measurements respectively, this temperature interval reveals the occurrence of the peak splitting, i.e. the distortion of the unit cell. As a consequence, the lattice distortion happens at ~193K and grows up rapidly until ~184K, leading to the formation of the six twinning domains.

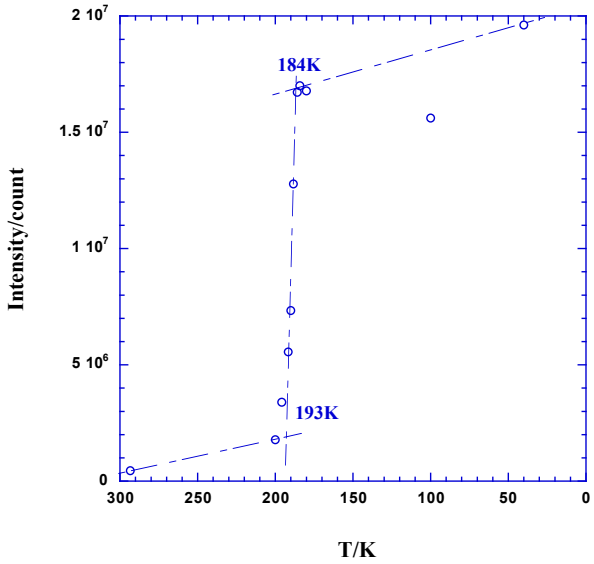

Figure 4.2.16 The summed intensity of the Bragg planes *hk*0.5 as a function of the temperature, abrupt increase happens between 193K and 184K, corresponding to the observation of the phase transition.

Up to now, much work has interpreted that the motions of tetrahedron atoms are responsible to the phase transition. The evolution of the tetrahedron with respect to temperatures is presented in details. Figures 4.2.17 illustrate the charge density distribution of the central tetrahedron derived from the single crystal diffraction measurements at different temperatures. The tetrahedron model above T_c is almost constant manifesting a well-defined cube octahedron shape. However, as we stated above, the tetrahedron sites transit from 24*g* to 48*h* at 196K which indicates the occurrence of the pretransition. Interestingly, in addition to the expected ordering tetrahedron, some other tetrahedron sites are partially occupied as well in particular just below T_c. This is speculated correlating to the completeness of the transition. As in the temperature interval from 192K to 184K, the phase transition was in progress but incomplete, therefore some additional occupancy was preserved. In other words, these transitional charge density shapes are superimpositions of the HT and LT phases. This is affirmed by the fully occupied tetrahedron arising at 184K where the phase transition has been completed.

The three most increased Cd-Cd bonds on the successive Cd-component polyhedra have been measured as indicated in Figure 4.2.18 (a). The d_1 corresponds to the innermost tetrahedron bond parallel to the cubic edges, d_2 demonstrates the distance between the two dodecahedron atoms adjacent to the related tetrahedron atoms, and d_3 denotes the relevant bond distance on the icosidodecahedron cluster. The temperature dependence of the three bonds is displayed in Figure 4.2.18 (b). An abrupt increase is observed for all three distances within the specific temperature interval. Moreover, the three bonds grow up simultaneously confirming that the lattice distortion indeed originates from the ordering of the tetrahedron. The variation before and after the transition displays the effect of thermal motions. In addition, comparing with the tetrahedron and dodecahedron shells, the distortion of the icosidodecahedron is much weaker, therefore the d_3 displays irregular behavior before and after the transition.

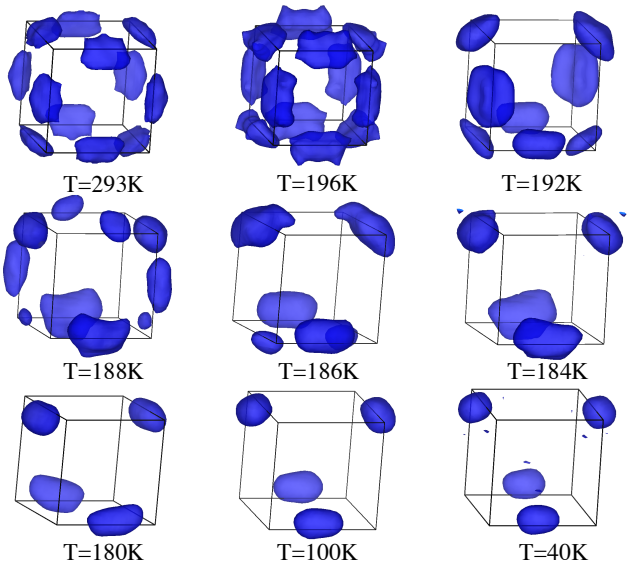

Figure 4.2.17 Charge density in the location of Cd_4 tetrahedron with respect to temperatures, The isosurfaces level for fully measured data, i.e. phi scan from 0° to 360°, is 28-e/Å^3.

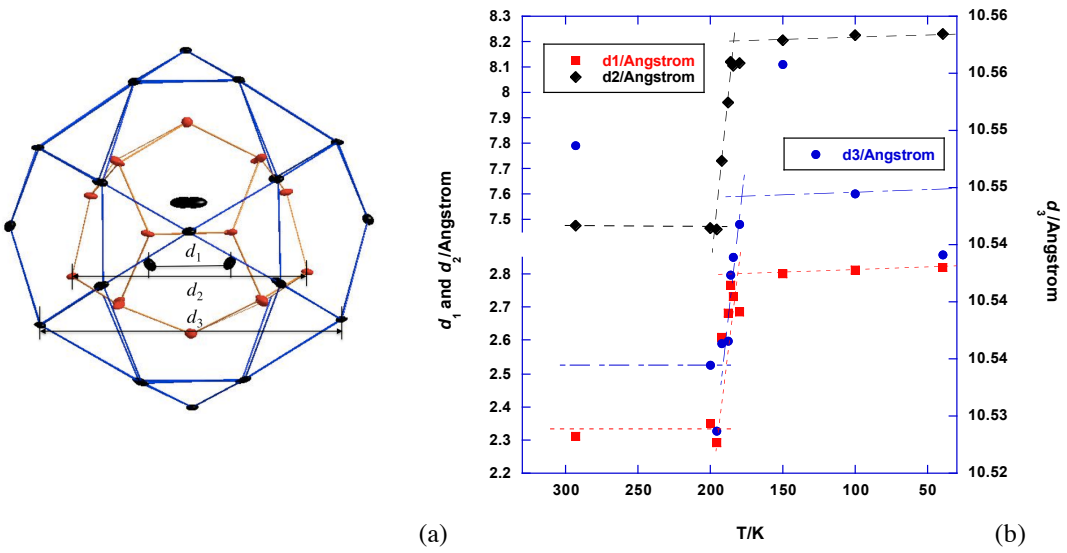

Figure 4.2.18 (a) The three defined distances on the three successive Cd-component shells are indicated. (b) The temperature dependence of the three distances varies simultaneously, demonstrating essentially the interacting between shells.

According to the thermal expansion, as a response to the decreasing temperatures, the Cd-Cd bonds should decrease in the cooling process. However, as indicated in Figure 4.2.18 (b) d_1 increases as temperature decreases. Indeed, not only d_1, but also the distances to the cluster center of the 4 tetrahedron atoms increase as illustrated in Figure 4.2.19 (b) . This phenomenon is again speculated corresponding to the constantly reorienting of the tetrahedron at HT. At high temperature, only an average distance can be evaluated because of large dynamical disorder. When the monoclinic distortion takes place, the degeneracy is

lifted and the distances are determined accurately. Similarly to the distances to the cluster center, the previously discussed tilting angles increase drastically as the temperature approaches to T_c indicating that this tilting angle is also a result of the increasing tetrahedron bonds. Figure 4.2.19 (a) displays the equivalent isotropic displacement parameters with respect to temperatures on the two unique tetrahedron atoms and the averaged values. An abrupt decrease is observed around T_c indicating the constant reorientation of the tetrahedron was suppressed. Moreover, the two atoms slow down together in an excellent agreement demonstrating that the tetrahedron behaves most likely as a single molecule.

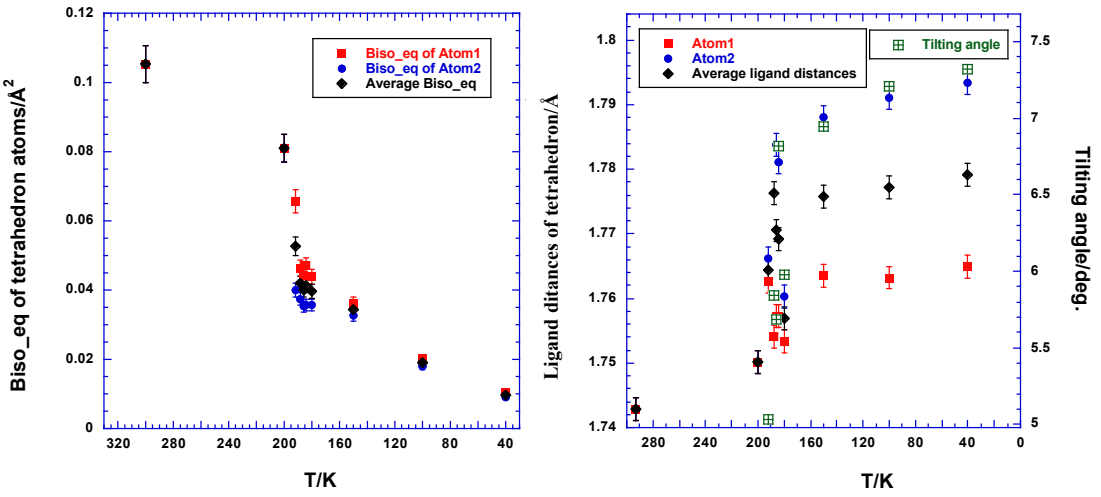

Figure 4.2.19 (a) The equivalent isotropic displacement parameters of the two unique tetrahedron atoms and the averaged values as a function of temperatures. (b) The temperature dependence of the tilting angle (green crossed square), the distances to the cluster center of the two unique tetrahedron atoms (red solid square for atom1 and blue solid circle for atom2) and the averaged values (black rhombus).

4.3 Conclusion

We have carried out a systematic in situ measurement on a single grain from RT down to 40K on the Crystal beam line located at the Soleil synchrotron. The structural phase transition is observed at about 190K evidenced by the splitting of the main Bragg peaks. Both single crystal and powder diffraction patterns demonstrate the abruptly increasing distortion from 190K to 184K. An anomaly is observed at ~45K, below which both the lattice parameter and the scattering angles do not change any more. This may be responsible to the irregular behavior of the electronic resistivity below ~40K.

Using different attenuation, we have collected integrated intensity in a large dynamical range, leading to more than 60000 unique reflections in the C2/c monoclinic low temperature phase. The final *w*R2 values for RT and 40K are equal to 0.0726 and 0.0905 respectively. The ordering of the innermost tetrahedron leads to the distortion of the successive shells. As initially proposed by Tamura *et al*[14] and Kim *et al*[15], the distances of the intracluster ionic Tb^{3+} bonds are compatible with the intercluster bonds. For the monoclinic phase, owing to the lattice distortion, the intracluster and intercluster interactions become more competitive

which is supposed playing a crucial role in promoting the formation of long-range magnetic order.

A temperature dependent study is carried out to the Cd_6Tb structures. A strong distortion of the successive shells is observed along the three-fold axis. Further investigation manifests that the distortion is originally induced by the ordering tetrahedron. The simultaneous behavior of the equivalent isotropic displacement parameters of the two unique tetrahedron atoms suggests that the tetrahedron behave as a single molecule. The increasing tetrahedron Cd-Cd bonds in the cooling procedure shows an exception to the contraction principle which could be interpreted by the dynamically reorienting of the tetrahedron above T_c.

As a counterpart of the quasicrystal, the results of 1/1 approximants are significant to study the stability of quasicrystals in particular the Cd_6Tb phase in which the long-range magnetic order was observed below 24K. The discovery of a series of binary magnetic icosahedral quasicrystals also paved the way for further investigation on this unique magnetic property.

Chapter 5. The stability of Cd_6M (M=Yb, Pr) 1/1 approximants

The phase transition taking place on Cd_6Tb has been evidenced for a series of Cd_6RE and Zn_6Sc isostructural compounds by transmission electron microscopy as well as specific heat and electrical resistivity measurements[12][6]. Among those, the Cd_6Yb and Cd_6Pr were reinvestigated in this thesis using X-ray diffraction. The diffuse scattering and s.r.o are measured with respect to temperatures.

5.1 Phase transition of Cd_6Yb

The Cd_6Yb phase was identified for the first time in 1964 by Johnson *et al* [16]. After that, many efforts have been made to solve its structure[17][4][18]. Especially the discovery of the first stable binary quasicrystal $Cd_{5.7}Yb$[2] and the observation of the order-disorder phase transition at a low temperature occurring to Cd_6Yb[19][20] have attracted the scientific community's attention and interests back to this fascinating system.

Sample preparation[3]

The Cd_6Yb sample was grown using flux methods. Pure elements of Cd(6N) and Yb(3N) with an atomic ratio of 9:1 were put into an alumina crucible and sealed into a quartz tube under an argon atmosphere. Then the sealed tube was set into a muffle furnace and heated to 973K for 24 hours. After being melt adequately, the liquid alloy was cooled down slowly with a cooling rate -5K/h to form an alloy and the remaining melt was decanted by centrifuge. An annealing process was performed to the obtained ingots for 24 hours at 673K to form a homogeneous phase. The sample was prepared by Tamura's group[19].

Experimental details

X-ray diffuse scattering was performed on single grain of Cd_6Yb on the beamline D2AM which is located at the European Synchrotron Radiation Facility (ESRF). A series of expected fundamental and superstructure reflections were measured over a temperature range from 20K to RT, in reflection geometry using an X-ray beam with energy of 18.2keV (λ=0.681Å). The measurements were carried out using a Kappa diffractometer collecting data with a scintillation point detector. A cryostat system was applied for controlling the temperature of the sample which is placed in an evacuated Be hemisphere.

To obtain an atomic view of the Cd_6Yb phase, single crystal XRD measurement was carried out using synchrotron beamline of CRYSTAL at SOLEIL. Sample was measured at three temperatures: 200K, 140K and 40K. To avoid extinguishing the weak superstructure reflections or saturating the strong main reflections, we collected four datasets with attenuation factors equal to 10000, 1000, 50 and 1 for the LT phase at 40K. For the same reason, two datasets with attenuation factors equal to 1000 and 50 were collected at 200K. The measurement was executed by rotating phi 180° with step size of 1.0°. The distance between sample and detector was set to 80mm. Furthermore, since the step size is too large to

[3] The sample is prepared by Tamura's group in Science University of Tokyo, Tokyo, Japan.

observe the split of Bragg peaks, additional Omega scan with step size being 0.025° and distance between sample and detector equaling 340mm was carried out at 200K, 140K and 40K respectively. The energy of beamline is 25.55keV, i.e. λ=0.4853Å. The data reduction is implemented using program *CrysAlisPro* (Version 1.171.35.6, Agilent Technologies, Yarnton, England, 2011). The images of Cd_6Yb sample were recorded by camera controlling by the crystallographic program *CrysAlis Pro* as illustrated in Figures 5.1.1 (a). By employing *CrysAlis Pro*, a 3-D model of the sample was rebuilt as shown in Figure 5.1.1 (b) and the shape was refined using the 1000 strongest reflections of the 200K dataset with attenuation factor equal to 50. Numerical absorption correction was carried out based on this model in *CrysAlis Pro*.

Powder XRD measurement was performed using the same beamline CRYSTAL at SOLEIL with energy equal to 25.55keV. The sample is the same as the single crystal discussed above but was grinded into smaller pieces. A set of systematic scans was carried out in a temperature interval from 250K to 10K. The measurement is done using 2-circle diffractometer with multi-analyzer. To reduce the preferred orientation effects, the sample was mounted on a rotating motor and two individual scans are performed for each temperature. The velocity is set as 0.02°/s and 0.05s for each step giving a step size equal to 0.001°.

Further diffuse scattering measurement was executed on Cd_6Yb in a temperature interval from RT to 20K using synchrotron beamline I16 of the Diamond Light Source. 6-circle diffractometer (in vertical 4-circle mode) is adopted with detector systems Medipix and Pilatus. The energy of beamline is set to 8keV (λ=0.9918Å). A series of reflections are tested as a function of temperature. 2-D and 3-D diffraction patterns are reconstructed in reciprocal space at both HT and LT via Matlab scripts. The picture of the single grain probed in experiment was recorded by camera as presented in Figure 5.1.2.

Results and discussion

5.1.1 Split of fundamental reflections

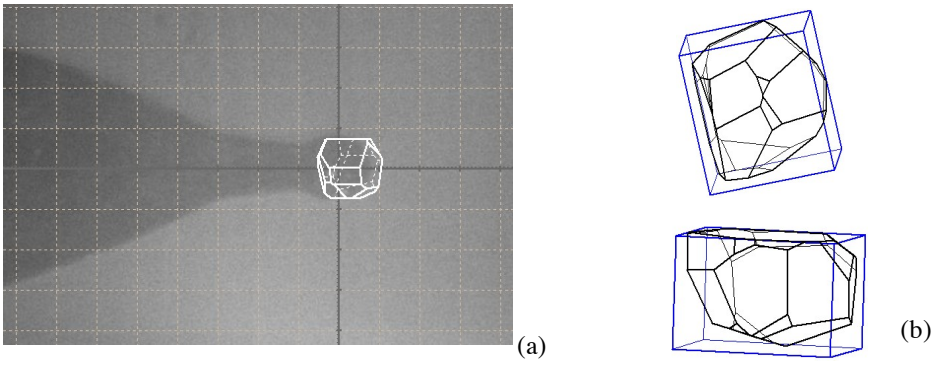

Figure 5.1.1 (a) Single grain of Cd_6Yb is glued on a sample holder; (b) A 3-D model is rebuilt using *CrysAlis Pro* program. The sample size is measured as ~160x160x90μm^3.

Figure 5.1.2 Camera view of Cd_6Yb single crystal glued on the sample holder.

The phase transition from space group $Im\bar{3}$ to $C2/c$ observed in most of Cd_6R approximants[12] leads to not only a doubled lattice by $\sqrt{2}a\times a\times\sqrt{2}a$ along $[\bar{1}01]$ direction, but also six domains with different orientations in the LT phase. In reciprocal space, the distorted monoclinic multiple domains results in a split of the fundamental reflections. The amount of split depends on both the composition and temperature. Therefore it is a significant sign for judging the formation of the monoclinic phase.

Single crystal XRD

The diffraction profiles of reflection (18 18 0) at 200K and 40K are compared and presented in Figures 5.1.3. The reflection alters from isotropic to anisotropic instead of splitting. Since the phase transition has been evidenced previously[20], we suppose that either the LT phase maintains a cubic lattice which is the conclusion of Xia *et al*[18] or the distortion is too small to be detected. In fact, the latter conclusion has been evidenced as it will be presented in the following paragraph.

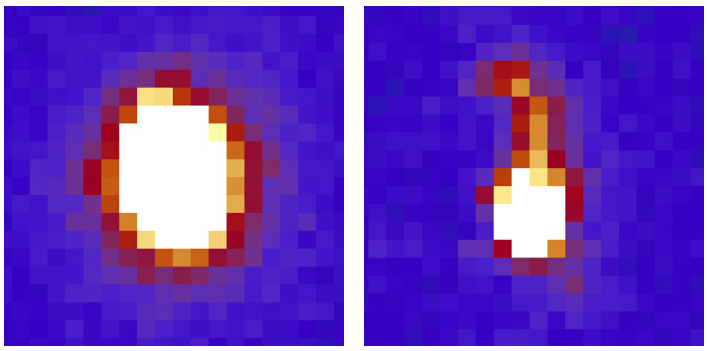

(a) (b)

Figure 5.1.3 Diffraction profiles of (18 18 0) at 200K (left) and 40K (right).

Powder XRD

Profiles of peaks (2 1 5) and (3 0 5) with respect to temperature are displayed in Figure 5.1.4. As denoted by arrows A, B, C and A', B', C', peaks split clearly from 100K suggesting that T_c is between 100K and 110K. This verifies the distortion of the cubic lattice and the multiple domains in the LT phase. It is also seen that the amount of split is very small which explains the absence of split from the diffuse scattering and single crystal XRD measurements. In addition, superstructure peaks are observed in LT phase as indicated by arrows D and E. Furthermore, the relevant peak of D and E is absent at 10K, and as shown by arrow F, the weak peak next to (3 0 5) is absent as well at 10K. This result implies either additional extinction appearing in the LT phase at 10K or experimental error.

The Q evolution of main peaks of (2 1 5) and (3 0 5) as a function of temperatures is generated and plotted in Figure 5.1.5. An obvious anomaly occurs at around 110K indicating the phase transition. This result agrees well with that of Tamura[19].

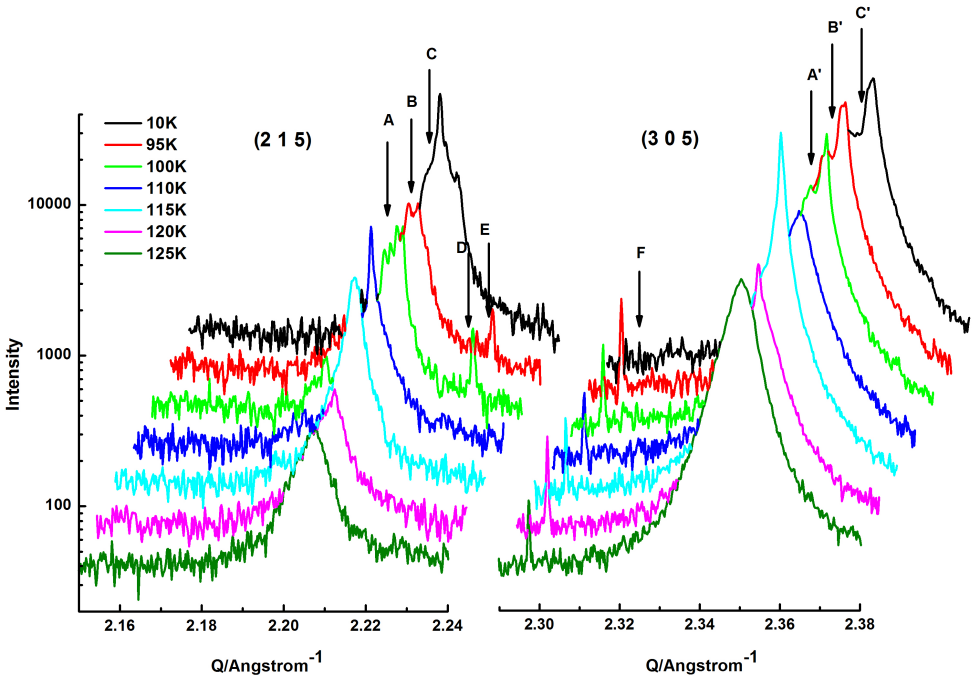

Figure 5.1.4 Evolution of rocking curves of (2 1 5) (left) and (3 0 5) (right) with respect to temperatures. Peak splitting becomes clearly visible from 100K as indicated by arrows A, B, C and A', B', and C'. Peaks denoted by D and E suggest the appearance of superstructure at LT.

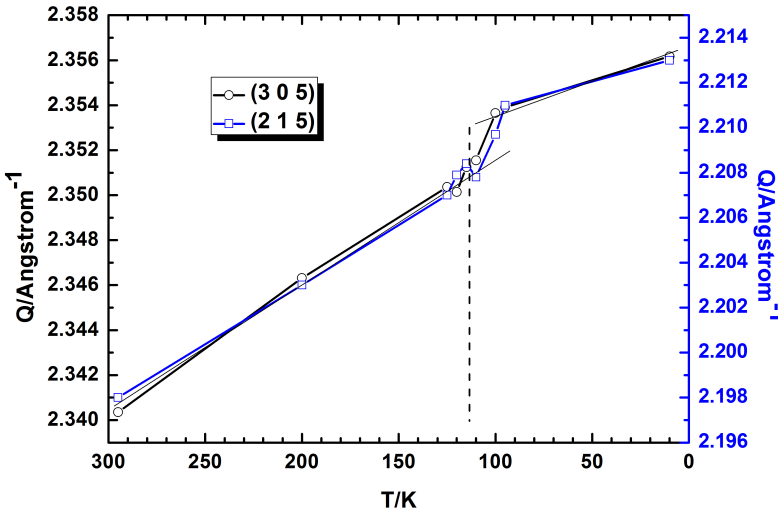

Figure 5.1.5 Variation of Q of peaks (3 0 5) (open circle) and (2 1 5) (open square) are illustrated as a function of T.

Diamond x-ray diffuse scattering

The temperature dependence of a selected fundamental reflection (10 0 10) was probed using synchrotron x-ray source as demonstrated in Figure 5.1.6. It is clearly seen that the peak splits into two subpeaks at 100K which suggests the formation of a distorted lattice. It is noteworthy that the step size here is 0.01° which is half of that in the experiment at D2AM where the split of (15 15 0) is missed. This fact reconfirms that the lattice distortion of Cd_6Yb is quite small. Moreover, the peaks diminish and broaden rapidly after phase transition, which is due to the effect of the LT domains size.

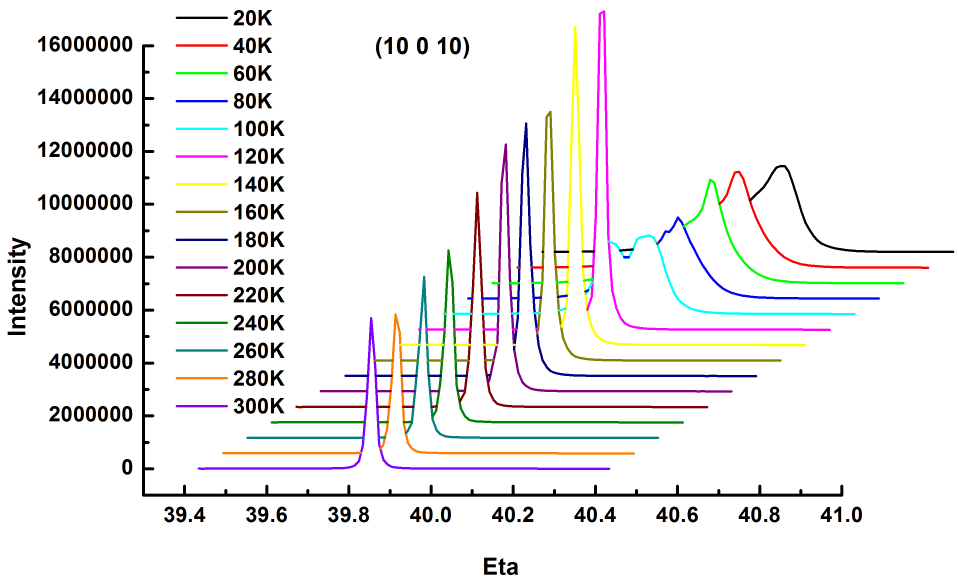

Figure 5.1.6 X-ray diffraction profiles of peak (10 0 10) over a temperature range from 20K to 300K; (b) Evolution of Eta of (10 0 10) as a function of temperature. An anomaly at 120K indicates the occurrence of phase transition.

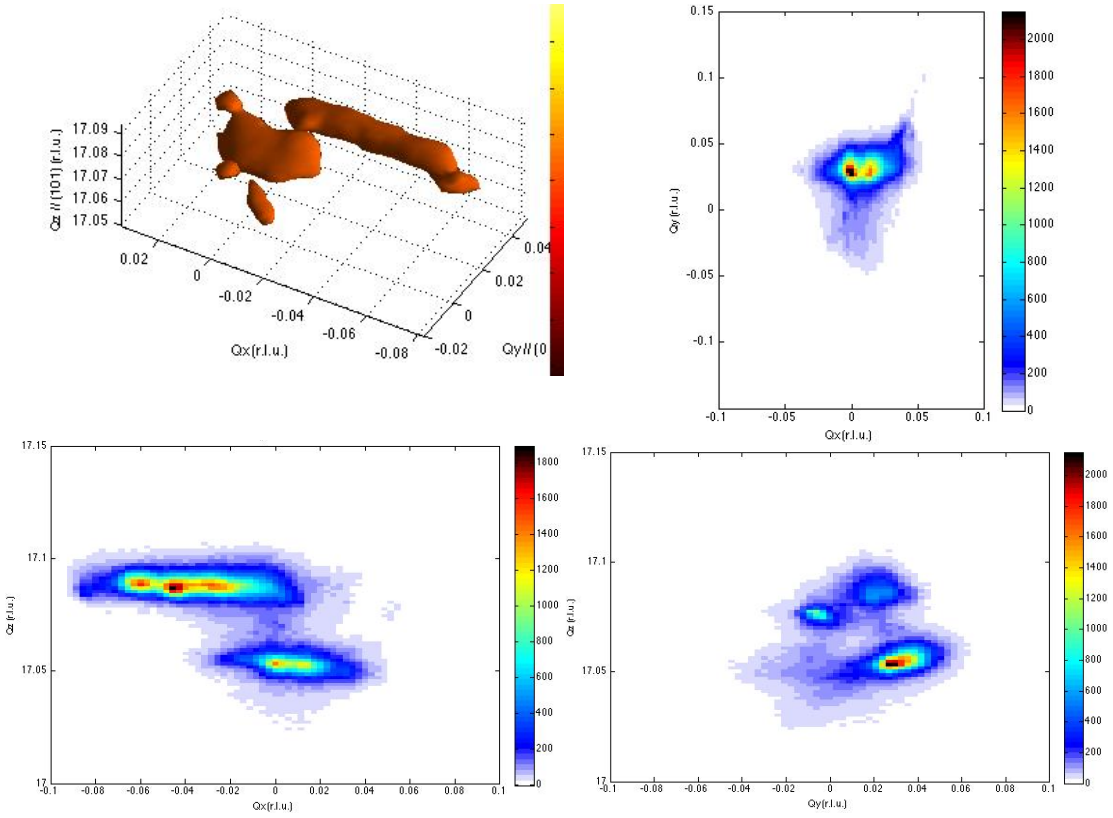

Figure 5.1.7 Reconstruction of reflection (10 0 10) in reciprocal space. (a) 3D image shows clearly the splitting of reflection; (b) 2D projection to Qx // [$\bar{1}$01] and Qy // [010] plane; (c) 2D projection to Qx // [$\bar{1}$01] and Qz // [101] plane; (e) 2D projection to Qy // [010] and Qz // [101] plane.

The 2D and 3D images of reflection (10 0 10) at 100K is reconstructed in reciprocal space as shown in Figures 5.1.7. It shows clearly the splitting reflections resulting from lattice distortion. The splitting reflections are incompatible with the calculated results derived from the model depicted in Section 4.1. One possible reason is that the cell parameters we used are not accurate enough. Therefore further analysis on the powder XRD data is desirable to obtain accurate cell parameters which are important not only to calculate the splitting reflections but also to the structure determination of the LT phase.

5.1.2 Superstructure reflections

The superstructure reflections result from the [110] doubling of the unit cell. The appearing rule of superstructure reflections is closely related to the ordering scheme of the central tetrahedron. Therefore it is an effective way to investigate the tetrahedron ordering mechanism[12]. In addition, they are also used to derive the correlation length of s.r.o.

D2AM x-ray diffuse scattering measurements

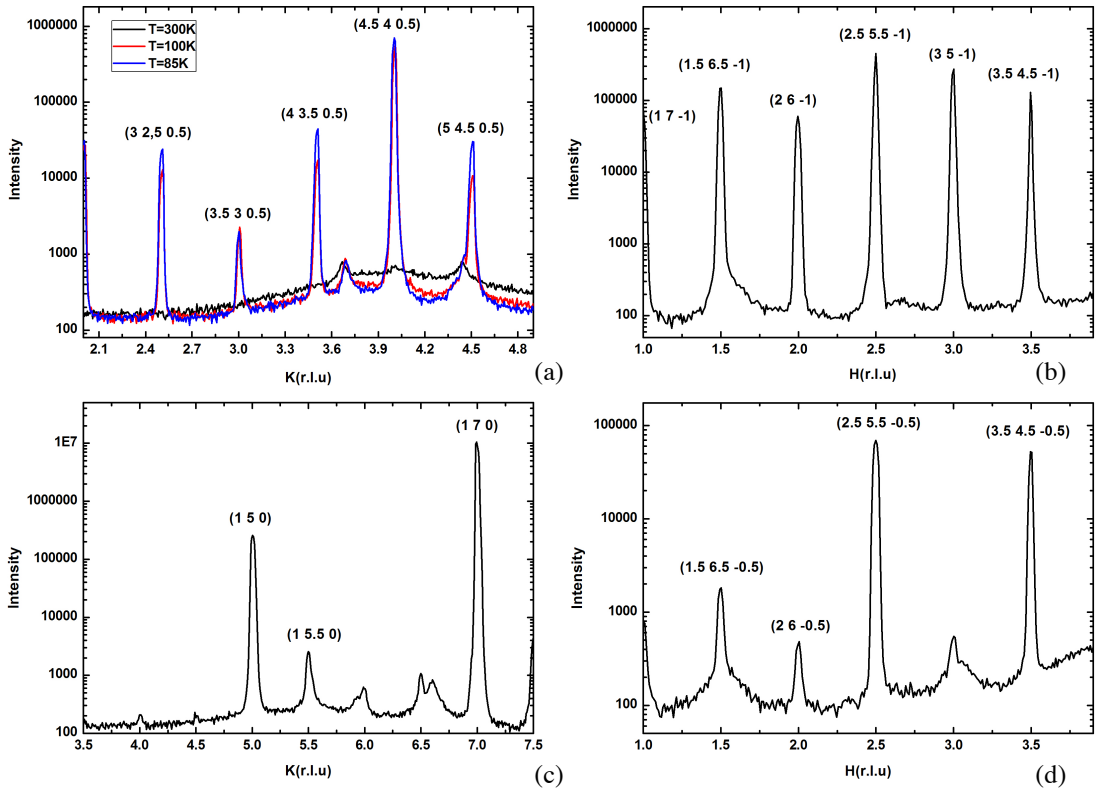

Figure 5.1.8 Line scans in different directions: (a) Line scans along [110] at different temperatures; (b) Line scan along $[1\bar{1}0]$ at 15K; (c) [1k0] scan with k from 3.5 to 7.5 at 15K; (d) Line scan along $[1\bar{1}0]$ at 15K with *l* being half integer.

Four line scans were implemented to search for possible superstructure reflections at LT. As shown in Figure 5.1.8 (a), line scan along [110] direction was carried out at different temperatures. No superstructure reflections visible at 300K, however, as temperature decreases, a bunch of superstructure reflections appear at 100K and 85K. Three other line scans were performed along $[1\bar{1}0]$, as shown in (b) and (d), and [1k0] with k varying from 3.5 to 7.5 at 15K as displayed in (c). The appearance of those reflections with half integers displays obvious contradiction with the model of Cd_6Yb at LT claimed by Xia *et al*[18]. It is noticed that there are many reflections with half-integer k, but we can not simply conclude that lattice is doubled along b axis, because as explained above, six domains with different orientation are transformed in the LT phase.

On the other hand, by means of group-subgroup analysis of Yamada[11], the relationship between indices of HT and LT is given precisely (see section 4.1). We analyzed the superstructure reflection emerging in above figures, and found that the appearance of (1.5 6.5 $\overline{0.5}$) and (3 5 $\bar{1}$) are forbidden in space group *C*2/*c*, suggesting that the phase transition of Cd_6Yb follows a different rout from others. This result updates the conclusion of Tamura in his early work[19].

Systematic scans on selected superstructure reflections were carried out as shown in Figure 5.1.9. The measurements were executed with a heating and a cooling process for each reflection. Note that all reflections are indexed with respect to the HT phase.

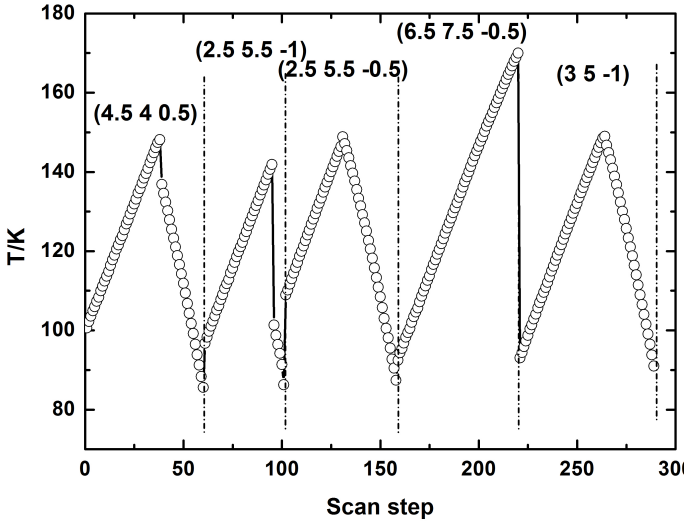

Figure 5.1.9 Systematic scans to five superstructure reflections. Sample was firstly heated and then cooled from ~80K to ~170K except (6.5 7.5 -0.5) which is measured only in the heating process.

The variation of integrated intensity of each reflection is plotted as a function of temperatures as illustrated in Figures 5.1.10. All intensities are normalized on the basis of different foils and scanning time. An obvious anomaly shows up at around 113K in both the heating and cooling process, demonstrating occurrence of the phase transition. Moreover, the transition of 2nd to 5th reflections indicates that the phase transition is reversible. An interesting phenomenon is that the variation of intensity in the heating process behaves differently from the cooling process which might correspond to different transitional process.

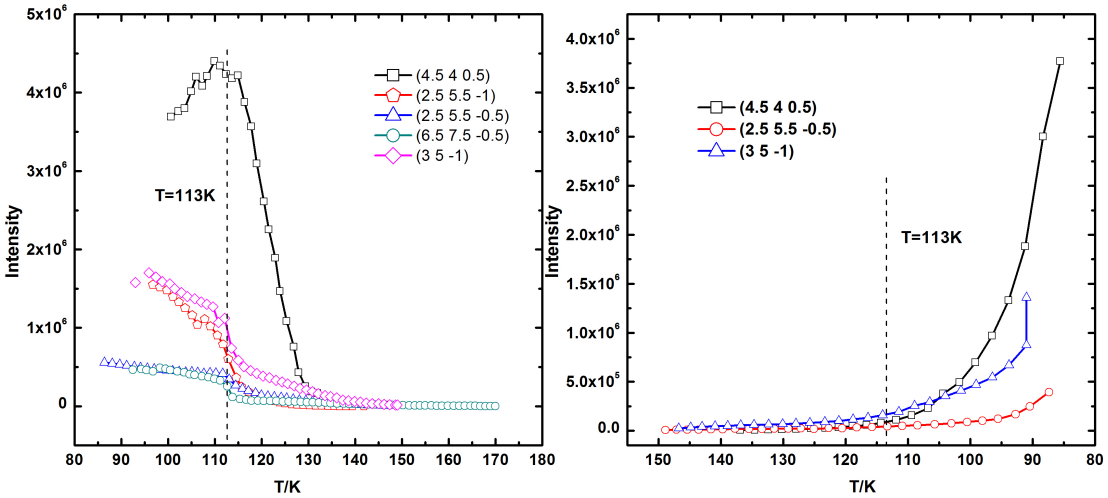

Figures 5.1.10 Variation of intensity of each reflection in heating and cooling process. An anomaly occurs at around 113K in both processes. The left figure displays the heating process, and the right shows cooling process.

Scattering profiles of all superstructure reflections are fitted using Pseudo-Voigt function, from which the full width at half maximum (FWHM) can be generated. The temperature dependence of correlation lengths given by $\xi \approx \pi/\Delta q$, where Δq is the FWHM of (4.5 4 0.5), (2.5 5.5 $\overline{0.5}$) and (3 5 $\bar{1}$) in the cooling process, is illustrated in Figure 5.1.11. As temperature approaches to T_c, the correlation lengths increase rapidly from ~200Å at RT to ~1100Å at 90K, demonstrating the formation of LT domains. The FWHM of the fundamental reflection (0 6 0) measured at 100K is 0.1° which gives a domain size of 1100Å according to the Scherrer equation. This means the maximum correlation length is limited by the domain size.

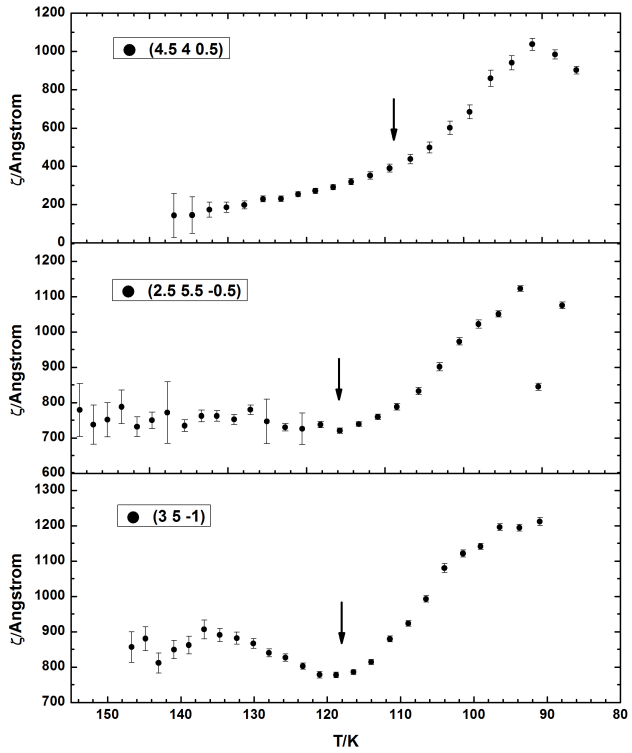

Figure 5.1.11 Correlation length of superstructure reflections (a) (4.5 4 0.5), (b) (2.5 5.5 $\overline{0.5}$) and (c) (3 5 $\bar{1}$) as a function of temperature in a cooling process. The arrows denote drastic increasing points, i.e. the T_c.

Single crystal XRD

The *hk*1 and *hk*0.5 layers at both 200K and 40K are reconstructed as illustrated in Figures 5.1.12. Comparing with the HT phase, a large number of superstructure reflections emerge inbetween the main reflections of the LT phase. Moreover, instead of background diffuse scattering shown at HT, clearly visible reflections turns up on the *hk*0.5 layer at LT. As aforementioned, the superstructure reflections are very weak which makes the structure determination and refinement of the LT phase very difficult.

Powder XRD

The diffraction spectra of Cd_6Yb at RT and 10K are displayed in Figure 5.1.13 where an offset is applied for better comparison. The peaks split at LT and an extra peak, as well as

two mismatching peaks are identified by arrow and dotted-line entangler respectively. This superstructure peak is confirmed absent in the spectra of Cd_6Tb at LT (see hereafter). As aforesaid, the phase transition of Cd_6Yb follows a different ordering scheme. Thus this superstructure peak is possibly the indicative of the otherwise phase. Moreover, the loss of diffuse scattering at LT is contributed by the suppression of thermal motions.

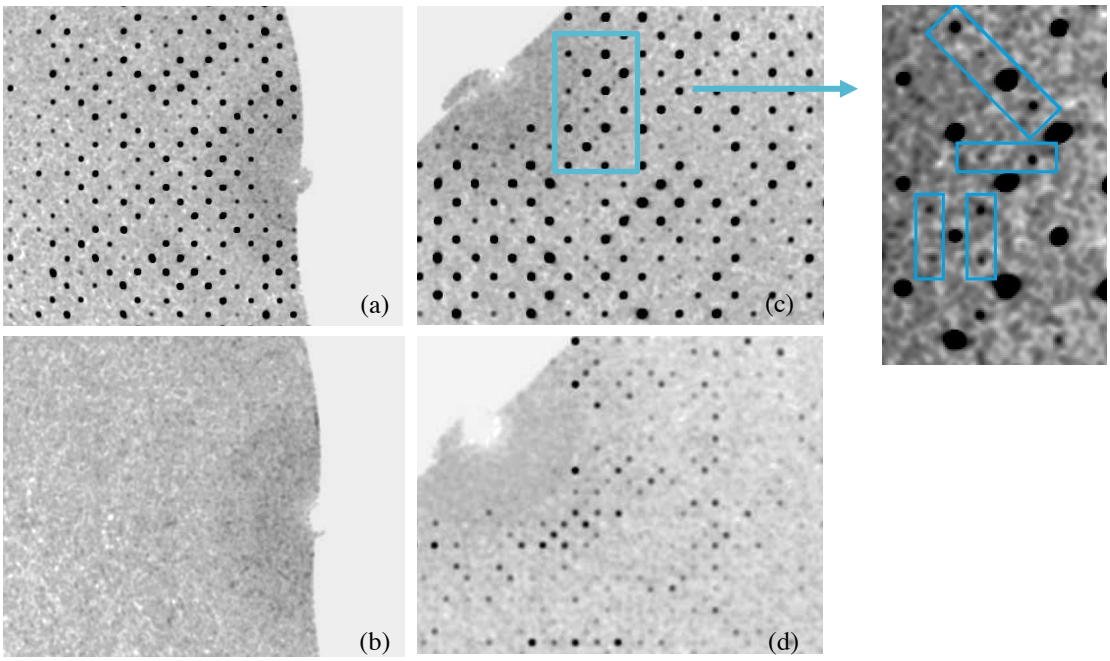

Figure 5.1.12 *hk*1 layer at 200K (a) and 40K (c), and *hk*0.5 layer at 200K (b) and 40K (d) are reconstructed in reciprocal space. Inset is the magnification of partial *hk*1 layer at 40K, and superstructure reflections are indicated by rectangles.

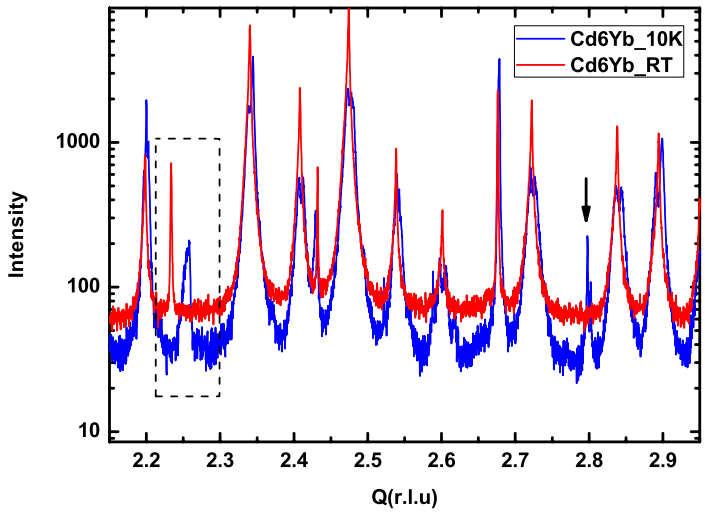

Figure 5.1.13 Peak profiles comparison between RT and 10K of Cd_6Yb, the mismatching and superstructure peaks are indicated by entangler and arrow respectively.

For further analysis, the diffraction spectra of Cd_6Yb and Cd_6Tb at RT and LT are compared and displayed in Figures 5.1.14 (a) and (b) respectively. It's noteworthy that Cd_6Tb follows the phase transition scheme as we depicted in Section 4.1. For a better view, the Q value of Cd_6Yb is shifted and an offset is applied to the intensity. Two unexpected peaks are observed in the Cd_6Yb phases of both two samples as indicated by black arrows. Besides, mismatching is found as well between the two compounds as shown in the dotted-line rectangle. Moreover, the supplementary diffuse scattering of Cd_6Yb disappears completely comparing with Cd_6Tb.

The same phenomena are observed in the LT phase. Since the HT phases of Cd_6Tb and Cd_6Yb share an identical skeletal network, the small difference between them only comes from the model of the central tetrahedron. The explanation to these extra and mismatching peaks most possibly lies on the impurity of the Cd_6Yb samples. Regarding the disappearance of the broad component of diffuse scattering in Cd_6Yb, it is not yet well understood but most likely either relates to the different mechanisms of phase transition or comes from the impurity of the Cd_6Yb samples.

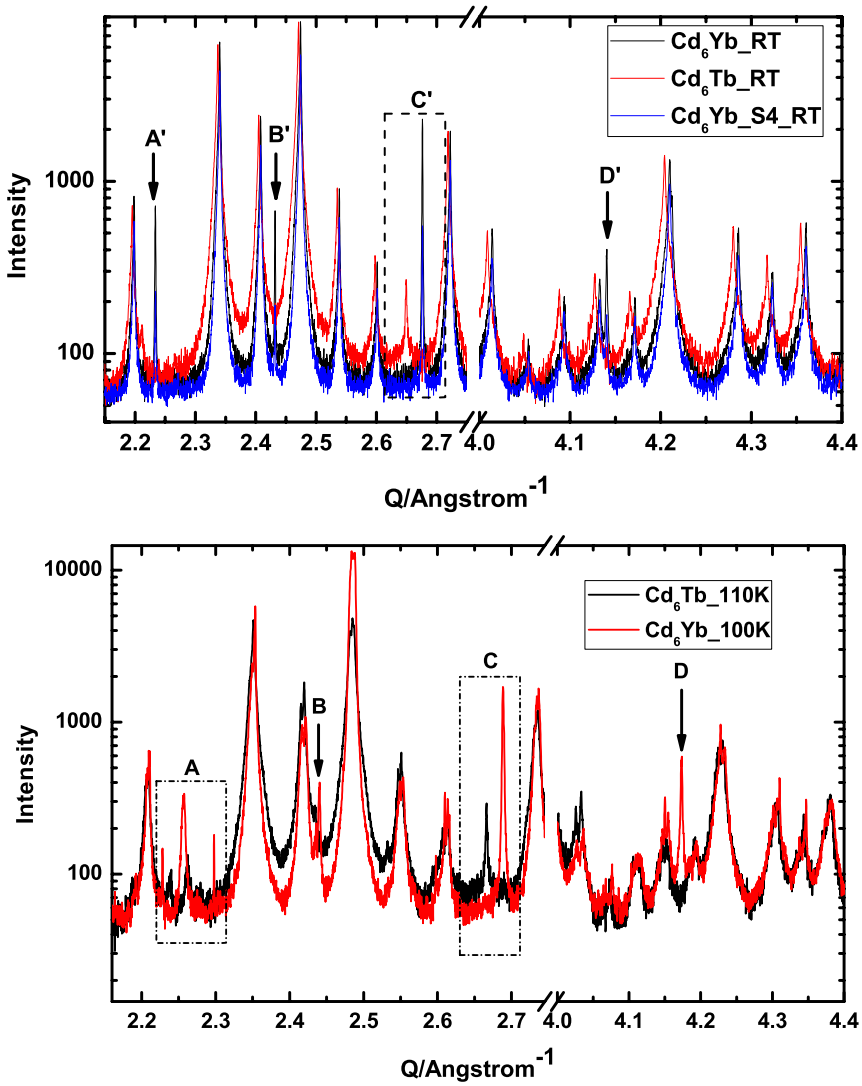

Figure 5.1.14 (a) Comparison of profiles between Cd_6Yb (black), Cd_6Tb (red) and another sample of Cd_6Yb (S4, blue) at RT; (b) Comparison of profiles between Cd_6Yb (red) and Cd_6Tb (black) at LT. T_c of Cd_6Yb and Cd_6Tb are around 110K and 190K respectively.

Diamond X-ray diffuse scattering

We executed measurements on some superstructure positions around (10 0 10) in a temperature interval from 20K to 300K, as shown in Figure 5.1.15. Two superstructure reflections that are forbidden at HT start appearing at 100K. Again the emergence of (10.5 0.5 10.5) is unexplainable with a doubled superstructure lattice $\sqrt{2}a\times a\times\sqrt{2}a$ but is compatible with the superstructure lattice $\sqrt{2}a\times 2a\times\sqrt{2}a$ proposed by Nishimoto[12].

A line scan was performed along [10.5 k 10.5] with k varies from -3 to 3 as shown in Figure 5.1.16. The intensity of each [10.5 k 10.5] distributes symmetric to [10.5 $\bar{k}$ 10.5], which suggests a two-fold axis along [10.5 0 10.5] with respect to the cubic setting at HT.

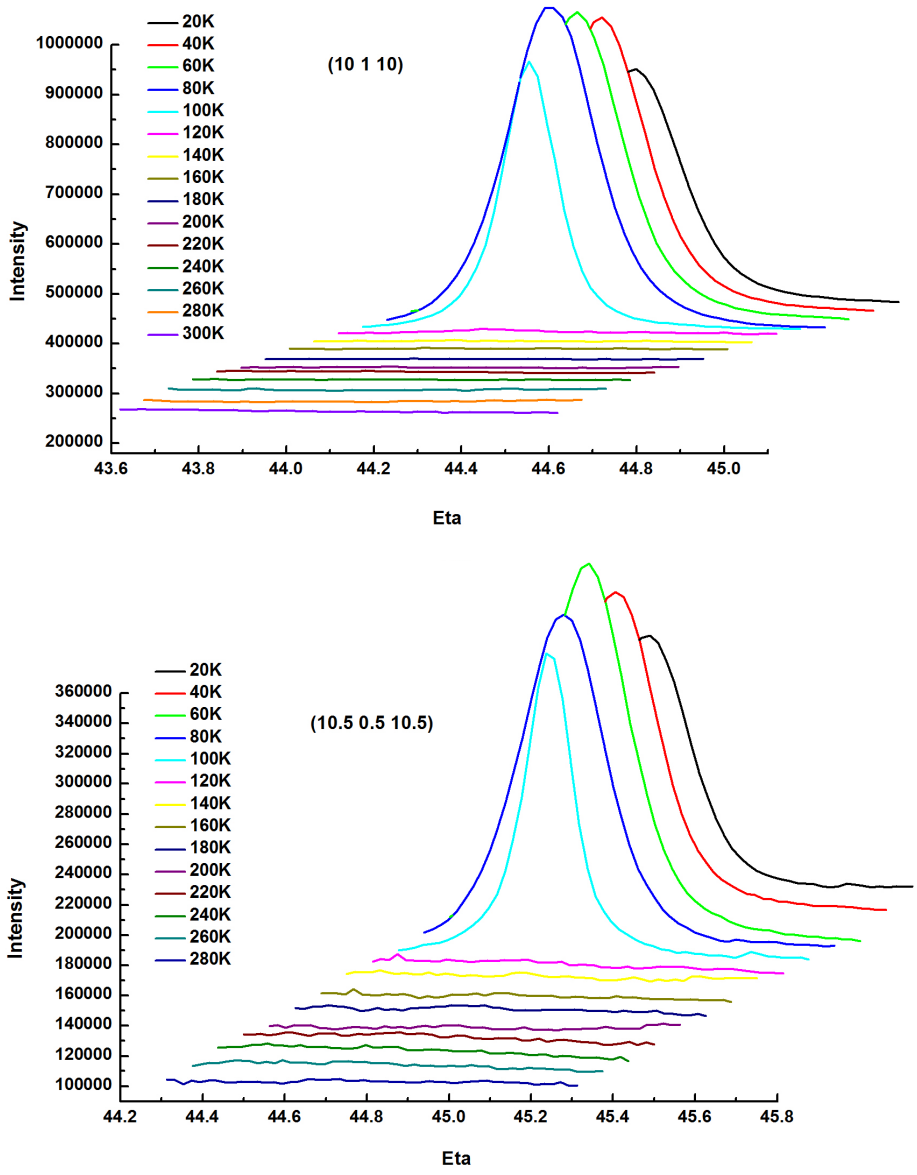

Figure 5.1.15 Variation of rocking curves of a series of superstructure reflections, (10 1 10) (left) and (10.5 0.5 10.5) (right), with respect to temperature. Both scans are implemented in direction [010].

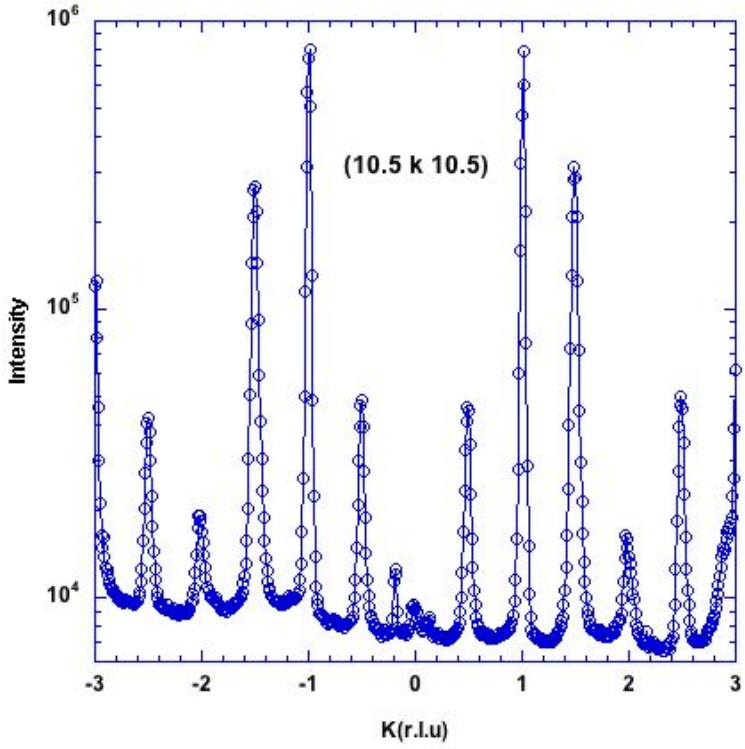

Figure 5.1.16 [10.5 k 10.5] line scan with k varying from -3 to 3. The distribution of intensity is equivalent for (10.5 k 10.5) and (10.5 –k 10.5), suggesting a 2-fold axis along [h0h].

Table 5.1 lists all reflections we have tested at LT, and as depicted above, space group *C*2/*c* with doubled unit cell propagating along $[\bar{1}01]$ has been excluded for Cd_6Yb. For the time being, *P*2/*m* with superstructure lattice $\sqrt{2}a \times 2a \times \sqrt{2}a$ can interpret these emergent and absent reflections. But it is still unknown whether superstructure with higher symmetry is possible or not. Therefore, it is of importance to character the structures of HT and LT phases. However, the multiple domains resulting from lattice distortion make it difficult to determine the LT phase.

Table 5.1 Summary of tested reflections at LT, all reflections are indexed with respect to HT phase

	Forbidden reflections	***General reflections***
ESRF T=15K	(1 4 0), (1 4.5 0)	(3 5 -1), (6.5 7.5 -0.5), (2.5 5.5 -0.5), (2.5 5.5 -1), (4.5 4 0.5), (2 6 -1), (1 7 -1)
Diamond T=7K	(5 0 4), (4 0 5), (6 0 3), (7 0 2), (8 0 1), (8 1 0), (8 -1 0), (10.5 0 10.5), (10 0.5 9), (15.5 0 0)	(5 -1 3), (5 1 3), (10 0.5 10.5), (10 -0.5 10.5), (10.5 -0.5 10), (10.5 0.5 10), (9.5 0.5 10), (9.5 -0.5 10), (9.5 0.5 10.5), (10.5 0.5 9.5), (10.5 0 10), (9 0.5 10), (10 0 10.5), (10 1 10)

5.1.3 Structure Characterization

As described above, two datasets were collected with different attenuators at 200K for structure determination. *Jana 2006*[117] is adopted for structure determination and refinement. The two datasets were combined by rescaling the reflections intensities using both *CrysAlis Pro* and *Jana*2006 (see Chapter 4 for details). Absorption correction was applied on the basis of the refined sample model as shown in Figure 5.1.1 (b). The atomic structure of HT phase is achieved. The crystallographic data and technique parameters of the Cd_6Yb are attached in Appendix II.

The structure solution is proved to be identical with the model proposed by C.P. Gómez *et al*[4]. The occupancy of central Cd tetrahedron atoms is confirmed to be 1/6. Figure 5.1.17 (a) displays the bcc packing of the RTH building blocks. Figure 5.1.17 (b) shows the innermost tetrahedron residing inside the dodecahedron. The model of the central tetrahedron can be described as a small cube each vertex of which splits into three positions to avoid an unrealistic distance to the dodecahedron atom in the outer shell.

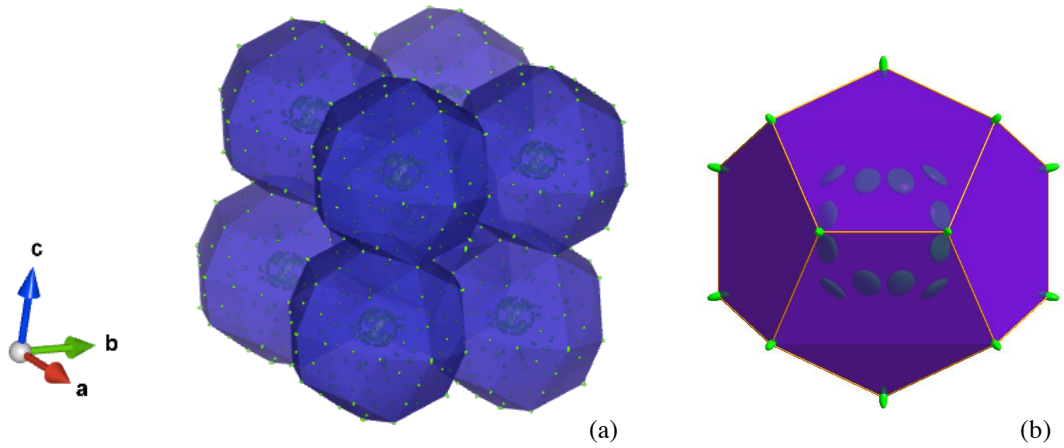

Figure 5.1.17 (a) Electron density isosurfaces at 15e/Å level, showing a triple splitting of the cubic vertices; (b) Dodecahedron with elongated displacement.

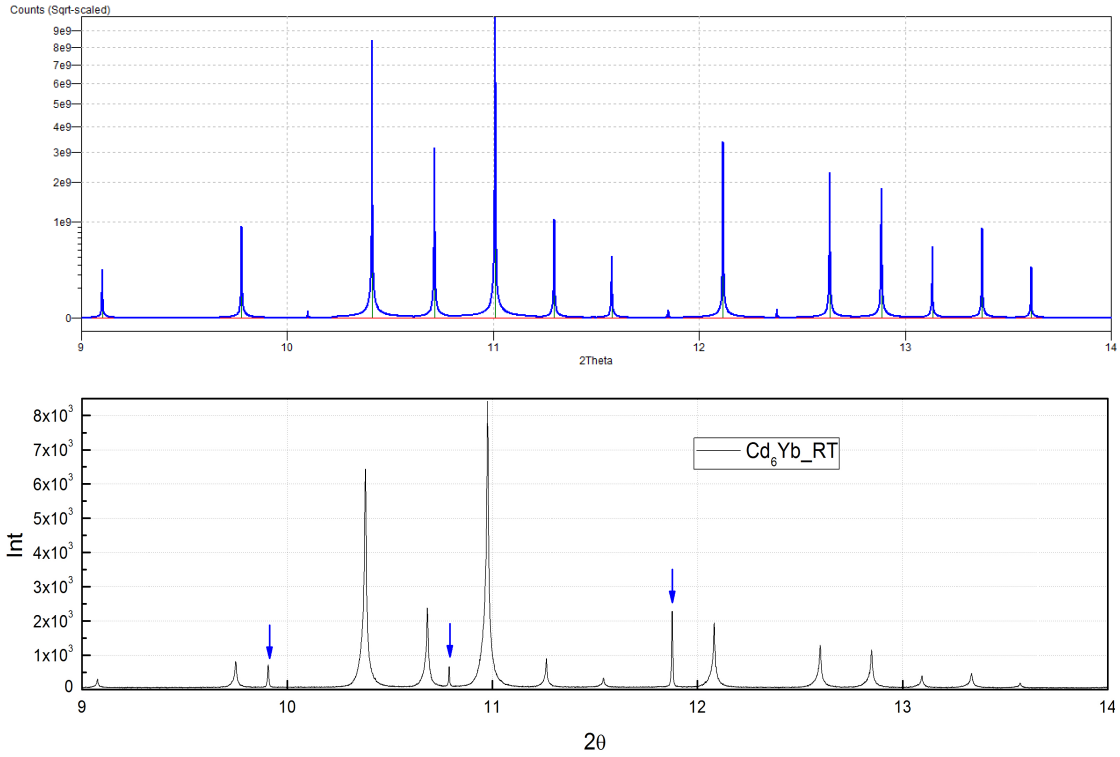

Figure 5.1.18 Powder diffractogram from calculation (up) and observed (down) over the 2θ range from 9° to 14°. Extra peaks are indicated by arrows.

The innermost Zn_4 tetrahedron of Zn_6Sc has been evidenced as dynamically orientational above T_c using quasielastic neutron scattering accompanied with molecular dynamic simulation[81]. The reorientation was clarified taking place within a time scale of a few ps, a distance scale of about 1.5Å and energy barrier of 60meV, which results in a strong distortion of the outer shells. The ellipsoid drawing of the Cd_{20} dodecahedron, as illustrated in Figure 5.1.17 (b), represents the displacement of each atom, and the elongation along 3-fold axis indicates the dynamical distortion driven by the reorientation of Cd_4 tetrahedra.

The details of atomic coordinates and equivalent isotropic displacement factors are attached in Appendix III.

To clarify the extra peaks appearing on Cd_6Yb at RT, we calculate the powder pattern using the structure model achieved from single crystal XRD measurements. The results are compared in Figures 5.1.18. It is obvious that these peaks are not essentially from Cd_6Yb, but most likely come from the impurity of the sample. Indeed, these three extra peaks have been confirmed coming from the remaining elementary Cd in the sample. The three peaks with 2θ equal to 9.91°, 10.79° and 11.88° are (0 0 2), (1 0 0) and (1 0 1) of the *hcp* Cd phase, respectively.

5.1.4 Discussion

As concluded above, the superstructure reflections of Cd_6Yb is quite weak which increases the difficulty of determining its structure of LT phase. On the other hand, integrating

intensities of reflections from multiple domains is also a troublesome question. Apart from an accurate atomic structure, analysis by transmission electron microscopy has given a schematic illustration of the superstructure for Cd_6Yb as presented in Figure 5.1.19. The superstructure has been affirmed belonging to space group $P2/m$ with a $\sqrt{2}$x2x$\sqrt{2}$ lattice which is compatible to all the known superstructure reflections[12]. The 2-fold axis of the ordered tetrahedra is parallel to b axis, and the mirror plane is perpendicular to b axis. In this case, there is no rule restricting the orientations of the tetrahedra locating on the mirror planes.

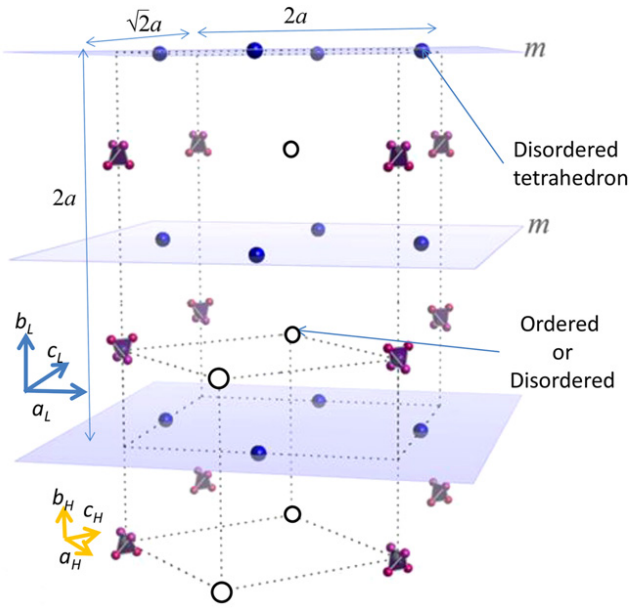

Figure 5.1.19 Ordering scheme of Cd_6Yb with respect to the orientations of the tetrahedra in the phase transition. Ref. [12]

5.1.5 Conclusion

We have performed synchrotron X-ray measurements to study the Cd_6Yb 1/1 approximant using different methods. The phase transition is evidenced and T_c is confirmed as around 113K, which is in good agreement with electrical resistivity and specific heat analysis[19]. The lattice distortion is observed from powder XRD and diffuse scattering measurements. It is noteworthy that the split of main reflections were not observed at ESRF but at Diamond on the same sample. The different results are most likely due to the long annealing time at RT. Appearance of reflection (6.5 7.5 $\overline{0.5}$) and (35$\overline{1}$) indicates that the mechanism of phase transition to Cd_6Yb is different from Zn_6Sc and other Cd_6RE phases. The correlation length increases rapidly after T_c up to ~1100Å which denotes the formation of LT phase and also the order of domain size.

According to previous reports, the central tetrahedra are considered dynamically oriented above T_c similar to Zn_6Sc, which leads to an exceptional dynamical flexibility. The reorientation of tetrahedra leads to a distortion of the outer shells especially the dodecahedra, which is represented by the displacement factors of dodecahedron atoms at 200K. The structure determination of the LT phase is stuck owing to the difficulties encountered from the multiple domains and weakness of superstructure reflections. According to the observed

and absent superstructure reflections, the space group of the LT phase of Cd_6Yb is most likely *P*2/*m* with a $\sqrt{2}x2x\sqrt{2}$ quadrupled lattice. Further analysis is certainly desirable in particular the structural determination of the LT phase.

5.2 Effect of Mg to phase transition of Cd_6Pr

The structure of Cd_6Pr at RT has been solved using single crystal XRD data by Gómez and Lidin[4]. It is identical to Cd_6Y and the occupancy of the central tetrahedron atoms are determined as around 0.216. The phase transition of Cd_6Pr has been investigated by Nishimoto *et al*[12] using transmission electron microscopy and a T_c around 150K is confirmed by the anomaly of electrical resistivity. It is suggested that the superstructure follows the mechanism we depicted in Section 4.1. However, some other results reported that a second type ordering occurs to Cd_6Ce and Cd_6Pr: the central Cd_4 tetrahedra are ordered along [111] and no lattice distortion is observed at LT[21]. Moreover, it is suggested as well that the addition of Mg element enhance the diffuse scattering of superstructure reflections. As a consequence, it is interesting to clarify the origin of tetrahedron ordering happening to Cd_6Pr and the role of Mg element to the diffuse scattering of superstructure reflections.

The samples of Cd_6Pr were prepared by a self-flux-growth method with a Cd-rich composition $Cd_{95}Pr_5$ in an Al_2O_3 crucible sealed inside a SiO_2 tube under Ar atmosphere[4]. The elements were melted at 973 K for 3 h and cooled to 898 K within 3h and then slowly cooled at the rate of 1 K/h to 848 K. Then, the Cd melt was removed from the single grains using a centrifuge. Single grains were annealed at 823 K for 100 h and slowly cooled at the rate of 5 K/h to 473 K and then annealed for about 600 h to remove quenched-in defects introduced during rapid cooling after the removal of Cd melt. The procedure for $(Cd\text{-}Mg)_6Pr$ at. 10% of Mg is the same as Cd_6Pr, and the starting composition is $Cd_{83.8}Mg_{11.2}Pr_5$.

A temperature dependent study was carried out on Cd_6Pr and $(Cd\text{-}Mg)_6Pr$ at. 10% of Mg by means of diffuse scattering using beamline D2AM at ESRF. Systematic scans are implemented to specific fundamental and superstructure reflections over a temperature range from RT to 20K. The energy of incoming X-ray beam is equal to 18.2keV, i.e. λ=0.681Å. The temperature is controlled by the cryostat system and samples are placed in a vacuumed Be dome.

5.2.1 Diffuse scattering of Cd_6Pr

The main reflection (0 6 0) is measured at 300K and 90K, as illustrated in Figure 5.2.1. The shoulder peak appearing at 300K implies that sample is twinned. As temperature deceases to 90K, the peak splits obviously, indicating the occurrence of a lattice distortion.

A line scan along [0k0] with k varying from 0.8 to 7.5 was executed at 90K as displayed in Figure 5.2.2 (a) where reflections are indexed with respect to the HT phase. It shows that reflections are allowed only when k is even, which is also the extinction rule of HT phase, meaning that no doubling of the unit cell is observed along b-axis. Furthermore, the line scan

[4] The sample is prepared by Tamura's group in Science University of Tokyo, Tokyo, Japan.

on (3 5 *l*) with *l* going from -0.5 to 1.5 was performed in a temperature range from 200K to 20K to check the ordering direction, as shown in Figure 5.2.2 (b). The reflection (3 5 1), which was observed in the Cd_6Yb case, does not turn up.

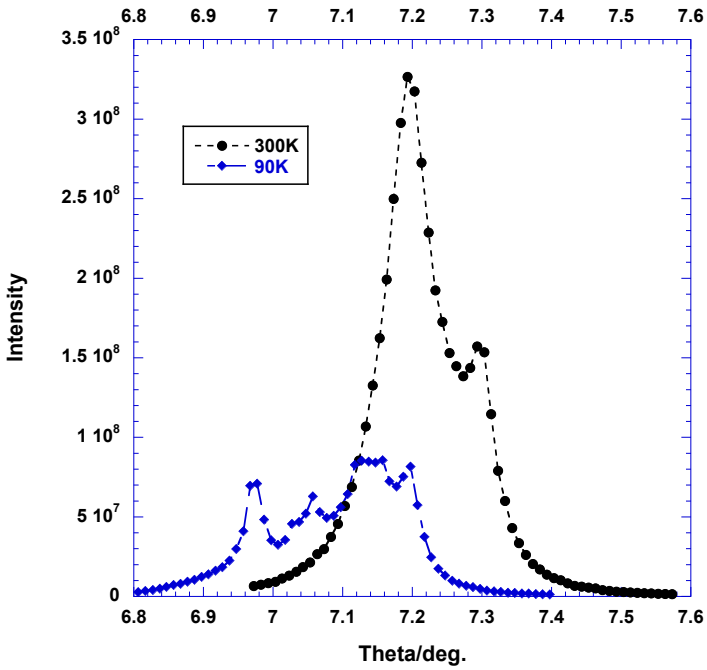

Figure 5.2.1 Profiles of reflection (0 6 0) at 300K and 90K.

Two other scans along [110] and [011] as a function of temperature were performed as shown in Figures 5.2.3 (a) and (b) respectively. A set of superstructure reflections are observed at and below 150K, and the intensity increases as temperature diminishes. The appearance of half-integer k is due to the multiple domains with different orientations. In Figure 5.2.3 (b), rocking curves at 90K are compared between two different processes, the good coherence of them implies that the transition is reversible. In addition, the superstructure reflection (2 5.5 -0.5) is clearly visible at RT although very weak, suggesting the existence of s.r.o.

Figures 5.2.4 (a) and (b) illustrate diffuse scattering of superstructure reflection (2 5.5 -0.5) at RT along [011] and [001] respectively. It is demonstrated that the diffuse scattering is quite anisotropic, i.e. the short-range order is stronger in direction [011] than [001]. The calculated correlation length ξ along [011] is 245Å, about 7 times longer than in direction [001].

Profiles of four specific superstructure peaks in a temperature interval from 200K to 20K are represented in Figures 5.2.5. Generally, superstructure reflections start emerging after 150K, i.e. the T_c of Cd_6Pr recently reported as by Nishimoto[12]. On the other hand, the intensity of superstructure reflections arises as temperature decreases except for 40K and 20K which could be the effect of experimental error.

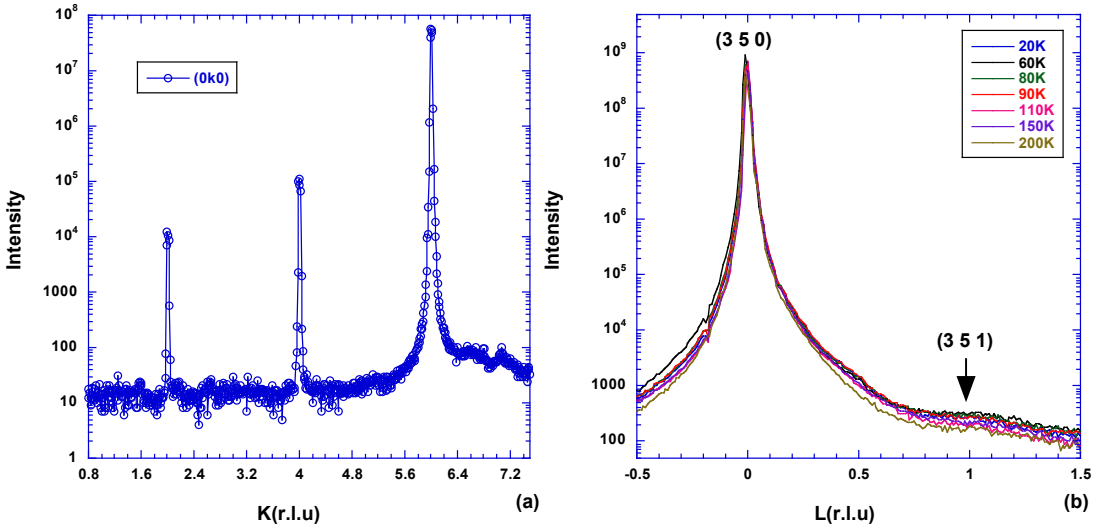

Figure 5.2.2 Line scan of (0 k 0) at 90K (a) and (3 5 *l*) from 200K to 20K (b).

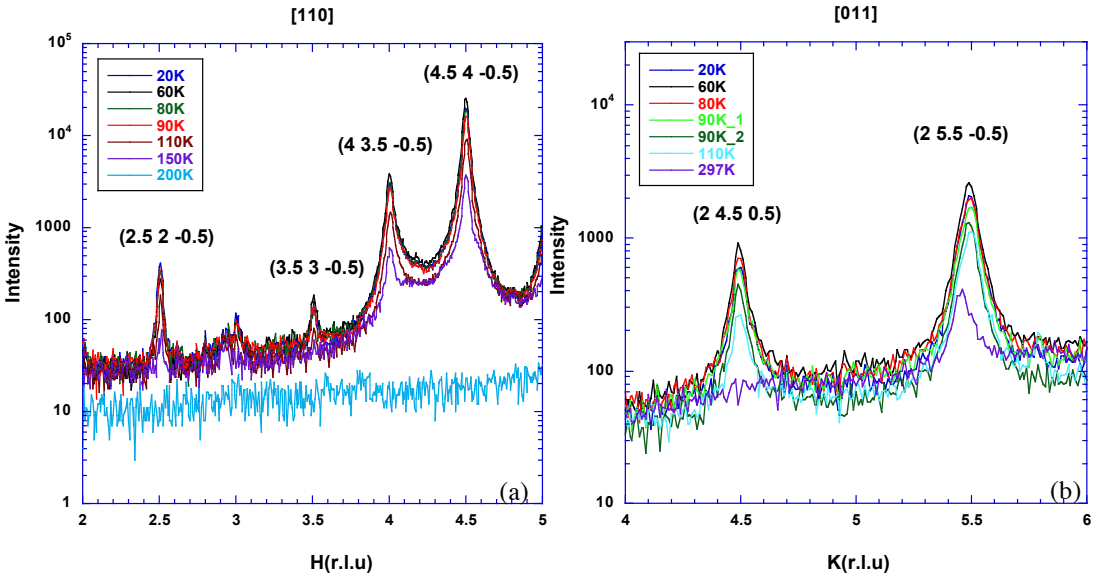

Figure 5.2.3 Line scans with respect to temperature along [110] (a) and [011] (b).

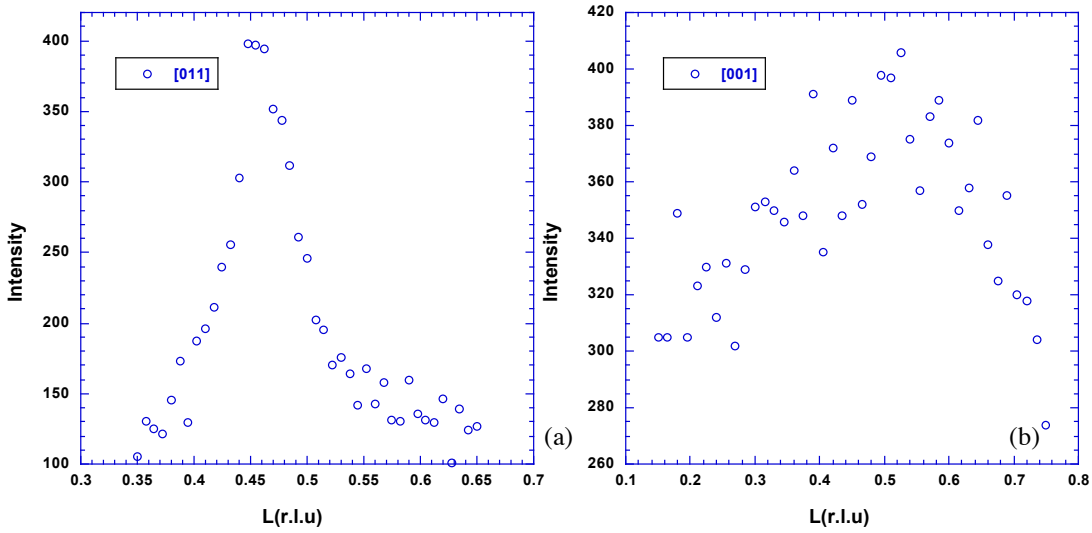

Figure 5.2.4 Profiles of superstructure reflection (2 5.5 -0.5) at 297K along [011] and [001] respectively.

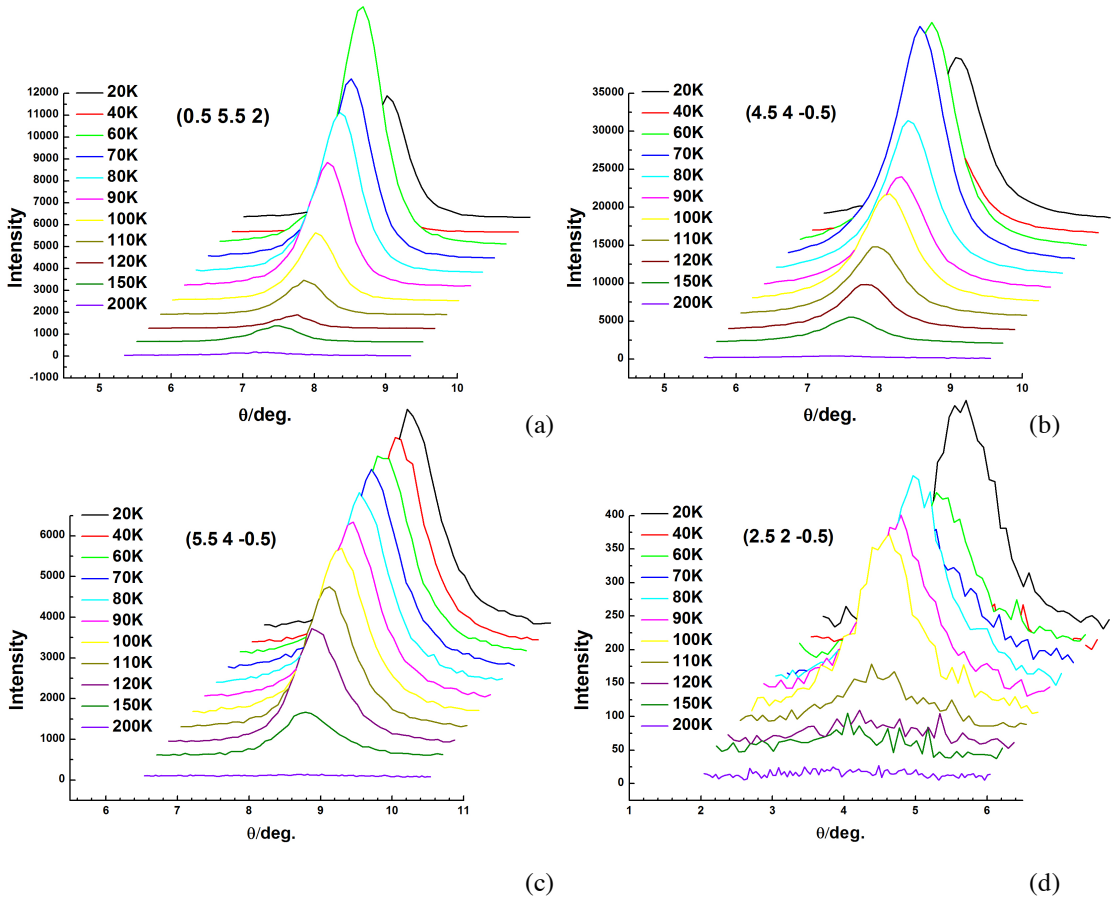

Figure 5.2.5 Variation of rocking curves of four superstructure reflections with respect to temperature, the reflections are indexed with respect to cubic setting, as indicated in insets.

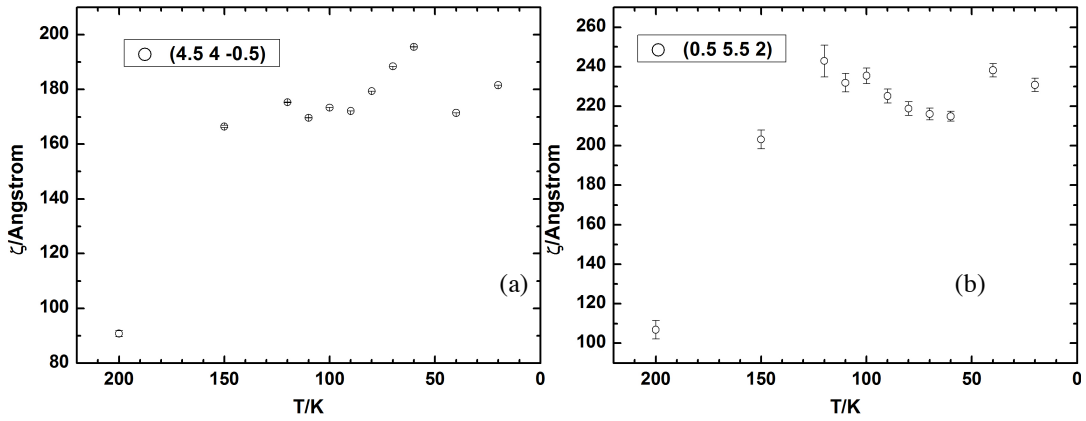

Figure 5.2.6 Correlation length of superstructure reflections (a) (4.5 4 -0.5), (b) (0.5 5.5 2) as a function of temperature.

We calculate the correlation lengths of superstructure reflections (4.5 4 -0.5) and (0.5 5.5 2) as a function of temperature. FWHM of each reflection is extracted from the fitting of rocking curves using Pseudo-Voigt function. The s.r.o becomes clearly visible from 150K, however, instead of sharpening, the s.r.o reaches to maximum at ~250Å and keeps unchanged after 120K as illustrated in Figures 5.2.6.

5.2.2 Diffuse scattering of $(Cd\text{-}Mg)_6Pr$ at. 10% of Mg

The fundamental reflections (0 6 0), (5 5 0) and (15 15 0) were probed at RT and 90K as illustrated in Figures 5.2.7. Unlike Cd_6Pr, split of peaks was not observed in the $(Cd\text{-}Mg)_6Pr$ phase indicating that no lattice distortion takes place.

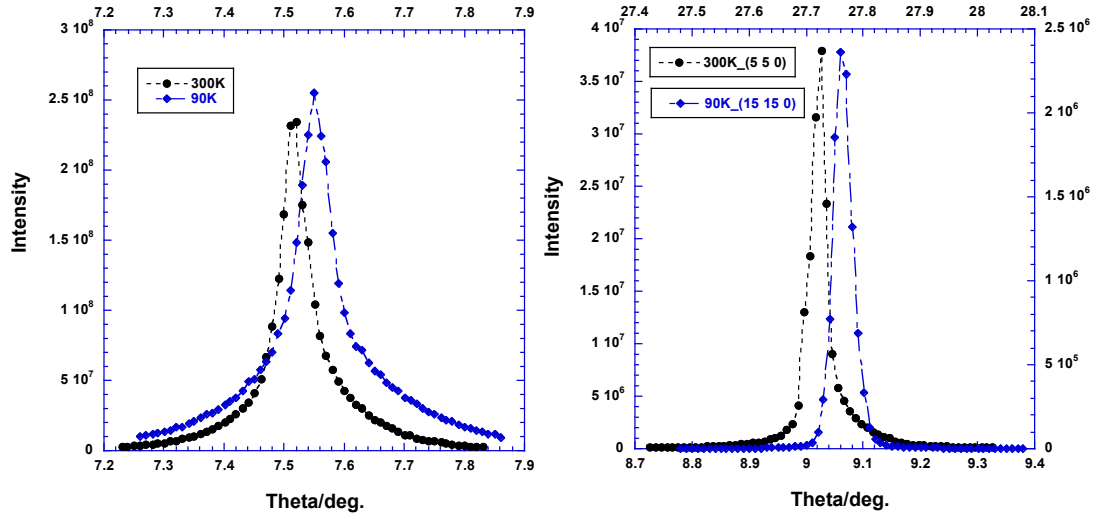

Figure 5.2.7 Rocking curves of main reflections ((0 6 0) for the left, (5 5 0) and (15 15 0) for the right) at 300K and 90K to $(Cd\text{-}Mg)_6Pr$.

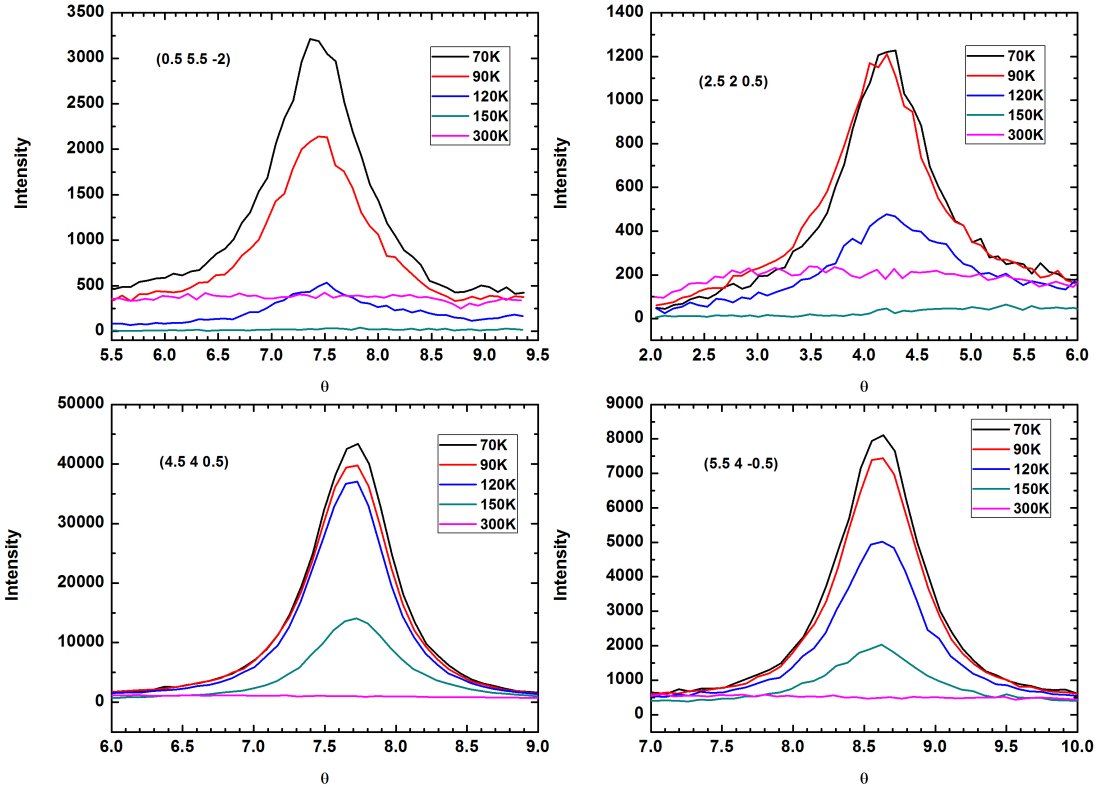

Figure 5.2.8 Rocking curves of superstructure reflections over a temperature range from 300K to 70K, all reflections are indexed with cubic setting at HT.

To elucidate the influence of the third element Mg to the diffuse scattering of Cd_6Pr, four relevant superstructure reflections of $(Cd\text{-}Mg)_6Pr$ at. 10% of Mg are measured and displayed in Figures 5.2.8. Similar to Cd_6Pr, weak reflections start emerging on superstructure positions at 150K. To take comparison quantitatively, the integrated intensity of each reflection at each temperature is normalized and compared with that of Cd_6Pr in Figures 5.2.9, where *hkl* is equivalent to $hk\bar{l}$. The normalization is applied based on the ratio of the Bragg peak intensities of each reflection between two compounds.

As denoted from the rocking curves, superstructure reflections become clearly visible from 150K, then followed by a rapid increase. By substitution of Mg element, the integrated intensities of superstructure reflections increase obviously except (0.5 5.5 2). Furthermore, the comparison of correlation lengths, presented in Figures 5.2.10, shows that the addition of Mg promotes the s.r.o in LT phase. Both results suggest the importance of chemical order in the s.r.o mechanism.

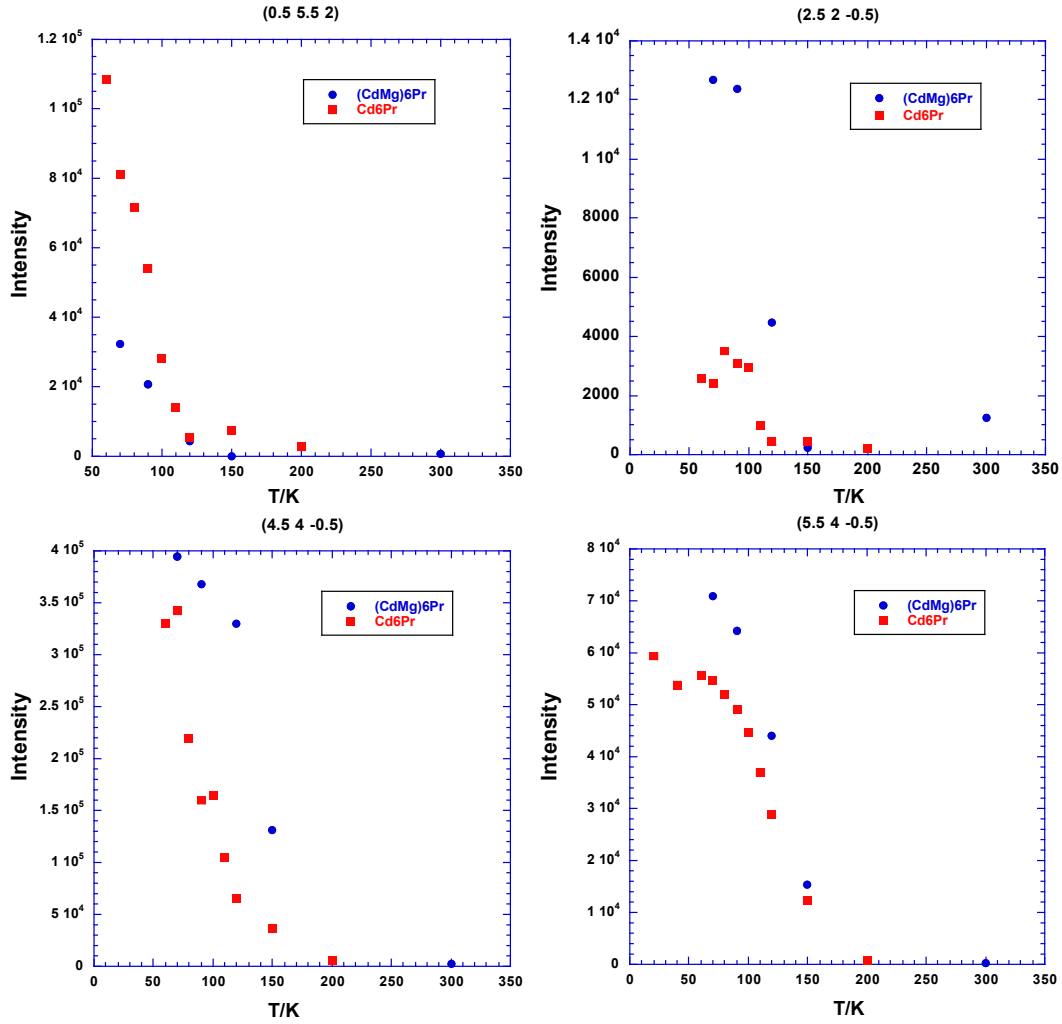

Figure 5.2.9 Intensity of each superstructure reflection of $(Cd\text{-}Mg)_6Pr$ as a function of temperature comparing with Cd_6Pr.

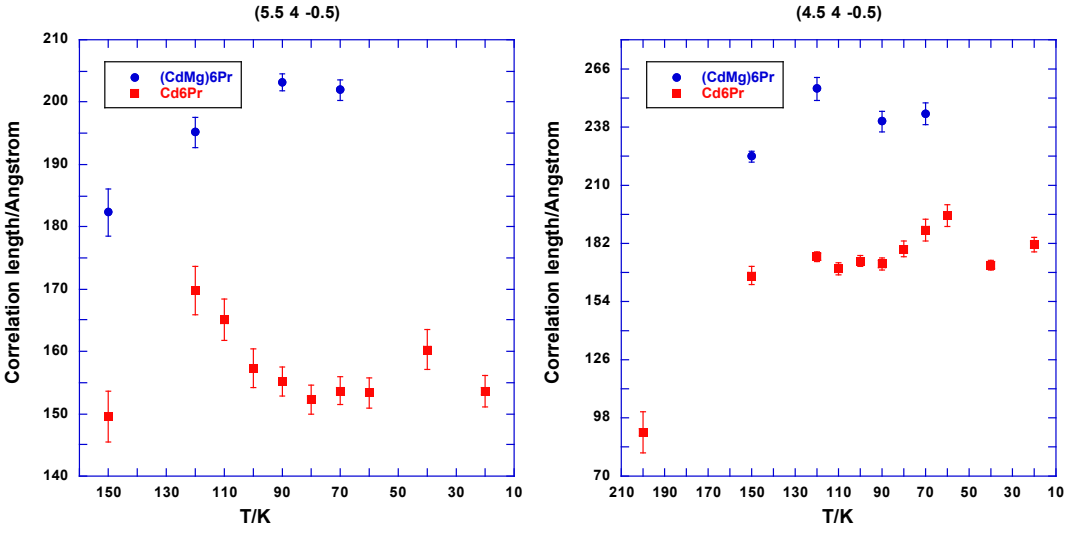

Figure 5.2.10 Comparison of correlation length between Cd_6Pr and $(Cd\text{-}Mg)_6Pr$ with respect to temperatures on superstructure reflections (5.5 4 -0.5) and (4.5 4 -0.5).

However, an exception was observed on (0.5 5.5 2) of which both intensity and correlation length of Cd_6Pr are stronger than those of $(Cd\text{-}Mg)_6Pr$ as illustrated in Figures 5.2.11 (a) and (b). Further analysis elucidates that the unusual behavior of (0.5 5.5 2) is most likely related to the Gaussian contribution. As aforementioned, all of the rocking curves are fitted using Pseudo-Voigt function, which involves two components, i.e. Gaussian and Lorentzian lineshapes. In most cases, Lorentzian curve is the only contribution to the shapes of the diffuse scattering profiles. Figure 5.2.11 displays the evolution of Gaussian fraction as a function of temperatures. It shows that the Gaussian fraction increases linearly as temperature decreases. However in case of $(Cd\text{-}Mg)_6Pr$, all Gaussian fractions are confirmed to be zero, meaning the Gaussian contribution to (0.5 5.5 2) disappears after addition of Mg element.

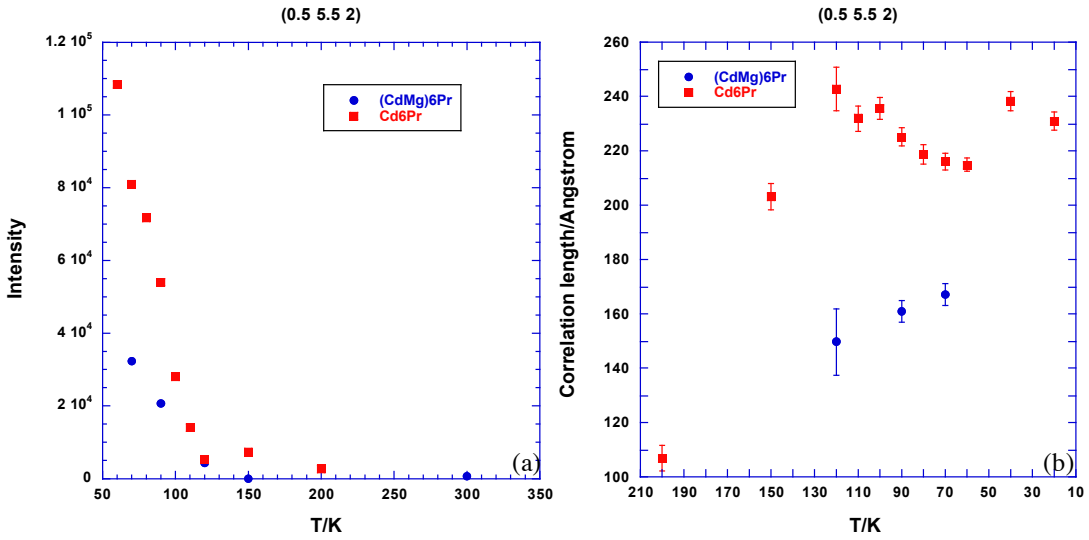

Figure 5.2.11 (a) Comparison of integrated intensity between Cd_6Pr and $(Cd\text{-}Mg)_6Pr$ as a function of temperature; (b) Correlation length of two 1/1 approximants with respect to temperature.

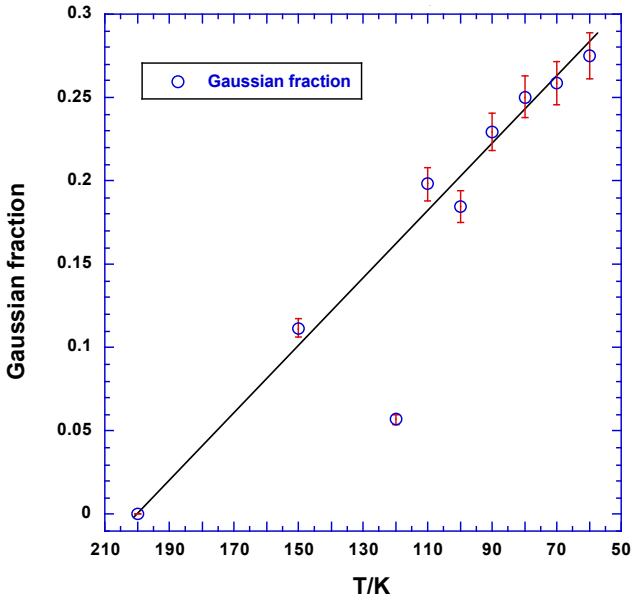

Figure 5.2.12 The evolution of Gaussian fraction of Cd_6Pr as a function of temperature.

Line scans were carried out on (3 5 *l*) with *l* going from -1.5 to 0.5 and along direction [110] on layer *hk*0.5 at different temperatures as shown in Figures 5.2.13 (a) and (b), respectively. As indicated by the arrow in Figure 5.2.13 (a), reflection (3 5 $\bar{1}$) is absent in the LT phase of $(Cd\text{-}Mg)_6Pr$ which is a space group restriction of *C*2/*m*. Comparing with the profile at 300K, a bunch of superstructure reflections turns up along [110] as shown in Figure 5.2.13 (b). The two results evidence that the superstructure happens along [110] and not along [111].

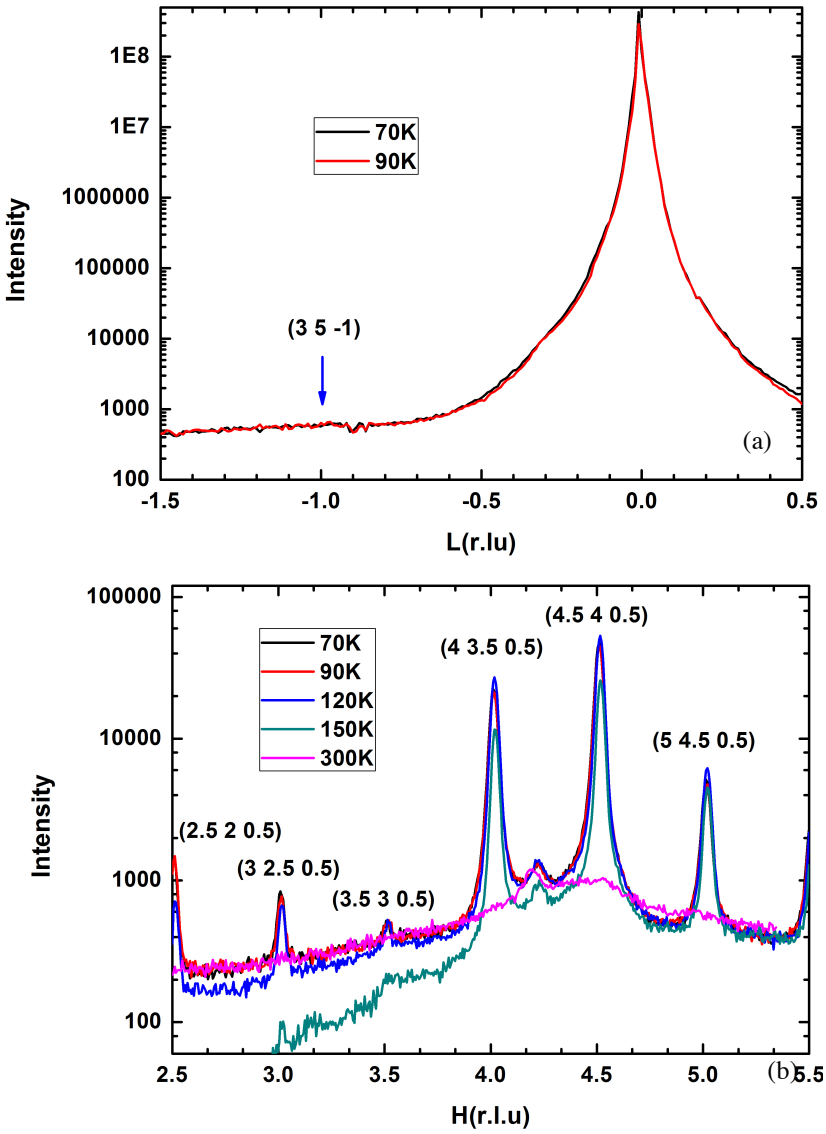

Figure 5.2.13 (a) Line scan of (3 5 *l*) with *l* varying from -1.5 to 0.5 at 90K and 70K; (b) Line scan along [110] with respect to temperature.

A comparison is taken to the line scan along [110] between Cd_6Pr and $(Cd\text{-}Mg)_6Pr$ at different temperatures as illustrated in Figure 5.2.14. The role of chemical order in $(Cd\text{-}Mg)_6Pr$ is shown clearly here. Reflection (3 2.5 0.5) is rather visible in $(Cd\text{-}Mg)_6Pr$ at LT (except 150K, where a problem occurs to the beam), however, it almost vanishes in Cd_6Pr. Moreover, the intensities of superstructure reflections in $(Cd\text{-}Mg)_6Pr$ are much stronger than

those in Cd_6Pr. Furthermore, as illustrated above, no peaks turn sharpening at LT suggesting very short correlation lengths.

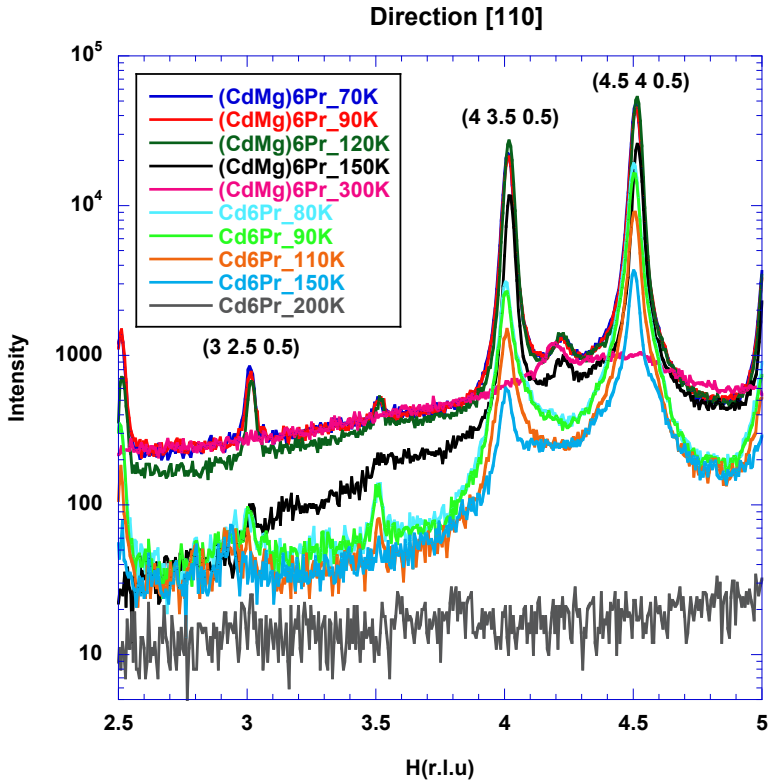

Figure 5.2.14 Comparison of line scans along [110] on the layer *hk*0.5 between Cd_6Pr and $(Cd\text{-}Mg)_6Pr$ over a temperature range from RT to 70K.

5.2.3 Discussion

Comparison between Cd_6Pr and $(Cd\text{-}Mg)_6Pr$ suggests that the chemical disorder is of importance to the ordering mechanism. The effect of substitution on the phase transition of Zn-based and Cd-based 1/1 approximants has been investigated by Yamada and Tamura[22], where small portion of Zn atoms are replaced by Cu. It is concluded that the introduction of the third element Cu occupies the dodecahedral sites and suppresses the ordering of the Zn_4 tetrahedron. According to the results of Lin and Corbett[23], theses ternary alloys keep the identical building clusters and symmetry with Zn_6Sc 1/1 approximant, and the additional Cu partially occupies Zn5 sites, i.e. the dodecahedral sites. The substitution of Cu reduces the bond distances of dodecahedral Zn atoms, leading to a smaller volume of the dodecahedron shell.

In case of Cd_6Pr, the third element Mg (~160pm) possesses larger atomic radius than the Cd (~151pm), which essentially enlarges the dodecahedron shell. As a consequence, owing to the steric effect, the suppression to the ordering of the Cd_4 tetrahedra is partially released. On the other hand, the lattice distortion resulting from the interaction between the tetrahedron and dodecahedron shells becomes smaller. Nevertheless, the difference between the two phases is not very large, demonstrating that the influence of the third element is very small.

5.2.4 Conclusion

Diffuse scattering measurements are carried out on Cd_6Pr and $(Cd\text{-}Mg)_6Pr$ with 10% at. Mg 1/1 approximants in a temperature range between 300K to 20K using synchrotron source D2AM at ESRF. Phase transition is evidenced to both systems. Other than the previously reported [111] type, [110] ordering mechanism is observed to both approximants. The T_c of Cd_6Pr is determined to be between 200K and 150K.

The superstructure signal of Cd_6Pr and $(Cd\text{-}Mg)_6Pr$ with 10% at. Mg is very weak. The substitution of Mg element may enlarge the dodecahedron cavity which slightly promotes the ordering of the central tetrahedron. However, the superstructure reflections do not get sharpening at LT in both cases, which leads to a very short correlation length. It is thus concluded that the influence of chemical disorder is very small.

Chapter 6. Molecular dynamic simulation to ZnSc approximants

The phason mode in QCs has been discussed in Chapter 1. Apart from the experimental techniques such as HRTEM and X-ray diffuse scattering, a few simulations have been executed to measure phasons in dodecagonal and icosahedral QCs[69][70][71]. To investigate the phason modes in atomistic scale one may encounter the following difficulties[57]: (i) the atomic model of QCs; (ii) corresponding Hamiltonian describing atomic interactions; and (iii) a plausible description of the phason move. A random tiling model[68] was proposed and applied for most of these simulations. In the scenario of this model, the QC is treated as a space-filling tiling where two or more defined tiles with distinct shapes are assembled following the absence of matching rule.

The first simulation was performed by Tang[69] who investigated the phason fluctuations and Fourier intensities in a 3D random-tiling *i*-QC. The calculated diffuse scattering was confirmed in good agreement with the predicted one by the hydrodynamics theory[68]. The long-rang positional order was also observed by variation of the so called 'finite-size scaling'. The temperature dependence of the two phason elastic constants were measured for the first time theoretically by Mihalkovič and Henley[71]. The simulation was carried out on a random-tiling *i*-QC using a Hamiltonian. The phason elastic constant K_2 changes its sign from positive to negative as temperature decreases and provides K_2/K_1=-0.64 which is compatible with the experiment results of *i*-AlPdMn[66], i.e. K_2/K_1=-0.5, however, disagrees with that of *i*-AlCuFe. This implies that even with analogical atomic structures, tile-scale Hamiltonian may be different depending on the chemical component.

It is noticed that all simulations mentioned above were executed using Monte Carlo method. Since the atomic structures of *i*-QCs and their ACs have been available by either canonical cell tiling or X-ray diffraction measurements. Adapted pair potential has also been achieved and proved efficiently describing the atomic interactions[25][80]. As is well-known, X-ray diffuse scattering is a crucial tool to investigate the phason modes in QCs. Thus by performing a MD simulation and applying Fourier transform to the snapshotting configurations, one may expect to reproduce the diffuse scattering of the target systems.

Hereby, we performed a set of MD simulations attempting to reproduce the diffuse scattering of ZnSc approximants at RT. Using a large approximant unit cell, e.g. 5/3 and 8/5 ACs, we expect to observe the complementary phason diffuse scattering characteristic to QCs. The temperature dependence of the diffuse scattering will also be discussed preliminarily. The results will be compared with the much studied systems in experiments.

On the other hand, the temperature dependence of the tetrahedron motions are also investigated to have a detailed insight to the tetrahedron ordering mechanism in different approximants. The MD simulation can be realized by using the oscillating pair potential of ZnSc which has been fitted efficiently against *ab-initio* data as shown in Figure 6.1.

The fitted empirical oscillating pair potential (EOPP), including six parameters as well as the Friedel oscillations, is of an analytic form:

$$V(r) = \left(\frac{a_0}{r}\right)^{a_1} + \frac{a_2}{r^{a_5}}\cos[2\pi(a_3 r + a_4)] \qquad 6.1$$

The first term describes the short-range repulsion, and the second term corresponds to the medium-range interactions as well as the long-range oscillating tails. The Friedel oscillations, i.e. the second and third neighboring wells are related to the Fourier transform of the Fermi surface which often control the energy difference between competing structures in complex metallic alloys. The relative weights of the first and second terms can be adjusted by parameters a_1 and a_5. The six parameters are considered independent in the fitting process. The cutoff distance in our work is determined as ~8.3Å, where both energy and force are negligible. The six parameters are fitted based on a database containing force and energy data of $ScZn_6$, $ScZn_2$ and Sc_4Zn_6 at both high and low temperature[25]. The structures containing both relaxed at T=0 data and high-temperatures *ab-initio* MD results offer 1977 force components and 51 energy data for fitting. This gives a resulting rms deviation of 0.1eV/Å for forces and 3.6meV/atom for energies. Since the pair potential has been fully validated by previous work[97][44] and the experimental data[81][80], therefore we chose it to carry out the simulation on this ZnSc system.

The simulation was implemented by the LAMMPS with a *NVT* ensemble, i.e. the number of atoms, the volume of system, and the temperature are constant. A Nosé–Hoover thermostat is used to control the temperature around the target value. In the case of solids, the application of Nosé–Hoover thermostat can result in undesirable oscillation of the volume or temperature. Therefore a drag factor, i.e. 3 for our systems, is introduced to the Nosé Hoover equations to damp the oscillations. The starting configurations are firstly optimized with an energy minimization process to release the initial strains. The energetic minimization is computed by algorithm of conjugate gradient (CG). At each iteration, associating with the previous iteration information, the force gradient is used to determine a new searching direction perpendicular to the previous one. Finally the minimum is reached by continuously conjugating iterations. Then the system is relaxed to the equilibrium at the target temperatures. All data are collected after structural relaxation. The details on simulation condition refer to Section 3.3.

Firstly, we performed MD simulations to the 1/1 Zn_6Sc approximant, and then turned to the 5/3 and 8/5. For the 1/1 approximant, a supercell containing 4x4x4 unit cells is applied to generate the information on s.r.o. Fourier Transform (FT) is executed to all configurations and all of the FTs are summed up to reproduce the reciprocal space.

6.1 Zn_6Sc 1/1 approximant

Experiment

Zn_6Sc is the 1/1 approximant with body-centered cubic lattice related to the ZnMgSc QC. A low-temperature phase transition has been evidenced by practical measurements such as an anomaly of temperature-dependent electrical resistivity, and the appearance of superstructure reflections[6]. The study on structures and s.r.o above and below T_c has been carried out by Ishimasa[8] and Yamada[11]. The lattice dynamics of both ZnMgSc quasicrystal and Zn_6Sc 1/1 approximant has been detailedly investigated by means of neutron and X-ray scattering and MD simulations[80][81][25]. Experimental analysis of diffuse scattering and phason

fluctuations have also been compared between the two compounds[60]. Furthermore, the discovery of the binary *i*-QC of $Sc_{12}Zn_{88}$[120][121] makes it more interesting to implement a further study on theses complex metallic compounds.

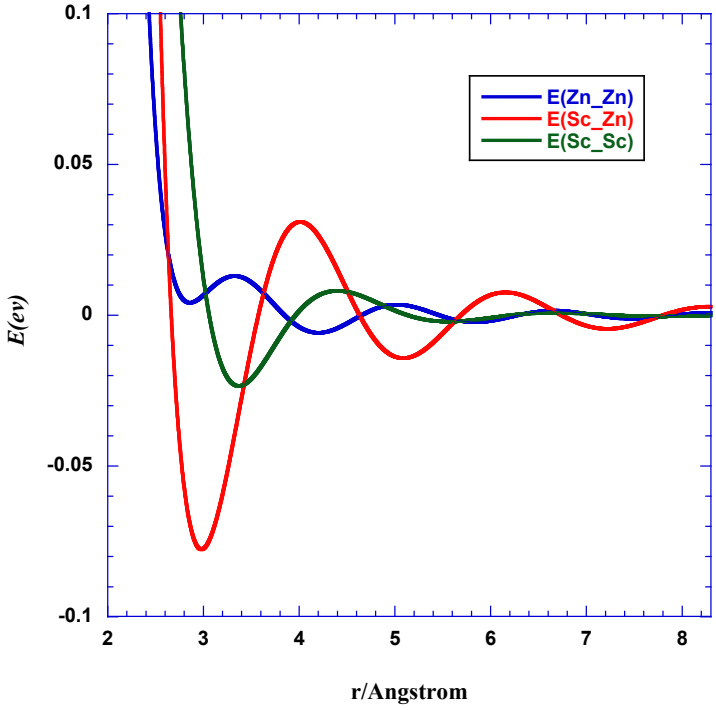

Figure 6.1 Oscillating pair potentials fitted against *ab-initio* database. The potential energies between Zn-Zn and Sc-Sc reach first minimum at 2.85Å and 3.34Å respectively. A cutoff is applied at 8.3Å, where both potential energy and interacting force become eligible.

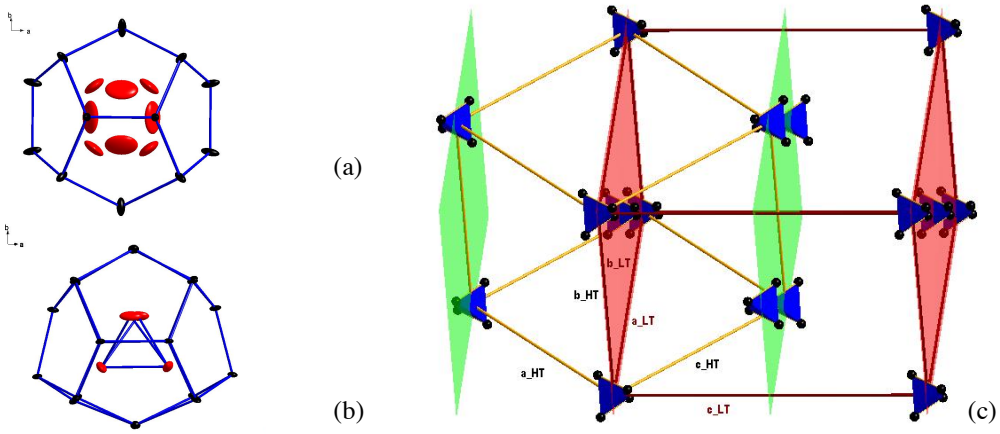

Figure 6.1.1 (a) Disordered tetrahedron residing in the dodecahedron shell; (b) Ordering tetrahedron inducing a distortion of the dodecahedron; (c) Schematic of the ordering scheme of the central tetrahedra along [$\bar{1}$01] direction with respect to the HT cubic setting. The two planes with different colors shows an antiparallel correlation. The unit cell is doubled below T_c.

In this work, the diffuse scattering of a series of ZnSc approximants with respect to temperatures will be presented. The correlation between diffuse scattering and the dynamics of the central tetrahedra will be discussed as well. Apart from these, it is also an attempt to have an insight on the phason mode in the quasicrystal by means of MD simulation.

The structural phase transition on the Zn_6Sc 1/1 approximant has been carefully discussed previously in experiments[11][8]. It follows the uniform procedure as we described above for the Cd_6Tb 1/1 isostructural phase. Figures 6.1.1 (a) and (b) present the disordered tetrahedron at HT residing inside the dodecahedron, and the ordering tetrahedron which results in a distortion of the dodecahedron shell, respectively. The distortion propagates along $[\bar{1}01]$ direction leading to a doubled monoclinic unit cell at LT, as illustrated in Figure 6.1.1 (c).

Simulation

The initial structure of the Zn_6Sc 1/1 approximant for MD simulation was optimized from VASP calculation. Following the energy minimization process, a 4x4x4 supercell was first relaxed to equilibrium at 500K, and then cooled from 400K to 60K using the software package LAMMPS. Intensive simulations with a temperature step 10K were carried out from 200K to 60K. At each temperature, 5 million steps were run out and 2000 configurations were collected for analysis. To avoid being trapped into a local minimum energy state, larger time steps were adopted at LT. The time step for each temperature is listed in Table 6.1.

Table 6.1. Time step settings for each temperature of Zn_6Sc 1/1 approximant

T/K	**400**	**300**	**200**	**190-130**	**120-100**	**90**	**80-70**	**60**
Time step/ps	0.004	0.007	0.01	0.008	0.01	0.012	0.015	0.018

The potential energy as a function of temperature is displayed in Figure 6.1.2. The energy varies linearly with respect to temperatures and no anomaly turns up indicating the phase transition. Indeed, although 10752 atoms are involved into simulations, the energy difference among tetrahedra with different orientations are so small, i.e. a few meV per cell according to [9], that it is unfeasible to observe energetic transition in such scale. The time dependence of the potential energy at 400K, 300K, 200K and 100K are presented in the insets, showing good convergences and energetic accuracies of $\pm 0.74 meVatom^{-1}$, $\pm 0.65 meVatom^{-1}$, $\pm 0.51 meVatom^{-1}$ and $\pm 0.19 meVatom^{-1}$ respectively, which is compatible to the value of *ab initio* calculation performed by Mihalkovič[24], i.e. $1 meVatom^{-1}$.

6.1.1 Diffuse scattering

Time-averaged FT is applied to all the 2000 configurations at 300K. The result is compared with the single crystal experiment data of Zn_6Sc as demonstrated in Figure 6.1.3 where the diffraction patterns are reconstructed from both experiments and simulations on the *hk*0 Bragg plane. The size of mark indicates the strength of intensities. The 2-fold and pseudo 5-fold axes are denoted by arrows. An overall similarity of intensity distribution is presented between real and modeling structures.

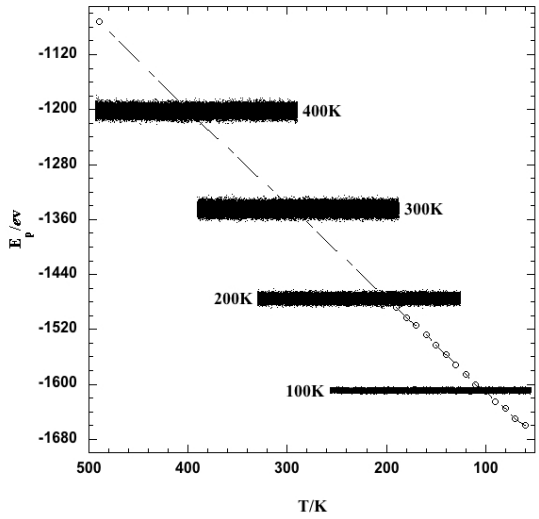

Figure 6.1.2 Evolution of the potential energy of Zn_6Sc 1/1 approximant with 4x4x4 unit cells as a function of temperature. The time dependent fluctuations of the energy are displayed.

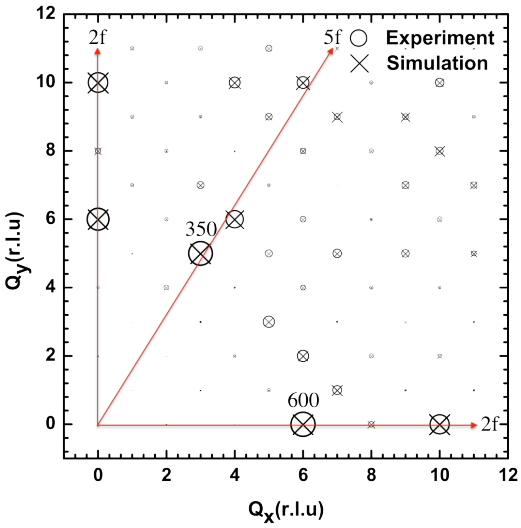

Figure 6.1.3 Diffraction pattern reconstructed on *hk*0 layer compared between experiment (open circle) and simulation (product mark) at RT. The sizes of marks reveal the intensity.

The reproduced *hk*0 Bragg planes of the Zn_6Sc 1/1 approximant at 400K, 300K, 200K and 100K calculated from MD simulations are illustrated in Figures 6.1.4, from left to right respectively. Diffuse scattering resulting from thermal motions is clearly observed at HT. As temperature decreases, the diffuse scattering sharpens as shown at 100K which is the result of the ordered central tetrahedra.

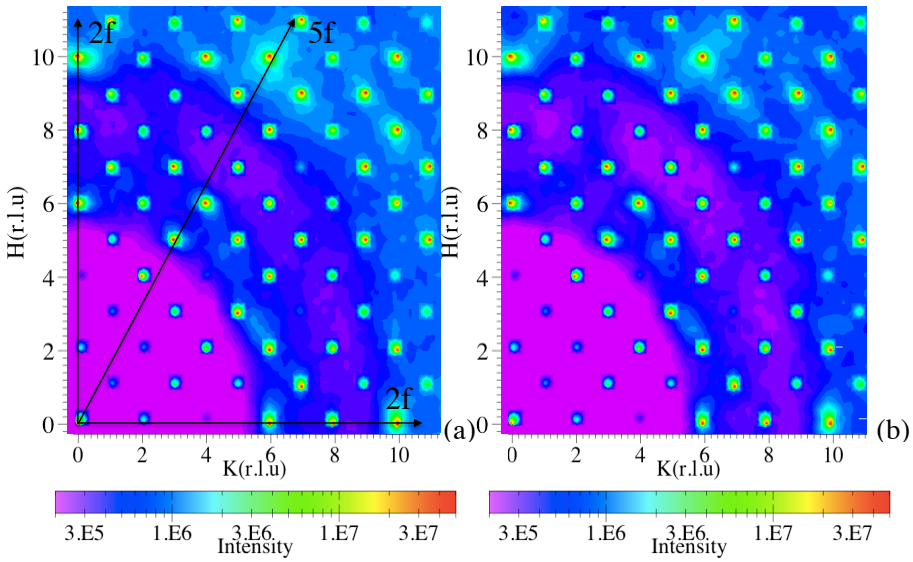

To be continued

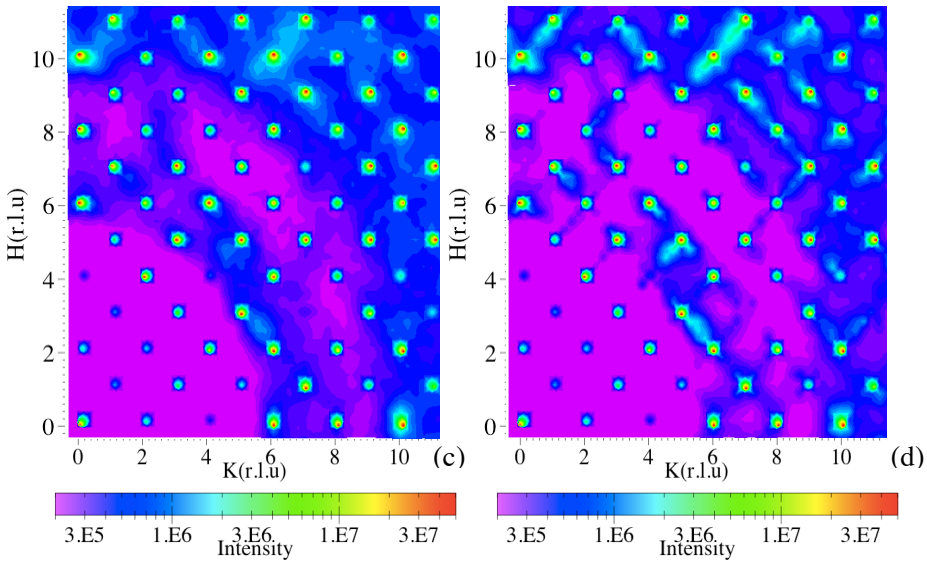

Figure 6.1.4 *hk*0 layer of 1/1 approximant generated from a 4x4x4 supercell, the temperature is 400K, 300K, 200K and 100K from (a) to (d).

Diffuse streaks on Fourier planes are observed at LT along <110> directions as shown in Figures 6.1.5, demonstrating the s.r.o along perpendicular directions in real space forming in the LT phase. According to Welberry's analysis on similar patterns[122], this sort of diffuse scattering most likely results from a preferred orientation of the local clusters. Therefore regarding the Zn_6Sc phase, the s.r.o is essentially induced by the preferred orientations of the central tetrahedra at LT. Moreover, the diffuse scattering is different on equivalent Bragg planes, e.g. 0*kl* and *h*0*l*, manifesting that the correlations of the s.r.o are dependent on different directions.

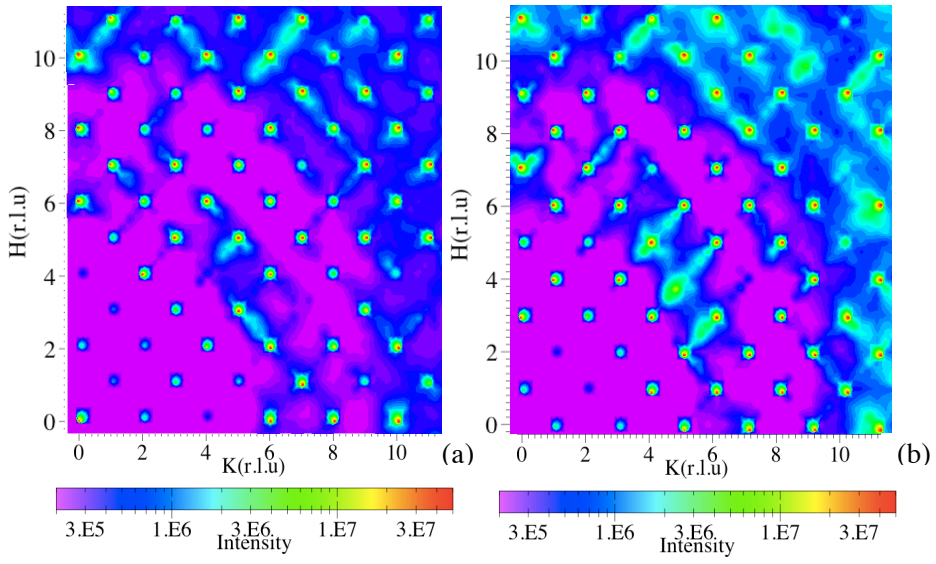

To be continued

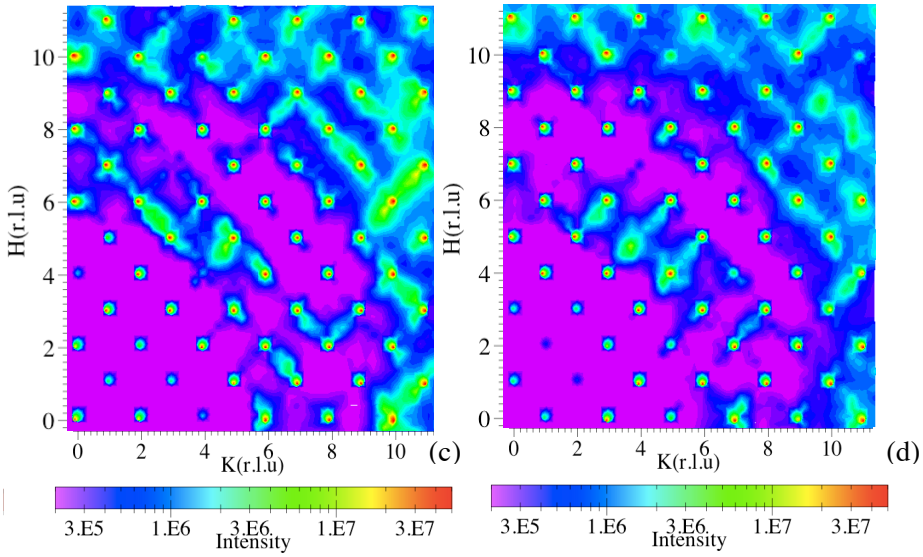

Figure 6.1.5 Bragg planes of Zn_6Sc at 100K, from (a) to (d): 0*kl*, 1*kl*, *h*0*l*, *h*1*l*. The inequivalent diffuse scattering implies the breaking of the cubic symmetry resulting from the ordered tetrahedra.

As it is elucidated in experiments, the ordering of the central tetrahedra leads to a double unit cell which results in the appearance of superstructure reflections on half-integer layers. As a consequence, we calculated the FT on half-integer layers with respect to temperatures as shown in Figures 6.1.6. We have to emphasize again that, the time scales of our simulations are tens to hundreds of nanoseconds and the length scale is 55.3244Å, which are large enough to reconstruct the diffuse scattering and the motions of tetrahedra, however, infeasible to reproduce the occurrence of the phase transition.

In Figures 6.1.6, again the evolution of the scattering intensity shows a sharpening tendency as temperatures decrease. To analyze it quantitatively, we made a slice along $[0\bar{1}0]$ on *hk*3.5 layers, i.e. h equals 2.5 and k varies from 0 to 11.5. The profiles of the four line scans are compared in Figure 6.1.6 (b) where a superstructure reflection (2.5 11 3.5) is indexed. It is clear that the intensity of (2.5 11 3.5) increases as the temperature decreases which is consistent with the experiment results.

The resulting diffuse scattering has exhibited the forming of the s.r.o in the LT phase of Zn_6Sc. The preferred orientations of the central tetrahedra at LT are supposed to be responsible to this s.r.o. The directions of the diffuse streaks suggest the s.r.o distribute mainly along $[1\bar{1}0]$ which is consistent with the experiments. However, other than superstructure reflections observed in experiments, no evidence proving the phase transition in the simulation. We suggest that a larger length scale of the supercell may promote the forming of a long range order.

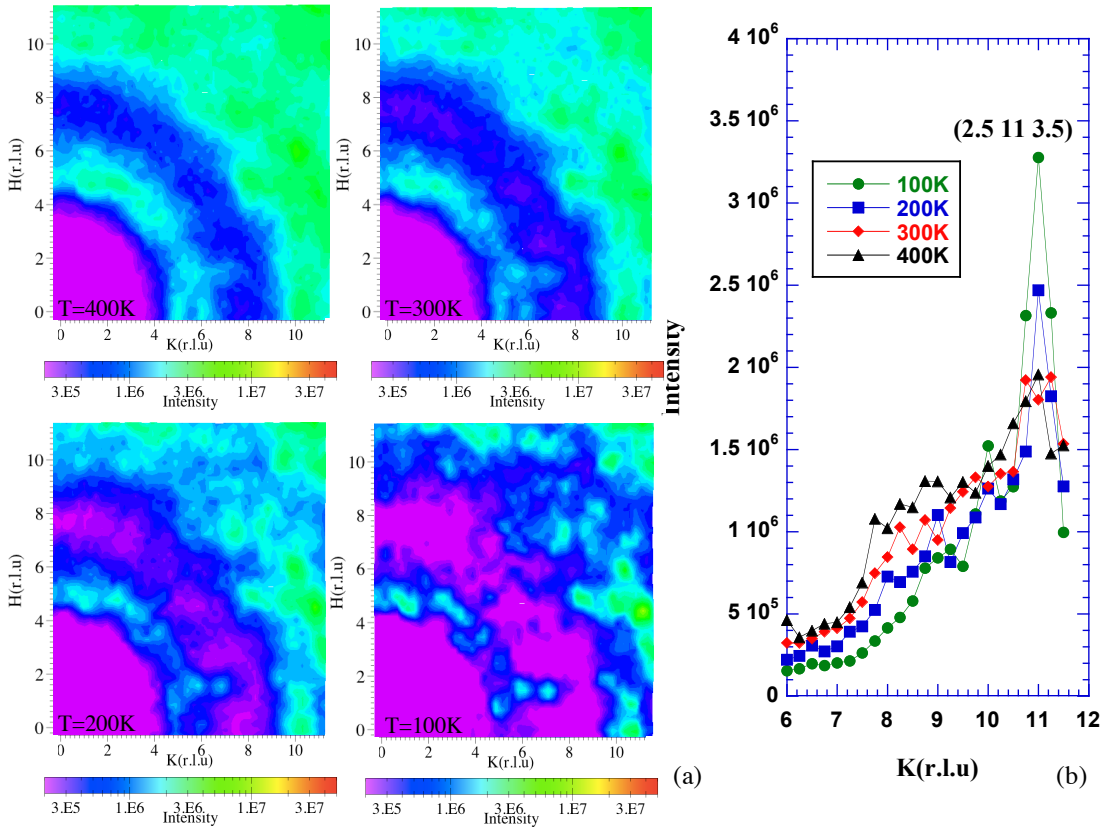

Figure 6.1.6 (a): The *hk*3.5 layers of Zn_6Sc 1/1 approximant from 400 K to 100K, a line scan was performed along [2.5k3.5]; (b): The profiles of four line scans with respect to temperatures, one superstructure reflection is indexed.

6.1.2 Tetrahedron dynamics

Both experiments and simulations have evidenced that the innermost tetrahedron is dynamically reorienting instead of being static[81]. A short simulation with a 2x2x2 supercell was carried out at 500K to observe the 'jumping' of the tetrahedron. The coordinates variation of one tetrahedron atom is shown in Figures 6.1.7. The top figures display the different orientations of the tetrahedron with respect to time. To follow the trajectory of the tetrahedron, we extracted the coordinates of one tetrahedron atom, i.e. atom 165, and plot them as a function of time. Each flip of the tetrahedron reveals a steep coordinates change as indicated by dashed lines. Altogether 18 flips are observed within 100ps giving an averaged time scale of ~5ps. It is noteworthy that this value is supposed to be higher than the real because some flips might be missing between two consecutive frames. Furthermore, the life time of each state differs from each other. For instance, the two orientations A and B indicated by shadows possess longer life time demonstrating that the tetrahedron has preferred orientations.

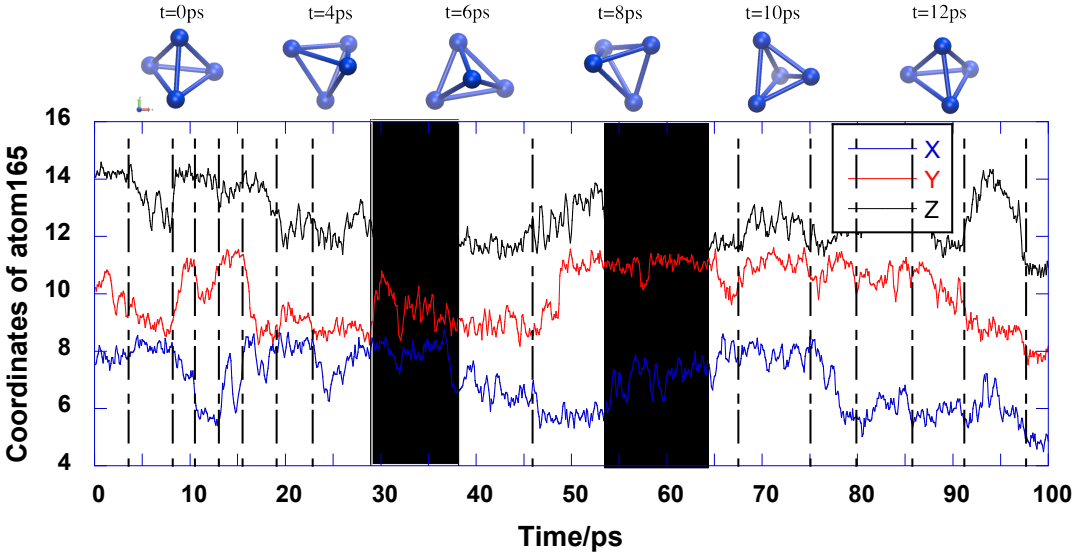

Figure 6.1.7 Follow-up of the innermost tetrahedron with respect to time. The chart displays coordinates of one of the tetrahedron atoms, and the lines indicate the tetrahedron 'jumping'.

The dodecahedron shell is composed of two crystallographic sites, the 3-fold axes of the cubic lattice 16f, and the 3-fold axes of the Sc_{12} icosahedron shell 24g. There are 8 and 12 atoms on each of the site respectively. Hereafter we defined the second type 3-fold axes as pseudo 3-fold axes which will be used for labeling the orientations of the central tetrahedra. The 12 dodecahedron Zn atoms located on pseudo 3-fold sites comprise a defective icosahedron as shown in Figure 6.1.8. To define the tetrahedron orientations, we first normalize the four vectors of the tetrahedron to one of the 12 icosahedral vectors by applying scalar products. The 12 icosahedral vectors are listed in Table 6.2. Then we obtain 4 icosahedral vectors and the sum of two, so called 'unhappy' vectors, is larger than the other two. For instance, $\boldsymbol{v}_1$, $\boldsymbol{v}_4$, $\boldsymbol{v}_5$, $\boldsymbol{v}_8$ constitute a tetrahedron in which $\boldsymbol{v}_1+\boldsymbol{v}_4$ is larger than $\boldsymbol{v}_5+\boldsymbol{v}_8$. The sum of the two 'unhappy' vectors indicates a 2-fold axes which is finally used to label the orientation of each tetrahedron. There are 30 edges in an icosahedron, meaning that the orientations are classified into 30 labels. The vectors of 30 2-fold axis are listed in Table 6.3. The graphics of the six orientations whose labeling 2-fold vectors are parallel to the cubic axis are presented in Figures 6.1.9.

Table 6.2 Icosahedral vectors of the 12 dodecahedron Zn atoms on 24g site.

Vector ID	Vector	Vector ID	Vector	Vector ID	Vector
1	1 0 τ	5	0 τ -1	9	-τ -1 0
2	0 τ 1	6	τ -1 0	10	1 0 -τ
3	τ 1 0	7	-1 0 - τ	11	0 -τ 1
4	-1 0 τ	8	0 -τ -1	12	-τ 1 0

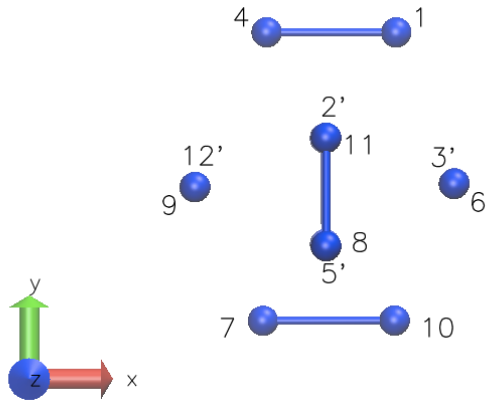

Figure 6.1.8 Icosahedral vectors viewing along $[00\bar{1}]$, *n*' denotes the vector on the back. Six of the thirty orientations are defined by the six 2-fold vectors parallel to the axis: $\boldsymbol{O}_1=\boldsymbol{v}_3+\boldsymbol{v}_6$; $\boldsymbol{O}_2=\boldsymbol{v}_2+\boldsymbol{v}_5$; $\boldsymbol{O}_3=\boldsymbol{v}_1+\boldsymbol{v}_4$; $\boldsymbol{O}_4=\boldsymbol{v}_9+\boldsymbol{v}_{12}$; $\boldsymbol{O}_5=\boldsymbol{v}_8+\boldsymbol{v}_{11}$; $\boldsymbol{O}_6=\boldsymbol{v}_7+\boldsymbol{v}_{10}$.

As we denoted above, when we dump trajectories in a large time scale some flips of tetrahedron would be missing. To obtain the average flipping frequency of one tetrahedron with proper accuracy, we performed a new calculation with a time scale 0.01ps and 2000 frames were dumped at each temperature over a cooling process from 400K to 60K.

Table 6.3 Twofold vectors of the 30 regular orientations defined based on the icosahedron edges.

Vector ID	Vector	Vector ID	Vector	Vector ID	Vector
1	1 0 0	11	0.5 0.809 0.309	21	-0.5 0.809 -0.309
2	0 1 0	12	-0.309 0.5 0.809	22	0.5 -0.809 -0.309
3	0 0 1	13	-0.5 0.809 0.309	23	0.809 -0.309 -0.5
4	-1 0 0	14	0.5 0.809 -0.309	24	0.5 -0.809 0.309
5	0 -1 0	15	0.809 0.309 -0.5	25	-0.309 -0.5 -0.809
6	0 0 -1	16	-0.809 -0.309 0.5	26	-0.809 -0.309 -0.5
7	0.309 0.5 0.809	17	-0.309 -0.5 0.809	27	-0.809 0.309 -0.5
8	0.809 0.309 0.5	18	-0.809 0.309 0.5	28	-0.5 -0.809 -0.309
9	0.809 -0.309 0.5	19	-0.309 0.5 -0.809	29	0.309 -0.5 -0.809
10	0.309 -0.5 0.809	20	0.309 0.5 -0.809	30	-0.5 -0.809 0.309

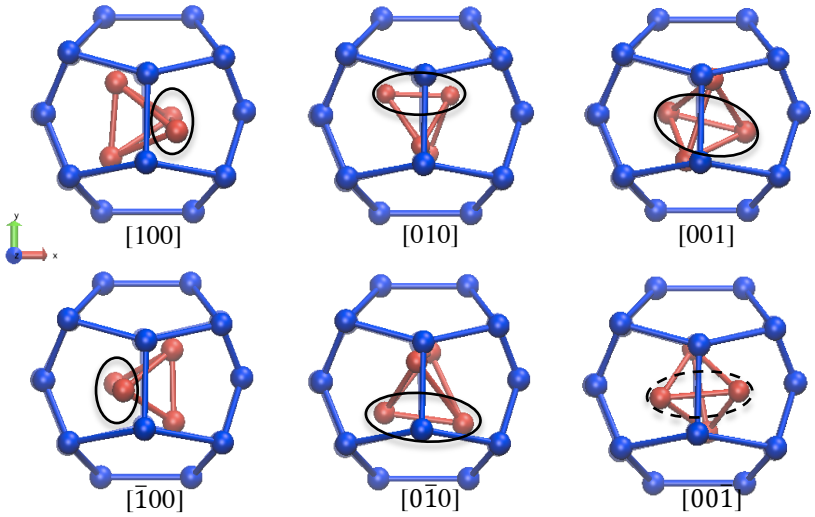

Figure 6.1.9 Definition of the six orientations of the tetrahedron referring to the dodecahedron, extracted from simulations. The blue and red spheres indicate dodecahedron and tetrahedron atoms respectively. The 'unhappy atoms' are indicated by open ellipses.

Firstly we calculated the orientations of all tetrahedra in all configurations. It is noteworthy that as we will depict in the next section, the tetrahedron atoms keep exchanging with the dodecahedron atoms, so in some possibilities, e.g. one tetrahedron atom moving out but the dodecahedron atom has not moved in yet, we could capture only a 'triangle' of the tetrahedron. Nevertheless, these 'bad' tetrahedra are observed only when temperature is higher than 200K, and for 400K the possibility is ~1.3% which is negligible. The second phenomenon impacting the accuracy of flipping frequency is the deformed tetrahedra, i.e. the intermediate states between the 30 regular orientations. Analysis manifests that the number of these intermediate states decreases rapidly with a decreasing temperature. Whereas, similar with the 'bad' tetrahedra, the deformed tetrahedra have a small proportion in all states, i.e. less than 5% even for 400K.

The average flipping frequency of an individual tetrahedron decreases with decreasing temperatures following the Arrhenius law perfectly as shown in Figure 6.1.10. It gives an activation energy equal to 34meV which is of the same order of Euchner's result from both experiments and simulation, i.e. 60meV[81]. The impact of the intermediate orientations is supposed responsible to the loss of the calculated activation energy. Moreover, the frequency at 300K is 1.94ps^{-1}, meaning a time scale of 0.52 ps which is compatible with the experiment data.

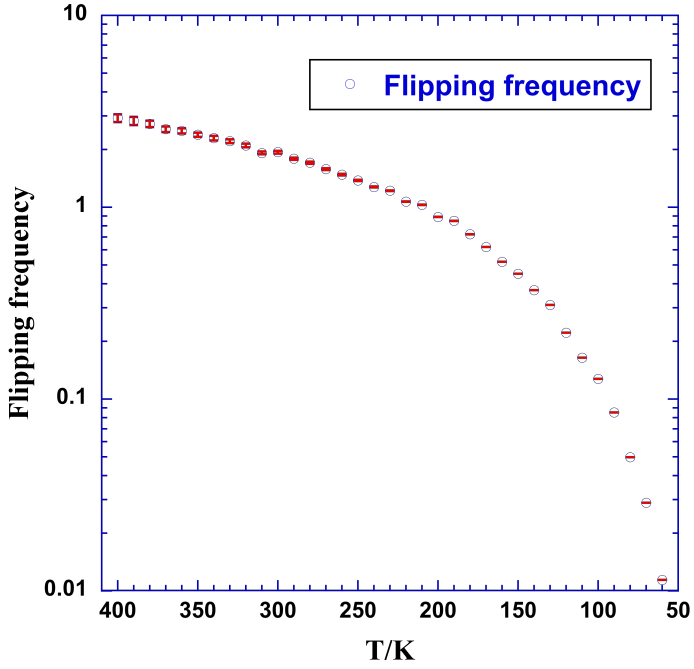

Figure 6.1.10 Temperature dependence of the average flipping frequency of individual tetrahedron on an Arrhenius plot. The R value indicates the fitting rate. Error bars give the proportion of deformed tetrahedra.

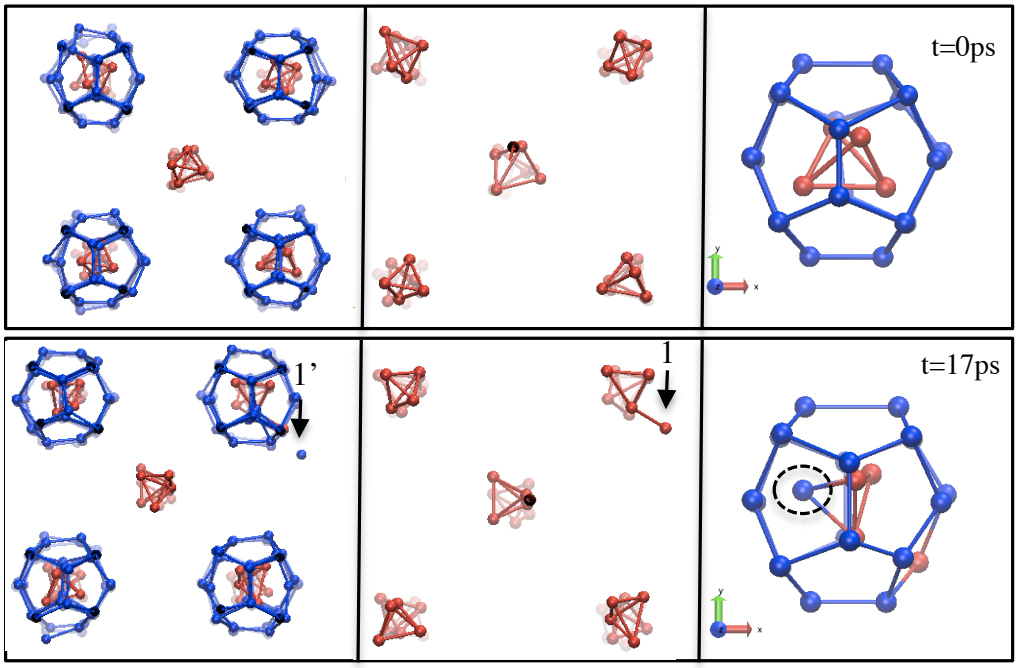

Figure 6.1.11 Illustration of the atomic diffusion, the blue and red spheres indicate dodecahedron and tetrahedron atoms respectively. The initial configuration (top) shows regularly positional occupation, however, after 17ps (bottom), one tetrahedron atom diffused and occupied a dodecahedron site, as indicated by the arrow 1. In the meanwhile, the relevant dodecahedron atom diffused simultaneously as denoted by the arrow 1'. To keep the system stable, the diffusing tetrahedron atom was supplemented by another dodecahedron atom, as shown in the rightbottom figure.

6.1.3 Atomic diffusion

It is found that the tetrahedron atoms have moved a lot from their original positions after a period of simulation time, which is implausible in real structures. Further investigation indicates that besides tetrahedron jumping, most tetrahedron atoms are involved in an atomic diffusion. The directions of the atomic diffusion for 1/1 approximant are confirmed along the space diagonal of the unit cell.

Figures 6.1.11 illustrate the occurrence of the atomic diffusion, i.e. atoms exchange between tetrahedron and dodecahedron shells. In the beginning of the simulation, the tetrahedron and dodecahedron clusters are well defined (top figures). After 17ps, one of the dodecahedron atom moved out of the dodecahedron shell. If we look into the inner tetrahedra, the movement of the relevant tetrahedron atom is actually responsible for this diffusion. Indeed, to keep the system stable, once one tetrahedron atom moving out, one dodecahedron atom will move in to complement the vacancy as displayed in the right panel of Figures 6.1.11. As a consequence, more and more atoms are involved in this atomic diffusion.

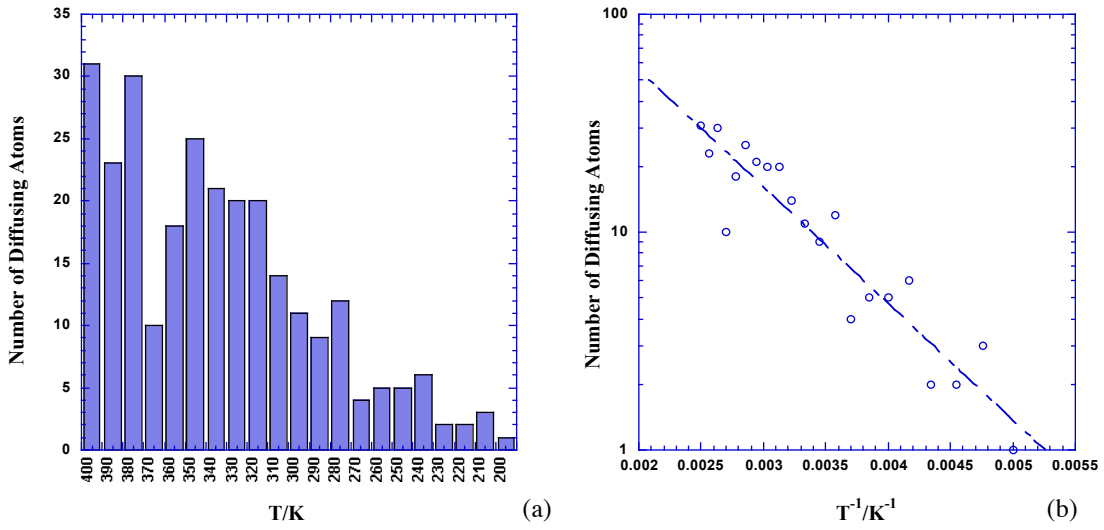

Figure 6.1.12 (a) The number of diffusing atoms varying with respect to T; (b) Arrhenius plot of the number of diffusing atoms, R factor indicates the fitting rate.

Figure 6.1.12 (a) displays the number of diffusing atoms with respect to temperatures. The atomic diffusion is suppressed at 200K. The variation of diffusing atoms follows the Arrhenius law roughly as shown in Figure 6.1.12 (b). It gives an activation energy equal to 106±11meV. This result is generated from the short simulations, therefore only a small number of diffusing atoms are available for statistics which leads to a relatively big deviation in the fitting.

To figure out the direction of the atomic diffusion, we extracted the coordinates of original tetrahedron atom 5206 which possesses the largest displacement throughout the whole cooling process. The trajectory of atom 5206 is displayed in Figures 6.1.13. Consecutive stages of the coordinates are clearly observed. Altogether, 8 sites are indicated in the figure.

Details of the 7 diffusing processes are listed in Table 6.4. Furthermore, whenever the atom moves Δx in x axis it moves $-\Delta x$ in y and z axis, suggesting the atom diffuses along $[1\bar{1}\bar{1}]$ direction. Study to all tetrahedron atoms demonstrates that the atomic diffusion takes place on almost all dodecahedron sites, however, distant diffusion can only happen along the space diagonal directions of the unit cell as presented in Figures 6.1.14. It is noteworthy that the 'short-range' diffusion occurs only to center clusters (or vertex clusters).

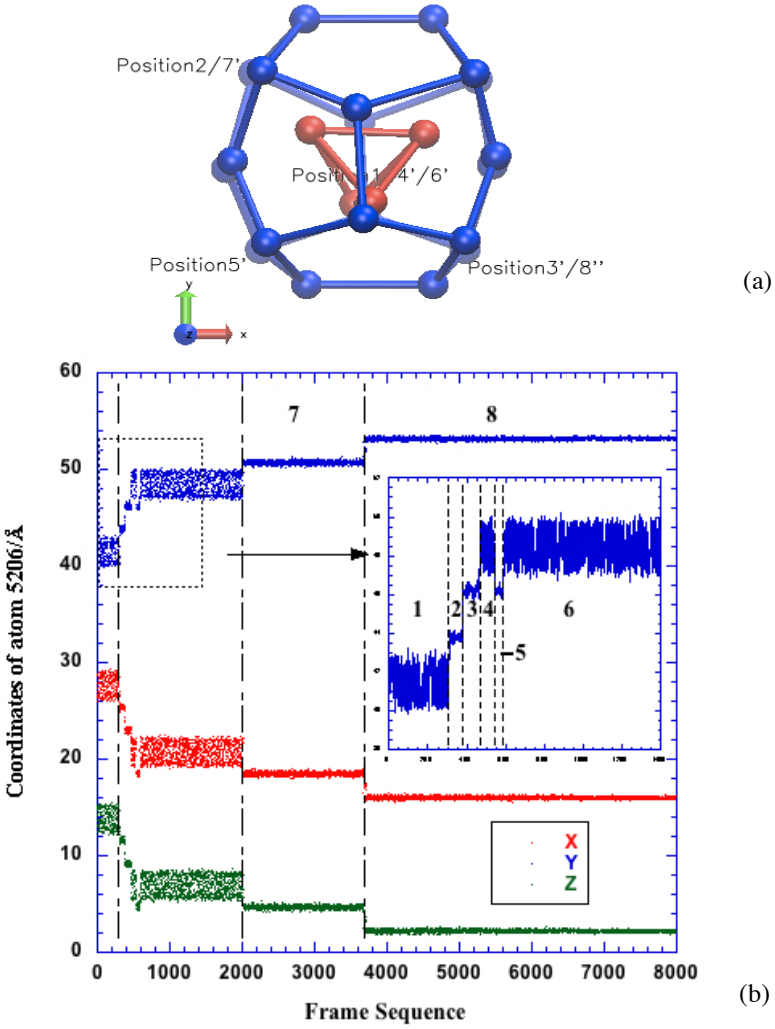

Figure 6.1.13 (a) Variation of coordinates of atom 5206 in the whole cooling process, each stage corresponds one diffusing process; (b) All 8 positions of atom 5206 during the whole simulation. Positions 1, 4' and 6' stand for tetrahedron sites, and positions 2, 3', 5', 7' and 8'' are equivalent dodecahedron sites. From position 2 to 3', the atom 5206 moves to a second dodecahedron shell. Position 8'' is located at the third dodecahedron shell.

Table 6.4 The information of atom 5206 from the 1st to the 7th diffusing processes.

The i^{th} Diffusion	Cluster center	T/K	Life time at the position/ps	Diffusing distance/Å
1	(1/2 3/4 1/4)	480	10	3.11
2	(1/2 3/4 1/4)	480	40	4.78

3	(3/8 7/8 1/8)	470	10	3.11
4	(3/8 7/8 1/8)	470	10	3.11
5	(3/8 7/8 1/8)	470	10	3.11
6	(3/8 7/8 1/8)	390	15	3.11
7	(1/4 1 0)	310	15	4.78

The 8 individual positions for atom 5206 are illustrated in Figure 6.1.13 (b) where positions *n*' stand for the equivalent positions on the second dodecahedron shell and *n*'' corresponds to the third shell. The average diffusing distance is confirmed as ~3.6Å. These results are in good agreement with the deduction of Goddens *et al*[123] who concluded a hopping process in the *i*-AlPdMn phase mainly occurring along 3-fold axes over a distance of 3.8Å from experiments.

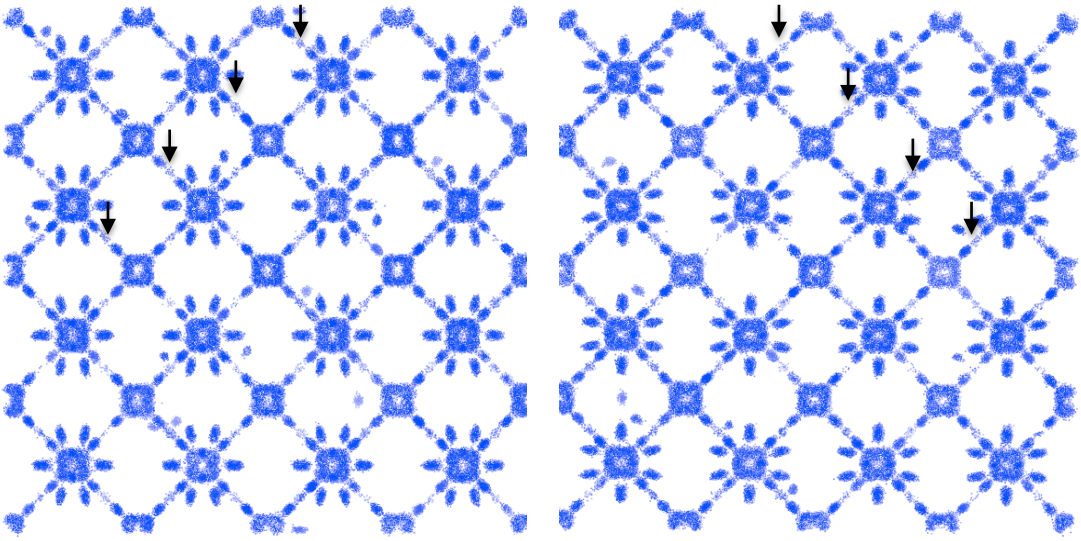

Figure 6.1.14 Trajectories of all original tetrahedron atoms at 500K. The left is graphic viewing along z axis, and the right is along x axis. Arrows indicate the additional positions inbetween two dodecahedron sites, which have been observed experimentally.

For the sake of better visualization, we extracted all positions of atom 5206 and atom 8723 which are original tetrahedron and dodecahedron atoms respectively. The trajectories of the two atoms referring to the supercell boundaries are shown in Figures 6.1.15. Intuitively, the two atoms diffuse along $[1\bar{1}\bar{1}]$ and $[11\bar{1}]$ respectively. Furthermore, besides the 8 positions depicted above, there are two additional positions which are crystallographically forbidden as indicated by arrows. These additional positions can be found all over the supercell as arrowed in Figures 6.1.14.

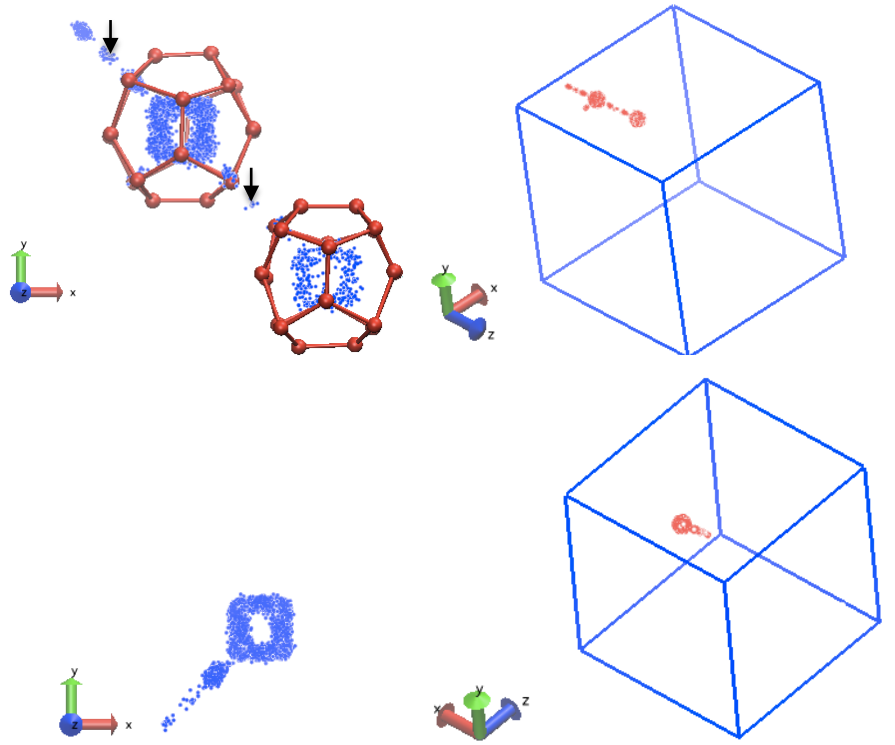

(a)

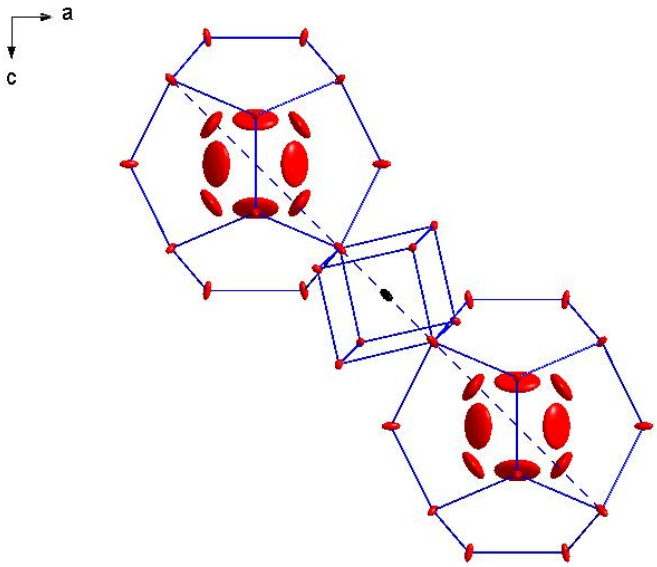

(b)

Figure 6.1.15 Blue small spheres demonstrate the trajectories of atom 5206 (top) and 8723 (bottom) at 500K, referring to the dodecahedron shell (larger red atoms). The blue cubes define the boundaries of the 4x4x4 supercell, inside red small spheres present the trajectories of atom 5206 (top) and 8723 (bottom) diffusing along $[1\bar{1}\bar{1}]$ and $[11\bar{1}]$ respectively. The two intermediate positions are indicated by arrows. The right graphic displays the two dodecahedron clusters connected by a Zn_8 cube, the additional intermediate position inside the cube is denoted by the black ellipsoid, and the dashed line indicates the diffusing direction along [111].

Analogical phenomenon was observed as well on these intermediate sites in experiments as illustrated in Figures 6.1.16 (refer to Gómez and Lidin[4]). The site of Cd4 represents the sharing atom of the Cd_8 cubes with the Cd_{20} dodecahedra as illustrated in Figure 6.1.15 (b). In our labels above it corresponds to positions 2 and 7'.

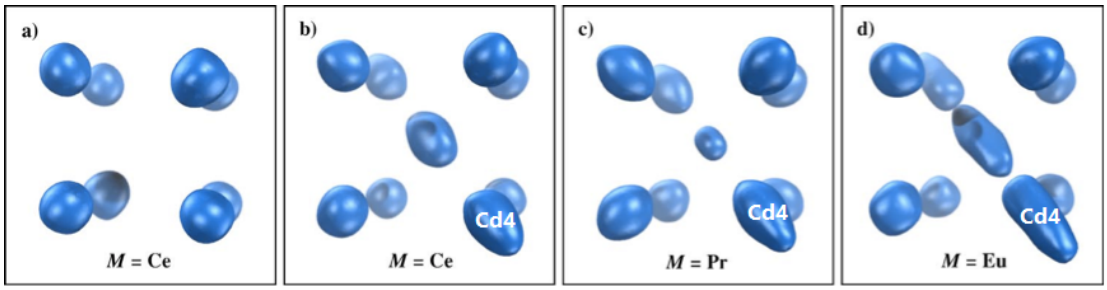

Figure 6.1.16 Electron density of the Cd_8 cubes on isosurfaces 10-*e*V/Å3. (a) and (b) The symmetry-independent vacant and fully occupied cubes, respectively, of the compound Ce_6Cd_{37}. (c) The appearance of the symmetry-equivalent cubes in the compound $Pr_3Cd_{18.18}$. (d) The appearance of the cubes in the compound Eu_3Cd_{19}. Additional occupancy and elongation along the space diagonal of the cube is visible in Ce_6Cd_{37}, $Pr_3Cd_{18.18}$, and Eu_3Cd_{19}. (Fig. 5 in [4])

In experiments, the elongations of Cd4 which propagates along [111] direction in the Fourier map are supposed to occur only when there is an additional atom inside the Cd_8 cubes. The additional atom, driving stoichiometry from 1:6 to 1:6.17 and 1:6.06 for Cd_6Ce and Cd_6Pr respectively, is also previously considered one of the reasons leading to the distortion of the Cd_{20} dodecahedra and the adjacent Cd_4 tetrahedra[4]. The other reason is the well-known dynamical reorientation of the innermost tetrahedra as we depicted above. However, according to our simulations, the additional occupancy is most likely from the atomic diffusion. As a consequence the stoichiometry should be exactly 1:6. In addition, the simulation results interpret as well why the elongations take place in only one direction of the Cd_8 cubes, i.e. [111]. Because, as we discussed above, the long-range diffusion of Cd/Zn atoms can only take place along the space diagonal tunnel.

To investigate the origin of the atomic diffusion, we computed the velocity, the force, the potential energy and the kinetic energy of the atom 4357 as demonstrated in Figures 6.1.17 (a-d) respectively. According to the coordinates evolution, the atom 4357 jumps from a dodecahedron site to a tetrahedron site at a specific moment along the $[\bar{1}\bar{1}1]$ direction. Through the whole process, the velocity and force fluctuate around zero, i.e. the atom vibrate around the equilibrated point, and no anomaly is observed. However, the atomic potential energy on the dodecahedron site is clearly lower than that on the tetrahedron site suggesting an energy gap between the two sites.

Furthermore, the order of the energy gap between the two sites, which is ~0.1eV as shown in Figure 6.1.17 (b), is well compatible with the calculated activation energy above, i.e. 106±11meV. As a consequence, the impetus of the atomic diffusion most likely lies in the potential energy difference between tetrahedron and dodecahedron sites. When the tetrahedron atoms move inside the dodecahedron cavity, they possess a tendency of diffusing

from higher potential energetic site to a relaxed lower site. After the diffusing, the vacancies promote the continuation of the atomic diffusion.

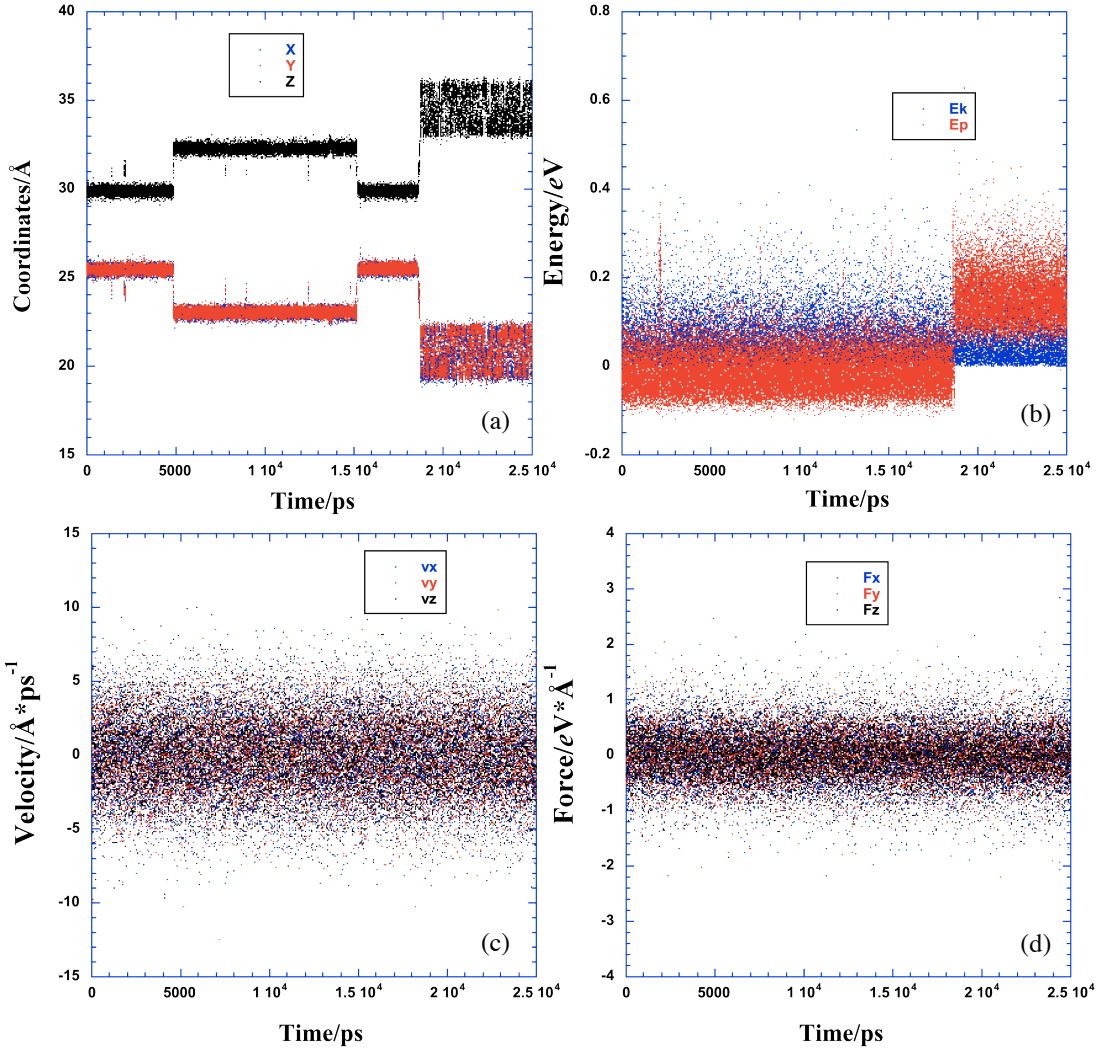

Figure 6.1.17 (a) Time dependence of the coordinates of the atom 4357; (b) Time dependence of the potential and kinetic energy of the atom 4357; (c) Time dependence of the velocities along three axis of the atom 4357; (d) Time dependence of the forces along three axis of the atom 4357.

6.1.4 Conclusion

We performed MD simulation on the Zn_6Sc 1/1 approximant in a cooling process, using pair potential fitted against *ab-initio* database. A detailed comparison with experiment results of Zn_6Sc and Cd_6M (M=Ce, Pr and Eu) is presented. The diffraction pattern is reconstructed on both *l*=0 and *l*=half-integer layers via FT. The diffuse scattering turns ordered as the temperature decreases which results from the ordering of the tetrahedra. The s.r.o along $<1\bar{1}0>$ directions is observed which is the indicative of a pre-phase transition.

The innermost tetrahedra is observed reorienting dynamically. The reorientation is slowed down as temperatures decrease and finally frozen on a specific state. The flipping frequency

follows Arrhenius rule and the energy barrier is determined as 34meV which is of the same order as that from experiment, i.e. 60meV.

The atomic diffusion along the space diagonals of the cubic cell is investigated in details. The activation energy of the atomic diffusion is confirmed as 106±11m*e*V, and it is almost suppressed below 200K. Furthermore, the atomic diffusion interpret well the additional occupancy in the center of the Cd_8/Zn_8 cubes, as well as the elongations of the sharing atoms of the Cd_8/Zn_8 cubes with the Cd_{20}/Zn_{20} dodecahedra observed in experiments.

The happening of the atomic diffusion is supposed to be related with the potential energy difference between the tetrahedron and dodecahedron sites. The tetrahedron atoms tend to diffuse to the lower energetic dodecahedron sites.

6.2 Model of the 5/3 approximant

High order approximants have never been observed experimetally. In the CdYb type quasicrystals, the largest observed approximant is the 2/1 cubic one. We have thus used large periodic approximant (5/3 and 8/5) to simulate the quasicrystal. The obtained 5/3 approximant possesses a unit cell size up to ~58.46Å and contains more than 10000 atoms per unit cell which makes it hard to experimentally determine the detailed structure of the 5/3 approximant. As for our MD simulations, the modeling structure is accomplished by placing the rhombic triacontahedron clusters on the vertices of the 5/3 approximant model achieved by canonical cell tiling, followed by a decorating procedure[24][25]. The final configuration was optimized by performing a total energy minimization process via *ab-initio* calculations using the DFT program VASP[26][27]. The details of the model determination are depicted in[24].

The finally adopted 5/3 approximant contains 136 rhombic triacontahedron units and 12744 atoms per unit cell with a cell parameter equal to 58.456Å. According to the configurations of local environments, the 136 clusters are classified into 5 groups: 5-7, 6-6, 6-7, 7-5 and 7-6, where *n* in *n-m* presents the number of 2-fold linkages around, and *m* stands for the number of 3-fold linkages[124]. The stoichiometry is about $Zn_{85.12}Sc_{14.88}$, i.e. 10848 Zn atoms and 1896 Sc atoms per unit cell.

6.2.1 Diffuse scattering of the 5/3 approximant

The 5/3 approximant was first equilibrated at 500K followed by a cooling process from 500K to 100K with a temperature step of -10K. At each temperature, 2 millions steps were performed and 400 configurations were extracted for analysis. The time step for each temperature is listed in Table 6.5. Only one single unit cell was adopted without periodic boundaries. Accordingly, in some extent, the single unit of 5/3 approximant can be viewed as QC.

Diffraction pattern on the *hk*0 Bragg plane was reconstructed by performing FT to every configuration and summing up the 400 frames at each temperature. The resulting pattern at 300K is compared with the experiment data of *i*-ZnMgSc quasicrystal as illustrated in Figure

6.2.1. The 5/3 approximant has shown a very good approximation of the QC. Both strong and weak reflections agree well with the quasicrystal up to high Q value.

Table 6.6 Time step setting for each temperature of 5/3 approximant

T/K	500-400	390-300	290-200	190	180	170	160	150
Time step/ps	0.001	0.0015	0.002	0.0025	0.003	0.004	0.005	0.006
T/K	140	130	120	110	100	90	80	
Time step/ps	0.007	0.008	0.009	0.01	0.02	0.03	0.04	

The results are compared as well with the 1/1 approximant as illustrated in Figures 6.2.2. The range of intensities are normalized to make a better comparison. The Bragg planes of 5/3 approximant display well-defined 5-fold and 2-fold axis as indicated by arrows. The pseudoicosahedral symmetry is demonstrated on the 1/1 approximant as well. To be better compared, the 5/3 approximant is expressed in the same indexing setting as the 1/1. Due to the difference of cell parameters, the strong 2-fold reflection in the 5/3 approximant, corresponding to the (6 0 0) in the 1/1 approximant, shifts rightward slightly. Furthermore, there are more Bragg reflections visible in the 5/3 approximant than in the 1/1. The related indices of the strong 2-fold and 5-fold Bragg reflections in the quasicrystal are displayed in the 5/3 approximant map, which is expressed as *N* and *M* indices[55].

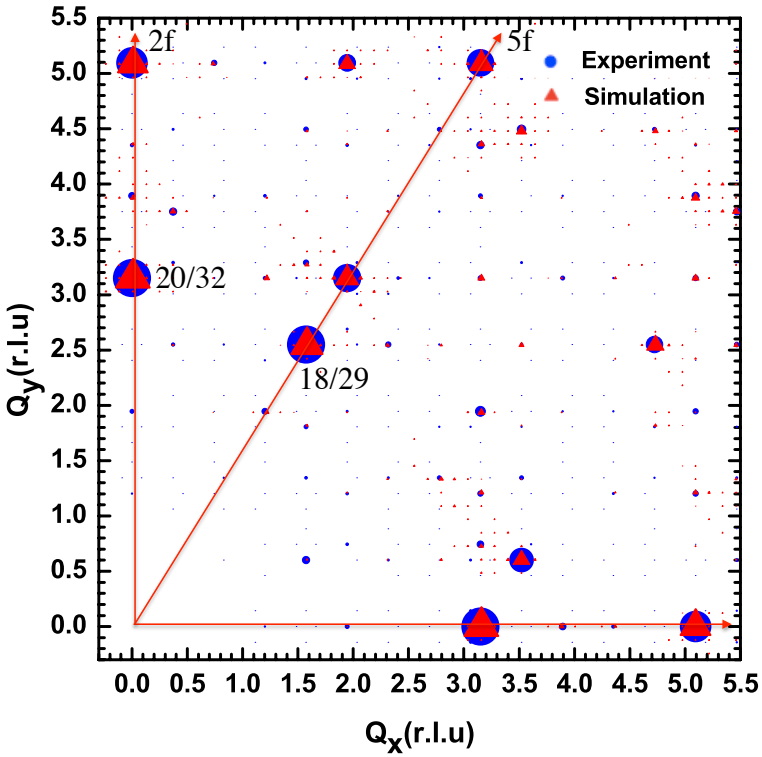

Figure 6.2.1 Diffraction pattern reconstructed on *hk*0 layer compared between experiment (blue circle) and simulation (red triangle) at RT. The surface of mark is proportional to the sqrt(I).

There are remarkable differences between the two approximants at all temperatures. For the 1/1 approximant, the shape of the diffuse scattering is identical around each reflection, i.e. the intensity distribution elongates along the direction transverse to the ***Q*** vector which reproduces well the experimental results[60]. Whereas, it is more complicated for the 5/3 approximant. The shape of diffuse scattering is dependent on reflections. Apart from that, as temperature decreases, the diffuse scattering difference between the two approximants becomes more obvious. The background diffuse scatterings in both phases contributed by thermal motions disappear gradually with decreasing temperatures. As discussed above, the diffuse scattering of the 1/1 approximant displays mostly along <110> directions at LT which reveals an ordering structure in the LT phase. In the case of the 5/3 approximant, however, the shape of most reflections are constant with respect to the temperatures.

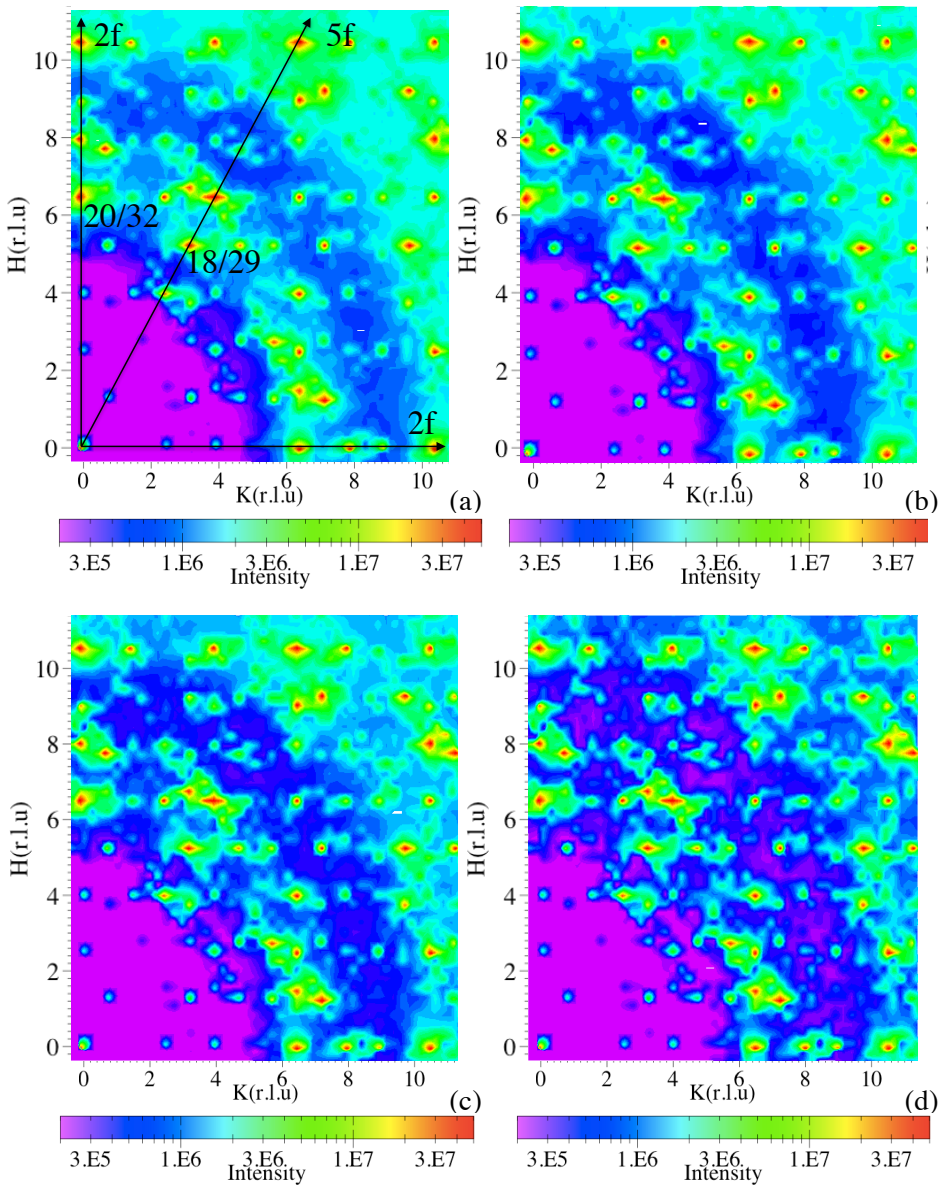

Figure 6.2.2 Fourier maps on *hk*0 Bragg planes of 5/3 (top) and 1/1 (bottom) approximants calculated from MD simulation. From the (a) to the (d), T equal 400K, 300K, 200K, 100K, respectively.

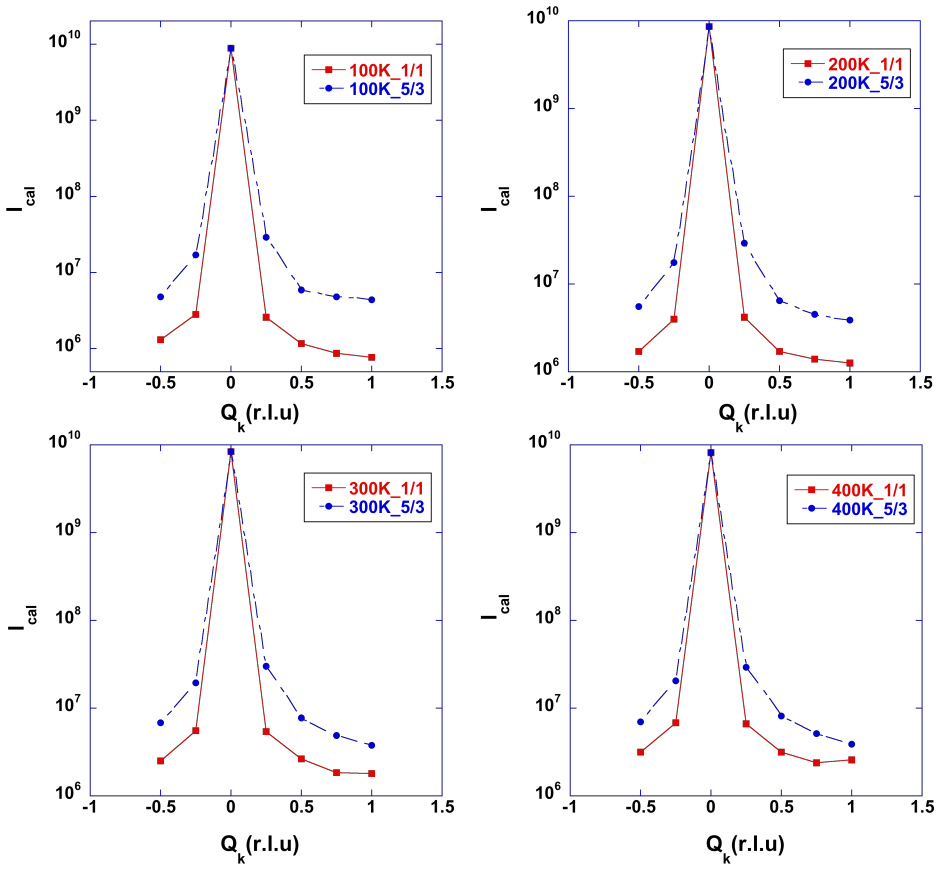

(a)

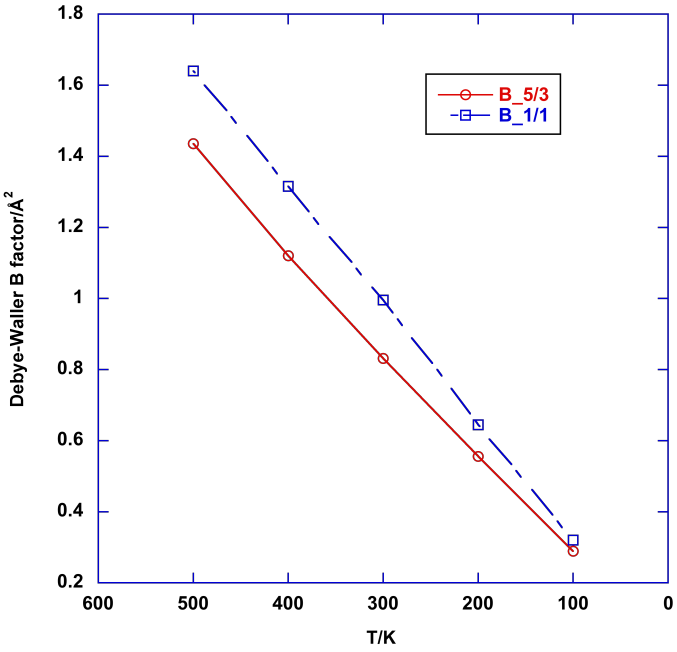

(b)

Figure 6.2.3 (a) Comparison of the diffuse scattering for the (6 0 0) reflection in the two approximants at different temperatures, the intensities of the 1/1 approximant have been normalized; (b) The temperature dependence of the integrated intensities in the two approximants.

A quantitative comparison has been made between the two approximants. A slice through the selected 2-fold reflection (6 0 0) along k direction is carried out on both phases at different temperatures as illustrated in Figures 6.2.3 (a). The phason diffuse scattering can be characterized in three aspects[61]: (i) the diffuse scattering decays as a function of $1/q^2$; (ii) the intensity is proportional to the $\boldsymbol{Q}_{perp}$; (iii) the shape anisotropy can be reproduced using the phason elastic constants. The phason elastic constants can be experimentally derived using the data from absolute scale measurements. Whereas in our simulations, the step size of the Bragg planes is 0.25Å^{-1} which is more than 10 times larger than that in experiments, meaning that there are no enough points to make an accurate analysis.

Nevertheless, in Figures 6.2.3 (a), the 5/3 approximant shows clearly broader peaks with excess intensities comparing with the 1/1 approximant at all temperatures which was confirmed as phason diffuse scattering in experiments[60]. The temperature dependence of the Debye-Waller B factors (DWBF) is calculated on reflection (10 0 0) on the two phases as shown in Figure 6.2.3 (b). Generally, the 1/1 approximant possesses larger displacements than the 5/3 approximant. As the tetrahedra are frozen at LT, the difference of B factors between the two approximants diminishes. This implies that the larger B factor difference most likely comes from the contribution of the central tetrahedra. The higher complexity of 5/3 approximant structure is supposed suppressing the atomic displacement.

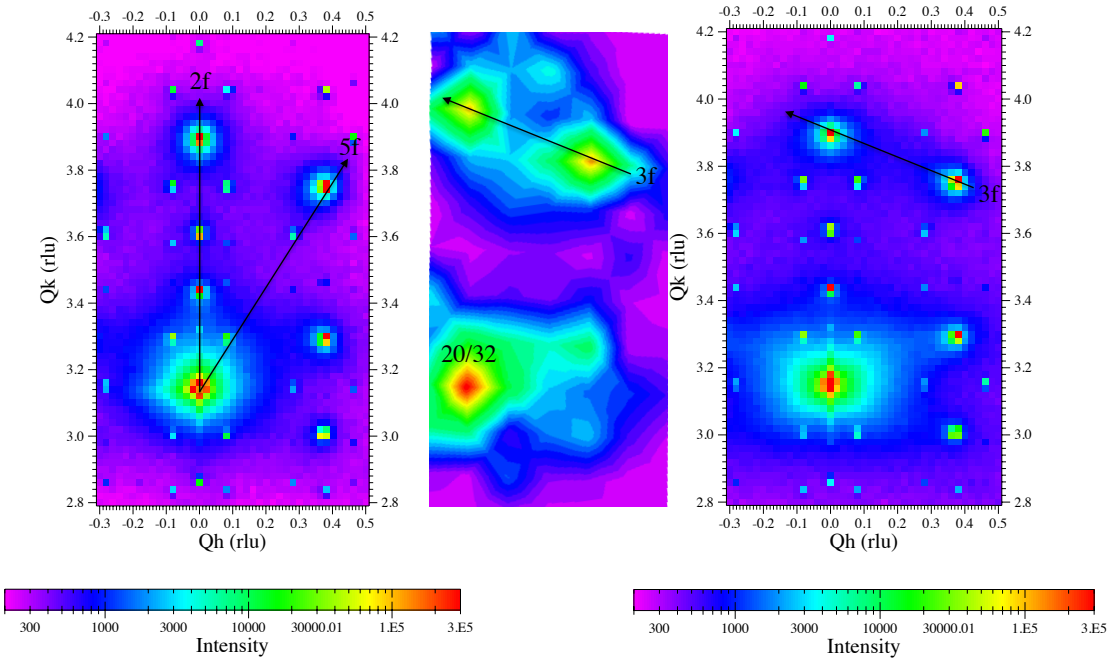

Figure 6.2.4 Diffuse scattering maps around the 2-fold reflection 20/32 at the same magnification for the AgInYb quasicrystal at RT (left) and 350℃ (right) and the ZnSc 5/3 approximant result from MD simulation (middle). Coordinates are expressed in $2\pi/a_{6D}$ and $2\pi/a$ units for quasicrystal and approximant respectively.

The diffuse scattering around reflection 20/32 of the 5/3 approximant at 300K is magnified to compare with the experiment results of the AgInYb quasicrystal. The diffuse scattering of AgInYb quasicrystal displays two types of distribution: one is along 5-fold axis at RT and the

other is along 3-fold axis at 350℃ as illustrated in Figures 6.2.4. As to the ZnSc 5/3 approximant, it shows a tendency of 3-fold distribution at RT. However, this result is not accurate enough due to the low resolution of the diffuse scattering map. Further improvement is certainly desirable for more accurate analysis.

The longitudinal and transverse slices crossing the (8 0 0) reflection are carried out and illustrated in Figures 6.2.5 (a) and (b) respectively. The (8 0 0) reflection, i.e. 32/48 for the quasicrystal indices, shows distinctly larger relative excess diffuse scattering comparing with the (6 0 0), i.e. 20/32 for the quasicrystal indices. This result is consistent with the experiments[60]. Furthermore, as it is aforementioned, the shape anisotropy of the diffuse scattering in the 1/1 approximant elongates transversely to the ***Q*** vector which is displayed in Figure 6.2.5 (c). The situation is quite different in the 5/3 as shown in Figure 6.2.5 (d), where the reflection has a shape anisotropy of the diffuse scattering elongated to the two weak peaks which are absent in the 1/1 AC.

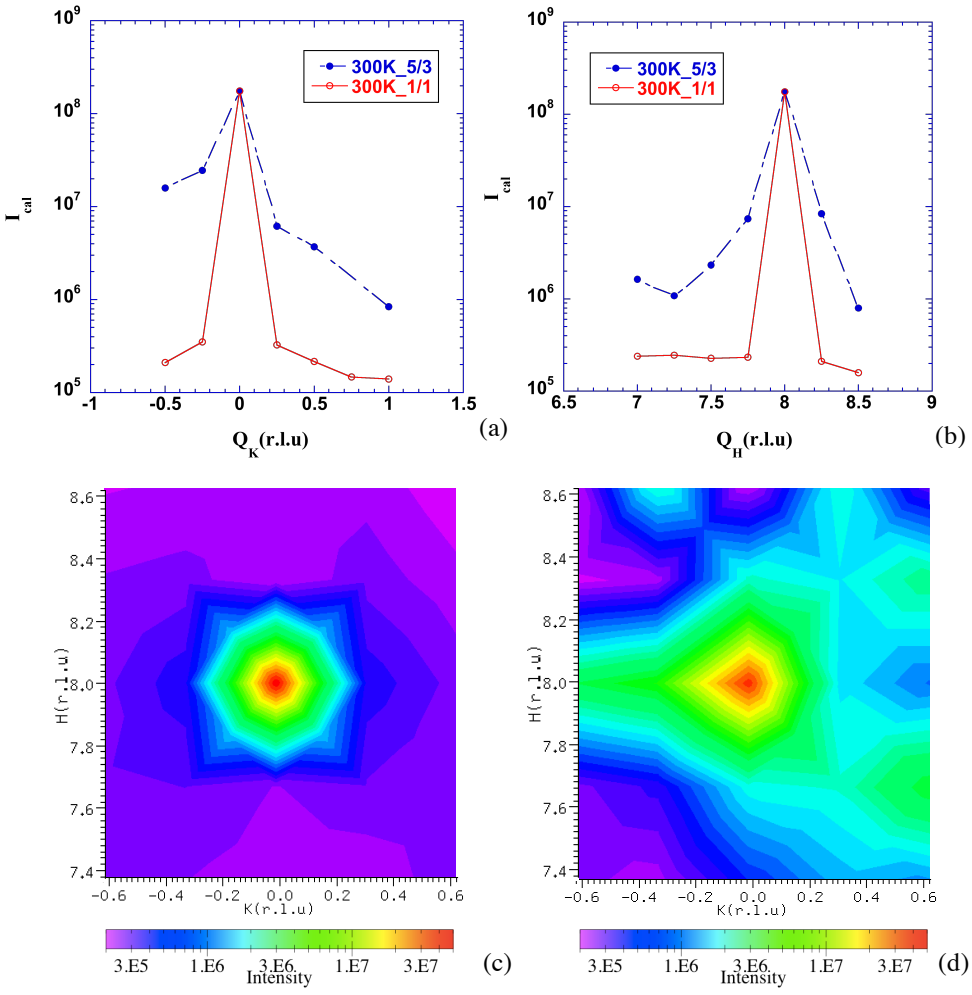

Figure 6.2.5 Longitudinal (left) and transverse (right) slices of the reflection (10 0 0) in the two approximants at 300K. The intensities of the 1/1 approximant have been normalized for comparison.

6.2.2 Tetrahedron dynamics in the 5/3 approximant

Similarly with the 1/1 approximant, the innermost tetrahedra in the 5/3 approximant are dynamically jumping among all possible orientations. To figure out the model of the central tetrahedra, we extracted the trajectories of the tetrahedron Zn atoms and visualized the charge density distribution as shown in Figures 6.2.6. The tetrahedron is collected over a timescale of 2.5 nanoseconds and 0.5 million frames are superimposed for charge density calculation. The visualization is carried out via the program VESTA under isosurfaces level of 1.5e-4e/Å^3 .

As illustrated, the tetrahedron model in 5/3 approximant is completely different from that in the 1/1 approximant. Three tracks are observed forming a local 3-fold axis. The directions of the 3-fold axis are supposed to be closely related to the local environments of relevant tetrahedra. In addition, this result also suggests that new definition of the tetrahedron orientations is in need.

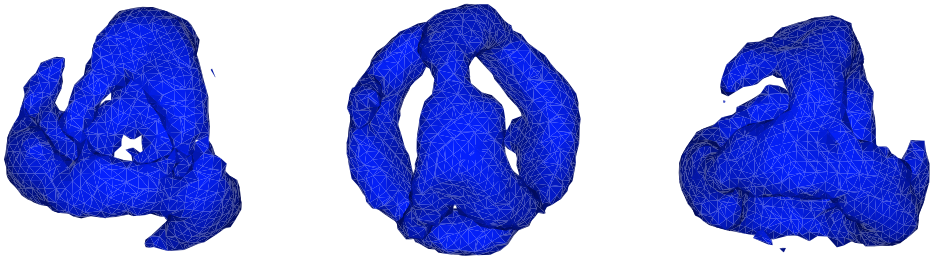

Figure 6.2.6 Charge density distribution of the central tetrahedron in the 5/3 approximant at 500K. A local defined 3-fold axis is distinct.

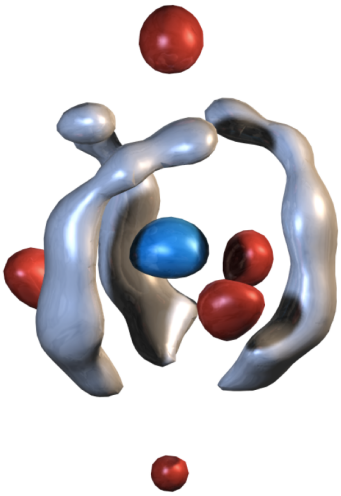

Figure 6.2.7 Electron density iso-surface at the 11.3 eÅ-3 level, in the location of the dodecahedral cavity of $Yb_{13}Cd_{76}$. The densities marked in red form a trigonal bipyramid, the central density is marked in blue (from [52]).

A new simulation was designed to study the tetrahedron flipping quantitatively. Configurations were dumped every 5fs and 10000 configurations were collected. The result shows four maximums, forming a regular tetrahedron as illustrated in Figures 6.2.8 (a) where each color represents one atom. The coordinates evolution of the four atoms with respect to time are plotted in Figures 6.2.8 (b). Each flip is indicated by a dashed line, and 7 flips are observed within 50 ps suggesting the time scale of flipping for tetrahedra in 5/3 approximant is about 7.2 ps at 500K. This value is much larger than that of the 1/1 approximant, i.e. 0.5 ps calculated with the same time step. Moreover, the atom 3666, i.e. the blue one in Figures 6.2.8 (a), stays at the same position much longer than the other three. Considering the complexity of the 5/3 approximant structure, the interaction between central tetrahedra and their local environments is supposed to be more complicated. As a consequence, the central Zn atoms are applied more restrictions which lead to a much smaller flipping frequency. The characteristic jumping distance is of the order of 2.5Å, i.e. about twice of that in the 1/1 approximant. It is worth noting that the studied cluster here only corresponds to one local environment. The complexity is also related to different environment of the clusters (2-fold and 3-fold linkages).

6.2.3 Atomic diffusion in the 5/3 approximant

The number of diffusing atoms with respect to temperatures is shown in Figure 6.2.9. Comparing with the 1/1 approximant, this atomic diffusion is suppressed at 410K for 5/3 approximant, implying a higher energy barrier compared with the 1/1 AC. Additionally, only less than 50 atoms out of 12744 were involved in diffusing at HT within 5nanoseconds.

Atom 12737 was tracked over the cooling process from 500K to 90K. The variation of coordinates and trajectory are presented in Figures 6.2.10. Other than the 1/1 approximant, the diffusing direction of 5/3 is more complicated. One point to emphasize is the setting of the time scale for dumping configurations which may result in omissive positions between frames. On the other hand, the relaxation process for each temperature is not recorded, therefore a more detailed study on the diffusing atoms is suggested. The local environments of central tetrahedra are supposed to play crucial role with the diffusing directions. As mentioned above, the diffusing is suppressed below 400K at which temperature the atom 12737 was frozen on an tetrahedron site.

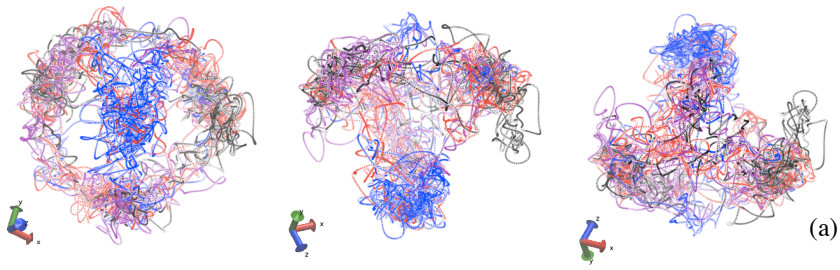

(a)

To be continued

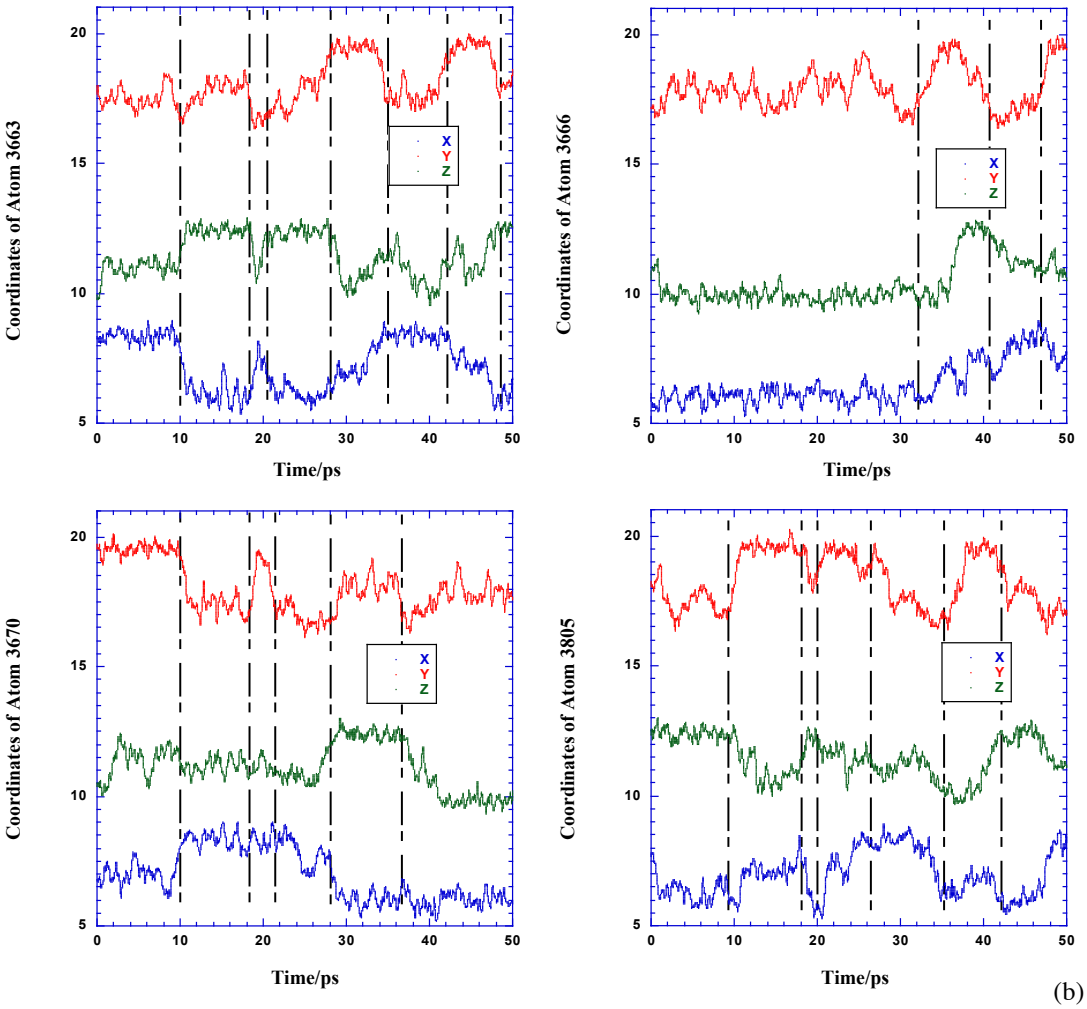

(b)

Figure 6.2.8 Representation of the tetrahedron jumps, time step for dumping is 5fs and 10000 frames are collected. (a) Trajectories of four tetrahedron atoms, each color displays one tetrahedron atom; (b) Coordinates evolution of the four atoms as a function of time. The flips are indicated by dashed lines.

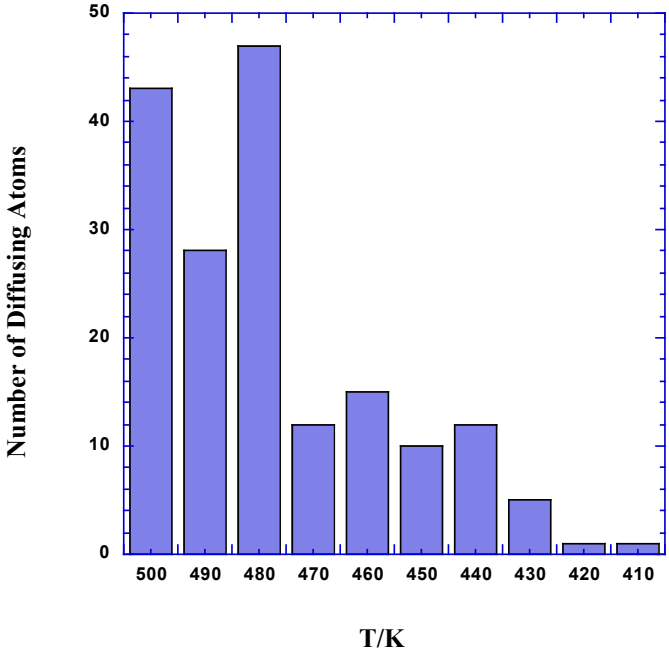

Figure 6.2.9 The number of diffusing atoms of 5/3 approximant within 5nanoseconds with respect to temperatures.

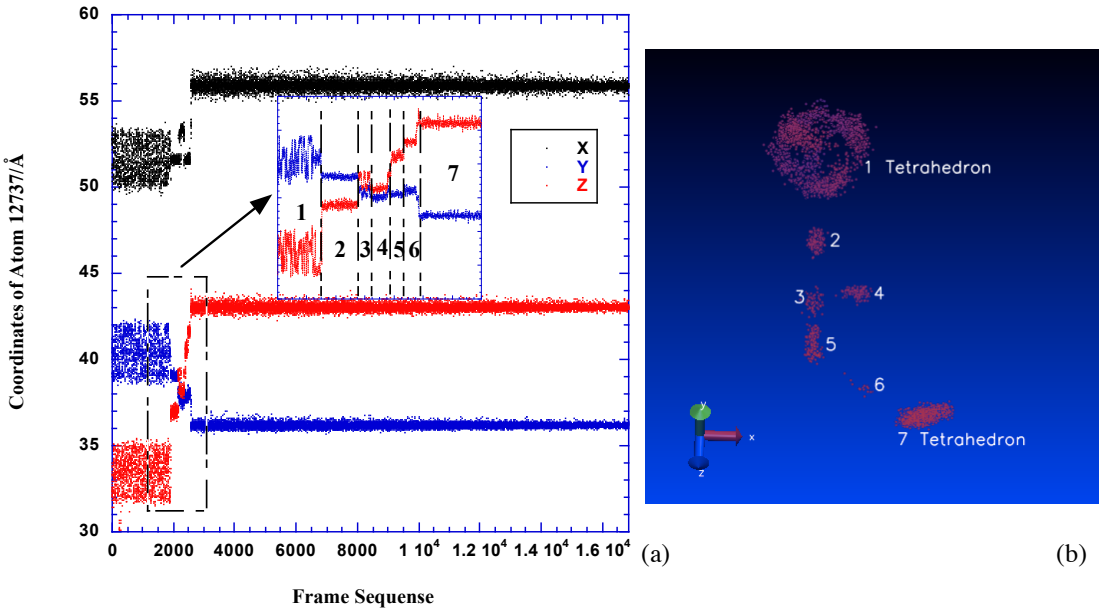

Figure 6.2.10 (a) Coordinates evolution of the atom 12737 over the cooling process, the steep changes are zoomed in in the inset; (b) The trajectory of the atom 12737, the relevant positions are indicated and the atom was frozen on a tetrahedron site finally.

Analogically with the 1/1 AC, additional positions with partial occupancy were found in 2/1 $Cd_{76}Yb_{13}$ AC as presented in Figures 6.2.11. The difference is these additional electron densities are not located in the center of the Cd_8 cube, but at the mid-center to the vertex positions as indicated in Figure 6.2.11 (a). Gómez regards the mid-center positions as the

results of the stacking fault of the interpenetrating RTH, thus only one of the two positions can be potentially complete. However, from the point of our simulation, these two positions are essentially from the diffusion of the same atoms (further study to 2/1 or 5/3 ACs may offer the evidence). Furthermore, this can also explain why the two positions are far from fully occupied: the diffusing atoms can not stay for a long time on these positions.

In addition, this atomic diffusion may attribute phasons in the ACs. As we aforementioned, the diffusing directions associating with the local 3-fold axes of the central tetrahedron may play crucial role in investigating the origin of this additional atomic dynamic. Otherwise, inelastic neutron scattering on these ACs may provide important support to this conclusion.

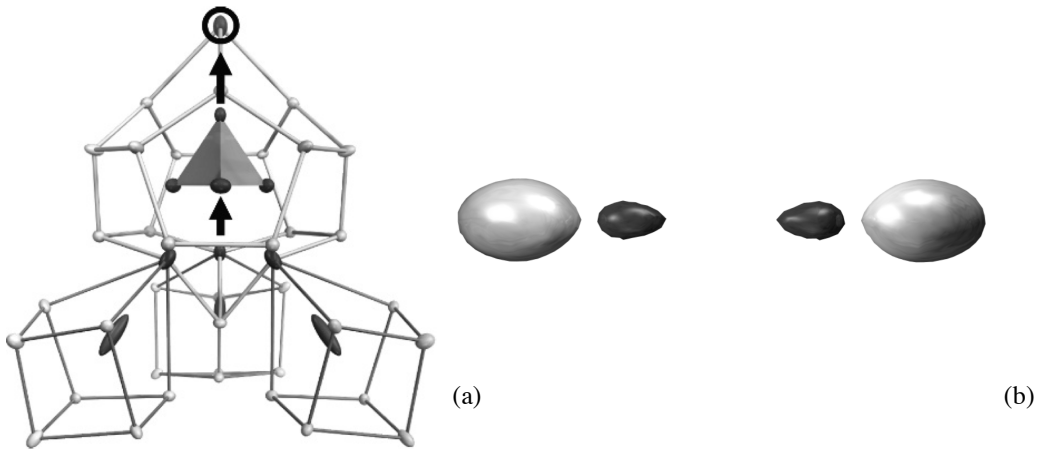

Figure 6.2.11 (a) Schematic representation of the local distortion of the dodecahedral cage in the 2/1 approximants. The shifted tetrahedron pushes a vertex of the dodecahedron into the position marked by a circle, this is the perfect position of a triacontahedral vertex. All the shifted atoms in the figure are colored dark. (from [64]); (b) Electron density iso-surface at the 11.3 eÅ^{-3} level, generated from F_{obs}-F_{cal} data. The image shows the electron densities found along the space diagonal of a Cd_8 cube in $Yb_{13}Cd_{76}$. The grey densities correspond to the two vertex atoms of the cube and the black densities correspond to the mid-center to vertex positions. (from [52])

6.2.4 Conclusion

The MD simulation is carried out on the 5/3 $Zn_{85.12}Sc_{14.88}$ approximant in a cooling process using oscillating pair potential via LAMMPS. The results are compared with the 1/1 approximant as well as experiment results. The *hk*0 Bragg planes are reconstructed for a set of temperatures based on FT. Additional amount of diffuse scattering is observed in the 5/3 approximant which agrees with the experiment results on the related quasicrystal. However, it is infeasible now to quantitatively confirm whether these excess diffuse scattering are contributed by the phason or not.

A new motion of the central tetrahedron is found in the 5/3 approximant which agrees well with the observed one in the 2/1 $Cd_{76}Yb_{13}$ AC. An inherent 3-fold axis is found in the tetrahedron model at HT, and the local environments are supposed to play crucial role in determining the orientations of the tetrahedra. In this work we studied only one local

configuration. Further studies are needed to complete the picture. Both the characteristic time scale and distance scale of the tetrahedron jumping are larger than those of the 1/1 approximant. Furthermore, the atomic diffusion is observed again which may attribute to the phasons in these ACs. Further analysis and experimental support are certainly desirable.

6.3 The model of 8/5 $Zn_{85.16}Sc_{14.84}$ approximant

The model of the 8/5 approximant is achieved by canonical cell tiling as described in last section. The initial structure is refined by a total energy minimization process via VASP. The obtained configuration contains 8032 Sc atoms and 46088 Zn atoms per unit cell with a cell parameter equal to 94.584Å. According to the configurations of cluster environments, 576 clusters are categorized into 6 groups: 5-7, 6-5, 6-6, 6-7, 7-5 and 7-6, where *n* in *n-m* presents the number of 2-fold linkages around and *m* stands for the number of 3-fold linkages. The initial strains in the structure is eliminated by the MD energetic minimization and the model is equilibrated at each temperature before data collection.

For each temperature, 5 million steps were performed and 500 frames were collected for analysis. The time step for each temperature is listed in Table 6.5. The potential energies per atom with respect to temperatures are illustrated in Figure 6.3.1 comparing with the 5/3 and 1/1 approximants. All three approximants display very similar temperature dependent behavior owing to close compositions. Moreover, the potential energy is the smallest in the 1/1 approximant, and it increases as the approximant approaches to quasicrystal.

Table 6.7 Time step setting for each temperature of the 8/5 approximant

T/K	500	400	300	200	100
Time step/ps	0.002	0.002	0.005	0.008	0.01

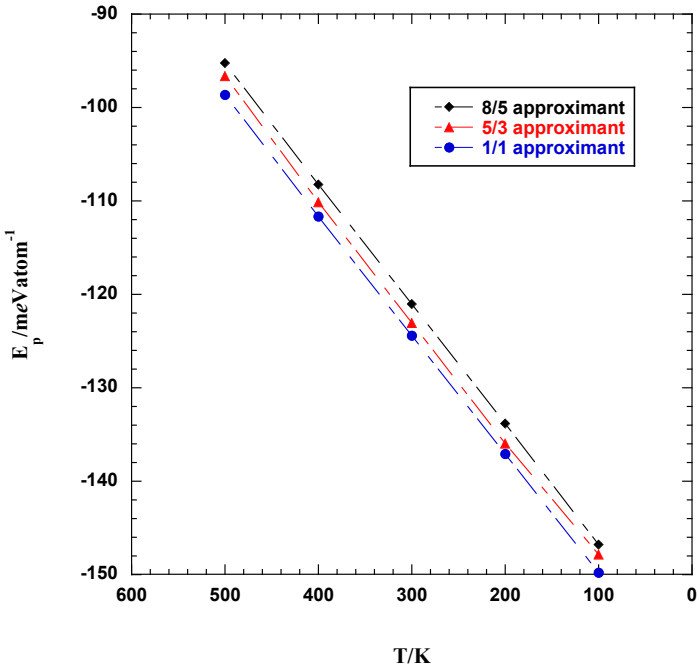

Figure 6.3.1 Temperature dependence of potential energies in the three approximants.

The model of central tetrahedra in 8/5 approximant is essentially the same as the 5/3 as shown in Figures 6.3.2. The visualization of charge density is carried out using the program VESTA at isosurfaces of 2e-5e/Å^3. 1million atomic positions are counted within 10ns. To evaluate the time scale of the tetrahedron flipping, we extracted the coordinates of the tetrahedron atom 43772 within 0.3ns at 500K. Each steep change corresponds one flip as indicated by dashed lines in Figure 6.3.4. The atom was dumped every 5 steps giving a time scale of 0.01ps.

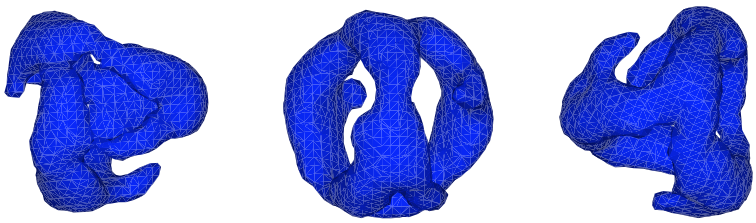

Figure 6.3.2 The model of central tetrahedron in the 8/5 approximant viewing along three directions.

In average, the time scale of the tetrahedron flipping in the 8/5 approximant at 500K is of the order of 17.6ps, much more stable than that of the 1/1 and 5/3 approximants. Accordingly, the flipping frequency of the tetrahedron seems closely related to the complexity of the approximant: the more complex the structure is, the more slowly the tetrahedron flips. In addition, it is also suggested that the activation energy of flipping increases as the structure complexity increases.

Around 3.1% of all atoms are observed diffusing at 500K within 10ns, and the diffusion has been suppressed at 400K. The largest displacement over the whole cooling process is about 14.5Å which is found on the atom 25082. The coordinates variation of the atom 25082 is displayed in Figure 6.3.5 (a) accompanying with the trajectory shown in Figure 6.3.5 (b). The four unique sites are indicated in both two figures respectively. It is noteworthy that because of the setting of the time scale for dumping configurations, many intermediate positions are omissive.

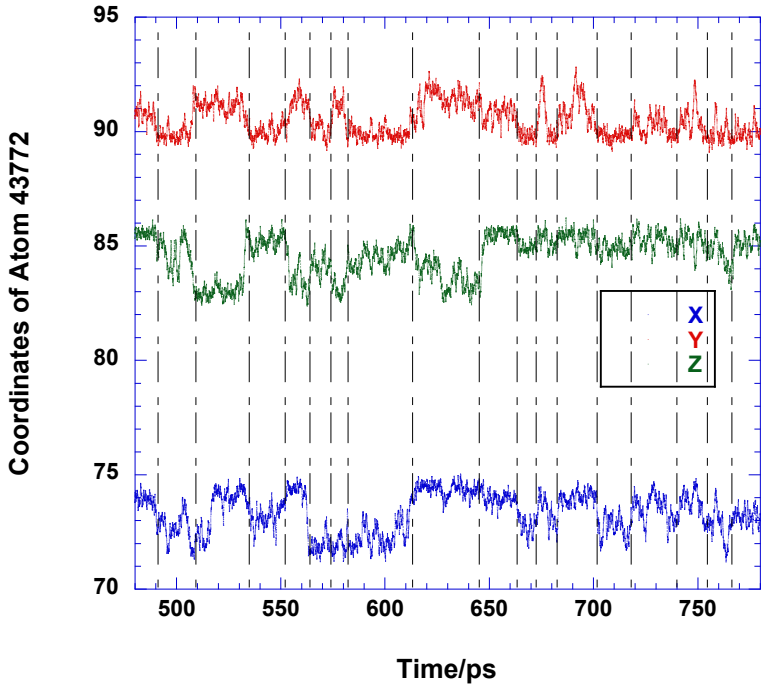

Figure 6.3.3 Evolution of coordinates of the atom 43772 at 500K within 0.3ns, each steep change corresponds to one flip, which is denoted by dashed line.

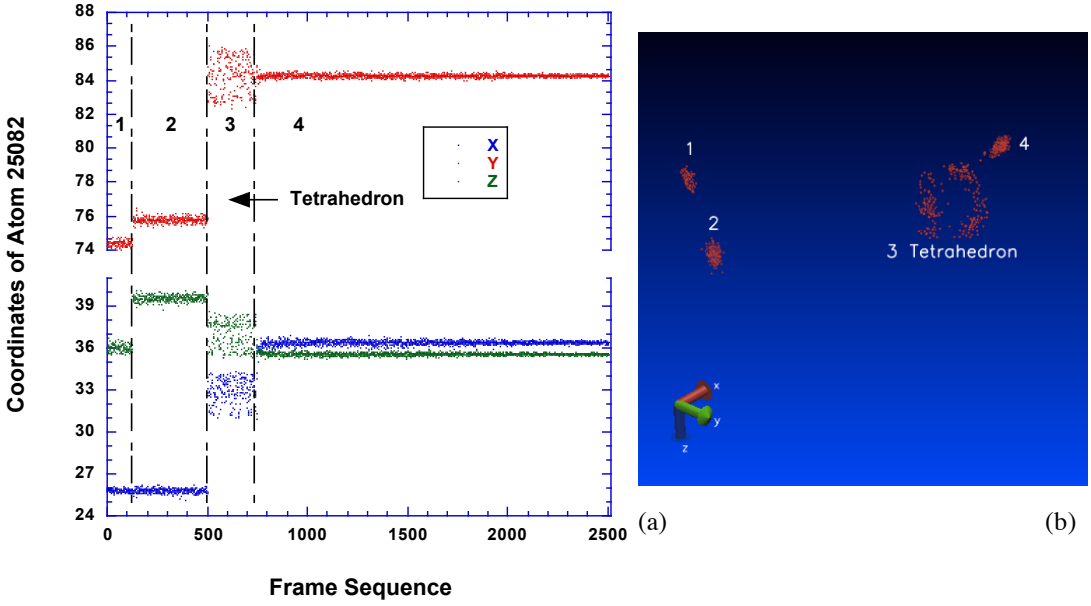

Figure 6.3.4 (a) Coordinates of the atom 25082 over the cooling process; (b) The trajectory of the atom 25082, the four sites are denoted in both figures.

6.4 Conclusion

We performed MD simulations on 1/1, 5/3 and 8/5 approximants of the i-ZnMgSc quasicrystal using oscillating pair potentials which have been fitted against *ab initio* data. Detailed comparison has been made with each other and the relevant experiments.

The diffuse scatterings in the 1/1 and 5/3 approximants are analyzed and compared detailedly. Excess components are distinctly observed in the 5/3 approximant. Further investigations are called to clarify whether this additional amount of diffuse scattering is contributed by phason motions or not. As temperature decreases, the diffuse scattering in the 1/1 approximant turns into ordered along <110> directions indicating a s.r.o in the LT phase. The motions of central tetrahedra which reorient constantly at HT and are frozen at LT are considered responsible to this s.r.o.

The tetrahedron reorientation in 1/1 approximant takes place with a time scale of 0.5ps at 500K and an energy barrier of the order of 34meV. For 5/3 and 8/5 approximants, the values of time scale at 500K are 7.2ps and 17.6ps respectively. It is suggested that the flipping frequency of tetrahedra is dependent on the structural complexity: the more complex the structure is, the more strictly the flipping of central tetrahedra is restrained. Moreover, the behavior of central tetrahedra in the 1/1 approximant fits well with the model proposed from experiments, and the tetrahedra in 5/3 and 8/5 shows completely different fashion from the 1/1.

Atomic diffusion is observed in all three approximants. It is shown that atoms exchange takes place between tetrahedron and dodecahedron shells. The potential energy difference between the two clusters is supposed to be responsible to this atomic diffusion. For the 1/1 approximant, a channel along which atoms can diffuse distantly is observed along space diagonal directions of the cubic unit cell. Furthermore, an additional position in between two dodecahedron sites is occupied partially. This phenomenon can interpret well the results reported previously by Gómez and Lidin[4]. The energy barrier of atoms diffusion in 1/1 approximant is confirmed as 106±11m*e*V which is compatible with the potential energy difference found between tetrahedron and dodecahedron sites. Moreover, comparing with the 1/1 approximant, less atoms of the 5/3 and 8/5 approximants are involved into diffusion and the diffusing behavior is suppressed at higher temperature with shorter displacements. The complex atomic structures of 5/3 and 8/5 approximants are supposed to play crucial role in restraining the diffusing process.

These results together with relevant experiments offer new perspectives for better understanding the stability of quasicrystals and their approximants. It also lays a foundation for further investigation on quasicrystal by atomic scale MD simulation. Additionally, more detailed studies are called for the 5/3 and 8/3 approximants.

Chapter 7. Conclusion

A series of isostructural compounds which are approximants to icosahedral quasicrystals have been investigated throughout the thesis both experimentally and using atomic scale simulations. Synchrotron x-ray diffuse scattering, single crystal and powder diffraction measurements are performed on the Cd-based 1/1 approximants. MD simulations are executed on Zn-based approximants using an effective pair potential via LAMMPS. The combination of experiments and simulations is of importance for not only current but also future work.

The Cd_6Tb 1/1 approximant was probed by means of single crystal and powder x-ray diffraction in a temperature range from 7K to RT. The structural phase transition is observed at ~190K evidenced by the splitting of main Bragg peaks. Both single crystal and powder diffraction patterns demonstrate an abruptly increasing distortion starting from 190K to 184K. An anomaly of the temperature dependent cell parameters is observed at ~45K below which both the lattice parameter and the scattering angles do not change any more. This phenomenon is supposed to be responsible to the irregular behavior of the electronic resistivity below ~40K.

Using different attenuations, we have collected integrated intensities in a large dynamical range leading to more than 60000 unique reflections in the *C*2/*c* monoclinic low temperature phase. The final *w*R2 values for RT and 40K are eventually refined to 0.0726 and 0.0905 respectively. As initially proposed by Tamura *et al*[14] and Kim *et al*[15], the distances of the intracluster ionic Tb^{3+} bonds are compatible with the intercluster bonds. For the monoclinic phase, owing to the lattice distortion, the intracluster and intercluster interactions become more competitive at LT which is supposed playing a crucial role in promoting the formation of long-range magnetic order.

A temperature dependent study is carried out to the Cd_6Tb structures. A strong distortion of the successive shells is observed along the three-fold axis of the cubic cell. Further investigation manifests that the distortion is originally induced by the ordering tetrahedron. The simultaneous behavior of the equivalent isotropic displacement parameters of the two unique tetrahedron atoms suggests that the tetrahedron behaves as a single molecule.

The temperature dependent diffuse scattering of Cd_6Yb 1/1 approximant was studied using synchrotron x-ray beam. Both the occurrence of peak splitting and the anomaly of Bragg angle variation evidence a reversible phase transition at ~113K. Observation of the superstructure reflections (13/2 15/2 $\overline{1/2}$) and (3 5 $\bar{1}$) indicates the ordering mechanism of Cd_6Yb is of [111] type rather than [110] type. The superstructure peaks get sharpening rapidly as temperature approaches to T_c providing a correlation length up to ~1200Å.

The effect of Mg substitution on the phase transition of Cd_6Pr 1/1 approximant was investigated by means of x-ray diffuse scattering. By adding Mg element, the Mg atoms partially occupy the dodecahedral sites of Cd which essentially enlarge the dodecahedron edges thus promote the ordering of the central tetrahedra. It is concluded that the effect of chemical order introduced by the third element is really dependent on the atomic radius of the

guest element. Furthermore, it is clarified that the ordering of the central tetrahedra in both Cd_6Pr and $(Cd\text{-}Mg)_6Pr$ with 10% at. Mg follows the [110] mechanism instead of the previously claimed [111] type.

MD simulations on 1/1, 5/3 and 8/5 approximants of the i-ZnMgSc quasicrystal using oscillating pair potentials that have been fitted against *ab initio* data was implemented at various temperatures. The diffuse scattering derived from the FT of outputting configurations is compared between the 1/1 and 5/3 approximants, and excess components are observed in the 5/3 approximant. Further investigations are desirable to clarify whether it is contributed by phason motions or not. As temperature decreases, the diffuse scattering in the 1/1 approximant turns into ordered along <110> directions implying a s.r.o forming in the LT phase along perpendicular directions. The s.r.o was suppressed due to the limitation of the supercell size, however, it evidences the occurrence of a structural pretransition. The motions of central tetrahedra, which reorient constantly at HT and are frozen at LT, are considered responsible to this phenomenon.

For the 1/1 approximant, the reorientation takes place in a time scale of 0.5ps at 500K and an energy barrier of the order of ~34meV. For 5/3 and 8/5 approximants, the values of time scale at 500K are 7.2ps and 17.6ps respectively. It is suggested that as the structural complexity increases, the flipping of central tetrahedra is restrained more strictly which leads to a larger time scale and activation energy. Moreover, the behavior of central tetrahedra in the 1/1 approximant fits well with the model proposed from experiments, and the tetrahedra in 5/3 and 8/5 shows completely different fashion from the 1/1 approximant.

An atomic diffusion between tetrahedron and dodecahedron shells is observed in all three approximants at high temperatures. For the 1/1 approximant, atoms can diffuse distantly only along space diagonal directions of the cubic unit cell. Further investigation provides an activation energy of ~0.1*e*V which is consistent with the atomic vacancy formation energy. The potential energy difference between tetrahedron and dodecahedron sites, i.e. ~0.1*e*V, is considered the initial impetus driving the first diffusion.

Moreover, additional positions inbetween two dodecahedron sites on the diffusing path are occupied and this phenomenon can interpret well the results reported previously by Gómez and Lidin who observed additional charge density on the same positions experimentally. Comparing with the 1/1 approximant, less atoms of the 5/3 and 8/5 approximants are involved into diffusion, and the diffusing behavior is suppressed at higher temperature with shorter displacements in the latter approximants. It is suggested that the complex atomic decorations of 5/3 and 8/5 approximants play significant role in restraining the diffusing process.

These results combining experiments and simulations offer new perspectives for better understanding the stability of quasicrystals and their approximants. The investigation on structures of Cd_6Tb provides helpful clues for researching the magnetic properties of related binary quasicrystals. Attempts of studying diffuse scattering of various ZnSc approximants lay a significant foundation for further investigation on quasicrystal by means of MD simulation. Apart from the above, we believe that the local configuration environments of

clusters, which reveals the complexity of the investigated phases, act important role in the stability of these CMAs.

References

[1] J. Q. Guo, E. Abe, and A. P. Tsai, "Stable icosahedral quasicrystals in binary Cd-Ca and Cd-Yb systems," *Phys. Rev. B*, vol. 62, no. 22, p. R14605, 2000.

[2] A. P. Tsai, J. Q. Guo, E. Abe, H. Takakura, and T. J. Sato, "Stable binary QC," *Nature*, vol. 408, no. 6812, pp. 537–537, 2000.

[3] A. I. Goldman, T. Kong, A. Kreyssig, A. Jesche, M. Ramazanoglu, K. W. Dennis, S. L. Bud'ko, and P. C. Canfield, "iR-Cd (R= Gd-Tm, Y): A new family of binary magnetic icosahedral quasicrystals," *ArXiv Prepr. ArXiv13031422*, 2013.

[4] C. Gómez and S. Lidin, "Comparative structural study of the disordered MCd6 quasicrystal approximants," *Phys. Rev. B*, vol. 68, no. 2, p. 024203, Jul. 2003.

[5] C. P. Gómez and S. Lidin, "Structure of Ca13Cd76: A Novel Approximant to the MCd5.7 Quasicrystals (M=Ca, Yb)," *Angew. Chem. Int. Ed.*, vol. 40, no. 21, p. 4037, Nov. 2001.

[6] R. Tamura, K. Nishimoto, S. Takeuchi, K. Edagawa, M. Isobe, and Y. Ueda, "Universal low-temperature phase transition in Zn- and Cd-based crystalline approximants," *Phys. Rev. B*, vol. 71, no. 9, Mar. 2005.

[7] R. Tamura, K. Edagawa, K. Shibata, K. Nishimoto, S. Takeuchi, K. Saitoh, M. Isobe, and Y. Ueda, "Group theoretical treatment of the low-temperature phase transition of the Cd6Ca 1/1-cubic approximant," *Phys. Rev. B*, vol. 72, no. 17, Nov. 2005.

[8] T. Ishimasa, Y. Kasano, A. Tachibana, S. Kashimoto, and K. Osaka, "Low-temperature phase of the Zn–Sc approximant," *Philos. Mag.*, vol. 87, no. 18–21, pp. 2887–2897, Jun. 2007.

[9] T. Hatakeyama, K. Nozawa, and Y. Ishii, "Ab initio studies on orientational ordering in cubic Zn–Sc," *Z. Für Krist.*, vol. 223, no. 11–12, Jan. 2008.

[10] K. Nozawa and Y. Ishii, "First-principles studies for structural transitions in ordered phase of cubic approximant Cd_6Ca," *J. Phys. Condens. Matter*, vol. 20, no. 31, p. 315206, Aug. 2008.

[11] T. Yamada, H. Euchner, C. P. Gómez, H. Takakura, R. Tamura, and M. de Boissieu, "Short-and long-range ordering during the phase transition of the Zn6Sc 1/1 cubic approximant," *J. Phys. Condens. Matter*, vol. 25, no. 20, p. 205405, 2013.

[12] K. Nishimoto, T. Sato, and R. Tamura, "Low-temperature superstructures of a series of Cd_6M (M = Ca, Y, Sr, Pr, Nd, Sm, Gd, Tb, Dy, Ho, Er, Tm, Yb and Lu) crystalline approximants," *J. Phys. Condens. Matter*, vol. 25, no. 23, p. 235403, Jun. 2013.

[13] K. Nishimoto, T. Sato, M. Muraki, and R. Tamura, "Low-temperature structural stability of Cd_6M (M = Ho, Er, Tm and Lu) cubic crystalline approximants," *Philos. Mag.*, vol. 91, no. 19–21, pp. 2587–2593, Jul. 2011.

[14] R. Tamura, Y. Muro, T. Hiroto, K. Nishimoto, and T. Takabatake, "Long-range magnetic order in the quasicrystalline approximant Cd_{6}Tb," *Phys. Rev. B*, vol. 82, no. 22, Dec. 2010.

[15]M. G. Kim, G. Beutier, A. Kreyssig, T. Hiroto, T. Yamada, J. W. Kim, M. de Boissieu, R. Tamura, and A. I. Goldman, "Antiferromagnetic order in the quasicrystal approximant Cd_{6}Tb studied by x-ray resonant magnetic scattering," *Phys. Rev. B*, vol. 85, no. 13, Apr. 2012.

[16]I. Johnson, R. Schablaske, B. Tani, and K. Anderson, "CeCd6-type rare earth- cadmium alloys. Trans Metall Soc AIME 1964;230:1485.," *Trans Met. Soc AIME*, vol. 230, p. 1485, 1964.

[17]A. Palenzona, "The ytterbium-cadmium system," *J. Common Met.*, vol. 25, no. 4, pp. 367–372, Dec. 1971.

[18]S. Xia and S. Bobev, "On the crystal structure of the quasicrystalline approximant YbCd6 at low temperature," *Intermetallics*, vol. 15, no. 4, pp. 550–556, Apr. 2007.

[19]R. Tamura, Y. Murao, S. Takeuchi, M. Ichihara, M. Isobe, and Y. Ueda, "A Low-Temperature Order-Disorder Transition in a Cubic Cd6Yb Crystalline Approximant," *Jpn. J. Appl. Phys.*, vol. 41, no. Part 2, No. 5A, pp. L524–L526, May 2002.

[20]N. Sorloaica, A. L. Pope, D. W. Winkler, T. M. Tritt, V. Keppens, D. Mandrus, and B. Sales, "Evidence of a Order-Disorder Transition in the Crystalline Phase of Cd6Yb, 1/1 cubic approximant of icosahedral Cd 5.7 Yb," *MRS Proc.*, vol. 793, Feb. 2003.

[21]G. C.P., *Aperiodic'09 Liverp. UK*, 2009.

[22]T. Yamada and R. Tamura, "Effect of atom substitution on the low-temperature phase transitions in Cd- and Zn-based 1/1 cubic approximants," *Z. Für Krist.*, vol. 224, no. 1–2, Jan. 2009.

[23]Q. Lin and J. D. Corbett, "Synthesis and Structure of Five $Sc_3Cu_yZn_{18-y}$ -Type Compositions ($0 \le y \le \sim 2.2$), 1/1 Crystalline Approximants of a New Icosahedral Quasicrystal. Direct Example of Tuning on the Basis of Size Effects and Hume–Rothery Concepts," *Inorg. Chem.*, vol. 43, no. 6, pp. 1912–1919, Mar. 2004.

[24]M. Mihalkovič and M. Widom, "Canonical cell model of cadmium-based icosahedral alloys," *Philos. Mag.*, vol. 86, no. 3–5, pp. 519–527, Jan. 2006.

[25]M. Mihalkovič, S. Francoual, K. Shibata, M. D. Boissieu, A. Q. R. Baron, Y. Sidis, T. Ishimasa, D. Wu, T. Lograsso, L.-P. Regnault, F. Gähler, S. Tsutsui, B. Hennion, P. Bastie, T. J. Sato, H. Takakura, R. Currat, and A.-P. Tsai, "Atomic dynamics of i-ScZnMg and its 1/1 approximant phase: Experiment and simulation," *Philos. Mag.*, vol. 88, no. 13–15, pp. 2311–2318, May 2008.

[26]G. Kresse and J. Hafner, "Ab initio molecular dynamics for liquid metals," *Phys. Rev. B*, vol. 47, no. 1, pp. 558–561, Jan. 1993.

[27]G. Kresse, "Efficient iterative schemes for ab initio total-energy calculations using a plane-wave basis set," *Phys. Rev. B*, vol. 54, no. 16, pp. 11169–11186, Oct. 1996.

[28]J.-M. Dubois and E. Belin-Ferré, *Complex metallic alloys fundamentals and applications*. Weinheim: Wiley-VCH Verlag, 2011.

[29]S. Sten, "Developments in the Structural Chemistry of Alloys Phases," *BC Giess. Ed Dev. Struct. Chem. Alloys Phases Plenum N. Y.*, p. 65, 1969.

[30] T. Janssen, G. Chapuis, and M. de Boissieu, *Aperiodic crystals: from modulated phases to quasicrystals*. Oxford: Oxford University Press, 2007.

[31] D. Shechtman, I. Blech, D. Gratias, and J. W. Cahn, "Metallic phase with long-range orientational order and no translational symmetry," *Phys. Rev. Lett.*, vol. 53, no. 20, pp. 1951–1953, 1984.

[32] "International Union of Crystallography Report of the Executive Committee for 1991," vol. A48, pp. 922–946, 1992.

[33] "Quasicrystal Introduction," *Httpwwwjcrystalcomsteffenweberqchtml4 Types Quasicrystals*.

[34] X. Zeng, G. Ungar, Y. Liu, V. Percec, A. E. Dulcey, and J. K. Hobbs, "Supramolecular dendritic liquid quasicrystals," *Nature*, vol. 428, no. 6979, pp. 157–160, Mar. 2004.

[35] X. Zeng, "Liquid quasicrystals," *Curr. Opin. Colloid Interface Sci.*, vol. 9, no. 6, pp. 384–389, Jun. 2005.

[36] G. H. Mehl, "Quasi-Periodic Organization in Soft Self-Assembling Matter," *Angew. Chem. Int. Ed.*, vol. 44, no. 5, pp. 672–673, Jan. 2005.

[37] A. Takano, S. Wada, S. Sato, T. Araki, K. Hirahara, T. Kazama, S. Kawahara, Y. Isono, A. Ohno, N. Tanaka, and Y. Matsushita, "Observation of Cylinder-Based Microphase-Separated Structures from ABC Star-Shaped Terpolymers Investigated by Electron Computerized Tomography," *Macromolecules*, vol. 37, no. 26, pp. 9941–9946, Dec. 2004.

[38] A. Takano, W. Kawashima, A. Noro, Y. Isono, N. Tanaka, T. Dotera, and Y. Matsushita, "A mesoscopic Archimedean tiling having a new complexity in an ABC star polymer," *J. Polym. Sci. Part B Polym. Phys.*, vol. 43, no. 18, pp. 2427–2432, Sep. 2005.

[39] R. Lifshitz and H. Diamant, "Soft quasicrystals–Why are they stable?," *Philos. Mag.*, vol. 87, no. 18–21, pp. 3021–3030, Jun. 2007.

[40] W. Steurer, "Twenty years of structure research on quasicrystals. Part I. Pentagonal, octagonal, decagonal and dodecagonal quasicrystals," *Z. Für Krist.*, vol. 219, no. 7–2004, pp. 391–446, Jul. 2004.

[41] C. L. Henley, M. Mihalkovič, and M. Widom, "Total-energy-based structure prediction for d (AlNiCo)," *J. Alloys Compd.*, vol. 342, no. 1, pp. 221–227, 2002.

[42] M. Mihalkovič, I. Al-Lehyani, E. Cockayne, C. Henley, N. Moghadam, J. Moriarty, Y. Wang, and M. Widom, "Total-energy-based prediction of a quasicrystal structure," *Phys. Rev. B*, vol. 65, no. 10, Mar. 2002.

[43] K. Edagawa, K. Suzuki, and S. Takeuchi, "HRTEM observation of phason flips in Al–Cu–Co decagonal quasicrystal," *J. Alloys Compd.*, vol. 342, no. 1, pp. 271–277, 2002.

[44] T. Janssen, "Crystallography of quasi-crystals," *Acta Crystallogr. A*, vol. 42, no. 4, pp. 261–271, 1986.

[45] A. Yamamoto, "Crystallography of Quasiperiodic Crystals," *Acta Crystallogr. Found. Crystallogr.*, vol. 52, p. 508, 1996.

[46] Q. Lin and J. D. Corbett, "A Chemical Approach to the Discovery of Quasicrystals and Their Approximant Crystals," in *Controlled Assembly and Modification of Inorganic Systems*, Springer, 2009, pp. 1–39.

[47] S. Weber and A. Yamamoto, "Application of the five-dimensional maximum-entropy method to the structure refinement of decagonal $Al_{70}Mn_{17}Pd_{13}$," *Philos. Mag. A*, vol. 76, no. 1, pp. 85–106, Jul. 1997.

[48] S. Weber and A. Yamamoto, "Noncentrosymmetric Structure of a Decagonal $Al_{70}Mn_{17}Pd_{13}$ Quasicrystal," *Acta Crystallogr. A*, vol. 54, no. 6, pp. 997–1005, Nov. 1998.

[49] H. Takakura, C. P. Gómez, A. Yamamoto, M. De Boissieu, and A. P. Tsai, "Atomic structure of the binary icosahedral Yb–Cd quasicrystal," *Nat. Mater.*, vol. 6, no. 1, pp. 58–63, Dec. 2006.

[50] A. Yamamoto and K. Hiraga, "Structure of an icosahedral Al-Mn quasicrystal," *Phys. Rev. B*, vol. 37, no. 11, p. 6207, 1988.

[51] M. Duneau and C. Oguey, "Ideal AlMnSi quasicrystal : a structural model with icosahedral clusters," *J. Phys.*, vol. 50, no. 2, pp. 135–146, 1989.

[52] C. Pay Gómez, Stockholms universitet, and oorganisk kemi och strukturkemi Institutionen för fysikalisk kemi, "Order and disorder in the RE-Cd and related systems," Institutionen för fysikalisk, oorganisk och strukturkemi, Stockholms univ., Stockholm, 2003.

[53] A. Yamamoto, H. Takakura, and A. Tsai, "Six-dimensional model of icosahedral Al-Pd-Mn quasicrystals," *Phys. Rev. B*, vol. 68, no. 9, Sep. 2003.

[54] H. Takakura, M. Shiono, T. Sato, A. Yamamoto, and A. Tsai, "Ab Initio Structure Determination of Icosahedral Zn-Mg-Ho Quasicrystals by Density Modification Method," *Phys. Rev. Lett.*, vol. 86, no. 2, pp. 236–239, Jan. 2001.

[55] J. W. Cahn, D. Shechtman, and D. Gratias, "Indexing of icosahedral quasiperiodic crystals," *J. Mater. Res.*, vol. 1, no. 01, pp. 13–26, 1986.

[56] A. W. Overhauser, "Observability of charge-density waves by neutron diffraction," *Phys. Rev. B*, vol. 3, no. 10, p. 3173, 1971.

[57] M. De Boissieu, "Phason modes in quasicrystals," *Philos. Mag.*, vol. 88, no. 13–15, pp. 2295–2309, May 2008.

[58] K. Edagawa, K. Suzuki, and S. Takeuchi, "High resolution transmission electron microscopy observation of thermally fluctuating phasons in decagonal Al-Cu-Co," *Phys. Rev. Lett.*, vol. 85, no. 8, p. 1674, 2000.

[59] S. Lyonnard, G. Coddens, Y. Calvayrac, and D. Gratias, "Atomic (phason) hopping in perfect icosahedral quasicrystals Al 70.3 Pd 21.4 Mn 8.3 by time-of-flight quasielastic neutron scattering," *Phys. Rev. B*, vol. 53, no. 6, p. 3150, 1996.

[60] M. de Boissieu, S. Francoual, Y. Kaneko, and T. Ishimasa, "Diffuse Scattering and Phason Fluctuations in the Zn-Mg-Sc Icosahedral Quasicrystal and Its Zn-Sc Periodic Approximant," *Phys. Rev. Lett.*, vol. 95, no. 10, Sep. 2005.

[61] M. de Boissieu, "Phonons, phasons and atomic dynamics in quasicrystals," *Chem. Soc. Rev.*, vol. 41, no. 20, p. 6778, 2012.

[62] S. Francoual, F. Livet, M. de Boissieu, F. Yakhou, F. Bley, A. Létoublon, R. Caudron, J. Gastaldi, and R. Currat, "Dynamics of long-wavelength phason fluctuations in the i-Al–Pd–Mn quasicrystal," *Philos. Mag.*, vol. 86, no. 6–8, pp. 1029–1035, Feb. 2006.

[63] S. Francoual, F. Livet, M. de Boissieu, F. Yakhou, F. Bley, A. Létoublon, R. Caudron, and J. Gastaldi, "Dynamics of Phason Fluctuations in the i-AlPdMn Quasicrystal," *Phys. Rev. Lett.*, vol. 91, no. 22, Nov. 2003.

[64] T. Fujiwara and Y. Ishii, *Quasicrystals*. Amsterdam; Boston: Elsevier, 2008.

[65] A. Letoublon, M. De Boissieu, M. Boudard, L. Mancini, J. Gastaldi, B. Hennion, R. Caudron, and R. Bellissent, "Phason elastic constants of the icosahedral Al-Pd-Mn phase derived from diffuse scattering measurements," *Philos. Mag. Lett.*, vol. 81, no. 4, pp. 273–283, Apr. 2001.

[66] M. Boudard, M. De Boissieu, A. Letoublon, B. Hennion, R. Bellissent, and C. Janot, "Phason softening in the AlPdMn icosahedral phase," *EPL Europhys. Lett.*, vol. 33, no. 3, p. 199, 1996.

[67] C. L. Henley, V. Elser, and M. Mihalkovic, "Structure determinations for random-tiling quasicrystals," *ArXiv Prepr. Cond-Mat0004126*, 2000.

[68] C. L. Henley, "Random tilings with quasicrystal order: transfer-matrix approach," *J. Phys. Math. Gen.*, vol. 21, no. 7, p. 1649, 1988.

[69] L.-H. Tang, "Random-tiling quasicrystal in three dimensions," *Phys. Rev. Lett.*, vol. 64, no. 20, p. 2390, 1990.

[70] T. Dotera and P. J. Steinhardt, "Ising-like transition and phason unlocking in icosahedral quasicrystals," *Phys. Rev. Lett.*, vol. 72, no. 11, p. 1670, 1994.

[71] M. Mihalkovič and C. Henley, "Temperature-dependent phason elasticity in a random tiling quasicrystal," *Phys. Rev. B*, vol. 70, no. 9, Sep. 2004.

[72] A. I. Goldman and R. F. Kelton, "RMP Colloquia," *Rev. Mod. Phys.*, vol. 65, no. 1, 1993.

[73] S. Piao, "Complexity of quasicrystal approximants: the $RECd_6$ and $RE_{13}(Zn/Cd)_{\sim 58}$ systems," Department of Physical, Inorganic and Structural Chemistry, Stockholm university, Stockholm, 2007.

[74] P. Donnadieu, Y. Shao, F. De Geuser, G. A. Botton, S. Lazar, M. Cheynet, M. de Boissieu, and A. Deschamps, "Atomic structure of T1 precipitates in Al–Li–Cu alloys revisited with HAADF-STEM imaging and small-angle X-ray scattering," *Acta Mater.*, vol. 59, no. 2, pp. 462–472, Jan. 2011.

[75] R. Tamura, K. Edagawa, C. Aoki, S. Takeuchi, and K. Suzuki, "Low-temperature structural phase transition in a Cd6Y 1/1 approximant," *Phys. Rev. B*, vol. 68, no. 17, Nov. 2003.

[76] R. Tamura, Y. Muro, T. Hiroto, H. Yaguchi, G. Beutier, and T. Takabatake, "Structural and magnetic transitions in the crystalline approximant Cd_{6}Sm," *Phys. Rev. B*, vol. 85, no. 1, Jan. 2012.

[77] T. Watanuki, A. Machida, T. Ikeda, K. Aoki, H. Kaneko, T. Shobu, T. Sato, and A. Tsai, "Pressure-Induced Phase Transitions in the Cd-Yb Periodic Approximant to a Quasicrystal," *Phys. Rev. Lett.*, vol. 96, no. 10, Mar. 2006.

[78] T. Yamada, G. Garbarino, H. Takakura, C. P. Gòmez, R. Tamura, and M. de Boissieu, "In-situ high-pressure X-ray diffraction on the Zn6Sc 1/1 periodic cubic approximant to a quasicrystal," *Z. Für Krist. – Cryst. Mater.*, vol. 229, no. 3, Jan. 2014.

[79] T. Watanuki, T. J. Sato, and A. P. Tsai, "Structural stability of an icosahedral Cd-Yb quasicrystal and its crystalline approximant under high pressure," *J. Phys. Conf. Ser.*, vol. 215, p. 012019, Mar. 2010.

[80] M. de Boissieu, S. Francoual, M. Mihalkovič, K. Shibata, A. Q. R. Baron, Y. Sidis, T. Ishimasa, D. Wu, T. Lograsso, L.-P. Regnault, F. Gähler, S. Tsutsui, B. Hennion, P. Bastie, T. J. Sato, H. Takakura, R. Currat, and A.-P. Tsai, "Lattice dynamics of the Zn–Mg–Sc icosahedral quasicrystal and its Zn–Sc periodic 1/1 approximant," *Nat. Mater.*, vol. 6, no. 12, pp. 977–984, Nov. 2007.

[81] H. Euchner, T. Yamada, H. Schober, S. Rols, M. Mihalkovič, R. Tamura, T. Ishimasa, and M. de Boissieu, "Ordering and dynamics of the central tetrahedron in the 1/1 Zn_6 Sc periodic approximant to quasicrystal," *J. Phys. Condens. Matter*, vol. 24, no. 41, p. 415403, Oct. 2012.

[82] R. Currat and T. Janssen, "Excitations in Incommensurate Crystal Phases," in *Solid State Physics*, vol. 41, Elsevier, 1988, pp. 201–302.

[83] V. L. Ginzburg and S. I. Syrovatskii, "Cosmic Magnetobremsstrahlung (Synchrotron Radiation)," *Annu. Rev. Astron. Astrophys.*, vol. 3, no. 1, pp. 297–350, Sep. 1965.

[84] J. Als-Nielsen and D. McMorrow, *Elements of modern X-ray physics*. New York: Wiley, 2001.

[85] *http://en.wikipedia.org/wiki/Synchrotron_radiation*.

[86] *http://en.wikipedia.org/wiki/Undulator*.

[87] C.-H. Chang, C. S. Hwang, T. C. Fan, F. Y. Lin, H. H. Chen, M. H. Huang, C. Wang, and J. R. Chen, "Development of Insertion Devices at NSRRC," 2004.

[88] K. Halbach, "Design of permanent multipole magnets with oriented rare earth cobalt material," *Nucl. Instrum. Methods*, vol. 169, no. 1, pp. 1–10, 1980.

[89] K.-J. Kim, "Characteristics of synchrotron radiation," 1989, vol. 184, pp. 565–632.

[90] B. D. Patterson, "A simplified approach to synchrotron radiation," *Am. J. Phys.*, vol. 79, no. 10, p. 1046, 2011.

[91] *http://www.esrf.eu/UsersAndScience/Experiments/CRG/BM02/optic*.

[92] *http://en.wikipedia.org/wiki/Medipix*.

[93] T. Taguchi, C. Brönnimann, and E. F. Eikenberry, "NEXT GENERATION X-RAY DETECTORS FOR IN-HOUSE XRD," *Int. Cent. Diffr. Data 2008*, pp. 61–68, 2008.

[94] *http://www.esrf.eu/UsersAndScience/Experiments/CRG/BM02/Goniometer/cryostat.html*.

[95] M. Born and R. Oppenheimer, "Zur Quantentheorie der Molekeln," *Ann. Phys.*, vol. 389, no. 20, pp. 457–484, 1927.

[96] *http://en.wikipedia.org/wiki/Hartree%E2%80%93Fock_method*.

[97] H. Euchner, "Lattice Dynamics of Complex Metallic Alloys," University of Stuttgart, 2011.

[98] D. Frenkel and B. Smit, *Understanding molecular simulation from algorithms to applications*. San Diego: Academic Press, 2002.

[99] J. E. Jones, "On the Determination of Molecular Fields. II. From the Equation of State of a Gas," *Proc. R. Soc. Math. Phys. Eng. Sci.*, vol. 106, no. 738, pp. 463–477, Oct. 1924.

[100] J. E. Lennard-Jones, "Cohesion," *Proc. Phys. Soc.*, vol. 43, no. 5, pp. 461–482, Sep. 1931.

[101] P. Morse, "Diatomic Molecules According to the Wave Mechanics. II. Vibrational Levels," *Phys. Rev.*, vol. 34, no. 1, pp. 57–64, Jul. 1929.

[102] M. Born and J. E. Mayer, "Zur Gittertheorie der Ionenkristalle," *Z. F*[illegible]*r Phys.*, vol. 75, no. 1–2, pp. 1–18, Jan. 1932.

[103] M. L. Huggins and J. E. Mayer, "Interatomic Distances in Crystals of the Alkali Halides," *J. Chem. Phys.*, vol. 1, no. 9, p. 643, 1933.

[104] M. Daw and M. Baskes, "Embedded-atom method: Derivation and application to impurities, surfaces, and other defects in metals," *Phys. Rev. B*, vol. 29, no. 12, pp. 6443–6453, Jun. 1984.

[105] M. W. Finnis and J. E. Sinclair, "A simple empirical *N* -body potential for transition metals," *Philos. Mag. A*, vol. 50, no. 1, pp. 45–55, Jul. 1984.

[106] M. Baskes, "Application of the Embedded-Atom Method to Covalent Materials: A Semiempirical Potential for Silicon," *Phys. Rev. Lett.*, vol. 59, no. 23, pp. 2666–2669, Dec. 1987.

[107] M. Baskes, J. Nelson, and A. Wright, "Semiempirical modified embedded-atom potentials for silicon and germanium," *Phys. Rev. B*, vol. 40, no. 9, pp. 6085–6100, Sep. 1989.

[108] T. J. Lenosky, B. Sadigh, E. Alonso, V. V. Bulatov, T. D. de la Rubia, J. Kim, A. F. Voter, and J. D. Kress, "Highly optimized empirical potential model of silicon," *Model. Simul. Mater. Sci. Eng.*, vol. 8, no. 6, pp. 825–841, Nov. 2000.

[109] M. Mihalkovič, C. L. Henley, M. Widom, and P. Ganesh, "Empirical oscillating potentials for alloys from ab-initio fits," *ArXiv Prepr. ArXiv08022926*, 2008.

[110] S. Nosé, "A unified formulation of the constant temperature molecular dynamics methods," *J. Chem. Phys.*, vol. 81, no. 1, p. 511, 1984.

[111] Sandia National Laboratories, *LAMMPS Users Manual*. .

[112] *http://en.wikipedia.org/wiki/parallel_computing*.

[113] A. C. Larson and D. T. Cromer, "The crystal structure of YCd6," *Acta Crystallogr. B*, vol. 27, no. 10, pp. 1875–1879, 1971.

[114] G. Bruzzone, M. L. Fornasini, and F. Merlo, *J -Common Met*, vol. 30, p. 361, 1973.

[115] F. E. Wang, *Acta Crystallogr*, vol. 22, p. 579, 1967.

[116] L. Palatinus and G. Chapuis, "*SUPERFLIP* – a computer program for the solution of crystal structures by charge flipping in arbitrary dimensions," *J. Appl. Crystallogr.*, vol. 40, no. 4, pp. 786–790, Aug. 2007.

[117] P. Vaclav, D. Michael, and P. Lukas, "The crystallographic computing system," *Jana2006*, 2006.

[118] D. B. Wiles and R. A. Young, "A new computer program for Rietveld analysis of X-ray powder diffraction patterns," *J. Appl. Crystallogr.*, vol. 14, no. 2, pp. 149–151, Apr. 1981.

[119] R. A. Young and D. B. Wiles, "Profile shape functions in Rietveld refinements," *J. Appl. Crystallogr.*, vol. 15, no. 4, pp. 430–438, Aug. 1982.

[120] P. C. Canfield, M. L. Caudle, C.-S. Ho, A. Kreyssig, S. Nandi, M. G. Kim, X. Lin, A. Kracher, K. W. Dennis, R. W. McCallum, and A. I. Goldman, "Solution growth of a binary icosahedral quasicrystal of Sc_{12}Zn_{88}," *Phys. Rev. B*, vol. 81, no. 2, Jan. 2010.

[121] A. I. Goldman, A. Kreyssig, S. Nandi, M. G. Kim, M. L. Caudle, and P. C. Canfield, "High-energy X-ray diffraction studies of i-$Sc_{12}Zn_{88}$," *Philos. Mag.*, vol. 91, no. 19–21, pp. 2427–2433, Jul. 2011.

[122] W. T. R., "Diffuse x-ray scattering and models of disorder," *Rep Prog Phys*, vol. 48, pp. 1543–1593, 1985.

[123] G. Coddens, S. Lyonnard, B. Hennion, and Y. Calvayrac, "Triple-axis neutron-scattering study of phason dynamics in Al-Mn-Pd quasicrystals," *Phys. Rev. B*, vol. 62, no. 10, p. 6268, 2000.

[124] C. L. Henley, "Cell geometry for cluster-based quasicrystal models," *Phys. Rev. B*, vol. 43, no. 1, p. 993, 1991.

List of Figures

List of Tables

Acknowledgements

Firstly, I would express my most sincere thanks to Dr. Marc de Boissieu for being an excellent supervisor and providing helpful guidance and advice all the time not only in research but also in my daily life. It is a great experience doing my PhD in SIMaP under the supervision of Marc whose professional suggestions always point me to the best directions. Merci beaucoup.

Special thanks to my colleague Dr. Guillaume Beutier and M.S. Maxime Dupraz for their significant discussions and careful reading and translation work of the manuscript.

Assoc. Prof. Ryuji Tamura and his group members deserve special mention for their support of samples. The same thanks to Prof. An Pang Tsai and his group who synthesized most of the intriguing quasicrystal samples.

Most of the experiments were carried out accompanying with Dr. Tsunetomo Yamada whose early work and suggestions helped me a lot for which I appreciate very much. It is also very impressive and pleasant to do experiments with Dr. Andreas Kreyssig, Prof. Alan Goldman and Takanobu Hiroto.

The data treatment was greatly supported by Dr. Václav Petříček and Dr. Michal Dusek, the main developers of the wildly used crystallographic program *Jana*2006, as well as Dr. Cesar Pay Gómez. The simulation work has been done with significant assistance from Dr. Marek Mihalkovič and Dr. Holger Euchner who helped me overcome many of the difficulties.

I am grateful to all synchrotron beamline staffs for their assistance with my experiments and all people I once worked with in particular M.S. Pierre-François Lorry and my office mates M.S. Simon Langlais.

Sincere thanks also go to my friends who give me great helps in my life in Grenoble: M.S. Qingquan Lai & Qianyu Su, Linna Zhu, Pavel Barta and his families, Cyril Claraz & Sanie Claraz, Chang Chen, Die Hu, Rachel Marker, Rebecca Elisabeth Nish, Ruping Cao, Gao Liangyezi, Shoujun Li, Mengxuan Zhao, Jingwen Ge, Lingyi Wu and Fanyu Liu.

Finally I would express my best love to my beloved families: my dearest parents, my sisters, my twin brother, my niece and nephews. You are my spiritual pillars for ever.

Appendix

I. Input script for Zn_6Sc 1/1 approximant LAMMPS simulation

```
# Sample LAMMPS input script for Zn6Sc 1/1 approximant
#===============Initialization==============================
units        metal # time=ps, energy=eV, force=eV/A, T=K,…
variable     T equal 400
variable     V equal vol
variable     dt equal 0.002 # 2 femtoseconds
dimension     3 # 3D simulation
boundary      p p p # periodic boundary condition
atom_style      atomic
#===============Atom definition=============================
read_data       two_tet.config # initial structure file
#===============Settings====================================
replicate       8 8 8 # replicating in x, y, z direction
pair_style      table spline 10000
pair_coeff      1 1 sczn_new.pot Sc 8.3 # potential file
pair_coeff      1 2* sczn_new.pot ScZn 8.3 # cutoff=8.3Angstrom
pair_coeff      2* 2* sczn_new.pot Zn 8.3
pair_write 1 1 10000 r 1.0 8.3 table11.txt Sc
pair_write 1 2 10000 r 1.0 8.3 table12.txt ScZn
pair_write 2 2 10000 r 1.0 8.3 table22.txt Zn
compute ea all pe/atom #define potential energy per atom as ea
compute eatoms all reduce sum c_eng
group tetrahedron type == 3 # define group 'tetrahedron'
reset_timestep 0
thermo 10 # output every 10 steps
thermo_style  custom  step  pe  lx  ly  lz  press  pxx  pyy  pzz
c_eatoms
#===============Running simulation==========================
min_style cg # conjugate gradient
minimize 1e-9 1e-7 1000 500 # minimization stopping criteria
run 0 # trigger simulation
timestep       ${dt}
velocity         all create $T 16 mom yes rot yes dist gaussian
fix         NVT all nvt temp $T $T 10 drag 0.2 # ensemble
run 100 # relaxation
dump 1 tetrahedron atom 100 tetra-400K.lammps # output setting
dump 2 all          atom 5000 all.lammps
dump 3 all       atom 1000000 sczn6.config
run 1000000
variable natoms equal "count(all)"
variable teng equal "c_eatoms"
variable length equal "lx"
variable ecoh equal "v_teng/v_natoms"
variable L equal "13.8311*8"
print "Total energy (eV) = ${teng};"
print "Number of atoms = ${natoms};"
print "Lattice constant (Angstoms) = ${length};"
print "Cohesive energy (eV) = ${ecoh};"
print "Box size (Angstrom) = $L"
print "All done!"
```

II. Crystallographic data and technic parameters for Cd_6Yb phase at 200K

Cd_6Yb	T=200K
Space Group	*Im*-3 (no. 204)
a axis/Å	15.5939(6)
Cell volume/ $Å^3$	3792.0(2)
F(000)	8602
Calculated density (g/cm^3)	8.9042
Absorption coefficient-mu/mm^{-1}	12.251
Range of theta/°	1.78-32.53
Independent reflections	3723
Reflections>3σ	3165
R_{int} (obs/all)	12.45/14.3
Number of parameters	49
R (all)	0.038
ωR_2 (all)	0.0719
Absorption correction	Numerical
T_{min}/T_{max} transmission factor	0.28657/0.40677
Δϱmax, Δϱmin	7.52/-6.89
Mean change/s. u.	0.0008

III. Crystallographic data and technic parameters for Cd_6Tb phase at 200K and 196K

Temperature/K	200	196
Space Group	Im-3	Im-3
a axis/Å	15.4650(4)	15.4559(5)
Cell volume/ $Å^3$	3698.71(15)	3692.18(19)
F(000)	8480	8855
Calculated density (g/cm^3)	8.9767	8.9925
Absorption coefficient-mu/mm^{-1}	11.156	11.176

Range of theta/°	1.8-32.55	1.8-32.57
Independent reflections	3650	3624
Reflections>3σ	3206	3061
R_{int} (obs/all)	9.44/9.45	14.48/14.77
Number of parameters	59	61
R (all)	0.0398	0.051
ωR2 (all)	0.0827	0.0992
Absorption correction	Numerical	Numerical
Δϱmax, Δϱmin	6.26, -10.83	9.98, -11.11
Mean change/s. u.	0.0007	0.0006

IV. Structural information of Cd_6Tb 1/1 approximant at 200K and 196K

Symbol	T/K	Wyckoff site	x/a	y/b	z/c	Occ	Biso/eq
Tb1	196	24g	0.18975(3)	0.29965(3)	0		0.0058(0)
	200		0.18974(3)	0.29964(3)	0		0.0059(0)
Cd1	196	16f	0.16087(2)	0.16087(2)	0.16087(2)		0.014()
	200		0.5	0.19056(3)	0		0.0099(1)
Cd2	196	12e	0.5	0.19051(3)	0		0.0096(1)
	200		0.75859(8)	0.09237(5)	0		0.0266(2)
Cd3	196	24g	0.24133(10)	0.09234(6)	0		0.0264(1)
	200		0.65941(1)	0.20038(1)	-0.11815(2)		0.0108(0)
Cd4	196	48h	0.34063(1)	0.20040(1)	0.11813(2)		0.0107(0)
	200		0.83912(2)	0.16088(2)	-0.16088(2)		0.0142(0)
Cd5	196	24g	0.5	0.09568(2)	0.15386(2)		0.0081(0)
	200		0.5	0.09569(2)	-0.15381(2)		0.0081(1)
Cd6	196	12d	0.40571(4)	0	0		0.0236(2)
	200		0.59428(4)	0	0		0.0236(2)
Cd7	196	48h	0.0757(3)	0.0837(2)	0.0152(4)	0.1667	0.058(2)
	200	24g	0.9241(2)	0.08395(19)	0	0.3333	0.0809(13)

V. Anisotropic displacement parameters (Å^2) of the Cd_6Tb 1/1 approximant at 200K and 196K

Symbol	T/K	U_{11}	U_{22}	U_{33}	U_{12}	U_{13}	U_{23}
Tb1	196	0.00578(6)	0.00699(6)	0.00472(6)	0.00058(3)	0	0
	200	0.00575(6)	0.00696(6)	0.00486(6)	0.00054(4)	0	0

Cd1	196	0.01404(8)	0.01404(8)	0.01404(8)	0.00750(8)	0.00750(8)	0.00750(8)
	200	0.01521(1)	0.00721(1)	0.00713(1)	0	0	0
Cd2	196	0.01489(1)	0.00700(1)	0.00705(1)	0	0	0
	200	0.0622(4)	0.00929(1)	0.00833(1)	- 0.01090(1)	0	0
Cd3	196	0.0623(4)	0.00904(1)	0.00794(1)	0.01081(1)	0	0
	200	0.00848(8)	0.00942(8)	0.01462(9)	0.00090(6)	- 0.00214(6)	- 0.00393(6)
Cd4	196	0.00837(8)	0.00938(8)	0.01436(9)	- 0.00085(5)	- 0.00203(5)	0.00387(6)
	200	0.01424(8)	0.01424(8)	0.01424(8)	- 0.00758(9)	0.00758(9)	- 0.00758(9)
Cd5	196	0.00914(9)	0.00709(9)	0.00797(9)	0	0	0.00164(6)
	200	0.00922(1)	0.00723(9)	0.0079(1)	0	0	- 0.00169(7)
Cd6	196	0.00939(1)	0.0520(5)	0.00958(1)	0	0	0
	200	0.00939(1)	0.0519(4)	0.00968(1)	0	0	0
Cd7	196	0.066(2)	0.0397(13)	0.067(5)	- 0.0422(15)	-0.007(2)	- 0.0035(17)
	200	0.0621(17)	0.0383(12)	0.142(3)	0.0394(12)	0	0

VI. Structural information of Cd_6Tb 1/1 approximant at 100K

Symbol	*Wyckoff site*	x/a	y/b	z/c	S.O.F	Biso/eq
Tb1	8f	0.14770(1)	0.43863(1)	0.10146(1)		0.0026(0)
Tb2	8f	0.15132(1)	0.06137(1)	0.09993(1)		0.0025(0)
Tb3	8f	0.75344(2)	0.25181(1)	0.19439(2)		0.0026(0)
Tb4	8f	0.94424(2)	0.2494()	0.00521(2)		0.0026(0)
Tb5	8f	0.40517(1)	0.05214(1)	0.15480(1)		0.0026(0)
Tb6	8f	0.40439(1)	0.45458(1)	0.15445(1)		0.0026(0)
Cd1	8f	0.65921(2)	0.41421(3)	0.20904(2)		0.0045(0)
Cd2	8f	0.74698(1)	0.44077(2)	-0.00354(1)		0.005()
Cd3	8f	0.54646(1)	0.51911(1)	0.20382(1)		0.0045(0)
Cd4	8f	0.95940(2)	0.59073(3)	0.41184(2)		0.0044(0)
Cd5	8f	0.87620(3)	0.75432(1)	0.22122(3)		0.0040(1)
Cd6	8f	0.97063(3)	0.75076(1)	0.12518(3)		0.0038(1)
Cd7	8f	0.54065(2)	0.40954(3)	0.09378(2)		0.0047(0)
Cd8	8f	0.90565(3)	0.75084(1)	0.34545(3)		0.0046(1)
Cd9	8f	0.84443(3)	0.74821(1)	0.09602(3)		0.0044(1)
Cd10	8f	0.88779(2)	0.55174(3)	0.52341(2)		0.0046(0)
Cd11	8f	0.61181(1)	0.83664(1)	0.36009(1)		0.0061(0)
Cd12	8f	0.79823(2)	0.59438(2)	0.04768(2)		0.0040(1)
Cd13	8f	0.73386(2)	0.54576(3)	0.35764(2)		0.0047(0)
Cd14	8f	0.65885(2)	0.59554(2)	0.25184(2)		0.0062(0)

Cd15	8f	0.77304(2)	0.44814(2)	0.13655(2)	0.0047(0)
Cd16	8f	0.77084(2)	0.62989(3)	0.18122(2)	0.0047(1)
Cd17	8f	0.82755(2)	0.34556(2)	-0.07707(2)	0.0040(1)
Cd18	8f	0.57036(2)	0.86703(3)	-0.01904(2)	0.0047(1)
Cd19	8f	1.00047(2)	0.40983(3)	0.40865(2)	0.0051(0)
Cd20	8f	0.83729(2)	0.41442(3)	0.25041(2)	0.0063(0)
Cd21	8f	0.49938(2)	0.58778(3)	0.08643(2)	0.0061(1)
Cd22	4e	0.5	0.35200(2)	0.25	0.0066(1)
Cd23	8f	0.67221(2)	0.34720(2)	0.07720(2)	0.0040(1)
Cd24	8f	0.84285(2)	0.59443(3)	0.29094(2)	0.0044(0)
Cd25	8f	0.79701(2)	0.90156(2)	0.04792(2)	0.0041(1)
Cd26	8f	0.39125(2)	0.54537(3)	0.01675(2)	0.0044(0)
Cd27	8f	0.57104(3)	0.74709(1)	0.08662(3)	0.0054(1)
Cd28	8f	0.42944(2)	0.36518(3)	0.02130(2)	0.0045(1)
Cd29	4e	0.5	0.16234(2)	0.25	0.0061(1)
Cd30	8f	0.66948(3)	0.74879(1)	0.17553(3)	0.0054(1)
Cd31	8f	0.72883(2)	0.36727(3)	0.32020(2)	0.0044(1)
Cd32	8f	0.69992(3)	0.75135(1)	0.04489(3)	0.0062(1)
Cd33	8f	0.70360(1)	0.77107(1)	0.45320(1)	0.0065(0)
Cd34	8f	0.63374(1)	0.65467(1)	0.38267(1)	0.0048(0)
Cd35	8f	0.95463(1)	0.49919(1)	0.29639(1)	0.0048(0)
Cd701	8f	0.53968(1)	0.67812(2)	0.30074(1)	0.0203(1)
Cd702	8f	0.55147(1)	0.81706(1)	0.20966(1)	0.0179(1)

VII. Anisotropic displacement parameters (Å^2) of the Cd_6Tb 1/1 approximant at 100K

Symbol	U_{22}	U_{33}	U_{12}	U_{13}	U_{23}
Tb1	0.00127(5)	0.00289(6)	0.00011(4)	0.00035(4)	-0.00030(5)
Tb2	0.00114(5)	0.00271(6)	-0.00028(4)	0.00038(4)	0.00007(5)
Tb3	0.00106(8)	0.00263(9)	0.00001(2)	0.00040(7)	0.00010(2)
Tb4	0.00064(9)	0.00316(9)	0.00004(2)	0.00089(8)	0.00005(2)
Tb5	0.00159(4)	0.00282(6)	-0.00013(4)	0.00090(4)	-0.00006(4)
Tb6	0.00172(4)	0.00272(6)	0.00016(4)	0.00102(4)	0.00024(4)
Cd1	0.00253(9)	0.00429(9)	0.00148(6)	0.00161(7)	0.00040(6)
Cd2	0.00215(8)	0.00575(8)	0.00075(4)	0.00242(6)	0.00070(4)
Cd3	0.00569(7)	0.00391(7)	-0.00007(6)	0.00090(5)	0.00034(7)
Cd4	0.00232(9)	0.00623(9)	-0.00019(7)	0.00119(7)	-0.00141(6)
Cd5	0.00363(9)	0.00295(12)	0.00014(5)	0.00055(9)	-0.00009(5)
Cd6	0.00204(13)	0.00485(15)	-0.00004(3)	0.00098(12)	0.00026(3)
Cd7	0.00248(9)	0.00660(9)	-0.00045(7)	0.00169(7)	-0.00115(6)
Cd8	0.00547(11)	0.00353(17)	-0.00021(4)	0.00050(9)	-0.00017(3)
Cd9	0.00192(9)	0.00492(16)	0.00016(4)	-0.00083(9)	-0.00001(4)

Cd10	0.00288(8)	0.00446(9)	-0.00107(6)	-0.00072(7)	0.00067(6)
Cd11	0.00301(6)	0.00758(7)	0.00087(5)	0.00257(5)	0.00086(5)
Cd12	0.00244(7)	0.00455(12)	-0.00041(7)	0.00014(6)	-0.00042(7)
Cd13	0.00243(8)	0.00749(9)	0.00011(6)	0.00002(6)	0.00092(6)
Cd14	0.00520(9)	0.00398(8)	-0.00450(7)	0.00044(7)	0.00043(7)
Cd15	0.00253(8)	0.00636(9)	-0.00052(6)	-0.00026(7)	0.00134(6)
Cd16	0.00488(11)	0.00466(11)	0.00055(8)	0.00074(9)	-0.00197(8)
Cd17	0.00239(8)	0.00356(12)	0.00093(9)	0.00097(7)	-0.00055(9)
Cd18	0.00456(11)	0.00397(10)	-0.00120(8)	0.00047(9)	0.00002(8)
Cd19	0.00302(9)	0.00807(10)	-0.00008(7)	0.00061(8)	0.00299(6)
Cd20	0.00563(10)	0.00345(8)	-0.00417(7)	0.00066(7)	0.00015(7)
Cd21	0.0051(1)	0.00858(10)	-0.00108(8)	-0.00050(8)	0.00470(7)
Cd22	0.00248(10)	0.00895(12)	0	-0.00233(8)	0
Cd23	0.00221(8)	0.00467(13)	-0.00035(8)	0.00093(7)	0.00110(9)
Cd24	0.00304(9)	0.00422(9)	0.00094(6)	0.00153(7)	0.00020(6)
Cd25	0.00235(7)	0.00457(12)	0.00048(7)	0.00014(6)	0.00080(7)
Cd26	0.00277(8)	0.00373(8)	-0.00087(6)	-0.00078(6)	0.00015(6)
Cd27	0.00242(11)	0.00788(14)	0.00000(4)	-0.00235(11)	-0.00036(5)
Cd28	0.00406(11)	0.00323(10)	0.00176(8)	0.00079(9)	0.00025(8)
Cd29	0.00256(10)	0.00781(11)	0	-0.00151(8)	0
Cd30	0.00159(12)	0.00592(15)	0.00093(4)	-0.00307(12)	-0.00041(3)
Cd31	0.00375(11)	0.00425(11)	0.00000(8)	0.00088(9)	-0.00152(8)
Cd32	0.0033(1)	0.00681(17)	-0.00024(4)	0.00445(11)	-0.00014(4)
Cd33	0.00800(8)	0.00544(6)	-0.00140(6)	0.00025(5)	-0.00139(5)
Cd34	0.00269(5)	0.00582(6)	-0.00037(5)	0.00124(5)	-0.00059(4)
Cd35	0.00632(7)	0.00414(7)	-0.00074(7)	0.00083(5)	0.00088(7)
Cd701	0.01087(9)	0.02450(13)	-0.00157(8)	-0.01701(10)	0.00665(8)
Cd702	0.00774(8)	0.02527(12)	-0.00184(7)	0.01732(9)	0.00136(8)

VIII. Structural information of Cd_6Tb 1/1 approximant at 150K

Symbol	*Wyckoff site*	x/a	y/b	z/c	Biso/eq
Tb1	8f	0.14783(7)	0.43861(6)	0.10147(7)	0.0088(2)
Tb2	8f	0.15137(7)	0.06124(6)	0.09996(7)	0.0085(2)
Tb3	8f	0.75374(10)	0.25167(2)	0.19457(9)	0.0085(4)
Tb4	8f	0.94413(9)	0.24943(2)	0.00515(11)	0.0091(5)
Tb5	8f	0.40481(6)	0.05213(6)	0.15520(6)	0.0089(2)
Tb6	8f	0.40405(6)	0.45435(6)	0.15488(6)	0.0089(2)
Cd1	8f	0.65954(11)	0.41385(13)	0.20897(11)	0.0125(4)
Cd2	8f	0.74703(4)	0.44070(12)	-0.00344(4)	0.0115(4)
Cd3	8f	0.54633(10)	0.51876(9)	0.20373(10)	0.0112(3)
Cd4	8f	0.95958(10)	0.59078(13)	0.41108(12)	0.0096(4)
Cd5	8f	0.87663(15)	0.75390(5)	0.22026(15)	0.0082(5)
Cd6	8f	0.97155(16)	0.75074(3)	0.12437(16)	0.0117(8)

Cd7	8f	0.54045(10)	0.40940(13)	0.09412(11)	0.0091(4)
Cd8	8f	0.90522(16)	0.75076(3)	0.34549(16)	0.0110(7)
Cd9	8f	0.84443(16)	0.74826(3)	0.09576(15)	0.0117(7)
Cd10	8f	0.88796(11)	0.55131(13)	0.52334(11)	0.0112(3)
Cd11	8f	0.61193(5)	0.83696(5)	0.36063(5)	0.0145(2)
Cd12	8f	0.79832(11)	0.59457(9)	0.04726(11)	0.0119(5)
Cd13	8f	0.73381(11)	0.54600(14)	0.35771(13)	0.0129(3)
Cd14	8f	0.65897(13)	0.59471(15)	0.25199(12)	0.0149(4)
Cd15	8f	0.77292(11)	0.44782(14)	0.13643(12)	0.0126(3)
Cd16	8f	0.77084(12)	0.63021(14)	0.18130(11)	0.0116(5)
Cd17	8f	0.82759(12)	0.34593(8)	-0.07689(10)	0.0102(6)
Cd18	8f	0.57022(12)	0.86727(15)	-0.01913(11)	0.0124(5)
Cd19	8f	1.00017(11)	0.40955(14)	0.40904(13)	0.0117(4)
Cd20	8f	0.83737(13)	0.41484(15)	0.25014(12)	0.0140(4)
Cd21	8f	0.49971(12)	0.58839(15)	0.08644(13)	0.0131(4)
Cd22	4e	0.5	0.35192(13)	0.25	0.0146(4)
Cd23	8f	0.67213(11)	0.34734(8)	0.07696(11)	0.0103(6)
Cd24	8f	0.84246(11)	0.59457(13)	0.29096(11)	0.0122(4)
Cd25	8f	0.79714(11)	0.90140(9)	0.04752(11)	0.0118(5)
Cd26	8f	0.39131(11)	0.54514(13)	0.01695(11)	0.0104(3)
Cd27	8f	0.57125(17)	0.74706(5)	0.08639(16)	0.0146(6)
Cd28	8f	0.42967(12)	0.36549(15)	0.02131(11)	0.0124(5)
Cd29	4e	0.5	0.16206(13)	0.25	0.0141(4)
Cd30	8f	0.66935(16)	0.74875(3)	0.17558(16)	0.0136(7)
Cd31	8f	0.72890(12)	0.36696(14)	0.32002(11)	0.0112(5)
Cd32	8f	0.7002(2)	0.75122(3)	0.04541(19)	0.0151(7)
Cd33	8f	0.70360(4)	0.77034(9)	0.45327(4)	0.0138(2)
Cd34	8f	0.63323(5)	0.65478(5)	0.38217(4)	0.0126(2)
Cd35	8f	0.95462(10)	0.49892(9)	0.29646(10)	0.0116(3)
Cd701	8f	0.53967(5)	0.67796(6)	0.30026(6)	0.0361(3)
Cd702	8f	0.55127(5)	0.81706(6)	0.20955(5)	0.0327(3)

IX. Anisotropic displacement parameters (Å^2) of the Cd_6Tb 1/1 approximant at 150K

Symbol	U_{11}	U_{22}	U_{33}	U_{12}	U_{13}	U_{23}
Tb1	0.0149(4)	0.0027(3)	0.0087(5)	-0.0002(3)	0.0023(3)	-0.0012(3)
Tb2	0.0147(4)	0.0025(3)	0.0084(5)	-0.0001(3)	0.0024(3)	0.0009(3)
Tb3	0.0131(7)	0.0007(6)	0.0117(8)	-0.00002(10)	0.0017(6)	0.00008(10)
Tb4	0.0134(7)	0.0006(7)	0.0132(9)	0.00005(8)	0.0038(6)	0.00002(8)
Tb5	0.0135(4)	0.0034(3)	0.0098(4)	0.0003(3)	0.0026(3)	-0.0005(2)
Tb6	0.0132(4)	0.0037(3)	0.0097(4)	0.0006(3)	0.0029(3)	-0.0002(2)
Cd1	0.0177(7)	0.0071(7)	0.0127(7)	0.0003(4)	0.0035(5)	0.0004(4)
Cd2	0.0190(7)	0.0036(6)	0.0117(6)	0.0007(2)	0.0042(5)	0.0010(2)

Cd3	0.0125(4)	0.0108(5)	0.0103(4)	-0.0007(4)	0.0008(3)	0.0008(4)
Cd4	0.0126(7)	0.0021(6)	0.0143(7)	-0.0010(4)	0.0022(5)	-0.0031(4)
Cd5	0.0131(9)	0.0040(8)	0.0074(9)	-0.0004(2)	0.0015(7)	0.0012(2)
Cd6	0.0171(13)	0.0003(11)	0.0175(15)	-0.00050(15)	0.0037(11)	0.00059(15)
Cd7	0.0130(7)	0.0023(6)	0.0121(7)	-0.0013(4)	0.0032(5)	-0.0026(4)
Cd8	0.0182(13)	0.0075(9)	0.0072(14)	-0.00018(15)	0.0023(7)	-0.00020(14)
Cd9	0.0183(13)	0.0030(7)	0.0138(13)	0.00014(17)	-0.0008(7)	-0.00017(17)
Cd10	0.0165(6)	0.0057(6)	0.0113(6)	-0.0006(4)	-0.0007(4)	0.0014(4)
Cd11	0.0209(5)	0.0043(3)	0.0183(5)	0.0014(3)	0.0046(3)	0.0025(3)
Cd12	0.0172(9)	0.0060(6)	0.0125(10)	0.0010(6)	0.0030(5)	-0.0010(5)
Cd13	0.0156(6)	0.0056(6)	0.0176(7)	0.0008(4)	0.0017(5)	0.0024(4)
Cd14	0.0230(7)	0.0122(7)	0.0097(6)	-0.0064(5)	0.0018(5)	-0.0002(4)
Cd15	0.0170(6)	0.0052(6)	0.0156(6)	0.0003(4)	0.0020(5)	0.0019(4)
Cd16	0.0155(8)	0.0083(8)	0.0111(9)	0.0002(6)	0.0028(7)	-0.0029(6)
Cd17	0.0211(12)	0.0019(6)	0.0077(11)	0.0026(6)	0.0038(5)	0.0008(6)
Cd18	0.0171(9)	0.0083(8)	0.0117(9)	-0.0019(6)	0.0021(7)	-0.0004(6)
Cd19	0.0129(7)	0.0037(7)	0.0184(7)	-0.0013(5)	0.0006(6)	0.0045(4)
Cd20	0.0229(7)	0.0092(6)	0.0101(6)	-0.0048(4)	0.0018(5)	0.0000(4)
Cd21	0.0141(8)	0.0074(7)	0.0178(7)	-0.0021(5)	0.0001(6)	0.0072(4)
Cd22	0.0200(7)	0.0053(7)	0.0186(8)	0	-0.0033(5)	0
Cd23	0.0205(12)	0.0012(6)	0.0091(11)	-0.0021(6)	0.0043(5)	0.0003(6)
Cd24	0.0177(7)	0.0060(6)	0.0129(7)	0.0005(4)	0.0035(5)	-0.0004(4)
Cd25	0.0177(9)	0.0055(6)	0.0123(10)	-0.0009(6)	0.0025(5)	0.0011(5)
Cd26	0.0161(6)	0.0045(5)	0.0106(6)	0.0007(4)	-0.0004(5)	0.0001(4)
Cd27	0.0203(11)	0.0062(10)	0.0173(12)	0.0004(2)	-0.0037(9)	-0.0009(2)
Cd28	0.0189(9)	0.0074(8)	0.0110(9)	0.0029(6)	0.0019(7)	0.0004(6)
Cd29	0.0190(7)	0.0066(7)	0.0167(8)	0	-0.0018(5)	0
Cd30	0.0279(15)	0.0017(10)	0.0114(12)	0.00125(17)	-0.0047(10)	-0.00053(15)
Cd31	0.0165(8)	0.0063(7)	0.0107(8)	-0.0008(6)	0.0031(7)	-0.0021(6)
Cd32	0.0274(15)	0.0057(8)	0.0120(13)	-0.00054(18)	0.0084(8)	-0.00045(17)
Cd33	0.0142(4)	0.0142(4)	0.0129(4)	-0.0023(4)	0.0007(2)	-0.0031(4)
Cd34	0.0204(4)	0.0041(3)	0.0132(4)	-0.0001(2)	0.0030(3)	-0.0009(2)
Cd35	0.0122(4)	0.0119(5)	0.0108(5)	-0.0015(4)	0.0008(3)	0.0012(4)
Cd701	0.0471(6)	0.0189(5)	0.0422(6)	-0.0016(3)	-0.0257(5)	0.0094(3)
Cd702	0.0405(5)	0.0140(4)	0.0436(6)	-0.0033(3)	0.0269(5)	0.0022(3)

X. Structural information of Cd_6Tb 1/1 approximant at 180K

Symbol	Wyckoff site	x/a	y/b	z/c	Biso/eq

Tb1	8f	0.34886(1)	0.06113(1)	0.09983(1)	0.004()
Tb2	8f	0.35211(1)	0.43872(1)	0.10125(1)	0.0041(0)
Tb3	8f	0.09480(1)	0.05186(1)	0.15487(1)	0.0041(0)
Tb4	8f	0.74637(2)	0.25153(1)	0.19447(2)	0.0040(1)
Tb5	8f	0.55549(2)	0.24947(1)	0.00529(2)	0.0044(1)
Tb6	8f	0.09547(1)	0.45412(1)	0.15462(1)	0.0042(0)
Cd1	8f	0.33067(5)	0.24874(1)	0.17560(4)	0.0111(2)
Cd2	8f	0.36725(1)	0.15476(2)	0.38180(1)	0.0100(1)
Cd3	8f	0.50044(3)	0.59011(4)	0.59101(3)	0.0088(1)
Cd4	8f	0.33727(3)	0.41429(4)	0.24958(3)	0.0106(1)
Cd5	8f	0.45915(3)	0.59090(3)	0.08875(3)	0.0074(1)
Cd6	8f	0.38765(2)	0.33713(2)	0.36090(2)	0.0122(1)
Cd7	8f	0.24725(1)	-0.44077(3)	0.00325(1)	0.0080(1)
Cd8	8f	0.34055(3)	-0.08613(3)	0.20928(3)	0.0079(1)
Cd9	8f	0.34252(3)	0.59387(3)	0.20929(3)	0.0079(1)
Cd10	8f	0.23334(2)	0.54581(4)	0.14203(3)	0.0082(1)
Cd11	8f	0.15544(4)	0.24837(1)	0.09598(4)	0.0074(1)
Cd12	8f	0.50055(3)	0.08819(4)	0.08685(3)	0.0108(1)
Cd13	8f	0.54087(3)	0.09060(3)	-0.09369(3)	0.0073(1)
Cd14	8f	0.22707(2)	-0.05147(4)	0.13661(3)	0.0078(1)
Cd15	8f	0.34078(3)	0.09460(4)	0.25142(3)	0.0115(1)
Cd16	8f	0.40573(4)	-0.24926(1)	0.15434(4)	0.0073(1)
Cd17	8f	0.4152(4)	0.2508(3)	0.0728(7)	-0.0044(17)
Cd17'	8f	0.42886(6)	0.24735(2)	0.08692(6)	0.0092(2)
Cd18	8f	0.38784(3)	0.44823(4)	0.47699(2)	0.0078(1)
Cd19	8f	0.39122(3)	0.04600(4)	0.48298(2)	0.0075(1)
Cd20	4e	0.5	0.66143(3)	0.25	0.0106(1)
Cd21	8f	0.45449(2)	0.49823(2)	0.20362(2)	0.0090(1)
Cd22	8f	0.42954(3)	0.63301(4)	0.48059(3)	0.0078(1)
Cd23	8f	0.42946(3)	0.13468(4)	-0.02141(3)	0.0075(1)
Cd24	8f	0.22908(3)	0.36746(4)	0.17987(3)	0.0073(1)
Cd25	8f	0.45354(2)	0.01812(2)	0.20381(2)	0.0081(1)
Cd26	8f	0.52924(3)	-0.24930(1)	0.12503(4)	0.0061(1)
Cd27	8f	0.22933(3)	0.12988(4)	0.18116(3)	0.0078(1)
Cd28	8f	0.37616(4)	-0.24617(2)	0.27886(3)	0.0065(1)
Cd29	8f	0.32755(3)	-0.15314(2)	0.07719(3)	0.0063(1)
Cd30	8f	0.20280(3)	0.40175(2)	0.04796(3)	0.0067(1)
Cd31	8f	0.30034(4)	0.25109(1)	0.04465(5)	0.0109(1)
Cd32	8f	0.29824(3)	0.40536(2)	-0.04768(3)	0.0066(1)
Cd33	8f	0.32727(3)	-0.34552(2)	0.07715(3)	0.0063(1)
Cd34	4e	0.5	-0.14885(3)	0.25	0.0114(1)
Cd35	8f	0.29646(2)	0.26934(3)	0.45323(2)	0.0119(1)
Cd701	8f	0.44913(2)	0.31691(3)	0.20934(2)	0.0391(1)
Cd702	8f	0.46025(3)	0.17799(3)	0.29994(3)	0.0439(2)

XI. Anisotropic displacement parameters (Å^2) of the Cd_6Tb 1/1 approximant at 180K

Symbol	U_{11}	U_{22}	U_{33}	U_{12}	U_{13}	U_{23}
Tb1	0.00540(9)	0.00255(6)	0.00395(9)	0.00048(6)	0.00069(5)	0.00014(7)
Tb2	0.00510(9)	0.00288(6)	0.00443(9)	-0.00031(6)	0.00092(5)	-0.00055(7)
Tb3	0.00433(8)	0.00350(6)	0.00455(9)	0.00027(6)	-0.00026(5)	-0.00020(6)
Tb4	0.00559(12)	0.0024(1)	0.00398(13)	-0.00002(3)	0.0000(1)	0.00017(3)
Tb5	0.00575(13)	0.00184(11)	0.00550(14)	-0.00012(3)	0.00052(11)	0.00007(3)
Tb6	0.00458(9)	0.00359(6)	0.00444(9)	-0.00032(6)	-0.00049(5)	0.00023(6)
Cd1	0.0188(3)	0.0041(2)	0.0105(3)	-0.00139(7)	0.0093(2)	-0.00058(6)
Cd2	0.01187(13)	0.00559(9)	0.01258(14)	0.00151(8)	-0.00379(9)	-0.00154(8)
Cd3	0.00563(15)	0.00632(14)	0.01439(18)	0.00004(11)	0.00026(14)	0.00590(11)
Cd4	0.01689(18)	0.00959(15)	0.00543(15)	-0.00735(12)	-0.00063(13)	0.00005(11)
Cd5	0.00708(15)	0.00372(13)	0.01124(17)	-0.00004(10)	-0.00126(12)	0.00228(10)
Cd6	0.01468(14)	0.00653(9)	0.01533(15)	-0.00268(9)	-0.00599(10)	0.00273(9)
Cd7	0.00982(16)	0.00396(12)	0.01024(17)	-0.00109(6)	-0.00322(11)	0.00115(6)
Cd8	0.01104(15)	0.00526(13)	0.00729(16)	-0.00244(10)	-0.00182(12)	0.00074(10)
Cd9	0.01050(15)	0.00610(13)	0.00715(16)	0.00208(11)	-0.00188(12)	-0.00098(10)
Cd10	0.00670(13)	0.00475(12)	0.01322(16)	-0.00016(9)	0.00176(11)	-0.00203(10)
Cd11	0.0114(3)	0.00376(12)	0.0070(2)	-0.00021(6)	0.00287(12)	-0.00008(6)
Cd12	0.00675(15)	0.00987(16)	0.01567(19)	0.00139(12)	0.00193(14)	0.00918(12)
Cd13	0.00760(15)	0.00388(13)	0.01037(16)	0.00039(10)	-0.00172(12)	-0.00166(10)
Cd14	0.00714(13)	0.00548(12)	0.01092(15)	0.00114(9)	0.00132(11)	0.00267(10)
Cd15	0.01736(18)	0.01120(15)	0.00609(15)	0.00942(13)	-0.00004(14)	0.00064(12)
Cd16	0.0063(2)	0.00969(15)	0.0060(2)	-0.00041(6)	0.00055(11)	0.00026(6)
Cd17	-0.011(2)	-0.012(2)	0.010(4)	0.0014(8)	-0.008(2)	0.0024(11)
Cd17'	0.0085(3)	0.00430(17)	0.0149(3)	0.00016(9)	0.0054(3)	-0.00017(9)
Cd18	0.01047(14)	0.00518(13)	0.00787(15)	0.00206(10)	0.00232(12)	0.00129(10)
Cd19	0.01124(14)	0.00528(12)	0.00606(13)	-0.00182(10)	0.00211(11)	-0.00056(10)
Cd20	0.0133(2)	0.00494(14)	0.0135(2)	0	0.00475(14)	0
Cd21	0.00582(12)	0.01435(12)	0.00672(13)	-0.00129(11)	-0.00041(8)	-0.00235(11)
Cd22	0.00743(16)	0.00895(16)	0.00697(17)	-0.00197(12)	-0.00026(13)	0.00052(13)
Cd23	0.00892(17)	0.00798(16)	0.00563(16)	-0.00297(12)	-0.00101(13)	0.00098(12)
Cd24	0.00702(16)	0.00734(15)	0.00754(18)	-0.00009(12)	0.00026(13)	0.00322(12)
Cd25	0.00586(12)	0.01218(11)	0.00628(12)	0.00104(10)	-0.00059(8)	0.00080(11)
Cd26	0.0059(2)	0.00448(18)	0.0079(2)	0.00015(5)	0.00079(16)	0.00045(5)
Cd27	0.00596(16)	0.00917(16)	0.00818(18)	-0.00084(12)	0.00030(13)	-0.00390(13)
Cd28	0.0083(2)	0.00650(15)	0.0047(2)	0.00007(7)	-0.00059(15)	0.00000(7)

Cd29	0.00806(19)	0.00412(10)	0.00676(19)	0.00090(12)	-0.00029(9)	0.00105(12)
Cd30	0.00779(18)	0.00481(10)	0.0075(2)	-0.00096(11)	0.00110(9)	0.00161(12)
Cd31	0.0150(3)	0.00646(14)	0.0114(3)	0.00027(6)	-0.00760(18)	-0.00007(6)
Cd32	0.00735(18)	0.00493(10)	0.0077(2)	0.00062(11)	0.00103(9)	-0.00099(12)
Cd33	0.00955(19)	0.00407(10)	0.00517(19)	-0.00162(12)	-0.00037(9)	-0.00048(12)
Cd34	0.0143(2)	0.00436(14)	0.0155(2)	0	0.00607(15)	0
Cd35	0.00873(12)	0.01772(12)	0.00910(13)	0.00250(12)	0.00053(9)	-0.00262(12)
Cd701	0.0444(3)	0.01803(16)	0.0548(3)	0.00477(16)	-0.0366(2)	0.00267(17)
Cd702	0.0543(3)	0.02405(19)	0.0533(3)	0.00128(19)	0.0380(2)	0.01339(19)

XII. Structural information of Cd_6Tb 1/1 approximant at 184K

Symbol	Wyckoff site	x/a	y/b	z/c	Biso/eq
Tb1	8f	-0.09984(2)	-0.06110(1)	-0.34886(2)	0.004()
Tb2	8f	-0.10124(2)	-0.43874(1)	-0.35206(2)	0.0042(0)
Tb3	8f	-0.15488(2)	-0.05183(1)	-0.09478(2)	0.0042(0)
Tb4	8f	-0.19448(2)	-0.25151(1)	-0.74634(2)	0.0041(1)
Tb5	8f	-0.00527(2)	-0.24949(1)	-0.55547(2)	0.0045(1)
Tb6	8f	-0.15462(2)	-0.45407(1)	-0.09546(2)	0.0043(0)
Cd1	8f	-0.17561(5)	-0.24875(1)	-0.33083(5)	0.0118(2)
Cd2	8f	-0.38169(2)	-0.15479(2)	-0.36737(2)	0.0105(1)
Cd3	8f	-0.59097(3)	-0.59010(4)	-0.50043(3)	0.0089(1)
Cd4	8f	-0.24961(3)	-0.41421(4)	-0.33728(3)	0.0109(1)
Cd5	8f	-0.08886(3)	-0.59091(4)	-0.45912(3)	0.0074(1)
Cd6	8f	-0.36101(2)	-0.33718(2)	-0.38754(2)	0.0127(1)
Cd7	8f	-0.00319(1)	0.44074(3)	-0.24729(1)	0.0080(1)
Cd8	8f	-0.20929(3)	0.08618(4)	-0.34050(3)	0.0080(1)
Cd9	8f	-0.20930(3)	-0.59381(4)	-0.34244(3)	0.0080(1)
Cd10	8f	-0.14196(3)	-0.54580(4)	-0.23330(3)	0.0083(1)
Cd11	8f	-0.09590(4)	-0.24840(1)	-0.15541(4)	0.0076(1)
Cd12	8f	-0.08686(3)	-0.08819(4)	-0.50054(3)	0.0109(1)
Cd13	8f	0.09372(3)	-0.09061(4)	-0.54088(3)	0.0073(1)
Cd14	8f	-0.13662(3)	0.05138(4)	-0.22712(3)	0.0079(1)
Cd15	8f	-0.25141(3)	-0.09458(4)	-0.34075(3)	0.0117(1)
Cd16	8f	-0.15432(4)	0.24926(1)	-0.40569(4)	0.0075(1)
Cd17	8f	-0.08695(8)	-0.24734(3)	-0.42906(8)	0.0092(2)
Cd17'	8f	-0.0735(6)	-0.2506(3)	-0.4154(5)	-0.0034(14)
Cd18	8f	-0.47702(3)	-0.44819(4)	-0.38789(3)	0.0079(1)
Cd19	8f	-0.48293(3)	-0.04614(4)	-0.39122(3)	0.0077(1)
Cd20	4e	-0.25	-0.66128(3)	-0.5	0.0107(1)
Cd21	8f	-0.20364(3)	-0.49812(3)	-0.45443(3)	0.0092(1)

Cd22	8f	-0.48051(3)	-0.63314(4)	-0.42952(3)	0.0080(1)
Cd23	8f	0.02145(3)	-0.13477(4)	-0.42945(3)	0.0076(1)
Cd24	8f	-0.17988(3)	-0.36760(4)	-0.22911(3)	0.0074(1)
Cd25	8f	-0.20381(3)	-0.01803(3)	-0.45350(3)	0.0083(1)
Cd26	8f	-0.12511(4)	0.24931(1)	-0.52927(4)	0.0062(1)
Cd27	8f	-0.18117(3)	-0.12976(4)	-0.22936(3)	0.0078(1)
Cd28	8f	-0.27885(4)	0.24623(2)	-0.37617(4)	0.0065(1)
Cd29	8f	-0.07716(3)	0.15314(2)	-0.32756(3)	0.0064(1)
Cd30	8f	-0.04793(3)	-0.40181(2)	-0.20276(3)	0.0068(1)
Cd31	8f	-0.04447(5)	-0.25107(1)	-0.30046(5)	0.0110(1)
Cd32	8f	0.04765(3)	-0.40535(2)	-0.29827(3)	0.0067(1)
Cd33	8f	-0.07713(3)	0.34555(2)	-0.32730(3)	0.0063(1)
Cd34	4e	-0.25	0.14891(3)	-0.5	0.0114(1)
Cd35	8f	-0.45325(2)	-0.26914(3)	-0.29644(2)	0.0122(1)
Cd701	8f	-0.20932(3)	-0.31691(3)	-0.44919(3)	0.0407(2)
Cd702	8f	-0.29994(3)	-0.17800(3)	-0.46027(3)	0.0456(2)

XIII. Anisotropic displacement parameters (Å^2) of the Cd_6Tb 1/1 approximant at 184K

Symbol	U_{11}	U_{22}	U_{33}	U_{12}	U_{13}	U_{23}
Tb1	0.00404(10)	0.00245(7)	0.00553(10)	0.00008(7)	0.00057(6)	0.00057(7)
Tb2	0.00451(10)	0.00275(7)	0.00532(10)	-0.00051(7)	0.00076(6)	-0.00040(7)
Tb3	0.00444(10)	0.00334(6)	0.00477(10)	-0.00017(6)	-0.00046(6)	0.00025(6)
Tb4	0.00383(14)	0.00247(11)	0.00585(13)	0.00016(3)	-0.00012(11)	0.00000(4)
Tb5	0.00563(15)	0.00156(12)	0.00624(15)	0.00007(3)	0.00019(13)	-0.00014(3)
Tb6	0.00429(10)	0.00350(6)	0.00497(10)	0.00023(6)	-0.00067(6)	-0.00031(6)
Cd1	0.0106(3)	0.0042(2)	0.0206(4)	-0.00057(7)	0.0099(3)	-0.00129(7)
Cd2	0.01331(16)	0.00561(10)	0.01247(15)	-0.00168(9)	-0.00431(10)	0.00167(9)
Cd3	0.0147(2)	0.00604(16)	0.00602(17)	0.00616(12)	0.00023(15)	0.00012(12)
Cd4	0.00562(17)	0.00978(16)	0.0172(2)	0.00005(13)	-0.00063(15)	-0.00753(13)
Cd5	0.01147(19)	0.00355(14)	0.00732(16)	0.00222(12)	-0.00149(14)	0.00001(11)
Cd6	0.01610(17)	0.00665(10)	0.01548(16)	0.00295(10)	-0.00654(11)	-0.00298(10)
Cd7	0.01028(19)	0.00375(13)	0.01003(18)	0.00109(7)	-0.00333(13)	-0.00108(7)
Cd8	0.00734(17)	0.00529(14)	0.01122(17)	0.00064(11)	-0.00187(14)	-0.00232(12)
Cd9	0.00717(17)	0.00621(15)	0.01072(17)	-0.00091(12)	-0.00200(14)	0.00210(12)
Cd10	0.01349(18)	0.00458(13)	0.00680(14)	-0.00217(12)	0.00175(13)	-0.00013(10)
Cd11	0.0066(3)	0.00370(14)	0.0124(3)	-0.00015(6)	0.00279(14)	-0.00020(6)
Cd12	0.0159(2)	0.00957(18)	0.00708(17)	0.00946(13)	0.00188(16)	0.00143(14)
Cd13	0.01025(18)	0.00373(14)	0.00782(17)	-0.00161(11)	-0.00193(13)	0.00037(11)
Cd14	0.01104(17)	0.00545(14)	0.00734(15)	0.00288(12)	0.00114(13)	0.00124(11)

Cd15	0.00625(17)	0.01130(17)	0.0177(2)	0.00049(13)	-0.00021(15)	0.00956(14)
Cd16	0.0062(3)	0.00983(17)	0.0066(3)	0.00027(6)	0.00049(13)	-0.00039(6)
Cd17	0.0152(4)	0.00421(19)	0.0082(4)	-0.00007(11)	0.0053(3)	0.00033(11)
Cd17'	0.00801(16)	0.00492(14)	0.01072(15)	0.00134(11)	0.00246(13)	0.00201(11)
Cd18	0.00628(15)	0.00530(13)	0.01146(16)	-0.00079(11)	0.00211(13)	-0.00178(11)
Cd19	0.0135(3)	0.00515(16)	0.0135(2)	0	0.00470(16)	0
Cd20	0.00684(14)	0.01476(14)	0.00600(13)	-0.00244(12)	-0.00045(9)	-0.00119(12)
Cd21	0.00722(19)	0.00884(18)	0.00786(19)	0.00052(14)	-0.00053(15)	-0.00202(13)
Cd22	0.00576(18)	0.00781(17)	0.00931(19)	0.00103(13)	-0.00121(15)	-0.00298(13)
Cd23	0.00754(19)	0.00734(17)	0.00740(18)	0.00338(14)	0.00011(15)	-0.00003(13)
Cd24	0.00640(14)	0.01241(13)	0.00597(13)	0.00086(12)	-0.00065(9)	0.00130(11)
Cd25	0.0082(3)	0.00417(19)	0.0062(2)	0.00044(6)	0.00063(18)	0.00017(6)
Cd26	0.0082(2)	0.00903(18)	0.00632(18)	-0.00394(14)	0.00016(15)	-0.00085(13)
Cd27	0.0048(2)	0.00650(17)	0.0083(2)	0.00000(8)	-0.00080(16)	0.00007(8)
Cd28	0.0068(2)	0.00396(11)	0.0085(2)	0.00111(14)	-0.0004(1)	0.00087(13)
Cd29	0.0077(2)	0.00460(11)	0.0081(2)	0.00168(13)	0.00096(11)	-0.00105(12)
Cd30	0.0116(3)	0.00645(15)	0.0150(3)	0.00005(7)	-0.0077(2)	0.00025(7)
Cd31	0.0078(2)	0.00461(11)	0.0076(2)	-0.00105(13)	0.00087(10)	0.00064(12)
Cd32	0.0051(2)	0.00392(11)	0.0100(2)	-0.00053(13)	-0.00048(10)	-0.00159(13)
Cd33	0.0156(3)	0.00424(15)	0.0145(3)	0	0.00593(17)	0
Cd34	0.00940(14)	0.01853(13)	0.00881(13)	-0.00268(14)	0.00054(10)	0.00268(13)
Cd35	0.0552(3)	0.0249(2)	0.0568(4)	0.0138(2)	0.0396(3)	0.0012(2)
Cd701	0.007(3)	-0.0093(17)	-0.007(2)	0.0013(9)	-0.004(2)	0.0013(7)
Cd702	0.0570(3)	0.01866(18)	0.0464(3)	0.00279(19)	-0.0381(3)	0.00497(18)

XIV. Structural information of Cd_6Tb 1/1 approximant at 186K

Symbol	Wyckoff site	x/a	y/b	z/c	Biso/eq
Tb1	8f	0.14833(2)	0.43892(2)	0.10085(2)	0.0049(1)
Tb2	8f	0.15139(2)	0.06094(2)	0.09950(2)	0.0043(1)
Tb3	8f	0.75381(2)	0.25149(1)	0.19467(3)	0.0049(1)
Tb4	8f	0.94493(2)	0.24949(1)	0.00519(3)	0.0051(1)
Tb5	8f	0.40544(2)	0.05147(2)	0.15511(2)	0.0049(1)
Tb6	8f	0.40479(2)	0.45430(2)	0.15487(2)	0.0047(1)
Cd1	8f	0.65926(3)	0.41345(4)	0.20884(3)	0.0080(1)
Cd2	8f	0.74739(1)	0.44062(4)	-0.00308(1)	0.0091(1)

Cd3	8f	0.54685(3)	0.51736(3)	0.20369(3)		0.0072(1)
Cd4	8f	0.95912(3)	0.59087(4)	0.41099(3)		0.0081(1)
Cd5	8f	0.87620(4)	0.75357(2)	0.22104(4)		0.0065(1)
Cd6	8f	0.97084(4)	0.75069(2)	0.12531(5)		0.0074(2)
Cd7	8f	0.54081(3)	0.40942(4)	0.09369(3)		0.0078(1)
Cd8	8f	0.90528(4)	0.75069(2)	0.34566(4)		0.0071(2)
Cd9	8f	0.84492(5)	0.74840(2)	0.09543(5)		0.0092(2)
Cd10	8f	0.88796(3)	0.55170(4)	0.52282(3)		0.0083(1)
Cd11	8f	0.61297(2)	0.83745(3)	0.36165(2)		0.0144(1)
Cd12	8f	0.79837(3)	0.59448(3)	0.04775(3)		0.0072(1)
Cd13	8f	0.73285(3)	0.54676(4)	0.35816(4)		0.0096(1)
Cd14	8f	0.65913(4)	0.59418(5)	0.25113(4)		0.0124(1)
Cd15	8f	0.77306(3)	0.44789(4)	0.13670(4)		0.0078(1)
Cd16	8f	0.77107(3)	0.62956(5)	0.18133(4)		0.0093(1)
Cd17	8f	0.82720(3)	0.34546(3)	-0.07716(3)		0.0070(1)
Cd18	8f	0.57037(3)	0.86785(5)	-0.01952(3)		0.0094(1)
Cd19	8f	1.00015(3)	0.40940(5)	0.40944(4)		0.0100(1)
Cd20	8f	0.83757(4)	0.41433(5)	0.25060(4)		0.0112(1)
Cd21	8f	0.49977(4)	0.58876(5)	0.08661(4)		0.0117(1)
Cd22	4e	0.5	0.35067(4)	0.25		0.0099(1)
Cd23	8f	0.67255(3)	0.34675(3)	0.07718(3)		0.0070(1)
Cd24	8f	0.84259(3)	0.59380(4)	0.29114(3)		0.0077(1)
Cd25	8f	0.79738(3)	0.90205(3)	0.04802(3)		0.0074(1)
Cd26	8f	0.39111(3)	0.54618(4)	0.01723(3)		0.0080(1)
Cd27	8f	0.57089(4)	0.74741(2)	0.08905(5)		0.0120(2)
Cd28	8f	0.42954(3)	0.36620(5)	0.02145(3)		0.0093(1)
Cd29	4e	0.5	0.16074(4)	0.25		0.0094(1)
Cd30	8f	0.67194(5)	0.74880(2)	0.17391(5)		0.0171(2)
Cd31	8f	0.72869(3)	0.36779(5)	0.31993(3)		0.0089(1)
Cd32	8f	0.70194(9)	0.75115(2)	0.04656(9)		0.0218(3)
Cd33	8f	0.70351(2)	0.76796(4)	0.45329(2)		0.0136(1)
Cd34	8f	0.63205(2)	0.65501(2)	0.38115(2)		0.0123(1)
Cd35	8f	0.95405(3)	0.49725(3)	0.29642(3)		0.0085(1)
Cd701	8f	0.54013(4)	0.67738(6)	0.29928(7)	0.917	0.0437(3)
Cd702	8f	0.55077(3)	0.81690(4)	0.20930(3)	0.882	0.0372(2)
Cd704	8f	0.5432(3)	0.8412(3)	0.2740(3)	0.125	0.0224(13)
Cd705	8f	0.5402(4)	0.6595(4)	0.2711(4)	0.076	0.0149(17)

XV. Anisotropic displacement parameters (Å^2) of the Cd_6Tb 1/1 approximant at 186K

Symbol	U_{11}	U_{22}	U_{33}	U_{12}	U_{13}	U_{23}
Tb1	0.00544(11)	0.00459(9)	0.00459(12)	0.00016(8)	-0.00207(7)	-0.00096(9)
Tb2	0.00477(11)	0.00422(8)	0.00377(12)	-0.00017(8)	-0.00107(7)	0.00052(9)
Tb3	0.00584(15)	0.00407(14)	0.00492(17)	-0.00006(4)	0.00047(13)	0.00008(4)

Tb4	0.00607(16)	0.00294(15)	0.00631(18)	0.00020(4)	-0.00230(14)	0.00004(4)
Tb5	0.00457(11)	0.00558(8)	0.00452(12)	-0.00066(8)	-0.00079(7)	-0.00041(8)
Tb6	0.00494(11)	0.00477(8)	0.00449(12)	0.00030(7)	-0.00051(7)	0.00005(8)
Cd1	0.01096(19)	0.00602(17)	0.0071(2)	0.00293(13)	0.00098(15)	0.00148(13)
Cd2	0.0107(2)	0.00551(17)	0.0109(2)	0.00091(8)	0.00311(16)	0.00089(8)
Cd3	0.00423(14)	0.01129(13)	0.00597(16)	-0.00164(12)	0.00033(10)	0.00094(13)
Cd4	0.00696(19)	0.00582(18)	0.0114(2)	-0.00001(14)	-0.00016(15)	-0.00255(14)
Cd5	0.0093(3)	0.0068(2)	0.0034(2)	0.00001(9)	0.00056(19)	0.00016(8)
Cd6	0.0069(3)	0.0077(3)	0.0076(3)	-0.00005(7)	-0.0018(2)	0.00036(7)
Cd7	0.00738(19)	0.00593(18)	0.0101(2)	-0.00036(14)	0.00047(15)	-0.00194(14)
Cd8	0.0052(3)	0.00913(19)	0.0071(3)	-0.00030(7)	-0.00134(16)	-0.00022(7)
Cd9	0.0121(3)	0.00625(18)	0.0091(3)	0.00037(8)	-0.00511(18)	-0.00037(8)
Cd10	0.01077(18)	0.00662(16)	0.00764(19)	-0.00196(13)	-0.00261(15)	0.00130(13)
Cd11	0.0174(2)	0.00713(12)	0.0186(2)	0.00337(12)	0.00901(14)	0.00329(13)
Cd12	0.0084(2)	0.00646(14)	0.0068(3)	-0.00061(15)	-0.00171(13)	-0.00085(15)
Cd13	0.00794(17)	0.00723(16)	0.0137(2)	-0.00127(13)	-0.00289(15)	0.00282(14)
Cd14	0.0172(2)	0.0134(2)	0.0065(2)	-0.00950(17)	-0.00004(18)	0.00105(16)
Cd15	0.00658(16)	0.00579(15)	0.01116(19)	0.00018(12)	-0.00139(14)	0.00187(13)
Cd16	0.0064(2)	0.0132(2)	0.0083(2)	0.00016(16)	-0.00089(17)	-0.00373(18)
Cd17	0.0114(2)	0.00575(14)	0.0038(2)	0.00140(16)	-0.00053(12)	-0.00059(15)
Cd18	0.0074(2)	0.0131(2)	0.0077(2)	-0.00272(17)	-0.00056(17)	-0.00187(18)
Cd19	0.00596(19)	0.0078(2)	0.0162(2)	0.00040(15)	-0.00088(18)	0.00609(15)
Cd20	0.0174(2)	0.01079(19)	0.00551(19)	-0.00765(16)	0.00075(17)	-0.00033(15)
Cd21	0.0070(2)	0.0120(2)	0.0162(2)	-0.00079(16)	-0.00194(18)	0.00988(16)
Cd22	0.0117(3)	0.00429(17)	0.0138(3)	0	-0.00476(18)	0
Cd23	0.0100(2)	0.00583(14)	0.0051(2)	-0.00079(16)	-0.00064(12)	0.00122(15)
Cd24	0.01000(19)	0.00618(16)	0.0071(2)	0.00204(13)	0.00062(15)	0.00047(13)
Cd25	0.0089(2)	0.00686(14)	0.0066(3)	0.00125(15)	-0.00170(13)	0.00140(15)
Cd26	0.01142(18)	0.00678(16)	0.00576(17)	-0.00160(13)	-0.00227(14)	0.00065(12)
Cd27	0.0107(3)	0.0088(2)	0.0163(3)	-0.00024(9)	-0.0073(2)	0.00173(10)
Cd28	0.0090(2)	0.0127(2)	0.0061(2)	0.00370(17)	-0.00004(17)	0.00177(17)
Cd29	0.0108(3)	0.00552(18)	0.0119(3)	0	-0.00353(17)	0
Cd30	0.0253(4)	0.0045(2)	0.0214(4)	0.00262(10)	-0.0185(3)	-0.00160(9)
Cd31	0.0073(2)	0.0117(2)	0.0078(2)	-0.00110(16)	-0.00067(17)	-0.00339(17)
Cd32	0.0300(6)	0.0092(2)	0.0263(6)	-0.00137(11)	0.0221(3)	-0.00092(11)
Cd33	0.00876(16)	0.02254(16)	0.00946(18)	-0.00227(17)	-0.00046(12)	-

Cd34	0.01509(19)	0.00632(12)	0.0156(2)	-0.00240(11)	0.00685(13)	0.00286(17) - 0.00245(11)
Cd35	0.00455(15)	0.01439(15)	0.00657(16)	0.00036(13)	0.00011(10)	0.00186(14)
Cd701	0.0516(5)	0.0246(3)	0.0551(8)	-0.0034(3)	-0.0396(4)	0.0164(4)
Cd702	0.0423(4)	0.0175(2)	0.0516(4)	-0.0041(2)	0.0352(3)	0.0029(2)
Cd704	0.022(2)	0.0044(12)	0.040(3)	-0.0076(12)	-0.003(2)	-0.0041(14)
Cd705	0.019(3)	0.007(2)	0.018(4)	0.0091(17)	-0.020(3)	-0.0004(19)

XVI. Structural information of Cd_6Tb 1/1 approximant at 188K

Symbol	Wyckoff site	x/a	y/b	z/c	Biso/eq
Tb1	8f	-0.09987(2)	-0.06085(2)	-0.34915(2)	0.0054(1)
Tb2	8f	-0.10091(2)	-0.43907(2)	-0.35144(2)	0.0056(1)
Tb3	8f	-0.15508(2)	-0.05121(2)	-0.09480(2)	0.0052(1)
Tb4	8f	-0.19479(2)	-0.25110(1)	-0.74581(2)	0.0054(1)
Tb5	8f	-0.00524(2)	-0.24964(1)	-0.55526(2)	0.0060(1)
Tb6	8f	-0.15488(2)	-0.45299(2)	-0.09527(2)	0.0054(1)
Cd1	8f	-0.17334(5)	-0.24918(2)	-0.32882(6)	0.0190(2)
Cd2	8f	-0.37930(3)	-0.15541(3)	-0.37020(3)	0.0182(1)
Cd3	8f	-0.59068(3)	-0.59040(4)	-0.50018(3)	0.0106(1)
Cd4	8f	-0.24988(4)	-0.41379(5)	-0.33740(4)	0.0132(1)
Cd5	8f	-0.08911(4)	-0.59063(4)	-0.45905(3)	0.0093(1)
Cd6	8f	-0.36430(3)	-0.33886(3)	-0.38485(3)	0.0228(2)
Cd7	8f	-0.00230(1)	0.44065(4)	-0.24805(1)	0.0104(2)
Cd8	8f	-0.20913(3)	0.08784(4)	-0.34099(4)	0.0097(1)
Cd9	8f	-0.20914(3)	-0.59330(4)	-0.34236(3)	0.0092(1)
Cd10	8f	-0.14103(4)	-0.54710(4)	-0.23203(3)	0.0103(1)
Cd11	8f	-0.09521(4)	-0.24889(2)	-0.15506(4)	0.0086(2)
Cd12	8f	-0.08773(4)	-0.08901(5)	-0.50023(3)	0.0126(1)
Cd13	8f	0.09262(4)	-0.09043(4)	-0.54091(3)	0.0095(1)
Cd14	8f	-0.13719(4)	0.05105(4)	-0.22762(3)	0.0090(1)
Cd15	8f	-0.25117(4)	-0.09260(5)	-0.33998(4)	0.0148(2)
Cd16	8f	-0.15429(4)	0.24947(2)	-0.40513(4)	0.0086(2)
Cd17	8f	-0.08847(5)	-0.24811(2)	-0.42940(5)	0.0137(2)
Cd18	8f	-0.47751(3)	-0.44898(4)	-0.38835(4)	0.0099(1)
Cd19	8f	-0.48177(3)	-0.04692(4)	-0.39076(4)	0.0101(1)
Cd21	8f	-0.20354(4)	-0.49502(4)	-0.45429(3)	0.0153(1)
Cd22	8f	-0.48039(3)	-0.63261(5)	-0.42939(3)	0.0094(1)
Cd23	8f	0.02106(3)	-0.13383(5)	-0.42930(3)	0.0092(1)
Cd24	8f	-0.17999(3)	-0.36800(5)	-0.22889(3)	0.0098(1)
Cd25	8f	-0.20368(3)	-0.01741(4)	-0.45370(3)	0.0117(1)
Cd26	8f	-0.12512(4)	0.24950(2)	-0.52908(4)	0.0079(2)
Cd27	8f	-0.18097(4)	-0.13005(5)	-0.22906(3)	0.0102(1)

Cd28	8f	-0.27866(4)	0.24731(2)	-0.37590(4)		0.0078(2)
Cd29	8f	-0.07720(3)	0.15345(3)	-0.32736(3)		0.0078(1)
Cd30	8f	-0.04749(3)	-0.40261(3)	-0.20235(3)		0.0079(1)
Cd31	8f	-0.04797(8)	-0.25080(2)	-0.29720(7)		0.0208(3)
Cd32	8f	0.04728(3)	-0.40508(3)	-0.29840(3)		0.0076(1)
Cd33	8f	-0.07719(3)	0.34559(3)	-0.32716(3)		0.0077(1)
Cd35	8f	-0.45356(4)	-0.26397(4)	-0.29653(4)		0.0198(1)
Cd20	4e	-0.25	-0.84914(5)	-0.5		0.0153(2)
Cd34	4e	-0.25	-0.65974(5)	-0.5		0.0142(2)
Cd701	8f	-0.3000(3)	-0.17632(19)	-0.4612(3)	0.52	0.0352(9)
Cd702	8f	-0.20959(8)	-0.31666(6)	-0.44898(7)	0.705	0.0386(4)
Cd703	8f	-0.2413(3)	-0.2518(2)	-0.4189(3)	0.247	0.072(4)
Cd704	8f	-0.3110(14)	-0.192(2)	-0.4675(13)	0.09	0.062(5)
Cd705	8f	-0.2773(3)	-0.3372(4)	-0.4555(3)	0.162	0.0326(14)
Cd706	8f	-0.2803(7)	-0.1709(5)	-0.4516(3)	0.214	0.0452(19)
Cd707	8f	-0.2857(9)	-0.1855(7)	-0.5550(9)	0.07	0.063(6)

XVII. Anisotropic displacement parameters (Å^2) of the Cd_6Tb 1/1 approximant at 188K

Symbol	U_{11}	U_{22}	U_{33}	U_{12}	U_{13}	U_{23}
Tb1	0.00534(13)	0.00363(8)	0.00709(12)	0.00062(9)	0.00204(8)	-0.00005(8)
Tb2	0.00582(13)	0.00383(8)	0.00713(12)	-0.00103(9)	0.00243(8)	-0.00001(8)
Tb3	0.00457(13)	0.00451(8)	0.00659(12)	0.00022(8)	0.00106(8)	0.00058(8)
Tb4	0.00370(16)	0.00328(13)	0.00907(17)	-0.00001(4)	0.00035(13)	0.00021(5)
Tb5	0.00674(17)	0.00227(13)	0.00885(17)	0.00004(4)	0.00197(14)	-0.00015(4)
Tb6	0.00462(13)	0.00481(8)	0.00678(13)	-0.00047(8)	0.00083(8)	-0.00044(8)
Cd1	0.0207(4)	0.00180(19)	0.0346(5)	-0.00122(9)	0.0233(4)	-0.00171(10)
Cd2	0.0224(3)	0.00683(14)	0.0252(3)	-0.00335(15)	-0.01369(18)	0.00335(16)
Cd3	0.0165(3)	0.00777(19)	0.0075(2)	0.00757(16)	0.0023(2)	0.00016(16)
Cd4	0.0073(2)	0.0112(2)	0.0210(3)	0.00022(17)	0.0001(2)	-0.00823(18)
Cd5	0.0132(3)	0.00465(17)	0.0099(2)	0.00274(15)	-0.00039(18)	-0.00005(15)
Cd6	0.0325(4)	0.00905(16)	0.0268(3)	0.00819(19)	-0.0187(2)	-0.00729(18)
Cd7	0.0125(3)	0.00510(17)	0.0136(3)	0.00081(9)	-0.00351(19)	-0.00081(9)
Cd8	0.0075(2)	0.00721(18)	0.0144(2)	0.00139(15)	-0.00051(18)	-0.00200(16)
Cd9	0.0075(2)	0.00651(17)	0.0137(2)	-0.00117(15)	-0.00032(18)	0.00092(16)
Cd10	0.0139(2)	0.00631(17)	0.0107(2)	-0.00335(15)	0.00477(18)	-0.00137(14)
Cd11	0.0093(3)	0.00443(17)	0.0121(3)	-0.00035(8)	0.00547(18)	-0.00023(8)
Cd12	0.0185(3)	0.0110(2)	0.0084(2)	0.01094(17)	0.0031(2)	0.00105(17)
Cd13	0.0135(3)	0.00465(17)	0.0104(2)	-0.00256(16)	-0.00061(19)	0.00016(15)
Cd14	0.0114(2)	0.00605(16)	0.00948(19)	0.00305(15)	0.00345(17)	0.00085(14)
Cd15	0.0076(2)	0.0148(2)	0.0221(3)	0.00065(18)	0.0006(2)	0.0110(2)
Cd16	0.0073(3)	0.00940(19)	0.0090(3)	0.00018(8)	0.00148(17)	-0.00015(8)
Cd17	0.0225(4)	0.0083(2)	0.0105(3)	0.00093(10)	0.0086(2)	0.00039(9)
Cd18	0.0101(2)	0.00653(17)	0.0129(2)	0.00178(15)	0.00357(18)	0.00243(15)

Cd19	0.0101(2)	0.00665(17)	0.0134(2)	-0.00163(15)	0.00345(18)	-0.00211(15)
Cd21	0.0097(2)	0.0288(2)	0.0073(2)	-0.00304(19)	0.00055(14)	-0.00262(18)
Cd22	0.0093(2)	0.0110(2)	0.0079(2)	0.00059(17)	0.00071(18)	-0.00313(16)
Cd23	0.0083(2)	0.0104(2)	0.0090(2)	0.00078(17)	0.00017(18)	-0.00370(16)
Cd24	0.0103(2)	0.0109(2)	0.0082(2)	0.00431(17)	0.00129(18)	-0.00121(16)
Cd25	0.0099(2)	0.01729(18)	0.00785(19)	0.00205(16)	0.00016(13)	0.00250(15)
Cd26	0.0112(3)	0.0063(2)	0.0062(3)	0.00035(8)	0.0021(2)	0.00014(8)
Cd27	0.0109(3)	0.0124(2)	0.0074(2)	-0.00479(18)	0.00136(18)	0.00041(16)
Cd28	0.0067(3)	0.0074(2)	0.0093(3)	0.00020(9)	0.0009(2)	0.00039(9)
Cd29	0.0068(2)	0.00484(13)	0.0117(2)	0.00147(15)	0.00077(14)	0.00097(15)
Cd30	0.0033(2)	0.00611(14)	0.0143(2)	0.00019(14)	0.00238(14)	-0.00180(15)
Cd31	0.0283(6)	0.0073(2)	0.0269(5)	-0.00110(11)	-0.0206(3)	0.00130(11)
Cd32	0.0036(2)	0.00548(13)	0.0137(2)	-0.00018(14)	0.00207(13)	0.00116(15)
Cd33	0.0056(2)	0.00480(13)	0.0127(2)	-0.00097(15)	0.00077(14)	-0.00137(15)
Cd35	0.0112(3)	0.0376(2)	0.0104(2)	-0.0035(2)	0.00035(17)	0.0016(2)
Cd20	0.0211(4)	0.0061(2)	0.0188(4)	0	0.0109(3)	0
Cd34	0.0189(4)	0.00602(20)	0.0177(4)	0	0.0092(2)	0
Cd701	0.042(2)	0.020(1)	0.0437(18)	0.0112(12)	0.0224(15)	-0.0015(12)
Cd702	0.0534(8)	0.0169(3)	0.0453(7)	0.0040(4)	-0.0389(6)	0.0020(4)
Cd703	0.0134(19)	0.186(13)	0.0152(18)	0.0031(13)	-0.0045(14)	0.0019(13)
Cd704	0.052(8)	0.078(9)	0.055(8)	0.066(8)	0.065(7)	0.063(7)
Cd705	0.043(3)	0.027(2)	0.028(2)	-0.0119(18)	0.003(2)	0.0248(17)
Cd706	0.041(4)	0.050(3)	0.045(3)	0.023(2)	-0.007(2)	-0.045(3)
Cd707	0.077(12)	0.021(4)	0.089(13)	0.028(5)	-0.089(11)	-0.033(6)

XVIII. Structural information of Cd_6Tb 1/1 approximant at 192K

Symbol	Wyckoff site	x/a	y/b	z/c		Biso/eq
Tb1	8f	0.34971(6)	0.06058(7)	0.09964(6)		0.0062(1)
Tb2	8f	0.35103(6)	0.43939(7)	0.10025(6)		0.0063(1)
Tb3	8f	0.09489(6)	0.05047(7)	0.15539(6)		0.0060(1)
Tb4	8f	0.74612(7)	0.25066(3)	0.19546(8)		0.0060(1)
Tb5	8f	0.55525(8)	0.24975(3)	0.00608(7)		0.0067(2)
Tb6	8f	0.09515(6)	0.45209(7)	0.15526(6)		0.0062(1)
Cd1	8f	0.33411(12)	0.24951(3)	0.17746(9)		0.0245(5)
Cd2	8f	0.37410(7)	0.15628(6)	0.37545(8)		0.0307(4)
Cd3	8f	0.49982(5)	0.58991(6)	0.59024(5)		0.0128(2)
Cd4	8f	0.33809(5)	0.41287(7)	0.25018(5)		0.0144(2)
Cd5	8f	0.46008(5)	0.58996(6)	0.08965(6)		0.0111(2)
Cd6	8f	0.38065(16)	0.34076(13)	0.36815(17)		0.0344(7)
Cd6'	8f	0.6130(3)	0.3401(3)	0.1361(2)	0.239	0.0071(8)
Cd7	8f	0.24896(2)	-0.44054(6)	0.00125(2)		0.0103(3)
Cd8	8f	0.34036(5)	-0.08980(7)	0.20790(5)		0.0107(2)
Cd9	8f	0.34111(5)	0.59302(6)	0.20794(5)		0.0102(2)

Cd10	8f	0.23085(5)	0.54826(7)	0.13986(5)		0.0118(2)
Cd11	8f	0.15539(7)	0.24939(3)	0.09540(6)		0.0101(2)
Cd12	8f	0.49986(5)	0.08900(7)	0.08843(5)		0.0140(2)
Cd13	8f	0.53989(5)	0.08988(6)	-0.09166(6)		0.0111(2)
Cd14	8f	0.22835(5)	-0.05052(7)	0.13768(5)		0.0105(2)
Cd15	8f	0.33968(6)	0.09084(7)	0.25094(5)		0.0154(2)
Cd16	8f	0.40431(6)	-0.24966(3)	0.15471(6)		0.0095(2)
Cd17	8f	0.42434(8)	0.24907(3)	0.08185(11)		0.0253(5)
Cd18	8f	0.38862(5)	0.44945(7)	0.47829(5)		0.0106(2)
Cd19	8f	0.38996(5)	0.04833(7)	0.48062(5)		0.0111(2)
Cd20	4e	0.5	0.65830(8)	0.25		0.0207(4)
Cd21	8f	0.45424(6)	0.49244(9)	0.20385(6)		0.0206(3)
Cd22	8f	0.43041(5)	0.63214(7)	0.47957(5)		0.0113(2)
Cd23	8f	0.43033(5)	0.13288(7)	-0.02127(5)		0.0112(2)
Cd24	8f	0.22982(5)	0.36745(7)	0.17914(5)		0.0102(2)
Cd25	8f	0.45396(6)	0.01508(9)	0.20394(6)		0.0184(3)
Cd26	8f	0.52905(6)	-0.24968(3)	0.12548(6)		0.0094(2)
Cd27	8f	0.22997(5)	0.13150(7)	0.17968(5)		0.0107(2)
Cd28	8f	0.37521(6)	-0.24850(3)	0.27903(6)		0.0084(2)
Cd29	8f	0.32696(4)	-0.15409(5)	0.07708(4)		0.0083(2)
Cd30	8f	0.20238(4)	0.40323(5)	0.04800(5)		0.0082(2)
Cd31	8f	0.29728(10)	0.25045(3)	0.04717(10)		0.0213(4)
Cd32	8f	0.29803(4)	0.40454(5)	-0.04789(5)		0.0081(2)
Cd33	8f	0.32689(4)	-0.34538(5)	0.07708(4)		0.0083(2)
Cd34	4e	0.5	-0.15306(8)	0.25		0.0222(4)
Cd35	8f	0.29704(9)	0.25789(6)	0.45276(9)		0.0252(4)
Cd702	8f	0.46282(17)	0.17465(20)	0.29784(19)	0.656	0.0640(11)
Cd701	8f	0.44894(12)	0.31743(14)	0.20930(13)	0.384	0.0426(9)
Cd703	8f	0.4654(4)	0.3325(5)	0.2923(5)	0.29	0.084(3)
Cd704	8f	0.4189(3)	0.2500(5)	0.2396(3)	0.274	0.058(4)
Cd705	8f	0.4229(2)	0.2502(3)	0.2648(3)	0.396	0.066(3)

XIX. Anisotropic displacement parameters (Å^2) of the Cd_6Tb 1/1 approximant at 192K

Symbol	U_{11}	U_{22}	U_{33}	U_{12}	U_{13}	U_{23}
Tb1	0.0086(2)	0.00354(14)	0.0063(2)	0.00081(14)	0.00336(16)	-0.00061(13)
Tb2	0.0085(2)	0.00361(14)	0.0068(2)	-0.00093(14)	0.00386(16)	0.00021(13)
Tb3	0.0080(2)	0.00508(14)	0.0050(2)	0.00046(14)	0.00182(15)	-0.00036(13)
Tb4	0.0092(3)	0.0037(2)	0.0052(2)	0.0002(1)	0.0019(2)	-0.00021(9)
Tb5	0.0093(3)	0.0026(2)	0.0081(3)	0.00004(9)	0.0022(2)	0.00010(9)
Tb6	0.0081(2)	0.00538(14)	0.0051(2)	-0.00038(14)	0.00175(15)	0.00003(14)
Cd1	0.0437(11)	0.0076(5)	0.0223(7)	0.0005(2)	0.0244(7)	0.0002(2)
Cd2	0.0413(7)	0.0068(3)	0.0440(8)	0.0053(4)	-0.0331(5)	-0.0053(4)
Cd3	0.0103(4)	0.0086(3)	0.0196(4)	-0.0019(3)	0.0013(4)	0.0082(3)

Cd4	0.0257(5)	0.0121(4)	0.0054(3)	-0.0103(3)	0.0024(4)	-0.0017(3)
Cd5	0.0067(3)	0.0060(3)	0.0205(5)	-0.0011(2)	-0.0005(3)	0.0041(3)
Cd6	0.0379(12)	0.0079(6)	0.0572(16)	-0.0084(6)	-0.0390(11)	0.0093(7)
Cd6'	0.0096(17)	0.0123(13)	-0.0005(12)	0.0048(13)	0.0131(11)	-0.0057(11)
Cd7	0.0138(5)	0.0056(3)	0.0116(5)	-0.00045(17)	-0.0035(3)	0.00059(16)
Cd8	0.0147(4)	0.0071(3)	0.0104(4)	-0.0016(3)	0.0009(3)	0.0019(3)
Cd9	0.0146(4)	0.0055(3)	0.0104(4)	0.0018(3)	0.0018(3)	-0.0006(3)
Cd10	0.0118(4)	0.0087(3)	0.0149(4)	-0.0037(3)	0.0051(3)	-0.0046(3)
Cd11	0.0171(5)	0.0054(3)	0.0079(4)	0.00000(17)	0.0065(3)	-0.00031(15)
Cd12	0.0109(4)	0.0102(3)	0.0210(4)	-0.0019(3)	0.0014(4)	0.0099(3)
Cd13	0.0072(3)	0.0056(3)	0.0204(5)	0.0012(2)	-0.0018(3)	-0.0042(3)
Cd14	0.0110(4)	0.0082(3)	0.0123(4)	0.0032(3)	0.0040(3)	0.0040(3)
Cd15	0.0257(5)	0.0148(4)	0.0058(3)	0.0115(3)	0.0026(4)	0.0022(3)
Cd16	0.0085(5)	0.0107(3)	0.0094(4)	0.00023(17)	0.0023(3)	0.00006(17)
Cd17	0.0207(7)	0.0034(4)	0.0519(12)	-0.00168(19)	0.0305(8)	-0.0020(2)
Cd18	0.0145(4)	0.0052(3)	0.0122(4)	0.0023(3)	0.0062(3)	0.0003(3)
Cd19	0.0155(4)	0.0053(3)	0.0123(4)	-0.0028(3)	0.0062(3)	-0.0003(3)
Cd20	0.0262(8)	0.0065(4)	0.0295(9)	0	0.0193(6)	0
Cd21	0.0094(4)	0.0405(6)	0.0120(5)	-0.0048(4)	0.0015(3)	-0.0056(4)
Cd22	0.0125(4)	0.0128(4)	0.0086(4)	-0.0035(3)	0.0021(3)	-0.0002(3)
Cd23	0.0130(4)	0.0127(4)	0.0078(3)	-0.0039(3)	0.0021(3)	-0.0002(3)
Cd24	0.0124(4)	0.0102(3)	0.0080(3)	-0.0032(3)	0.0011(3)	0.0029(3)
Cd25	0.0100(4)	0.0325(5)	0.0126(5)	0.0046(4)	0.0014(3)	0.0038(4)
Cd26	0.0098(5)	0.0090(4)	0.0094(4)	0.00011(16)	0.0039(3)	0.00029(16)
Cd27	0.0116(4)	0.0117(4)	0.0090(4)	0.0031(3)	0.0008(3)	-0.0038(3)
Cd28	0.0137(5)	0.0052(3)	0.0062(4)	0.00062(17)	0.0014(3)	-0.00018(15)
Cd29	0.0108(4)	0.0048(2)	0.0094(4)	0.0027(2)	0.0015(2)	-0.0007(2)
Cd30	0.0095(4)	0.0062(2)	0.0091(4)	-0.0021(2)	0.0030(2)	0.0010(3)
Cd31	0.0225(8)	0.0079(3)	0.0334(10)	0.00073(19)	-0.0190(5)	-0.0003(2)
Cd32	0.0093(4)	0.0057(2)	0.0095(4)	0.0017(2)	0.0031(2)	-0.0006(3)
Cd33	0.0112(4)	0.0045(2)	0.0091(4)	-0.0026(2)	0.0015(2)	0.0010(2)
Cd34	0.0270(9)	0.0075(4)	0.0320(9)	0	0.0218(6)	0
Cd35	0.0120(6)	0.0494(7)	0.0142(6)	-0.0002(3)	0.0014(4)	-0.0001(3)
Cd702	0.075(2)	0.0376(11)	0.079(2)	-0.0010(12)	0.0368(17)	0.0376(12)
Cd701	0.0501(18)	0.0180(9)	0.0596(19)	0.0059(10)	-0.0371(14)	0.0019(10)
Cd703	0.095(6)	0.044(3)	0.114(7)	-0.010(3)	0.057(5)	-0.062(4)
Cd704	0.0060(17)	0.161(12)	0.007(2)	0.0040(18)	-0.0075(11)	-0.002(3)
Cd705	0.0103(16)	0.167(9)	0.021(3)	-0.0065(15)	0.0153(16)	-0.004(2)